Oxy-fuel Combustion for Carbon Capture using Computational Fluid Dynamics

Alexander John Black

Submitted in accordance with the requirements for the degree of
Doctor of Philosophy

The University of Leeds
Energy Technology and Innovation Initiative

May, 2014

The candidate confirms that the work submitted is his own, except where work which has formed part of jointly authored publications has been included. The contribution of the candidate and the other authors to this work has been explicitly indicated below. The candidate confirms that appropriate credit has been given within the thesis where reference has been made to the work of others.

The work in Chapter 6 of the thesis has appeared in the publications as follows:
Black S., Szuhánszki J., Pranzitelli A., Ma L., Stanger P.J., Ingham D.B., and Pourkashanian M. Effects of firing coal and biomass under oxy-fuel conditions in a power plant boiler using CFD modelling. *Fuel*, 113:780-786, 2013.
Szuhánszki J., Black S., Pranzitelli A., Ma L., Stanger P.J., Ingham D.B., and Pourkashanian M. Evaluation of the Performance of a Power Plant Boiler Firing Coal, Biomass and a Blend Under Oxy-fuel Conditions as a CO_2 Capture Technique. *Energy Procedia*, 37:1413-1422, 2013.
In both papers, I was responsible for the CFD modelling and set-up of the oxy-fuel cases, Janos Szuhánskzi performed the air-fired cases and the original mesh was generated by Doosan Babcock, improved by Dr P Stanger and further optimised by Dr A Pranzitelli. Supervision was provided by Dr L Ma, Prof D. B. Ingham and M. Pourkashanian.

Acknowledgements

It is my belief that a thesis is near impossible to complete without the support of your supervisors, friends and loved ones. I am indebted to my supervisors, Prof. Mohamed Pourkashanian, Dr Lin Ma and Prof. Derek Ingham and for their guidance and support. A special thank you goes to my partner, Debbie, for all of the encouragement, support and putting up with the never ending task of doing a PhD. I do not want to think about the amount of coffee consumed over the past 4 years and I am eternally grateful to all of my friends at Leeds for many helpful discussions. In particular, thank you to Janos for his tremendous help at the beginning and throughout the PhD to help answer countless questions, Alessandro for his guidance and honesty, Alastair for his enthusiasm and constantly questioning everything. Outside of the PhD, I really did enjoy the lengthy walks in the Yorkshire Dales with Sam, Ray and Janos. Finally, I want to acknowledge the financial support from the EPSRC-OxyCAP project that supported this PhD.

I. Distribution of work

The research has been carried out by a team which has included Janos Szuhánskzi, Alastair Clements, Dr R Porter, Dr P Stanger (Edge), Dr Alessandro Pranzitelli from the University of Leeds and Benjamin Franchetti and Fabrizio Cavallo Marincola from Imperial College. Also, Prof DB Ingham, Dr L Ma and Prof M Pourkashanian provided supervision and advice. My own contributions, fully and explicitly indicated in the thesis as well as the other members of the group and their contributions are as follows:

In Chapter 4, the in-house code for the CRIEPI and 100 kW oxy-fuel combustion test cases were provided by the Imperial College group. I implemented and tested the NO_x model for both of these cases and performed some parameter studies which are explained in Chapter 4. The experimental data in Chapter 5 was performed by Janos Szuhánskzi under the supervision of Dr B Nimmo. I was present during the experiments and developed a program to extract the data. The CFD simulations were set-up and performed by myself however the FSCK model was developed by Dr R Porter and optimised by Alastair Clements. Chapter 6 includes two jointly authored papers, entitled *Effects of firing coal and biomass under oxy-fuel conditions in a power plant boiler using CFD modelling* and *Evaluation of the Performance of a Power Plant Boiler Firing Coal, Biomass and a Blend Under Oxy-fuel Conditions as a CO_2 Capture Technique.* In both cases, the CFD modelling and set-up of the oxy-fuel cases were performed by myself, Janos Szuhánskzi performed the air-fired cases and the original mesh was generated by Doosan Babcock, improved by Dr P Stanger and further optimised by Dr A Pranzitelli.

Abstract

The combustion of fossil fuels, in particular coal, meets the majority of energy demand worldwide, but produces carbon dioxide, which is believed to be the main cause of climate change. Since the majority of energy comes from coal-fired power stations, the deployment of carbon capture and storage (CCS) technologies, which remove the CO_2 by either utilisation or storage, are necessary to mitigate climate change.

Oxy-fuel combustion is one of the leading options for CCS. The fuel combusts in a mixture of oxygen and recycled flue gas, rather than in air and the change in the oxidiser environment poses questions relating to combustion characteristics such as heat transfer, emissions and burnout. To gain a further understanding of the process, the use of modelling and simulation techniques can be employed and in this thesis, Computational Fluid Dynamics (CFD) is used to model air and oxy-fuel environments using advanced combustion sub-models.

An in-house Large Eddy Simulation (LES) CFD code has been updated to include models suitable for the prediction of NO. The model is verified and compared against available experimental data for three cases involving methane, coal and oxy-coal combustion.

Advanced simulations of a 250 kW_{th} combustion test facility (CTF) are validated against experimental measurements of air-coal combustion. The geometry set-up and simplifications are discussed followed by a sensitivity study of grid refinement, turbulence models and approaches in modelling gaseous radiative properties. The validated CFD simulation of the facility were then numerically examined under a number of oxy-fuel environments.

Finally, CFD simulations were performed on a full-scale utility boiler at 500 MW_e to examine the effects of firing coal and biomass under air and oxy-fuel environments. This included an assessment of the heat transfer as a method of addressing the performance of the boiler under these conditions.

Contents

List of Tables

List of Figures

Nomenclature

Abbreviations

a.r.	as received
ASU	air separation unit
BET	Brunauer-Emmett-Teller
CAD	computer-aided design
CBK	carbon burnout kinetics
CCD	charge-coupled device
CCS(U)	carbon capture and storage (and utilisation)
CFD	computational fluid dynamics
CIA	carbon in ash
CNG	compressed natural gas
CPD	Chemical Percolation Devolatilisation
CRIEPI	Central Research Institute of Electrical Power Industry
CTF	combustion test facility
d.a.f.	dry ash free
DNS	Direct Numerical Simulation
DO(M)	discrete ordinates (model)
DTM	discrete transfer methods

EDC	eddy dissipation concept
EDM	eddy dissipation model
EOR	enhanced oil recovery
ESP	electrostatic precipitator
EWBM	exponential wide band model
FDF	filtered density function
FEED	front end engineering design
FG-DVC	Functional Group Deployment Vapourisation Cross Linking
FGD	flue gas desulphurisation
FRH	final reheater
FSCK	full spectrum correlated-k
GHG	greenhouse gases
I.D.	inner diameter
IFRF	International Flame Research Foundation
IGCC	integrated gasification combined cycle
LCPD	Large Combustion Plant Directive
LDV	laser doppler velocimetry
LES	Large Eddy Simulation
LES_IQ	LES index resolution quantity
LIF	laser-induced fluorescence

MEA	monoethanolamine
P.A.	proximate analysis
PACT	pilot-scale advanced capture technology
PDE	partial differential equation
PDF	probability density function
PIV	particle image velocimetry
ppm	parts per million
RANS	Reynolds-averaged Navier-Stokes
RFG	recycled flue gas
RNG	renormalisation group
RSM	Reynolds stress model
RTE	radiative transfer equation
SCR	selective catalytic reduction
SGS	sub-grid scale
SNB	statistical narrow band
SNCR	selective non-catalytic reduction
SPDA	shadow Doppler particle analyser
SSH	secondary superheater
SST	shear stress transport
TCI	turbulent chemistry interaction

TRI	turbulent radiation interaction
TVD	total variation diminishing
U.A.	ultimate analysis
UDF	user defined function
UKCCSRC	United Kingdom carbon capture and storage research centre
UNFCC	United Nations Framework on Climate Change
URANS	unsteady Reynolds-averaged Navier-Stokes
WSGG(M)	weighted sum of gray gas (model)

Greek Symbols

β	temperature exponential / beta function	-
Δ_i	cell width in $i = x$, y or z direction	m
Δ_w	filter cut off width used in LES	m
δij	Kronecker delta $\delta ij = 1$ if $i = j$, 0 if $i \neq j$	-
ϵ	emissivity	1/m
κ	absorption coefficient	1/m
κ_w	wavenumber $= \frac{2\pi f}{U}$	$1/\mathcal{L}$
λ	wavelength	1/m
μ	dynamic viscosity of the fluid	kg/m-s
μ_L	Kolmogorov length scale	m
ν	kinematic viscosity of the fluid	m^2/s

ϕ	scalar value	-
ϕ_{eq}	equivalence ratio	-
ρ	density of a gas	kg/m^3
σ_p	particle scattering factor	
σ_s	scattering coefficient	1/m
σ_h	Prandtl number $= c_p\mu/k$	-
σ_{sb}	Stefan-Boltzmann constant $= 5.67 \times 10^8$	W/m^2-K^4
τ_{ij}	stress tensor	kg/m-s^2
ε	rate of dissipation of turbulent kinetic energy per unit mass	m^2/s^3

Roman Symbols

$\mathcal{E}$	energy spectrum function	m
$\mathcal{L}$	characteristic length scale	m
$\mathcal{U}$	characteristic velocity	m/s
$\nu''_{i,r}$	stoichiometric coefficient of product i in reaction r	-
$\nu'_{i,r}$	stoichiometric coefficient of reactant i in reaction r	-
σ^2	variance	-
A	surface area	m^2
A_r	pre-exponential factor	1/s
A_{BET}	BET surface area	m^2/kg
c_p	specific heat at constant pressure	J/kg-K

$c_{particles}$	concentration of particles	kg/m^3
C_{sgs}	Smagorinsky constant	-
D_i	mass diffusivity of species i	m^2/s
E	specific energy $= h - p/\rho + (u_1^2 + u_2^2 + u_3^2)/2$	J/kg
E_a	activation energy	J/kmol
g_i	gravity component in the i direction	m/s^2
h	enthalpy per unit mass	J/kg
h_c	heat transfer coefficient	W/m^2-K
h_i	sensible enthalpy of species i	J/kg
I_λ	spectral radiance	W/sr-m^3
k	kinetic energy	J
k	reaction rate of the form $= A_r T^\beta \exp(-E_a/(RT))$	1/s
k_{th}	thermal conductivity	W/m-K
k_{wall}	thermal conductivity of the wall	W/m-K
Le	Lewis number $= k_{th}\rho^{-1}c_p^{-1}D_i^{-1}$	-
m	mean value	-
m_i	mass of property i	-
MW_i	molecular weight of species i	g/mol
N_{split}	nitrogen split	-
p	pressure	kg/m-s^2

Q	high temperature volatile yield	-
q_r	radiant flux i	W/m^2
$q_{rad,wall}$	heat flux at the wall due to radiation	W/m^2
Q_{wall}	heat flux at a thin wall	W/m^2
R	universal gas constant = 8314.47	J/kmol-K
r	radial component / radius	mm
R_i	reaction rate of reaction i	mol/m^3
R_{inner}	inner radius of a pipe	m
R_{outer}	outer radius of a pipe	m
Re	Reynolds number $=\mathcal{U}\mathcal{L}/\nu$	-
S	swirl number	-
S_Φ	source term of property Φ	kg/m^3-s
S_g	geometric swirl number $= U_s/W_s$	-
S_{ij}	strain tensor $= \frac{1}{2}\left(\frac{\partial u_i}{\partial x_j} + \frac{\partial u_j}{\partial x_i}\right)$	1/s
S_{mfr}	mass flow rate in secondary register	kg/s
$S_{sec,ter}$	mass flow split between secondary and tertiary registers	-
Sc	Schmidt number $= \nu/D$	-
SF	shape factor	-
T	temperature	K
t	time	s

T_{mfr}	mass flow rate in tertiary register	kg/s
U_c	bulk axial velocity of coflow	m/s
U_f	bulk axial velocity of fuel	m/s
u_i	velocity component in the i direction	m^2/s
U_s	bulk axial velocity of swirled primary air	m/s
U_{bulk}	average / bulk velocity	m/s
U_{max}	maximum velocity	m/s
V	cell volume	m^3
W_i	molecular weight of chemical species	kg/kmol
W_s	bulk tangential velocity of swirled primary air	m/s
X_i	mole fraction of species i	-
x_i	spatial component in the i direction	m
Y_i	mass fraction of species i	-
z	axial component / distance	mm
Z_{st}	stoichiometric mixture fraction	-
s	particle surface area of equivalent sphere	m^2

Subscripts

b	backward reaction rate
eff	effective component, sum of laminar and turbulent quantities
f	forward reaction rate

l	laminar quantity
num	numerical component
p	particle component
sgs	sub-grid scale quantity
t	turbulent quantity

Mathematical Symbols

$\langle\Phi\rangle$	time-averaged quantity of an instantaneous variable Φ	-
$\overline{\Phi}$	spatial filter operator on Φ	-
Φ'	fluctuating component of an instantaneous variable Φ	-
$\widehat{\Phi''}$	Favre-averaged fluctuation value $= 0$	-
$\widehat{\Phi}$	Favre-averaged value $= \langle\rho\Phi\rangle \,/\, \langle\Phi\rangle$	-
$\widetilde{\Phi''}$	Favre-filtered fluctuation value	-
$\widetilde{\Phi}$	Favre-filtered value $= \overline{\rho\Phi}/\overline{\Phi}$	-
[X]	molecular concentration of chemical species X	kmol/m^3

Chapter 1

Introduction and motivation

World energy consumption has increased 52% in the past 20 years, from 8,196 equivalent million tonnes of oil (Mtoe) in 1992 to 12,476 Mtoe in 2012 [1]. In the next 20 years, the consumption of energy is expected to grow approximately 36% [2]. Evidence of this comes from China and India where rapid industrialisation and economic growth has led to a surge of energy demand in recent years [3]. Unfortunately, the demand for energy still outweighs the consumption of energy and approximately 1.3 billion people worldwide still remain without electricity [3]. The population is predicted to increase another 36% in the next 20 years and it is expected that demand will grow twice as fast as consumption. It is therefore clear that an increase in energy production will therefore be required to meet demand.

The power generation industry uses a combination of fossil fuels, renewable sources, hydro and nuclear power to generate electricity worldwide. The fuel mix has changed due to prices, technological developments and policies and the change in fuel sources from 1970 to 2012 is shown in Figure 1.1. Oil contributed a significant percentage to power generation before 1970, but due to high prices was replaced by nuclear power in 1970 to 1980. During 1990 and 2000, the percentage of gas rose mainly due to combined cycle gas turbine technology, but coal usage also increased, reflecting growing markets in emerging economies [2]. Policies surrounding climate change, as well as government subsidies, have led to an increase in ‘greener’ technologies such as renewables, which includes the use of biomass, in the energy mix. Predictions up to 2030 expect fossil fuels to still be the dominant fuel source but with a significant increase in renewables [2].

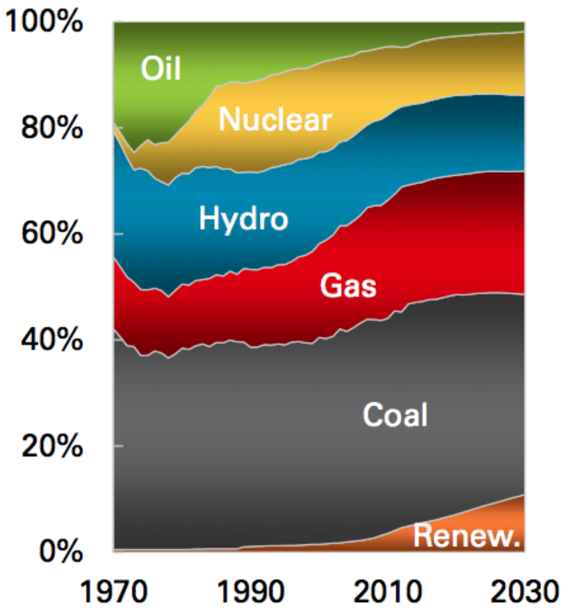

Figure 1.1: Fuel sources for power generation from 1970 to 2012 with predictions up to 2030 [2].

From 2000 to 2010, the growth in coal in emerging economies was 45% compared to 25% in non-fossil fuel power generation [3, 4]. China attributed to half of the world's coal consumption in 2012 and accounted for the overall net world growth [5]. Developments in shale gas technologies have also led to an increased use of gas fired power generation. However, projections into the future energy mix still see coal, which is currently used to fuel approximately 40% of the worldwide electricity generated, as a dominant fuel source despite the increases in shale gas availability and developments in renewable energy technologies [2–4].

Coal has been used as a fuel source since the beginning of the industrial revolution due to its wide availability and high energy density. Coal is a dominant fuel source in the energy mix and if the current rate of production is maintained, coal is still optimistically predicted to last for over 100 years [5]. In 2012, coal attributed 30.3% of the total market share to meet the overall global energy consumption, compared to oil and gas at 33.1% and 23.7%, respectively, with the remaining 12.9% being derived from non-fossil fuel technologies [5]. However, the combustion of coal can release toxic products from power stations which can be harmful to the environment and human health. Emissions of greenhouse gases, such as sulphur oxides (SO_x) and nitrogen oxides (NO_x), contribute to the formation of acid rain. Power stations can use flue gas desulphurisation (FGD) to remove the sulphur dioxide from the flue gas and produce gypsum which can be sold to the building industry. The use of low-NO_x burners or selective catalytic reduction techniques can be used to lower the emissions of NO_x either in-flame or after combustion. In general, the motivation behind these technological developments has been driven by environmental policies and government legalisation which may impose hefty fines if power stations fail to comply with these limits.

Carbon dioxide is another greenhouse gas which has received much attention over the past two decades and is believed to be the main contributor to global warming. Carbon dioxide currently accounts for approximately 15% of the flue gas concentration by volume in coal combustion. The energy sector emits approximately 60% of the greenhouse gases [6] and therefore recent focus has been on the power sector to cut down on CO_2 emissions by developing CO_2 mitigating technologies in the hope this will reduce the impact of global warming.

1.1 Global warming

Global warming describes the increase in temperature of the world's oceans and atmosphere from the beginning of the 20th century. The average temperature of the land and seas over a 100 year period (1906-2005) has increased by about 0.74 °C [7]. Observation of reduced snow cover, melting of glaciers and rising sea levels also support the evidence for global warming. The cause of global warming is believed to be due to the increased concentrations of greenhouse gases[1] (GHG) in the atmosphere, and the source is highly likely to be due to human activity [7].

---

[1] Greenhouse gases consist of carbon dioxide (CO_2), methane (CH_4), nitrous oxide (N_2O), hydrofluorocarbons (HFCs), Perfluorocarbons (PFCs) , sulphur hexafluoride (SF_6) and nitrogen trifluoride (NF_3) [8].

The climate is determined from the energy from the sun which is absorbed, reflected and emitted by the Earth's atmosphere and surface. Changes in the concentrations of gases in the atmosphere can therefore alter this flux of energy. Greenhouse gases primarily act to increase the absorption properties of the atmosphere from the outgoing radiation of the Earth's surface. Therefore, an accumulation of these gases can lead to a net increase in radiative forcing[2] [7].

Carbon dioxide is an anthropogenic GHG, which has increased from approximately 280 parts per million (ppm) before the time of the industrial revolution to nearly 400 ppm in 2013 [9]. Before the industrial revolution, the levels of CO_2 concentrations varied between 180-330 ppm[3].

One of the possible reasons for the increased levels of CO_2 emissions over the past 250 years is the burning of fossil fuels. The carbon dioxide emissions from fossil fuel combustion are shown in Figure 1.2. It is apparent that an exponential increase in CO_2 emissions started to occur from around 1750-1850; at the same time as the beginning of the industrial revolution. This trend is expected to increase unless the growth of energy is decreased, the source of energy is made cleaner and government policies to tackle climate change are adapted [3, 4, 10].

Governments policies have begun to tackle climate change at national and international levels. The Kyoto Protocol was introduced in 1997 and implemented in 2005, which committed countries who are part of the United Nations Framework on Climate Change (UNFCC) to reduce GHG emissions [12]. The first stage of assessment was evaluated at the end of 2012 and an amendment to the Kyoto Protocol was implemented in December 2012 called the Doha Amendment which covers the second commitment period between 2013 - 2020 [8]. In this period, countries are committed to reducing greenhouse gas emissions by 18% below the levels recorded in 1990.

---

[2] Radiative forcing is a term used by the Intergovernmental Panel on Climate Change to describe a factor that measures the influence of incoming and outgoing energy from the Earth's atmosphere system.

[3] Based on ice-core measurements which can give data up to 650,000 years.

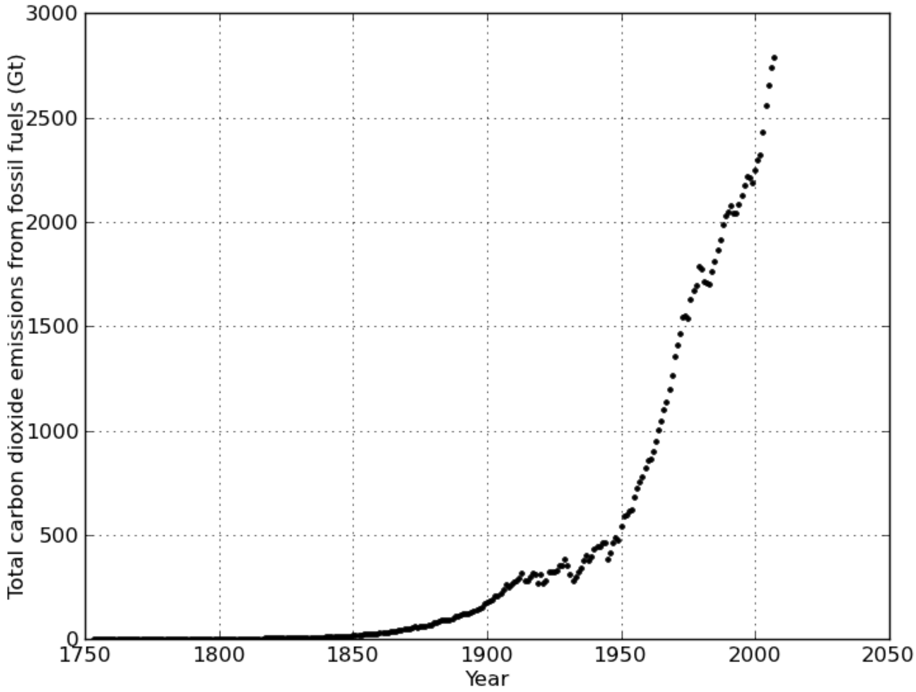

Figure 1.2: Total carbon dioxide emissions from fossil fuel combustion for the world from 1752 to 2007 as given by [11].

In the European Union, power generation is overseen by the EU Emission Trading Scheme which was first implemented in 2005. The overall volume of greenhouse gas emissions are regulated by means of an allowance which is decreased yearly to encourage lower emissions every year. Factories, power plants and other heavy industry receive or can purchase an allowance to cover their greenhouse gas emissions, if the allowance is exceeded a heavy penalty can be imposed.

The Large Combustion Plant Directive (LCPD, 2001/80/EC) specifies limits on NO_x, sulphur dioxide and dust emissions in Europe. The legislation is part of the Industrial Emission Directive 2010/75/EU. The UK has 25 GW of coal-fired power generation, however the legislation has led to over 7 GW of coal-fired power plants opting to close rather than meet the costs of emissions by 2016 [4].

The Industrial Emission Directive 2010/75/EU for new power plants also imposes stricter limits on emissions [13]. For power plants between 100-300 MW_e, the emissions of NO_x and sulphur dioxide are both 200 mg/Nm^3 corrected to 6% O_2 in the flue gas and particulates are 20 mg/Nm^3. Power plants with a capacity greater than 300 MW_e have emission limits of 150 mg/Nm^3 for NO_x and sulphur dioxide, and 10 mg/Nm^3 for particulates.

In the United Kingdom, the introduction of the Climate Change Act 2008 [14] has committed the country to a 34% reduction in the levels of GHG by 2020 and 80% reduction by 2050 compared with those levels recorded in 1990. The UK government has proposed the Electricity Market Reform whereby a strike price is agreed between the government and the generator through a Contract for Difference. If the market revenue (£/MW_h) is lower than the agreed strike price, the government will contribute the difference between the strike price and the market revenue. If the market revenue is higher than the agreed strike price, the generator will pay back the difference. As part of the Electricity Market reform, the Emissions Performance Standard has recommended the limit of 450 g CO_2/kWh for new coal and gas power stations [4].

Other countries such as Australia, China, India, Indonesia and the United States have begun to implement similar taxes and policies to mitigate GHG emissions [4].

1.2 Conventional coal-fired power station overview

A typical pulverised coal power plant layout is shown in Figure 1.3. As an overview, heat is generated from the combustion of coal in a steam boiler which converts cooler water entering the boiler into steam. The steam is then passed through a steam turbine which generates the electricity. The steam is condensed and recycled back to the boiler where the process is repeated.

The correct distribution of heat transfer from the combustion process is important for the steam cycle. The tube banks carry the water and steam from the boiler to the turbines and generally consist of water walls, superheaters (19), reheaters (21)

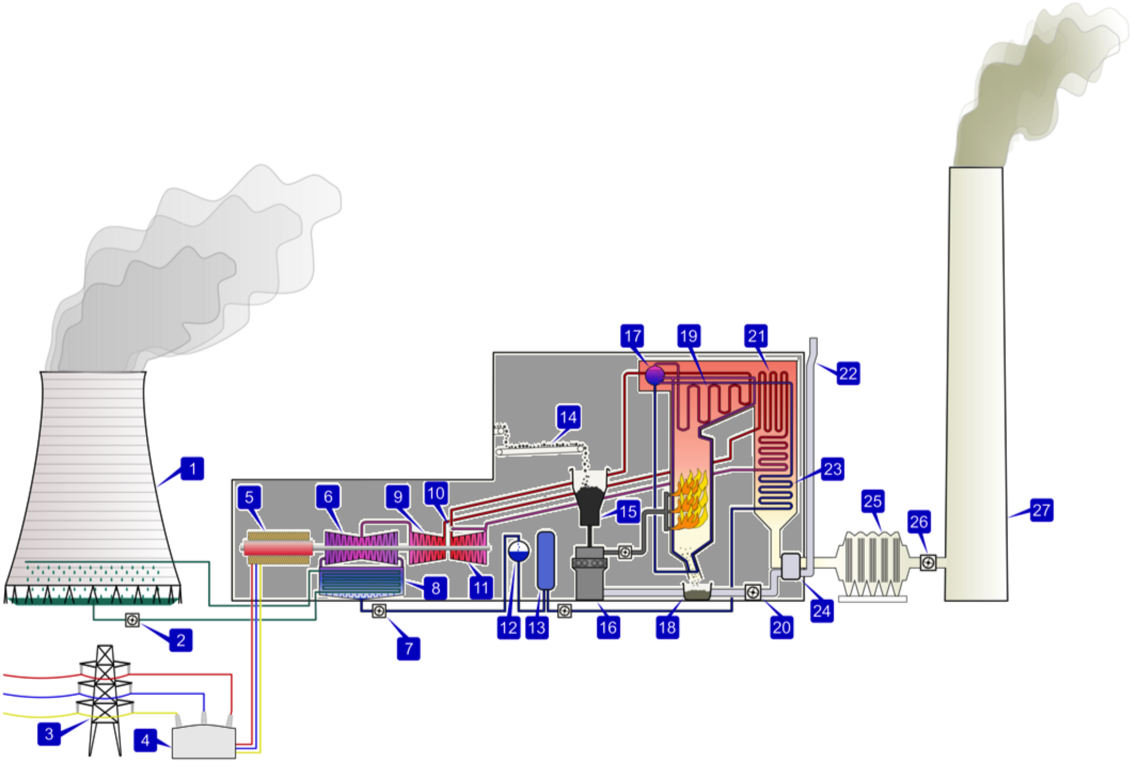

Figure 1.3: Schematic of the layout of a power station.

and economisers (23). Water is passed into the economiser (23) before entering the steam drum (17), located at the top of the boiler which contains pressurised water. The water is passed down numerous tubes surrounding the boiler, called the water walls, and partially evaporates due to the heat from the combustion process. Due to the change in density, the water recirculates back to the water drum. The steam generated is then passed to the superheater sections (19) where it is further heated before being passed to the high pressure turbine (11). The steam from the high pressure turbine is then passed back into the boiler further downstream where the hot combustion gases heat the tube banks in the reheater section (21). The reheated steam is then passed to the intermediate pressure turbine (9) and then the low pressure turbine (6). Once the steam exits the low pressure turbine it is condensed, and after any filtration, is passed to the economiser where the cycle is repeated. A generator (5) converts the mechanical energy of the turbines into electrical energy.

To provide the heat for the steam cycle, coal is used as the fuel. Coal is transported along a conveyer (14) to a hopper (15) before being fed to a mill (16). Coal is typically pulverised to a size less than 300 μm before entering the boiler as this increases the surface area available for combustion. Carrier air is blown up through the mill carrying the smaller particles to the boiler and allowing the larger particles to remain in the mill. A forced draft fan generally controls the air to the furnace while an induced fan (26) removes the flue gas and controls the furnace pressure.

The pulverised coal and air enters the boiler through a burner. A burner is typically installed to achieve desired criterion, such as low emissions of pollutants and high carbon burnout by inducing turbulence and therefore mixing between the coal particles and oxidiser, which is conventionally air. A burner may include blades to produce swirled combustion air, a flame holder to root the flame and help with flame stability and a refractory quarl. Preheated combustion air can also be used to assist with the combustion and emission levels, as well as lowering the heat loss from the power plant. A boiler will typically contain an arrangement of burners. The configurations include wall-fired boilers where the burners are placed at one side of the wall or tangentially fired boilers where the burners are placed at opposite ends.

Combustion takes place inside the furnace section of the boiler and the heat is transferred to the tube banks, such as the water walls and superheaters (19), mainly by radiative heat transfer. Away from the flame, the flue gas temperature is still high and heat transfer to other tube banks, such as the reheater (21) and economiser (23), is mainly caused by convective heat transfer. The bottom ash is collected at the bottom of the boiler (18) and the remaining flue gas contains pollutants such as fly ash, NO_x and SO_x. The induced fan (26) draws the flue gas from the boiler, but modern power stations have a variety of flue gas cleaning equipment before it is vented out of the stack (27). Examples of flue gas equipment include electrostatic precipitators (ESP) to remove fly ash, flue gas desulphurisation (FGD) units to remove SO_x and post-NO_x cleaning equipment, such as selective catalytic reduction (SCR) technology.

A typical coal-fired power station can release 880 kg/MWh of CO_2 from the stack, which is a significant source of CO_2 emission [4, 15]. Since it is believed increased concentrations of CO_2 in the atmosphere contribute to global warming, carbon reducing technologies must therefore be considered to mitigate the high levels of CO_2 released from a power station.

1.3 Carbon reducing technologies

Policies and incentives have encouraged operators of coal-fired power plants to consider different technologies and fuels to reduce carbon dioxide emissions in the flue gas. Two methods that have been proposed are firing with biomass or carbon capture and storage or utilisation (CCSU), or a combination of both approaches.

Biomass has the advantage that it could contribute to the energy mix and increase energy security[4] [16]. Biomass still emits carbon dioxide, however if the biomass is sustainably produced, it could be optimistically stated that it is a carbon neutral fuel as the carbon dioxide is expected to be removed from the atmosphere by the growth of a new generation of crops. Biomass can also decay to form methane which has a more detrimental effect to the environment than CO_2 and therefore combustion of the biomass could also help mitigate greenhouse gases [17].

In the UK, electricity suppliers are obligated to supply a portion of the electricity produced from renewable sources, which includes the use of biomass. Renewable Obligation Certificates are issued for each MW of renewable electricity produced. Power stations commonly co-fire around 10-15% biomass with the remainder of fuel being coal [4], however, some power generators have recently converted to 100% biomass firing, such as Drax Power Station, Yorkshire, England.

---

[4] Energy security is a term used to describe the fuel availability in a country, e.g. a reliance on imported fuels may decrease energy security.

Carbon capture, storage and utilisation (CCSU) refers to the overall process where the CO_2 is prevented from being released into the atmosphere and is either stored or alternatively utilised. The purpose of the storage process is to remove the CO_2 from the carbon cycle so that it may be stabilised, however there are no commercial sized plants that exist with CCS technology. The CO_2 is captured from the combustion process and then transported to a suitable storage site which could include depleted oil and gas reservoirs or saline aquifers. Alternatively, the CO_2 may be utilised, for example for enhanced oil recovery. The technologies have predominantly been focused for use in the power industry, however could be adapted for use in other heavy industries.

According to projections of future energy consumption, the deployment of CCS is necessary to meet government targets and stabilise the carbon cycle [18]. A further benefit of CCS could be if it was combined with sustainably sourced biomass and could lead to carbon negative emissions.

1.4 Carbon capture storage and utilisation

Carbon capture, storage and utilisation (CCSU) can generally be considered as three categories which are capture, transportation and storage or utilisation. For CCSU to be a commercially viable option for CO_2 emission reduction, it is important that these categories work in tandem since they are interconnected technologies.

Carbon capture technologies can be classified into three categories as outlined in Figure 1.4:

(i) Post-combustion

(ii) Pre-combustion

(iii) Oxy-fuel combustion

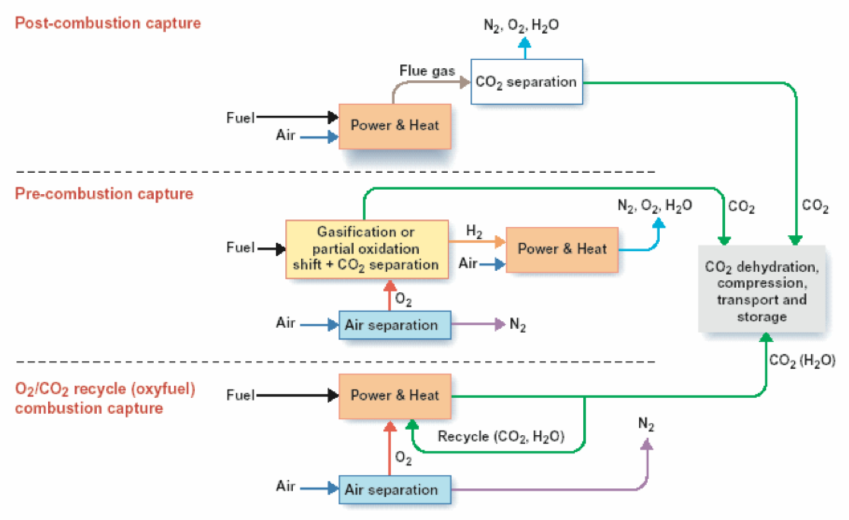

Figure 1.4: Schematic of post-combustion, pre-combustion and oxy-fuel combustion capture technologies [19].

1.4.1 Post-combustion

The post-combustion process is a viable option of CO_2 capture and would occur downstream of the furnace in the flue gas cleaning section, as shown in Figure 1.4, where the separation of CO_2 from the flue gas is performed through solvent based scrubbing. The CO_2 is usually passed through a solvent, such as monoethanolamine (MEA) or hot carbonate, and absorbed [15, 20]. Changes in temperature (MEA) or pressure (hot carbonate) are then used to release the CO_2 as well as regenerate the solvent. Post-combustion technology already exists and is used in the gas sweetening industry and therefore it could be retrofitted to existing power plants. However, a major challenge is the low concentration of CO_2 in the flue gas, resulting in a significant energy requirement for CO_2 release and solvent regeneration as steam is typically bled from the steam cycle. This would result in a power plant efficiency penalty of approximately 10% [21]. Furthermore, the use of flue gas desulphurisation (FGD) units are essential to the process for the current range of solvents since sulphur dioxide (SO_2) adversely affects the capture process by binding to the solvent [20], which may lead to further initial and operational costs.

The largest pilot scale test facility in the UK, Carbon Capture 100+ captured 100 tonne/day of CO_2 from the flue gas at the coal-fired power plant, Ferrybridge Power station in Yorkshire, UK between 2011-2013. The project demonstrated the technology was possible for use with flue gas from coal combustion at a pilot scale, however the project only demonstrated CO_2 capture and not storage. Instead, the CO_2 rich stream was diluted at the end of the process with the cleaned flue gas and vented into the atmosphere. A commercial post-combustion plant on a gas-fired power station at Peterhead power station near Aberdeen in the UK is currently planned. A CCS project is also underway at Boundary Dam in Saskatchewan, Canada which will capture and store 1 million tonnes/year of CO_2 from a 110 MW coal fired power plant.

1.4.2 Pre-combustion

Figure 1.4 shows the process of pre-combustion where the capture of CO_2 occurs before combustion. Using a controlled amount of oxygen (O_2) from an air separation unit and water, the hydrocarbon fuel is gasified to produce a synthesis gas, which consists mainly of carbon monoxide (CO) and hydrogen (H_2). Downstream, the addition of steam to the synthesis gas produces CO_2 and hydrogen through a water gas shift reaction, followed by an absorption process to separate the two gases. The hydrogen gas can then be used in a gas turbine or a fuel cell, while the CO_2 can be transported to a storage site. For coal combustion, this process would be ideally suited for use in an integrated gasification combined cycle (IGCC) with CCS. The main disadvantage of this technology is the cost of building new power plants since this option is not able to be retrofitted to existing coal-fired power plants. However, pre-combustion technology has a lower efficiency point penalty of 7-9% compared to that of post- and oxy-fuel combustion [21], and so is still an option for CCS. In the UK, the Don Valley project in South Yorkshire has proposed a new build 650 MW IGCC power plant, however it has yet to receive government funding.

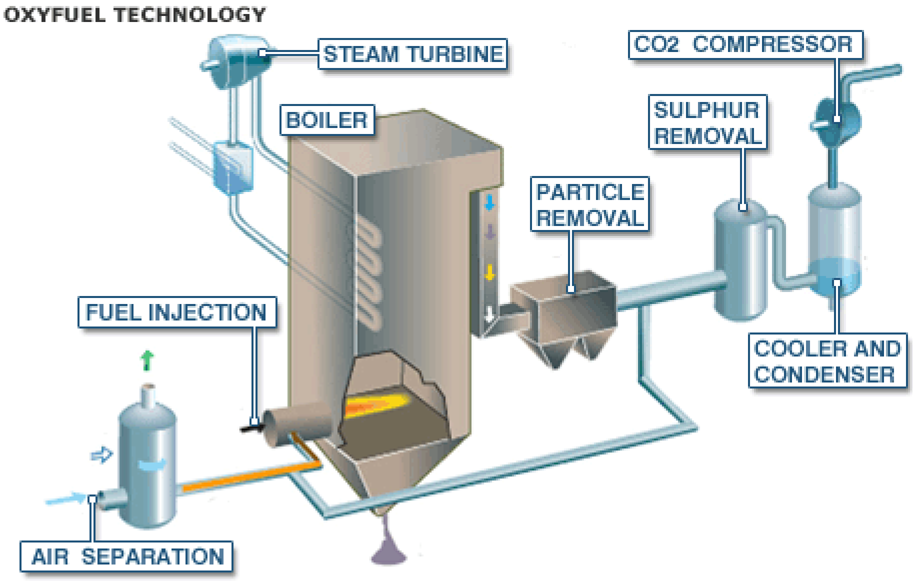

Figure 1.5: An illustrated image of a simple configuration of oxy-coal technology [22].

1.4.3 Oxy-fuel combustion

Oxy-fuel combustion is where the fuel is combusted in a combination of oxygen and recycled flue gas instead of air. The recycled flue gas (RFG) consists of a high concentration of CO_2 and water vapour, which after drying takes place, can be passed into a CO_2-processing unit where it is compressed suitable for storage or utilisation.

A configuration of oxy-coal technology retrofitted to a conventional air-fired plant is depicted in Figure 1.5. Air is separated into oxygen and nitrogen by an air separation unit (ASU). The oxygen is then mixed with the recycled flue gas (RFG), and the pulverised coal is entrained into the mixture shortly before entering the burner. Using the correct ratio of O_2/RFG, which has been reported to be about 30%/70% by volume on a dry basis, combustion can take place with similar temperatures and heat characteristics as air-fired combustion [15, 23]. At the exit of the boiler and after particle removal, the composition of the flue gas is mainly CO_2 and water vapour. Some of the flue gas can either be recycled directly (wet recycle) or passed through a drying unit (dry recycle) before re-entering the boiler, or a combination, as burners usually contain multiple inlets. The CO_2 which is not entered back into a recycle is passed to the CO_2-processing unit where compression takes place.

Several options exist as to the extent of clean-up of the flue gas before being recycled [15]:

(i) Particle removal which can be controlled through the use of electrostatic precipitators (ESP). This is a necessary step to remove the fly ash as it may cause blockage or damage to the recycle line and burners.

(ii) Moisture removal can remove the moisture from the flue gas which can mitigate corrosion issues with acidic gases forming in the pipework. Commercial burners usually have a primary register, which carries some oxidiser (known as carrier gas) and the coal, and a secondary register for the remainder of the oxidiser. It may be useful to dry the carrier gas to prevent agglomeration of wet coal or ignition issues.

(iii) The removal of SO_x from the flue gas can be included by using a flue gas desulphurisation unit (FGD). This may be necessary if moisture is present in the recycle line in order to prevent the formation of sulphuric acid and therefore possible corrosion issues.

(iv) Selective catalytic reduction (SCR) can be used to remove NO_x from the flue gas. The NO_x from the flue gas could also be recycled into the burner where reburn reactions would help reduce in-flame NO_x emissions. Low NO_x burners are also typically installed in most commercial plants, however some optimisation or redesign may be necessary to take advantage of reburn reactions. The removal of NO_x from SCR may be necessary if it is above pipeline requirements, or if the plant can operate on air-fired mode and needs to adhere to emission limits.

One of the major energy penalties comes from the ASU due to the large volume and high purity of oxygen required (typically $> 95\%$) for the process. This technology is currently commercially available in the form of cryogenic distillation units and typically, the efficiency penalty for the overall oxy-fuel combustion process is calculated at approximately 10% points [21]. However, emerging technologies, such as membrane separation technology, in particular ion transport membranes which can potentially use less energy than cryogenic distillation, could significantly reduce this efficiency penalty [21].

1.4.4 Transportation

The transportation of CO_2 is likely to be through pipelines, however ships and trucks may also be utilised. The technology is seen as a mature since in the United States there are over 6000 km of CO_2 pipes and regulations are in place regarding impurities and safety issues [18]. Before entering the pipeline, the CO_2 will be compressed to conditions around 80-200 bar and 0-50 °C, however a preference of 100-110 bars and temperatures above the critical temperature 31.1 °C will allow CO_2 to be in a supercritical state [15]. Compared to gaseous and liquid CO_2, supercritical CO_2 has a higher density than gaseous CO_2 allowing for a larger volume of CO_2 to be transported and stored but also has a lower viscosity than liquid CO_2 which can over come frictional drops that may occur in the pipeline [15]. Impurities may increase the pressures and temperatures needed for a supercritical state, however recent research has shown that NO_x, SO_2 and mercury could be removed during the compression stages [24].

1.4.5 Storage and utilisation

The possible storage options for CO_2 currently considered include the use of geological formations, oceans and the use of minerals. The most widely discussed storage option involves injection into deep underground formations, such as depleted oil and gas reservoirs and saline aquifers [15]. The CO_2 is injected into a rock formation, which has a layer of impermeable cap-rock above it to prevent the escape of CO_2. Alternatively, the CO_2 may be injected into a declining oil reservoir to enhance the production, known as enhanced oil recovery or into unminable coal fields where the CO_2 will be absorbed by the coal and release methane.

For example, the North Sea has an abundant supply of storage space and has been used to store over 13 million tonnes of CO_2 in the Utsira formation outside of Norway since 1996 [25]. Furthermore, in the UK there is a legal framework, known as the EU CCS Directive, which has been put in place for the safe storage of CO_2 in geological formations.

1.5 Oxy-fuel combustion: current status

The use of oxyfuel technology is well known in the materials industry for welding and cutting [15]. The oxygen is usually combined with a fuel, such as acetylene, to reach a high temperature that can cut or weld various metals.

The concept of oxy-coal combustion was first proposed by Abraham et al. [26]. The technique was suggested as a means of producing high purity CO_2 that could be used for enhanced oil recovery (EOR). At the same time, Horn et al. [20] likewise demonstrated the economic feasibility of oxy-coal combustion to produce CO_2 for EOR but also suggested using oxy-coal combustion to reduce the adverse effects on the environment from harmful gases emitted from coal fired power stations. The benefits of EOR have led to experimental studies in an O_2/CO_2 environment carried out in the Argonne National Laboratory with numerical studies also being performed [27].

The debate over climate change and the influence of CO_2 on the environment in the early 1990s lead to the first oxy-coal studies in Japan [28–30]. In Europe, the first oxy-coal combustion test facility with recycled flue gas was undertaken by the EC Joule Thermie Project [31]. In 1997, the Kyoto Protocol was passed, which committed countries to reducing greenhouse gas emissions. Oxy-coal conditions were researched by CANMET using their 300 kW_{th} vertical combustor research facility and computational fluid dynamics (CFD) was also performed to understand flame characteristics and species concentrations [32].

In the past decade a number of pilot scale test facilities (< 3 MW_{th}) have successfully demonstrated oxy-fuel combustion [33–35]. Larger pilot scale plants have also successfully demonstrated oxy-fuel combustion. In 2008, Vattenfall initiated a 30 MW_{th} oxy-lignite pilot plant in Schwarze Pumpe, Germany. The pilot plant contains an ASU, a recycled flue gas line and a CO_2 processing unit. A suitable storage site was also suggested for the storage of the captured CO_2, however adequate permission was not granted [36]. In 2009, Doosan Babcock began tests on their 40 MW_{th} oxy-coal burner in Renfrew, Scotland. The pilot plant recycles the flue gas, however oxygen is supplied from tanks [37]. In 2011, a 30 MW_{th} retrofitted oxy-coal power plant began operation in Callide, Australia. The aim of the project is to have a demonstration plant that would transport the captured CO_2 for storage in the North Denison Trough [38].

Future plans for large-scale demonstration are underway. In the UK, the White Rose project proposes a 426 MW oxy-coal power plant is built near Drax Power Station in Yorkshire with a storage site offshore in the North Sea. As of 2014, front end engineering design (FEED) studies are underway and a government decision should be made in 2015. In the USA, the FutureGen 2.0 project has proposed a 200 MW retrofit to an existing coal-fired power plant in Illinois which includes a storage site 30 miles from the facility.

1.6 Combustion modelling

Combustion modelling can give insight into the combustion process. Computational fluid dynamics (CFD) is an engineering tool which can be used to model the combustion process. Equations which represent the transport of mass, momentum, energy and species are solved in three dimensions in a defined space over a finite number of cells, or nodes, called a mesh [39]. The terms which include the generation or destruction of chemical species are called source terms and are modelled through chemical rates which are usually defined by various mathematical models.

Increased computational power over the last decade has led to an increased use of CFD in academia as well as in the industry for coal and biomass combustion simulations. The main advantages of CFD are that it can be cheaper, less time consuming and provide detailed insight compared to experimentation therefore assisting in the understanding of complex problems, or helping to improve product design. In the case of oxy-fuel combustion, this is an important tool for assessing the effects of new build and retro-fitting of existing power plants with this technology. However, in order to gain confidence in a CFD simulation, it must be closely linked with experimental data to validate and justify the modelling assumptions.

Turbulence is an important feature in coal combustion which is used to enhance mixing and control pollutant formation. CFD uses three different approaches to describe a turbulent flow field, which are the Reynolds Averaged Navier Stokes (RANS), Large Eddy Simulations (LES) and Direct Numerical Simulations (DNS) methods.

Most developments for the simulation of coal combustion have been using the steady Reynolds-Averaged Navier-Stokes (RANS) simulation, which gives a steady-state solution and is based fully on mathematical models of turbulence. A number of RANS simulations have been performed for oxy-coal [32–35, 40], co-firing with coal and biomass [41], a small number of biomass cases [42] and relatively little literature on oxy-biomass [43, 44]. The use of DNS directly resolves all scales of turbulence and its application in coal combustion simulation is not presently computationally feasible. On the other hand, Large Eddy Simulations (LES) resolves the largest scales of turbulence present in a flow field, and models the smaller ones, giving a time-dependent solution. However, only a limited number of coal and oxy-coal combustion simulations have been performed using LES [33, 35, 40, 45, 46].

1.7 Aims and objectives

The project was sponsored by the OxyCAP-UK project which involved six other universities and was part-funded by E-ON. The main objectives of the PhD as part of the project are listed below:

(i) Collaborate with Imperial College and develop a CFD model for oxy-coal combustion.

(ii) Perform time-averaged RANS and LES in a combustion test facility (CTF) under air and oxy-fuel conditions and investigate suitable sub-models for oxy-coal combustion.

1.8 Scope of the PhD thesis

In this chapter, the background and motivation for the thesis has been presented. Oxy-fuel combustion has been proposed as a potentially viable technology to help reduce carbon dioxide emissions from power stations and help mitigate global warming. In particular, CFD modelling has been identified as an important engineering tool that can help assist and evaluate oxy-fuel technology, especially at a large scale.

In Chapter 2, a critical literature review of CFD modelling techniques for air and oxy-fuel combustion is presented and the experimental facilities studied in the subsequent chapters along with experimental data used for CFD model validation are described in Chapter 3.

In Chapter 4, a novel implementation of a NO_x model is included into an in-house LES code and validated against experimental data for an air-methane flame, air-methane-coal flame and an oxy-coal case. The impact of turbulent chemistry interaction and the NO_x modelling approach in LES is investigated.

In Chapter 5, CFD modelling studies of a 250 kW combustion test facility are performed and the CFD simulations are compared against measured experimental data. An advanced gaseous radiative property model, suitable for air and oxy-fuel environments, is validated against radiative heat flux measurements. Further, a CFD study is performed for a number of oxy-fuel environments.

In Chapter 6, CFD simulations are performed on a full-scale utility boiler for coal and biomass combustion in an air and oxy-fuel environment. The study investigates the differences in heat transfer when a utility boiler switches to firing 100% biomass and examines the effect on using oxy-fuel for coal and biomass.

Finally, in Chapter 7, conclusions are drawn from the results and uncertainties, limitations and future improvements are discussed.

Chapter 2

Literature review

In this chapter, a review of the literature surrounding CFD combustion modelling in air and oxy-fuel environments is presented. The governing equations used to represent the physics of the combustion process are given in Section 2.1 and approaches to modelling turbulent flows are introduced in Section 2.2. Mathematical models representing the combustion of a single particle are considered in Section 2.3 followed by the modelling of heat transfer in Section 2.4.

2.1 Governing equations

The physics of combustible fluid flow can be described by partial differential equations. The fluid is considered as a continuum, whereby molecular structures are ignored and macroscopic properties are used to describe a continuous mass. Macroscopic properties Φ include the velocity, pressure, density, temperature and species concentration. In general, the flux into and out of a physical system along with any source or sink of a property Φ can be described by a general partial differential equation (PDE):

$$\underbrace{\frac{\partial \Phi}{\partial t}}_{\text{time-derivative}} + \underbrace{\frac{\partial \Phi u_j}{\partial x_j}}_{\text{convective term}} = \underbrace{\frac{\partial}{\partial x_j}\left(D\frac{\partial \Phi}{\partial x_j}\right)}_{\text{diffusion term}} + \underbrace{S_\Phi}_{\text{source term}} , \tag{2.1}$$

where t, D, x_j and u_j denote time, the diffusion constant, space vector component and velocity vector component, respectively.

2.1.1 Conservation of mass

From the first law of thermodynamics it is known that mass cannot be created or destroyed and the *conservation of mass* is given by

$$\frac{\partial \rho}{\partial t} + \frac{\partial}{\partial x_j}(\rho u_j) = 0, \tag{2.2}$$

where ρ denotes the density. Equation (2.2) is valid for both reactive and non reactive flows.

2.1.2 Conservation of momentum

Momentum, given by ρu_i, is conserved in a closed system and will therefore only change if acted upon by an external force. This is evident from Newton's second law, $\partial_t(\rho u_i) = F_i$ where ∂_t is the partial derivative with respect to time t. From (2.1), the *conservation of momentum* is given by

$$\frac{\partial}{\partial t}(\rho u_i) + \frac{\partial}{\partial x_j}(\rho u_i u_j) = \frac{\partial}{\partial x_j}\tau_{ij} - \frac{\partial p}{\partial x_i} + \rho g_i, \tag{2.3}$$

where the density, velocities, pressure and gravitational forces are given by ρ , u_i, p and g_i respectively. The source term in (2.3) can be taken to be the sum of the pressure and gravitational forces, $S_{u_i} = -\partial p/\partial x_i + \rho g_i$. The stress tensor, denoted by τ_{ij} is given by

$$\tau_{ij} = \mu\left(\frac{\partial u_i}{\partial x_j} + \frac{\partial u_j}{\partial x_i}\right) - \frac{2}{3}\mu\frac{\partial u_k}{\partial x_k}\delta_{ij},$$

where $\mu = \rho\nu$ is the dynamic viscosity and δ_{ij} is Kroneker delta ($\delta_{ij} = 1$ if $i = j$ and $\delta_{ij} = 0$ if $i \neq j$). Furthermore, if the flow is incompressible (where $\partial u_i/\partial x_i = 0$) and viscosity is constant then along with (2.2), Equation (2.3) reduces to the Navier-

Stokes equations for an incompressible Newtonian flow [47],

$$\rho\left(\frac{\partial u_i}{\partial t}+u_j\frac{\partial u_i}{\partial x_j}\right)=\mu\frac{\partial^2 u_i}{\partial x_j^2}-\frac{\partial p}{\partial x_i}+g_i. \tag{2.4}$$

2.1.3 Species transport equation

The mass fraction Y_k of a species k is defined as the ratio of a mass of species k in the mixture, m_k, with respect to the total mass of the mixture, m_{total},

$$Y_k=\frac{m_k}{m_{\text{total}}}.$$

Using Equation (2.1), the *species transport equation* can be written as

$$\frac{\partial}{\partial t}(\rho Y_k)+\frac{\partial}{\partial x_j}(\rho Y_k u_j)=\frac{\partial}{\partial x_j}\left(\rho D_k\frac{\partial Y_k}{\partial x_j}\right)+S_{Y_k}, \tag{2.5}$$

where the source term S_{Y_k} denotes whether a chemical species with mass fraction Y_k is destroyed or generated in the system. The term D_k denotes the diffusion coefficient of the species k, assuming Fick's first law[1] [48].

2.1.4 Energy equation

Energy is a conserved quantity and in combustion problems mainly takes the form of thermal and chemical energy. The *energy equation* can be defined by the specific energy $E=h-p/\rho+(u_1^2+u_2^2+u_3^2)/2$, or the total enthalpy $h=E+p/\rho$, as

$$\frac{\partial}{\partial t}(\rho h)+\frac{\partial}{\partial x_j}(\rho h u_j)=\frac{\partial}{\partial x_j}\left[\frac{\mu}{\sigma_h}\frac{\partial h}{\partial x_j}\right]+\frac{\partial p}{\partial t}+S_{rxn}+S_{rad}, \tag{2.6}$$

---

[1] Fick's first law assumes flux goes from high to low concentrations and is proportional to the concentration gradient.

where the dynamic viscosity and Prandtl number are given by μ and σ_h, respectively. The Prandtl number represents the rate of viscous to thermal diffusion,

$$\sigma_h = \frac{c_p \mu}{k_{th}},$$

where c_p and k_{th} are the specific heat and thermal conductivity, respectively. Furthermore, Equation (2.6) is only valid under the assumption that the Lewis number, which is the rate of energy to mass transport, is unity, as defined by

$$Le = \frac{k_{th}}{\rho c_p D_m} = 1,$$

where D_m is the mass diffusivity. The source terms for the change by reaction and radiation are given by S_{rxn} and S_{rad}.

In summary, Equations (2.2), (2.3), (2.5) and (2.6) must be solved simultaneously in combustion problems. However, no analytical solutions exist to these equations and numerical methods must be used to provide an approximate solution. To perform the numerical solution, the three-dimensional space representing the fluid medium can be discretised into a number of finite volumes containing a value for each of the macroscopic properties in the governing equations, a process known as the finite volume method. Alternative methods include finite differences and finite element methods. The collection of all of the finite volumes or cells is called a mesh and if the equations sufficiently describe the physics, then the accuracy of the numerical solution is governed by the mesh resolution.

2.2 Turbulence

Turbulent flows are encountered in many engineering problems. Turbulent flows are three-dimensional, highly unsteady, dissipative and are composed of rotating flow structures, called eddies or vortices, with a wide range of length and time scales [49]. In combustion, chemical reactions occur at a molecular level when chemical species are mixed by diffusion, however the effect of turbulent flow can enhance the contact of chemical species as well as the dispersion of heat from those reactions.

Laminar and turbulent flow can be quantified by the Reynolds number [47] which defines the ratio of inertial to viscous forces acting upon the fluid and is defined by, $\mathrm{Re} = \mathcal{U}\mathcal{L}/\nu$, where $\mathcal{U}$, $\mathcal{L}$ and ν describe the average velocity, characteristic length, and kinematic viscosity, respectively, of the flow field. This characterisation of turbulent flow provides a non-dimensional description of the extent of turbulence present in the flow. Higher Reynolds numbers describe turbulent flow, while small Reynolds numbers describe laminar flow, but this is highly dependent on the flow configuration.

Eddies are created by shear forces, such as in boundary layers, obstructions in the flow field or interactions between other eddies. The development and dispersion of eddies can be described through an energy spectrum, as shown in Figure 2.1. The spectrum shows how turbulent kinetic energy contained within an eddy is distributed as a function of its size, represented by the wave number κ_w [50]. As the wave number increases, the relative size of an eddy decreases. An energy spectrum function $\mathcal{E}(\kappa_w)$ is used and if integrated over all wave numbers, κ_w, for isotropic turbulence is equal to the turbulent kinetic energy k [50],

$$k = \int_0^\infty \mathcal{E}(\kappa_w) d\kappa_w.$$

The three main regions which exist in an energy spectrum are (a) the energy containing range, (b) the inertial range, and (c) the dissipation range. The energy containing range describes the formation of eddies which have acquired kinetic en-

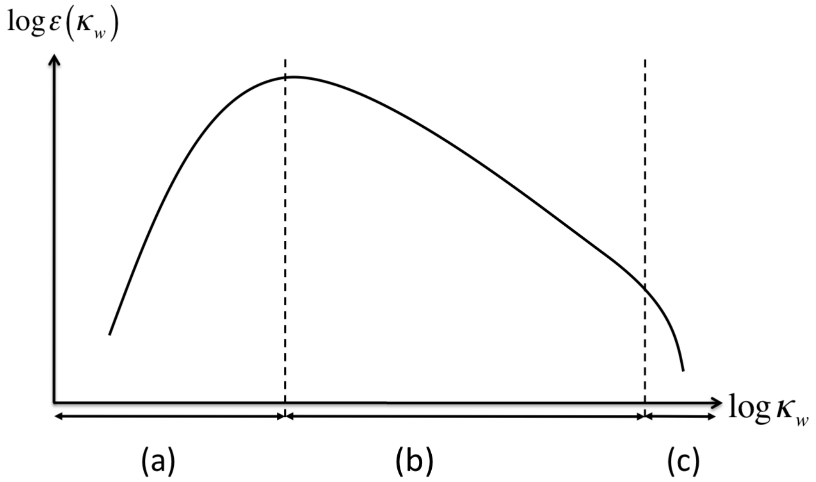

Figure 2.1: Schematic of an energy spectrum. There are three main regions in the diagram: (a) the energy containing range where eddies accumulate energy from the mean flow, (b) the inertial range where the larger eddies pass kinetic energy to smaller eddies (the energy cascade) and (c) the dissipation range where viscous forces dissipate kinetic energy.

ergy from the mean flow. Velocity gradients can also distort the size and result in anisotropic vortices. Eddies may also decrease in size, but conservation of angular momentum increases the rate of rotation [39]. Smaller eddies are present in the inertial range, which are altered in size by the larger eddies rather than the mean flow. In this stage, kinetic energy is assumed to be transferred from larger to smaller eddies by internal forces until the energy is dissipated by viscous forces at the smallest scales of turbulence, a process known as the energy cascade proposed by Richardson [51]. Kolmogorov theorised at high Reynolds numbers, small-scale eddies lose their directional orientation and become isotropic and the smallest scales of turbulence are known as Kolmogorov scales η_L [52]. In the dissipation range, viscous forces cause the kinetic energy to dissipate and the energy is converted into heat.

It is commonly accepted that turbulent flows can be described by the Navier-Stokes equations along with additional equations, such as the conservation of mass and energy as well as appropriate boundary conditions. However, for turbulent flow, the inertial term must be included which is highly non-linear and therefore no analytical solutions exist. Due to the variety of length and time scales present in turbulent flows, a numerical simulation would need a sufficiently fine mesh resolution and small time step to capture all of the turbulent features. Three approaches can be used to approximate the solution of the governing equations:

(i) Direct Numerical Simulation (DNS),

(ii) Reynolds-averaged Navier-Stokes (RANS),

(iii) Large Eddy Simulation (LES).

2.2.1 DNS

Direct numerical simulation (DNS) is a method which resolves the entire turbulent temporal and spatial scales, from the largest down to the smallest scales (Kolmogorov scales). Significant computational resources are needed, and it is suggested that the grid point requirement is proportional to $\mathrm{Re}^{9/4}$ which means even non-reactive turbulent flows on a relatively small domain can be difficult to model [39]. The computational cost makes DNS almost impractical, however a limited number of pulverised fuel combustion simulations have been attempted. A laboratory scale pulverised coal burner was simulated by Luo et al. [53] using a mesh of 700 million cells. The simulation was computed over 3 months using 1024 nodes to resolve only 11 ms of data and yet only a moderate agreement was achieved with the available experimental data. Where experimental data does not exist or is limited, DNS could offer validation of other approaches such as RANS or LES [54]. A review into DNS applied to turbulent combustion is given by Hawkes et al. [55].

2.2.2 RANS

Only the statistical mean of the solution is calculated in the Reynolds-averaged Navier-Stokes (RANS) approach. For an instantaneous scalar $\Phi(\mathbf{x}, t)$, it may be decomposed as

$$\Phi = \langle \Phi \rangle + \Phi',$$

where the statistical mean and fluctuating components are given by $\langle \Phi \rangle$ and Φ', respectively, a process also known as Reynolds decomposition. The statistical mean of the quantity Φ is often considered as time-averaged and may be defined as

$$\langle \Phi \rangle = \frac{1}{\Delta t} \int_{t_0}^{t_0+\Delta t} \Phi(t) dt, \tag{2.7}$$

where t_0 is the initial value and $t_0 + \Delta t$ is a larger value in time, which theoretically should tend towards infinity, in steady flow calculations. Furthermore, if the mean of the fluctuations is taken, the following relationship holds,

$$\langle \Phi' \rangle = \frac{1}{\Delta t} \int_{t_0}^{t_0+\Delta t} \Phi'(t) dt = 0. \tag{2.8}$$

Additional terms consisting of fluctuating components appear when the governing equations are decomposed and these are represented by a turbulence model.

In combustion problems, the flow varies with density and additional terms can arise that would need to be modelled [39]. The density-weighted (or Favre) averaging can be used where

$$\widehat{\Phi} = \frac{\langle \rho \Phi \rangle}{\langle \rho \rangle},$$

such that the decomposition of the transported quantity Φ is now given by

$$\Phi = \widehat{\Phi} + \Phi'',$$

and the density weighted average of the fluctuation now holds a similar property to $\langle \Phi' \rangle$,

$$\widehat{\Phi''} = \frac{\left\langle \rho(\Phi - \widehat{\Phi}) \right\rangle}{\langle \rho \rangle} = 0.$$

The resulting Favre-averaged equations for combustible flows are given by

$$\frac{\partial \langle \rho \rangle}{\partial t} + \frac{\partial [\langle \rho \rangle \widehat{u_j}]}{\partial x_j} = 0, \tag{2.9}$$

$$\frac{\partial [\langle \rho \rangle \widehat{u_i}]}{\partial t} + \frac{\partial [\langle \rho \rangle \widehat{u_i} \widehat{u_j}]}{\partial x_j} = -\frac{\partial [\langle \rho \rangle \widehat{u_i'' u_j''}]}{\partial x_j} + \frac{\partial \langle \tau_{ij} \rangle}{\partial x_j} - \frac{\partial \langle p \rangle}{\partial x_i} + \langle \rho \rangle g_i, \tag{2.10}$$

$$\frac{\partial [\langle \rho \rangle \widehat{Y_k}]}{\partial t} + \frac{\partial [\langle \rho \rangle \widehat{Y_k} \widehat{u_j}]}{\partial x_j} = -\frac{\partial [\langle \rho \rangle \widehat{u_j'' Y_k''}]}{\partial x_j} + \frac{\partial}{\partial x_j} \left(\langle \rho \rangle D_k \frac{\partial \widehat{Y_k}}{\partial x_j} \right) + \langle S_{Y_k} \rangle , \tag{2.11}$$

$$\frac{\partial [\langle \rho \rangle \widehat{h}]}{\partial t} + \frac{\partial [\langle \rho \rangle \widehat{h} \widehat{u_j}]}{\partial x_j} = -\frac{\partial [\langle \rho \rangle \widehat{u_j'' h''}]}{\partial x_j} + \frac{\partial}{\partial x_j} \left\langle \frac{\mu}{\sigma_h} \frac{\partial h}{\partial x_j} \right\rangle + \frac{\partial \langle p \rangle}{\partial t} + \langle S_{rad} \rangle \tag{2.12}$$

where all variables have been discussed in Section 2.1, but are time-averaged. An additional non-linear term, $\widehat{u_i'' u_j''}$, appears on the right hand side of Equation (2.10) which corresponds to the Reynolds stresses. This term is unresolved and can be closed by models such as eddy viscosity models or Reynolds stress models.

Linear eddy viscosity models rely on the Boussinesq hypothesis where Reynolds stresses are assumed to be related to the mean rate of deformation. Turbulent stresses have been shown to increase as the rate of deformation increases [39]. Therefore, the Reynolds stresses can be approximated to

$$-\langle \rho \rangle \widehat{u_i'' u_j''} = \mu_t \left(\frac{\partial \widehat{u_i}}{\partial x_j} + \frac{\partial \widehat{u_j}}{\partial x_i} \right) - \frac{2}{3} \langle \rho \rangle k \delta_{ij}$$

where μ_t, k and δ_{ij} is the turbulent viscosity, kinetic energy and Kronecker delta, respectively. A limitation of this approach is that it is assumed the flow is isotropic, and therefore highly anisotropic flows, such as swirling flows that are typical in pulverised fuel combustion may not be represented correctly. A number of approaches can be used to describe the turbulent viscosity μ_t.

Mixing length models describe the turbulent viscosity as a function of the length scale. For example, Prandtl's mixing length model (zero-equation model) describes turbulent viscosity as an algebraic expression of the length scale and mean velocity gradient and the Spalart Allmaras model [56] (one-equation model) describes the turbulent viscosity as a length scale function and solves one transported equation for a viscosity parameter. These models have generally been developed for aerodynamic applications, low Reynolds number flows and flows with adverse pressure gradients.

The standard k-ε model [57] is a two-equation model which solves two transport equations for the turbulent kinetic energy k and the rate of dissipation of turbulent kinetic energy per unit mass ε. The equation for k is derived mathematically, whilst the equation for ε is based on physical assumptions. The turbulent viscosity is defined as a function of k and ε. This model is widely used in a number of industrial applications, including some examples of pulverised fuel combustion [58]. The models assume that the flow is fully turbulent but relies on empirical constants, which have been tuned from experiments involving the flow of air and water [59]. The flow physics in combustion systems differ and in a bluff body methane flame, the empirical constant $C_{1\varepsilon}$ was altered from 1.44 to 1.6 to improve the predictions against experimental data [60]. Therefore, the constants can be altered to suit a variety of flow problems which may include oxy-fuel combustion systems. A variation of the standard model is the RNG (renormalisation group) k-ε model [61], which is formulated to give improved predictions of low-Reynolds, near wall and highly swirling flows and also provides an analytical expression for the Prandtl number. Similarly, this model also defines the turbulent viscosity as a function of k and ε.

This model has been used by a number of authors for pulverised fuel combustion since highly swirling flow is present [42, 62, 63]. Another variation is the realisable k-ε model [64] which involves a mathematically derived transport equation for ε and therefore satisfies mathematical constraints in line with flow physics unlike the standard and RNG variants [59]. An alternative formulation for turbulent viscosity is also given. This model has also been used by a number of authors in pulverised coal and biomass combustion simulations [41, 43, 44].

The standard k-ω model [65] and k-ω SST model [66] are another set of two-equation models which solve a transport equation for the turbulent kinetic energy k and the specific dissipation rate $\omega = \varepsilon/k$. Similar to the mixing length models, the standard k-ω model is also applicable for near wall, low-Reynolds number flows and flows with adverse pressure gradients. The k-ω SST model uses a blending function so that the standard k-ω model is used near the wall and the standard k-ε model is used far from the wall.

The Reynolds stress model (RSM) solves for each of the Reynolds stresses plus an extra equation for the rate of dissipation ε, giving a total of 7 extra transport equation to solve in three dimensions. The advantage over the linear eddy viscosity models is the isotropic hypothesis is abandoned thus offering the potential for higher accuracy in anisotropic flows such as highly swirling flows found in combustion systems. However, the additional transport equations will also increase the computational cost of the model compared with the two-equations models.

In general, RANS equations are solved in steady state and the time-dependent term on the left hand side of Equations (2.9) - (2.12) is neglected. In unsteady RANS (URANS), the RANS equations are solved but the time-dependent term is retained. This approach is useful where the mean flow contains small or regular variations with time that are not believed to be turbulent [65]. Variations in the mean flow may be imposed, such as by time-dependent boundary conditions, or from oscillating flow features, such as vortex shedding.

2.2.3 LES

Selection of an appropriate RANS model to deal with a wide variety of flow conditions is challenging since all scales of turbulence must be modelled. Large eddy simulation (LES) is a technique which aims to resolve larger turbulent eddies through numerical methods and model the smaller eddies. In general, the computational cost is reduced compared to DNS as the smaller length scales are not directly resolved, but increased compared to RANS methods.

LES applies a low pass spatial filter to the governing equations with a filter cut off width Δ_w to eliminate the small scale eddies from a transported quantity Φ such that it is decomposed into a filtered and sub-filtered value. This is unlike RANS where the quantities are decomposed into a time-averaged and fluctuating value. In general, the operation of a filter function G on a scalar Φ is defined as

$$\overline{\Phi}(\mathbf{x}) = \int \Phi(\mathbf{x}^*)G(\mathbf{x} - \mathbf{x}^*)d\mathbf{x}^* \tag{2.13}$$

where $\mathbf{x} = (x_1, x_2, x_3)$ is taken to be a vector in space and the bar denotes a filtered scalar.

Common filtering functions include the top-hat filter, Gaussian filter and spectral cut-off [39]. The filtering function may be implicit or explicit [67, 68]. Implicit filtering occurs when the gird and numerical discretisation scheme is considered to be the low-pass spatial filter. The finite grid resolution and numerical scheme therefore govern the size of the resolved eddies. Mesh independence is therefore an issue with implicit filtering since a change in mesh resolution will change the solution. Generally, a *grid convergence* can be obtained by examining the statistical quantities of interest for successively finer meshes until they become invariant to the resolution of the grid [69]. Speziale noted that a *good* LES would tend towards a DNS as the mesh size approached Kolmogorov length scales [70]. This is because the contribution of the sub-grid scale model would decrease until it had negligible impact on the solution, effectively representing a DNS. Explicit filtering occurs when a known filter function is applied to the governing equations. The filtered governing equations will contain resolved scales and sub-filter scales. The explicit filter width will have to be larger than the grid resolution and this allows the sub-filter scales to be further decomposed into resolvable sub-filter and unresolvable sub-filter (sub-grid) scales that have to be modelled. Grid independence could be achieved since the filter and discretisation operations are separate, however since it is necessary to use a mesh resolution much finer than the smallest scale given by the explicitly-filtered governing equations, a significant increase in computational effort is required compared to implicit filtering [68, 69].

A common approximation for the filter width is the approach by Deardorff where it is of the same order of magnitude as the grid size and may be described by $\Delta_w = \sqrt[3]{\Delta x \Delta y \Delta z}$ where Δx, Δy and Δz are the cell lengths in the x, y and z-directions, respectively [71]. For an equidistant cartesian mesh, Δ_w is equal to the cell width.

To summarise, the larger eddies above the cut-off width Δ_w are numerically resolved, while the information regarding the smaller turbulent eddies below the cut-off width Δ_w is lost and must be modelled through sub-grid-scale (SGS) models. As with Favre-averaging in the RANS equations, the technique can be applied using a slightly different approach called Favre-filtering. A Favre-filtered quantity, $\widetilde{\Phi}$, is defined by

$$\overline{\rho}\widetilde{\Phi}(\mathbf{x}) = \int \rho\Phi(\mathbf{x}^*)G(\mathbf{x}-\mathbf{x}^*)d\mathbf{x}^*. \tag{2.14}$$

Therefore, the decomposition of a transported quantity Φ can be written in terms of a Favre-filtered value $\widetilde{\Phi}$ and its fluctuation Φ'', such that $\Phi = \tilde{\Phi} + \Phi''$. Unlike the Favre-averaged fluctuation, the Favre-filtered fluctuation is non zero, $\widetilde{\Phi''} \neq 0$.

The Favre-filtered governing equations for the mass, momentum, species and enthalpy are given by Equations (2.15), (2.16), (2.17) and (2.18), respectively.

$$\frac{\partial}{\partial t}(\overline{\rho}) + \frac{\partial}{\partial x_j}(\overline{\rho}\widetilde{u_j}) = 0, \tag{2.15}$$

$$\frac{\partial}{\partial t}(\overline{\rho}\widetilde{u_i}) + \frac{\partial}{\partial x_j}(\overline{\rho}\widetilde{u_i}\widetilde{u_j}) = -\frac{\partial}{\partial x_j}\left[\overline{\rho}(\widetilde{u_i u_j} - \widetilde{u_i}\widetilde{u_j})\right] + \frac{\partial}{\partial x_j}\widetilde{\tau_{ij}} - \frac{\partial \overline{p}}{\partial x_i} + \overline{\rho}g_i, \tag{2.16}$$

$$\frac{\partial(\overline{\rho}\widetilde{Y_k})}{\partial t} + \frac{\partial(\overline{\rho}\widetilde{Y_k}\widetilde{u_j})}{\partial x_j} = -\frac{\partial}{\partial x_j}\left[\overline{\rho}(\widetilde{u_j''Y_k''} - \widetilde{u_j}\widetilde{Y_k})\right] + \frac{\partial}{\partial x_i}\left(\overline{\rho}D_k\frac{\partial\widetilde{Y_k}}{\partial x_i}\right) + \overline{S_{Y_k}} \tag{2.17}$$

$$\frac{\partial(\overline{\rho}\widetilde{h})}{\partial t} + \frac{\partial(\overline{\rho}\widetilde{h}\widetilde{u_j})}{\partial x_j} = \frac{\partial}{\partial x_i}\overline{\left[\frac{\mu}{\sigma_h}\frac{\partial h}{\partial x_i}\right]} - \frac{\partial}{\partial x_j}\left[\overline{\rho}(\widetilde{u_j h} - \widetilde{u_j}\widetilde{h})\right] + \frac{\partial\overline{p}}{\partial t} + \overline{S_{rad}} \tag{2.18}$$

Due to the filtering operation, unresolved quantities that describe the effect of small scale turbulence occur which must be modelled. The unknown quantities are as follows:

- The unresolved SGS stresses $\tau_{ij,sgs} = \widetilde{u_i u_j} - \widetilde{u_i}\widetilde{u_j}$.
- The unresolved species and enthalphy fluxes given by $\widetilde{u_j''Y_k''} - \widetilde{u_j}\widetilde{Y_k}$ and $\widetilde{u_j h} - \widetilde{u_j}\widetilde{h}$ respectively.

- The filtered chemical reaction rate and diffusion of enthalpy given by $\overline{S}_{Y_k}$ and $\overline{\left[\frac{\mu}{\sigma_h}\frac{\partial h}{\partial x_i}\right]}$, respectively.

Sub-grid-scale (SGS) models are used to account for these unresolved stresses. The unresolved SGS stresses $\tau_{ij,sgs}$ can be written as the sum of the Leonard stresses, cross-stresses and Reynolds stresses. Leonard stresses describe the interactions between large scale eddies, Reynolds stresses are caused by interactions in the SGS stresses and the cross-stresses describe the interaction between SGS stresses and the resolved flow [39, 50]. However, a typical approach is to ignore Leonard and cross-stresses and collect everything together as SGS stresses [71, 72]. Typical models used in SGS modelling are the *Smagorinsky-Lilly model*, *Dynamic Smagorinsky Model* and *wall-adapting local eddy viscosity model (WALE).* Other methods include the dynamic kinetic energy sub-grid-scale model [59].

The Smagorinsky-Lilly Model is a basic SGS model that assumes the unresolved eddies are approximately isotropic and can be described by the Boussinesq hypothesis. Therefore the unresolved SGS stresses can be approximately modelled by

$$\tau_{ij,sgs} = \widetilde{u_i u_j} - \widetilde{u}_i\widetilde{u}_j = 2\nu_{t,sgs}S_{ij} - \frac{2}{3}\nu_{t,sgs}\frac{\partial \widetilde{u}_k}{\partial x_k}\delta_{ij} + \frac{1}{3}\frac{\tau_{kk}}{\overline{\rho}}\delta_{ij}$$

where

$$S_{ij} = \frac{1}{2}\left(\frac{\partial \widetilde{u}_i}{\partial x_j} + \frac{\partial \widetilde{u}_j}{\partial x_i}\right)$$

where $\nu_{t,sgs}$ is the turbulent sub-grid viscosity. Similar to Prandtl's mixing length model, the Smagorinsky-Lilly model can approximate the turbulent eddy viscosity $\nu_{t,sgs}$ by defining a length and velocity scale, taken to be the filter width Δ_w and the deformation-velocity tensor S_{ij}, respectively. The SGS viscosity is therefore given as

$$\nu_{t,sgs} = \frac{\mu_{t,sgs}}{\rho} = (C_{sgs}\Delta_w)^2\sqrt{2S_{ij}S_{ij}}$$

The value of the proportionality constant C_{sgs} depends on the flow problem, and typical values vary between 0.065 and 0.3 [73]. Lilly suggested that C_{sgs} should be approximately 0.185 or 0.21 [74, 75], however these values were found by Deadorff to cause excessive damping and a value of 0.1 was chosen [71]. Kempf et al. studied a bluff body methane flame using an error analysis with experimental data to determine the appropriate grid resolution and value of C_{sgs}. It was found that a value of 0.13 was the most appropriate with a fine grid resolution [76]. Further, the filter width can be represented by the approach by Deardorff mentioned previously. An alternative definition by Scotti et al. [77] is also proposed for the Smagorinsky-Lilly model on anisotropic grids,

$$C_{sgs} = 0.16 \cosh \sqrt{\frac{4}{27}\left[\left(\ln\frac{\Delta x}{\Delta z}\right)^2 - \ln\left(\frac{\Delta x}{\Delta z}\right)\ln\left(\frac{\Delta y}{\Delta z}\right) + \left(\ln\frac{\Delta y}{\Delta z}\right)^2\right]},$$

where Δz is the largest dimension of the cell.

For wall-bounded flow problems, the Smagorinsky-Lilly model can predict high levels of turbulent viscosity near the wall. To allow for zero viscosity at the wall, a damping function could be applied, for example that of van Driest [78]. Nicoud and Ducros [79] suggested an alternative model called wall-adapting local eddy viscosity model (WALE) model which offers an alternative formulation that allows zero turbulent viscosity [59].

A weakness of the Smagorinsky-Lilly model is that it provides a global value of C_{sgs} which can vary for a variety of flow problems. The Dynamic Smagorinsky Model, proposed by Germano et al. [80], uses a mathematical formalism to dynamically compute C_{sgs} and therefore the model can eliminate the need to specify values of C_{sgs}. The methodology of this model is described in most CFD textbooks [39, 73]. Negative values can occur in this model and clipping is necessary since these negative values can lead to numerical instabilities [73].

An eddy diffusivity assumption can be applied to the unresolved fluxes in Equation (2.17),

$$\widetilde{u_j'' Y_k''} - \widetilde{u}_j \widetilde{Y}_k = Y_{k,sgs} \approx D_{k,t} \frac{\partial \widetilde{Y}_k}{\partial x_i} \tag{2.19}$$

where $D_{k,t}$ is the turbulent diffusivity for species k. Using the definition of the Schmidt number Sc, the diffusivity D_k and viscosity ν can be related by

$$Sc_l = \frac{\nu}{D_k} \approx \frac{\widetilde{\nu}}{\widetilde{D_k}} \qquad , \qquad Sc_t = \frac{\nu_t}{D_{k,t}} \tag{2.20}$$

where the subscript l or t represents the laminar or turbulent components, respectively. Substituting the approximations of Equation (2.19) and (2.20) in Equation (2.17) yields

$$\frac{\partial(\overline{\rho}\widetilde{Y}_k)}{\partial t} + \frac{\partial(\overline{\rho}\widetilde{Y}_k \widetilde{u}_j)}{\partial x_j} = \frac{\partial}{\partial x_j}\left(\overline{\rho}\left(\frac{\widetilde{\nu}}{Sc_l} + \frac{\nu_t}{Sc_t}\right)\frac{\partial \widetilde{Y}_k}{\partial x_j}\right) + \overline{S_k} \tag{2.21}$$

The uncertainty in an LES comes from the numerical error and sub-grid-scale model [81]. The numerical error may be caused by the smaller turbulent scales being the same order of magnitude as the filter width. To reduce this effect, it is commonly suggested to use second-order or higher discretisation schemes [39]. The influence of numerical error from the mesh resolution is different in LES compared to RANS. In general, a RANS solution can become mesh independent where refinements in the mesh do not alter the solution. In an implicit LES, the filter width is usually taken to be proportional to the grid size which therefore determines the cut-off width for resolved and modelled turbulent eddies. As a mesh is refined, a larger proportion of eddies are resolved and therefore the solution cannot be grid independent.

Verification of the quality of an LES can therefore be accomplished by a *posteriori* approach where the model is implemented and the results from the LES solution are compared to experimental data, or alternatively DNS data if computationally feasible. Alternatively, a sub-grid model may be tested without performing a LES, known as *a-priori* approach, which generally involves comparison against filtered DNS data. Further information on *posteriori* and *a-priori* approaches for sub-grid-scale modelling can be found in the review by Meneveau and Katz [82].

The use of *quality indicators* is an alternative approach which attempt to provide a means of assessing a mesh for LES. As noted by Celik et al. [81], a good grid resolution may not provide accurate solutions and the indicators are generally a means of indicating whether the mesh is suitable for LES. They are used as a means of verifying the grid and should not be used for validation; caution should therefore be advised when using these indicators.

Pope estimated the difference between large anisotropic and smaller isotropic eddies that occur at length scales of $\mathcal{L}_{EI} \approx \frac{1}{6}\mathcal{L}$, where $\mathcal{L}$ is taken to be the characteristic length scale of the energy containing eddies [50]. Furthermore, for isotropic turbulence at high Reynolds numbers, 80% of the kinetic energy could be resolved if a filter width of $\Delta_w \approx \frac{\mathcal{L}}{12}$ is used [50,81]. Therefore, the grid quality for an LES may be estimated from a preliminary RANS simulation. Let $\mathcal{L} = k^{1.5}/\varepsilon$, where k and ε are estimated from the RANS solution, $\mathcal{L}_{LES} = \mathcal{L}/12$ be the length scale required for an LES and $\mathcal{L}_{cell} = \sqrt[3]{\Delta x \Delta y \Delta z}$ be the characteristic cell length, then if

$$\left(\frac{\mathcal{L}_{cell}}{\mathcal{L}_{LES}}\right)\begin{cases} \leq 1 & \text{mesh may be sufficient,} \\ \\ > 1 & \text{mesh may need to be refined.} \end{cases}$$

Celik proposed an alternative quality indicator, known as LES_IQ (LES Index of Resolution Quality) given by

$$\text{LES\_IQ} = \frac{1}{1 + 0.05 \left(\frac{\nu_{eff}}{\nu_l}\right)^{0.53}}.$$

where ν_{eff} is the effective viscosity, which is the sum of the turbulent viscosity ν_t and numerical viscosity ν_{num}, and the molecular viscosity is given by ν_l. The indicator is used for an LES solution and is only valid for flows away from the wall if wall-functions are used, or for fine meshes which sufficiently resolves the flow near the wall [81]. A value of 80% and above corresponds to a good LES, and an arbitrary value of 95.2% corresponds to a DNS. Celik assumes that the filter width for an LES should be approximately 25 times larger than the Kolmogorov scale, and this is equivalent to the ratio of effective and molecular viscosity to be estimated as $\nu_{eff}/\nu_l \approx 20$ [81]. For a DNS, the filter width is approximately equal to the Kolmogorov length scale and the ratio ν_{eff}/ν_l can be assumed to be close to 1. Furthermore, an estimation of the mesh size of $\Delta_w \approx L/8$ is suggested for a good quality LES [81].

Boundary conditions for LES generally need more information than for a RANS simulation. In general, a RANS simulation requires the estimations of the mean velocities, turbulent kinetic energy, dissipation and sometimes the Reynolds stress components. These relations can be estimated from experimental data or empirical relations. In LES, the velocity fluctuations are resolved and must be specified at the boundary [54, 83]. When experimental data is not available, approaches that can be used include using simulations from an LES upstream of the inlet condition or algorithms to generate artificial turbulence such as those by Klein et al. [84] and Kempf et al. [83]. In general, it is computationally less expensive to use algorithms.

2.3 Particle combustion modelling

In order to describe the combustion of pulverised fuel, it is simpler if a single particle is considered. The combustion process of a solid particle can be modelled in four main stages:

(i) Evaporation / drying

(ii) Devolatilisation

(iii) Volatile combustion

(iv) Char combustion

A schematic of this process is shown in Figure 2.2. As a pulverised particle heats up, moisture is evaporated (evaporation) followed by the release of light gases and tars (devolatilisation) which then reacts with the oxygen in the oxidiser (volatile combustion). The char is then oxidised in a slower reaction compared to evaporation and devolatilisation (char combustion). This is a simplistic representation where the reactions occur in sequence and is typically followed in CFD, however in reality some of the steps may occur simultaneously. Also, sub-models are present to describe the formation of pollutants and slagging behaviour. Physical models which represent the heat transfer and flow dynamics are also used to represent the interaction between combustible particles and the gas phase.

2.3.1 Evaporation and devolatilisation

The process of drying a particle involves the extraction of moisture from the surface and inner core whereby it escapes through a series of the pores. The particle may shrink, which can lead to a reduction in pore size, causing internal cracking or the breakup of the particle, however this is generally ignored during the modelling stages. The water may be free water, where it exists as moisture inside the pore or

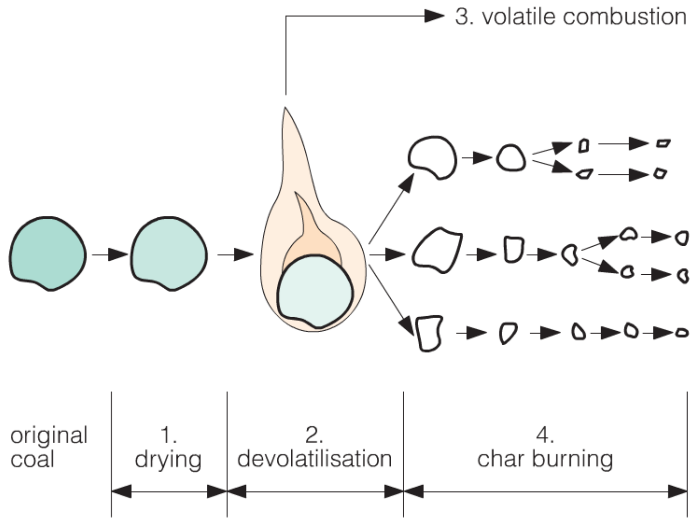

Figure 2.2: Schematic of the combustion of a single coal particle [85].

bound either chemically or physically [17]. The rate of evaporation of free water is governed by a diffusion gradient between the vapour concentration at the particle surface and bulk gas whereas bound water is generally released during chemical reactions. However modelling approaches typically ignore the differences between free and bound water.

The latent heat of water can cause cooling in the flame zone and can be significant in some fuels. For example, biomass can have a higher moisture content than coal and is suggested to cause lower flame temperatures. Chen et al. [86] modelled the heat transfer to a particle in air and oxy-fuel environments at a constant temperature in conditions typical of a mill and a furnace. The results indicated little difference in the evaporation time of the particle in air and oxy-fuel conditions with the main differences occurring due to particle heating rate. However, the model was only applied to a single spherical particle at 100 μm, and may not be applicable for larger particles.

Upon further heating of the particle, the onset of devolatilisation occurs at a temperature of approximately 600 - 700 K [86–88]. Volatile matter inside the particle is converted into organic compounds, such as light gases and tars, which leave through the pores of the particle into the gas phase. The particle may soften and a swelling phenomena can be observed which can be related to the volatile matter attempting to escape the coal particle, forming bubbles which will burst when they reach the surface [88]. The process is endothermic and is strongly governed by fuel type, temperature history, the composition of surrounding gases as well as pressure [86]. After devolatilisation, the remaining particle is char, a hollow sphere with a different structure and porosity from its original form [87].

Experiments by Kimber et al. [89] and Badzioch et al. [90] demonstrated that at high heating rates, similar to those experienced in a boiler, the volatile yield is larger by a factor of Q compared to the measurement by the proximate analysis. The factor Q is called the high temperature yield factor and is defined as the ratio of volatile yield from devolatilisation over the volatile yield measured by the proximate analysis, with typical values for coal ranging from 1.3 to 1.8 [88–90].

The single-rate devolatilisation model was first proposed by Badzioch and Hawksley [90] and uses a single Arrhenius expression to describe the rate of release of volatiles from the particle. The rate can be determined from experiments or from network computer models. In general, a pulverised fuel particle releases a combination of tars and light gases at different rates and therefore a single rate may be an inadequate description of the process. An alternative method may be that of the two-competing rate model first proposed by Kobayashi et al. [91]. A report by Sandia National Laboratories [92], where detailed experimental results of coal are compared with some constants given in the literature, found the values used by Kobayahsi et al. did not provide satisfactory results over a range of coals and it was found that the constants used by Ubhayakar et al. [93] provided a better agreement.

Network models, such as FG-DVC (Functional Group Deployment Vapourisation Cross Linking) [94], Flashchain [95] and CPD (Chemical Percolation Devolatilisation) [96], require chemical structures as well as detailed compositions of a particular coal. Recent codes have also been developed for biomass, such as FG-BioMass [97] and Bio-CPD [98], which includes databases of a selection of biomasses. These models can predict the yields of volatiles at high heating rates as well as the release of tars and light gases during devolatilisation [99]. The partitioning of nitrogen between the volatiles and nitrogen can also be predicted and this is useful for modelling the formation of $\mathrm{NO_x}$. When the coal or biomass is not included in the database of the network models, the fuel can be interpolated from the database of known fuels. The network model can be used as a pre-processor for the CFD simulation when experimental data is unknown and single or two-step rates can be interpolated from the predictions. This is of particular use when modelling high heating rates in an industrial furnace, which are of the order of 10^5 K/s and may be difficult to achieve in experimental facilities, such as drop tube furnaces. For example, the FG-DVC model was used by Backreedy et al. [62] as *a-priori* for rates and elemental compositions in their CFD simulations of a wide range of coals.

Drop tube furnace experiments and network models were compared with predictions from FG-DVC, CPD and Flashchain models by Williams et al. [100] for a variety of coals. High temperature volatile yield predictions were in good correspondence with the experimental data, however there were differences in predictions between the models.

Single-rate, two-step and CPD models used in CFD were compared against experimental data for ignition points in an ignition test facility of a bituminous coal [101]. A more advanced FG model was also implemented and tested. The results showed good agreement for the CPD model and implemented FG model in air and O_2/CO_2 conditions whereas single-rate and two-step model failed to predict ignition points correctly for the majority of cases studied. The authors recommended the use of the FG model or CPD where possible, but it should be noted that the authors did not mention where the kinetic rates for the single-rate and two-step models were obtained and ultimately this could have led to significant errors.

The devolatilisation models mentioned above are very dependent on the coal type, which can cause problems when a detailed analysis of the coal is unknown. The single rate model is computationally inexpensive but is dependent on the values used in the kinetic rate which varies widely depending on coal composition and heating rate [101]. Network models can be used as a pre-processor where experimental data is unavailable and the use of these models can be used to produce single or two step kinetic rates, high temperature volatile yields and nitrogen partitioning.

Experiments have shown that there may be differences between air and oxy-fuel environments. Rantham et al. [102] conducted drop tube furnace experiments in N_2 and CO_2 and found for temperatures above 1030K the weight loss of the coal in CO_2 was higher compared to N_2. Furthermore, volatile yields of four coals were studied and found to have higher volatile yields between 5-25% in CO_2 compared to N_2 when the wall temperature of the furnace was maintained at 1673K. The higher yields have been suggested to be related to char-CO_2 gasification reactions.

Devolatilsation experiments are usually performed in inert atmospheres, such as nitrogen, but to replicate oxy-fuel conditions, researchers have typically conducted experiments in CO_2. Network models, such as FG-DVC, are designed for inert atmospheres and may therefore be unsuitable for predicting volatile yields with long residence times in high temperature oxy-fuel conditions since gasification reactions are not taken into account [103]. Alvarez et al. [104] performed CFD simulations of an entrained flow reactor with FG-DVC modelling predictions used for devolatilisation rates and compared against experimental values of burnout, NO and oxygen concentrations for air and O_2/CO_2 mixtures of 21%/79%, 30%/70% and 35%/65%. The predictions showed an improvement over typical values used in a commercial code, Ansys fluent.

2.3.2 Volatile combustion

Volatile products are released during the devolatilisation process, which consist mainly of light gases and tar. Products that may be produced include CO_2, CO, H_2O, C_2H_6, C_2H_4, C_2H_2, C_6H_6 and CH_4 [105]. The hydrocarbons react with oxygen in the oxidiser to form carbon dioxide and water. The exact composition and concentration of chemical species released during devolatilisation is difficult to quantify and is highly dependent on heating rates and fuel type. Experiments or network computer models may be used, such as FG-DVC to approximate the species [106].

A large number of intermediate species and reactions are involved in the combustion of hydrocarbons and detailed chemical mechanisms can be used to describe the process which usually contains hundreds of species and thousands of reactions. This would be computational prohibitive to solve, even for simple CFD problems, due to the increased number of transport equations needed and strongly coupled reactions make the solution numerically stiff. Reduced chemical mechanisms are also available, such as the GRI 3.0 mechanism for methane combustion, however this contains 53 species and 325 reactions [107].

Global mechanisms may be used to represent the volatiles as a single species $C_xH_yO_z$ and therefore chemical kinetics can be neglected. The volatiles can be assumed to burn via a two-step reaction [106],

$$
\begin{aligned}
C_xH_yO_z + \alpha O_2 &\rightarrow x\mathrm{CO} + \frac{y}{2}\mathrm{H_2O}, \qquad \text{where } \alpha = \frac{x-z}{2} + \frac{y}{4} \\
\mathrm{CO} + \frac{1}{2}\mathrm{O_2} &\rightarrow \mathrm{CO_2}
\end{aligned}
$$

The combustion process can be physically controlled where turbulent mixing limits the reactions or kinetically controlled where chemical kinetics limit the reaction rate. Kinetically controlled combustion occurs when the reaction is slower than mixing process, where as physically controlled combustion occurs in turbulent diffusion flames such as in pulverised coal or biomass combustion.

Finite rate combustion models include the reaction rates of chemical species which can include both global and intermediate species. Chemical mechanisms are used where each chemical species is solved by a transport equation and the source term is computed from an Arrhenius rate.

Turbulent mixing is assumed to limit the reaction rates of the volatiles in the eddy dissipation model (EDM) [108], which was an adaption of the eddy breakup model by Spalding [109]. This model is mixing limited and the chemical kinetics are ignored. Therefore it is only valid for one-step or two-step reactions without reversible steps. This model is commonly used in coal combustion simulations where the flow is fully turbulent [33, 35, 43, 110]. However, the approach also uses model constants to limit or enhance the rate of destruction of reactants and creation of products. In oxy-fuel combustion, a higher concentration of products (CO_2 and H_2O) appear in the oxidiser stream of the burner, which may lead to an enhanced reaction rate predicted by the EDM for model constants suited to air, and therefore the values may need to be altered for oxy-fuel conditions [86]. Breussin et al. [111] found the predictions of CO of an oxy-methane flame from a “mixed-is-burnt” approach, similar to the EDM model, did not compare well against experimental data.

In oxy-fuel combustion, reversible reactions between CO and CO_2 may also be important and this cannot be implemented in the EDM. An improvement is the finite-rate eddy dissipation model which can be used to incorporate chemical kinetics where the reaction rate is taken as the minimum of the eddy dissipation or the finite rate reaction. This approach was used by Toporov et al. to model a 100 kW combustion test facility firing under oxy-fuel conditions [34].

The Eddy Dissipation Concept (EDC) [112] is an extension of the Eddy Dissipation Model. The model allows for a detailed mechanism to be coupled with a turbulent flow field. The chemical reaction of each species is solved along with a turbulent time-scale that governs how close the reaction is to equilibrium. Andersen et al. used the EDC model for a propane oxy-fuel flame together with a 2 step Westbrook and Dryer mechanism [113] and a 4 step Jones and Lindstedt mechanism [114] which the authors modified for oxy-fuel combustion. However, the simulation was only performed in two-dimensions as a balance between computational effort and accuracy [115].

Pre-computed tabulated models use detailed chemistry and/or a thermodynamic database to define a table that is a function of a conserved scalar, called the mixture fraction. The mixture fraction is a number between 0 and 1 which corresponds to pure oxidiser and pure fuel, respectively. The pre-computed table consists of instantaneous relationships between the mixture fraction, species, density and temperatures. However, in CFD, the cell values are averaged (either in time or space) and the fluctuating scalars can be related to their average value using a probability density function (PDF). The shape of the PDF is usually unknown and has to be presumed, for example with the use of a β-PDF shape. The chemistry used in the table can be computed from equilibrium values or by a non-equilibrium approach such as the flamelet model.

The steady flamelet model assumes within a turbulent flow field that there exists a group of laminar, one-dimensional flamelet structures [116]. This concept may be represented by a laminar counterflow flame where the fuel and the oxidiser are opposed jets set a certain distance apart. A reduction in distance between the fuel and oxidiser inlets increases the strain of the flame until it extinguishes. The problem can be rewritten in mixture fraction space instead of physical space such that the temperature, species and density are a function of only mixture fraction and strain rate. Coupled with a PDF, the model is applicable for turbulent flames. Equations representing the mixture fraction, strain rate and variance, needed for the PDF, are solved. The model assumes that the chemical reactions occur at the same time-scale and slow forming species, such as NO may be incorrectly predicted [117]. Models, such as the unsteady flamelet model [117] or a post-processing technique, may improve these predictions.

If the chemical species and reaction rates of the products released from the volatiles are known, the use of the EDC or tabulated approaches allows for detailed chemistry to be taken into consideration. However, the composition of volatiles is generally unknown, and if intermediate species are not required and the reaction is limited by turbulent mixing, the EDM may be used. However, reversible reactions cannot be considered in the EDM which may limit the applicability of the model in oxy-fuel combustion simulations.

2.3.3 Char combustion

After the volatile matter of a coal particle has been released, the remaining substance left is char. The char is a porous hollow sphere and combustion occurs when the oxygen reacts with the char particle. Due to the high heating rates during coal combustion, the char particles typically burn at a constant diameter and it is the density of the particle that decreases as the thin-walled shells are eroded [87]. The overall reaction rate of char combustion is complicated and may be limited by a number of parameters, including porosity, pore size, surface area, available oxygen and the reactivity of the particle itself. Furthermore, different types of coal will also burn at different rates.

Char combustion is mainly governed by the reaction of carbon within the char, C(s), and oxygen to produce CO followed by CO_2. A char particle is assumed to be surrounded by a boundary layer of gas equivalent to several particle diameters. It is assumed that the gas is CO and, for small particles ($< 100\ \mu$m) the CO oxidises to CO_2 outside the boundary layer (known as a single film model), but for larger particles (> 1 mm) CO_2 and CO may oxidise inside the boundary layer [118, 119]. Additional endothermic gasification reactions with steam (H_2O) and CO_2 may also be important at higher temperatures due to their higher activation energy. The char reactions are given by the equations:

$$\begin{aligned} \mathrm{C(s)} + \frac{1}{2}\mathrm{O_2} &\rightarrow \mathrm{CO}, && (2.22) \\ \mathrm{C(s)} + \mathrm{H_2O} &\rightarrow \mathrm{CO} + \mathrm{H_2}, && (2.23) \\ \mathrm{C(s)} + \mathrm{CO_2} &\rightarrow 2\mathrm{CO}. && (2.24) \end{aligned}$$

Chen et al. [86] summarised kinetic rate values, based on published literature, for air and oxy-fuel environments for Equations (2.22)-(2.24). These constants may be used to model oxy-fuel combustion in CFD through a multiple surface reaction model using an approach similar to the kinetics/diffusion limited model [87, 120].

The diffusion limited model was first proposed by Baum and Street [87], and considers the overall reaction rate of char to be limited by the diffusion of oxygen to the char particle. However, the model neglects any limiting effect by chemical kinetics. An improvement to the diffusion limited model is the kinetic/diffusion limited model [87, 120] where the inclusion of a kinetic rate assumes that the total reaction of char may be limited either by the diffusion of oxygen or the kinetic reaction of char.

The intrinsic model [121] is similar to the kinetics/diffusion limited model because it also includes the effects of the diffusion and kinetics on limiting char combustion. However, the kinetic reaction rate is expressed in terms of the intrinsic reactivity of the char particle and pore diffusion rates. The intrinsic reactivity is defined as the rate of reaction per unit area of the pore surface when mass transfer restrictions of oxygen are negligible [122]. Since the oxygen concentration in the particle is assumed to decrease from the surface, an effectiveness factor is introduced. The effectiveness factor describes the ratio between the actual rate of combustion in the particle compared to the rate of combustion that would occur if the oxygen concentration at the surface was constant throughout the particle. In this model, the porosity and internal surface area of the particle are also taken into consideration. Coal particles are very small, and for high rank chars, the pores are typically less than 0.001 micron in size. When the pores are extremely small, the molecules of oxygen collide more frequently with the walls of the particle than with other molecules, this is known as Knudsen diffusion. The diffusion of oxygen in the intrinsic model therefore considers both bulk diffusion and Knudsen diffusion. Williams et al. [100] compared the predictions of the kinetic/diffusion limited model with the intrinsic model against experimental measurements of burnout. The kinetics/diffusion limited model over predicted the burnout, while the intrinsic model gave more realistic results.

The Carbon Kinetics Burnout (CBK) model [123] is a variant of the intrinsic model. The model is based on a general carbon kinetics package and is designed to predict carbon burnout using a prescribed temperature and oxygen concentration.

Gharebaghi et al. [124] extended the CBK model to incorporate gasification reactions and other improvements suitable for oxy-fuel combustion. The modified version was shown to significantly improve the predictions of burnout against experimental data for both N_2 and CO_2 environments.

Kuhr et al. [125] performed a CFD analysis of a 20 kW furnace both with and without the C-CO_2 reaction (Equation (2.24)) for O_2/CO_2 conditions with walls heated to 1300°C. The inclusion of the C-CO_2 reaction improved the oxygen profiles with respect to the measured experimental data. Guo et al. [126] also found that higher char consumption rates were also present in an $O_2/H_2O/Ar$ environment compared to a O_2/Ar environment and this demonstrates that the char-H_2O gasification reaction may also be important. Gasification reactions could also lead to higher concentrations of CO being produced in oxy-coal combustion compared to air-coal combustion [15]. In contrast, Várhegyi et al. [127] examined a number of coals for a range of oxygen concentrations from 5-100% in CO_2 and N_2 atmospheres and found little difference in char consumption rates, however the experiments were all conducted at temperatures below 900°C.

Char burnout measurements were conducted for air and a synthetic dry recycle in a 0.5 MW_{th} CTF by Smart et al. [128]. Two different coals were examined and for one of the coals a lower carbon in ash was reported for oxy-fuel environments compared to air-firing when the same exit oxygen concentration was maintained. However conclusions could not be drawn from the other coal due to the low carbon in ash values measured. The authors attributed this to higher flame temperatures and longer residence times of the coal in oxy-fuel environments, but did not highlight the impact of gasification effects.

A review by Chen et al. [86] on char combustion concluded that at high temperatures and sufficient oxygen concentration ($> 5\%$), the reaction of char is limited by the diffusion of oxygen to the particle. Therefore, in oxy-fuel combustion, the burnout may be lower in these conditions since O_2 has a lower binary diffusivity in CO_2 than in N_2. However, at high temperatures and lower oxygen concentrations, char gasification reactions (Equation (2.23) and (2.24)) may be favoured as high concentrations of CO_2 and H_2O surround the char particle which may increase the probability of additional reactions other than char-oxidation to occur with the char particle, therefore leading to an increase in the rate of char consumption.

In a CFD simulation of oxy-fuel combustion, the inclusion of gasification reactions may be important. Low oxygen concentrations (typically around 0-5%) and high temperatures exist in the later regions of a boiler and gasification reactions are expected to be important in this zone. However, if oxygen is higher then gasification reactions may not play an important role.

2.3.4 Pollutant formation

Coal is an organic substance and small quantities of pollutants such as CO, NO_x and SO_x can be formed. Mathematical models are available to model the rates of pollutant formations, which are discussed below.

Nitric oxides

In coal combustion, nitric oxides can be formed and reduced from three main routes: thermal NO_x from the separation of oxygen and nitrogen molecules in the air to form NO at high temperatures, prompt and reburn NO_x from the interaction of fuel-derived hydrocarbons and nitrogen in the atmosphere and fuel-NO_x from the nitrogen bound in the fuel. The route which leads to the production of NO is complex and the mechanisms are shown in Figure 2.3. The mechanisms used usually describe the formation of nitric oxide (NO), since this occurs at high temperatures typical of a

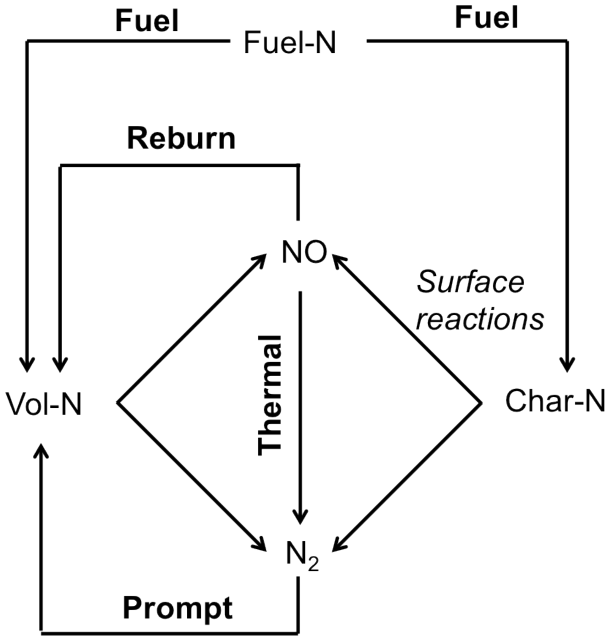

Figure 2.3: NO formation and destruction mechanisms.

combustion simulation but is a precursor of NO_2 which forms at lower temperatures and contributes to acid rain [129].

Thermal NO formation is the formation of NO from O_2 and N_2 at high temperatures. This mechanism may contribute less than 30% of the overall NO formation in air-coal and air-biomass combustion [130], but in oxy-fuel combustion this is expected to be significantly lower due to the lack of atmospheric nitrogen.

Prompt NO formation was first identified by Fenimore [131] and involves the formation of NO from atmospheric nitrogen and CH_i radicals, which would be intermediate products of the combustion of volatiles in coal and biomass. The mechanism occurs mainly in fuel-rich conditions, however it is only believed to contribute around 5% of the total formation of NO in coal combustion in air [132]. The NO can also be reduced by a reburn NO_x mechanism which describes the destruction of NO with interactions with CH_i radicals in fuel-rich conditions. In oxy-fuel combustion with recycled flue gas, reburn NO may be a more dominant mechanism than in air combustion as NO may be recycled and introduced back into the fuel-rich region of the flame [86].

The dominant formation of NO from coal and biomass combustion is from the fuel-NO_x mechanism. The fuel bound nitrogen (fuel-N), is split between the volatiles (vol-N) and char (char-N) during the devolatilisation process [129]. The nitrogen in the volatiles is released mainly as hydrogen cyanide (HCN) or ammonia (NH_3) where the concentrations depend on the coal rank and temperature [133]. The volatile-N can then be oxidised to form NO or reduced back to N_2. Heterogeneous reactions may also be present on the char surface which may either form NO or reduce to form N_2. The char-N tends to produce mainly NO and the char-N to NO conversion factor is about 75-100% for a single particle at high temperatures. However, surface reactions on the char may reduce the NO to N_2 [133].

One of the most challenging components in modelling fuel NO formation is the distribution between char-N and volatile-N since it is generally unknown. This is generally important for NO_x control in a boiler where formation of NO_x during volatile combustion is easier to control than during char combustion [130]. The distribution may be obtained from experiments, such as in a drop tube furnace or with the use of network pyrolysis models as discussed in Section 2.3.1. Network models can predict yields of char-N and volatile-N as well as the ratio of HCN and NH_3 for a given coal composition which include the FG-DVC [94], FLASHCHAIN [95] and CPD models [96]. Recent biomass models can also predict the nitrogen yield, such as FG-BioMass and Bio-CPD [98].

Jones et al. [134] compared devolatilisation rates from the literature and FG-DVC against experimental results of NO from a drop tube furnace using CFD. It was found that using the rate of tar as the devolatilisation rate and nitrogen partitioning from FG-DVC yielded the best predictions, but the predictions were improved with the inclusion of soot-NO_x interaction. Other authors have also used the tar devolatilisation rate for the single step devolatilisation model in CFD [100, 103].

Alvarez et al. [103] examined different approaches to modelling the routes of vol N and char N using CFD and experimental data from an entrained flow reactor for five coals of various ranks. It was concluded that using the HCN/NH_3 ratio predicted by FG-DVC for the route of volatiles and for the route of char N using a conversion factor gave good predictions for all coals examined in air and oxy-fuel combustion. However, the results were only under low temperatures (1273K) and it is known that at lower temperatures more NH_3 is produced [133]. A further study [104] used CFD to examine the NO results using devolatilisation rates computed by FG-DVC and average rates collated over a number of coals. It was concluded that FG-DVC was able to predict trends related to heating rates and temperatures but FG-DVC was unable to give differences in air and oxy-fuel combustion and is therefore limited to inert atmospheres.

Toporov et al. [34] performed experiments and CFD simulations of oxy-coal combustion in a 100 kW_{th} pilot scale combustion test facility which included in-flame NO measurements and predictions. The authors used the standard models in the commercial software package Ansys fluent and achieved reasonable predictions. It was arbitrarily assumed 80% of the volatiles were released from fuel as volatile-N. The results showed predictions were not captured adequately near the burner and the authors attributed this to differences in the predicted flame shape. However, it has been suggested the radical species O and OH used in Ansys fluent for volatile-N oxidation reactions are inaccurate for fuel-rich regions such as in the near flame zone [135]. An alternative set of correlations has been proposed for coal and biomass over fuel-rich and fuel-lean conditions by Hansen and Glarborg [135]. Furthermore, a different choice in volatile-N partitioning based on experiments or network models may also alter the solution.

In general, trace species such as NO_x and SO_x can be decoupled from the solution process since they have negligible effect on temperature and species. Most of the models applied in CFD are based on laminar rates and turbulence chemistry interaction can be included through the use of a probability density function, such as the β-PDF. A mean reaction rate is therefore given in each cell which considers turbulent fluctuations of temperature and chemical species.

The emission of NO based on mg/MJ basis is reported as lower in oxy-fuel combustion with recycled flue gas compared to air-coal combustion [86, 129]. This has been attributed to the reburning mechanism of NO in the flame zone from the recycled flue gas. This is further highlighted when compared to once-through experiments where little difference is reported between air and oxy-fuel NO_x emissions [129].

Conventional reduction techniques for NO include low-NO_x burners in the flame zone, SCR (Selective Catalytic Reduction) and reburning. An interesting reduction technique for NO_x and SO_x suitable for oxy-fuel combustion is sour-gas compression whereby the flue gas is compressed in stages and released as nitric and sulphur acid resulting in a purer compressed CO_2 stream suitable for transport and storage [24].

Sulphur oxides

Coal is an organic compound which also contains sulphur. The fuel bound sulphur oxidises in the combustion process to form SO_2 but can also form SO_3. Corrosion of industrial equipment can occur due to the formation of sulphuric acid from SO_3.

Much as in the fuel NO model, sulphur is assumed to be released during devolatilisation, known as volatile S, and during char combustion, known as char S.

Concentrations of SO_2 and SO_3 have been reported to be higher in oxy-coal compared to air-coal combustion at a value of about four times [136]. However, on a mass per unit energy input (mg/MJ), the SO_3 emission is lower compared to air-fired combustion.

Soot

Soot is mainly formed during the devolatilisation process from reactions with tar. It is a pollutant, and it is important in the combustion processes as its radiative properties can effect the heat transfer. Neglecting soot when modelling coal combustion can result in a significant temperature difference [137]. However, a reliable soot model has not yet been developed and detailed validation data is still required [138].

A coal-derived soot model has been developed by Brown and Fletcher [137], however the model relies on empirical constants and was only validated for combustion in air. Studies have also shown that the stoichiometric ratio is the main contributor to soot formation, suggesting negligible differences between air and oxy-fuel environments [139]. However, other studies have reported lower soot intensity in oxy-fuel conditions compared to air and a further reduction when recycled flue gas is used [140].

2.4 Heat transfer

During combustion, chemical energy is released as heat which is fundamental to boiler operation. Heat is passed from the combustion of pulverised fuel to the steam cycle through various water jackets converting water into superheated steam which drives steam turbines to produce electricity. Thermal heat transfer can be categorised as conductive, convective and radiative. In a typical utility boiler, the dominant form of heat transfer in the furnace section is radiative, while further downstream away from the flame, convective heat transfer becomes important. Heat must be transferred from the surrounding environment to the particles entering the boiler. The modelling of heat transfer to a single particle will first be described followed by approaches to modelling radiative heat transfer.

2.4.1 Particle shape, size and heating

The transfer of heat to the particle is given as:

$$m_p c_p \frac{dT_p}{dt} = h_c A_p (T_g - T_p) + \epsilon_p A_p \sigma_{sb} (\theta_R^4 - T_p^4), \tag{2.25}$$

where T_p, m_p, c_p, A_p, ϵ_p represent the temperature, mass, heat capacity, surface area and emissivity of the particle. The constants T_g, h_c, σ_{sb}, θ_R give the surrounding gas temperature, convective heat transfer coefficient, Stefan-Boltzmann constant (5.67×10^8 Wm^{-2}K^{-4}) and radiation temperature, respectively.

A common modelling assumption is that particles are spherical. Based on experimental observations, coal particles can be assumed to be approximately spherical. However biomass particles are generally of different shapes and can be considered as a combination of spheres, cylinders and slabs [17]. Furthermore, due to the fibrous nature of biomass particles, it usually has a lower grindability than coal and therefore the pulverised size of biomass is generally larger than coal. Coal particles are generally pulverised to a size less than 300 μm [121], however pulverised biomass particles may range from 10 - 1000 μm [141].

A shape factor SF can be used to account for the difference in particle surface area, A_p, between a sphere and another shape. This is a typical approach used when modelling biomass particles since the particles are not generally spherical. It is commonly described as the ratio of surface area of a sphere with volume equal to that of a particular shape s, divided by the surface area of the particular shape S [142]. Therefore, the area of the particle may be approximated by

$$A_p = S = \frac{s}{SF}.$$

The shape factor can be used to describe particle dynamics by considering a drag coefficient, for example by equations proposed by Haider and Levenspiel [143].

The convective heat transfer h_c also is affected by particle shape and can be estimated from correlations of the Nusselt number, which is the ratio of convective and conductive heat transfer to the particle. Examples of correlations for spherical particles are given by Ranz and Marshall [144].

A common assumption is to have a uniform gradient of temperature from the surface to the centre of a particle, however it has been suggested that these thermal gradients cannot be ignored for particles greater than about 150-200 μm [17, 141]. In smaller particles, the rate of reaction is dominant and different shapes will have similar trends [17]. However, CFD simulations of biomass combustion generally neglect thermal gradients [43, 145].

A thermal gradient model for biomass was created and validated using CFD against a drop tube furnace study [146]. Improvements against experimental data were also found in a 0.5 MW_{th} combustion test facility and a 300 MW tangentially fired boiler when the thermal gradient model was included [41].

The difference between air and oxy-fuel environments for particle heat-up can be attributed to the thermodynamic properties of the oxidiser. Radiative effects will

Property	Units	O_2	N_2	H_2O	CO_2
Density	[kg m^{-3}]	0.278	0.244	0.157	0.383
Specific Heat	[kJ $kmol^{-1}$ K^{-1}]	36.08	34.18	45.67	57.83
Mass diffusivity	[m^2s^{-1}]	—	1.7×10^{-4}	—	1.3×10^{-4}

Table 2.1: Properties of O_2, N_2, H_2O and CO_2 at a temperature of 1396K [15].

influence the gas temperature surrounding the particle but are discussed in Section 2.4.2. The different properties of O_2, N_2, H_2O and CO_2 at a temperature of 1396 K are listed in Table 2.1. From the Table it is evident that the molar specific heats of H_2O and CO_2 are much larger than for O_2 and N_2, which will lead to a lower gas temperature for the same O_2 concentration. To achieve a similar flame temperature for oxy-fuel conditions compared to air-coal combustion, the oxygen concentration must be increased and for bituminous coals, typical values have been reported to be in the region of 28-35% by volume [15]. The mass specific heat c_p in Equation (2.25) is only marginally larger in CO_2 than N_2 due to the difference in molecular weight and therefore the main differences in particle temperature may come from the surrounding gas temperature and radiative heat transfer.

2.4.2 Radiative heat transfer

Thermal radiation is the dominant form of heat transfer in the furnace section since it is dependent to the fourth power of temperature. Radiation can be described by the quasi-steady radiation transfer equation (RTE) [147]:

$$\frac{dI_\lambda\left(\mathbf{r},\mathbf{s}\right)}{dt} = \kappa_\lambda I_{\lambda,b}\left(\mathbf{r},\mathbf{s}\right) - (\kappa_\lambda + \sigma_{s,\lambda})I_\lambda\left(\mathbf{r},\mathbf{s}\right) + \frac{\sigma_{s,\lambda}}{4\pi}\int_{4\pi} I'_\lambda\left(\mathbf{s}_i\right)\Phi\left(\mathbf{s}_i,\mathbf{s}\right)d\omega_i \tag{2.26}$$

The intensity of radiation at a particular wavelength λ and position $\mathbf{r}$ in the direction $\mathbf{s}$ is given by $I_\lambda\left(\mathbf{r},\mathbf{s}\right)$. As radiation travels through a fluid medium, such as a combustion environment, it is attenuated by absorption and scattering effects and is augmented by emissions and in-scattering. Absorption and scattering effects can be described by the absorption coefficient κ_λ and the scattering coefficient $\sigma_{s,\lambda}$ and are, in general, also dependent on wavelength. A scattering phase function $I'_\lambda(\mathbf{s}_i)$ also describes the scattering to be dependent of direction, which may also vary with wavelength. The term on the right hand side involves the integration over a unit sphere.

In the Energy Equation (see Equation (2.6)), the radiative source term S_{rad}, ignoring scattering and particle effects, is described by the divergence of the radiative flux $q_\lambda(\mathbf{r})$ at a particular wavelength and position, and is given by

$$\nabla \cdot q_\lambda(\mathbf{r}) = \kappa_\lambda(4\pi I_{\lambda,b} - G_\lambda)$$

where

$$G_\lambda = \int_{4\pi} I_\lambda(\mathbf{r}, \mathbf{s})\, d\omega$$

If radiation is assumed to be independent of wavelength, then it is called gray and the integration over the spectrum is not needed. Therefore, the notation of λ could be dropped in Equation (2.26).

Analytical solutions of the RTE are impossible, with the exception of very simple situations [147]. Several methods are available for solving the RTE which include Monte Carlo, Discrete Ray Tracing Method (DRTM) and Discrete Ordinates (DO) methods.

The Monte Carlo method is based on statistical methods and uses a certain number of rays to track the radiation intensity through the domain. A random number generator is typically used to generate the direction of the rays and the intensity is tracked until it is terminated by absorption from a gas or by a wall. Accuracy is improved as the number of traced bundles is increased, however, processing power also significantly increases.

The discrete transfer method (DTM) [148] is also a ray-tracking approach similar to the Monte Carlo Method, however the directions of rays are explicitly defined and are tracked until they reach another surface. Accuracy can also be improved using a greater number of rays. The DTM is implemented into some CFD codes, however sometimes scattering is ignored, which is important in optically thick media, as present in coal combustion.

The DO method [149] solves the RTE over a number of discrete solid angles based on a Cartesian grid rather than ray tracing. The RTE is converted into a number of coupled differential equations which are solved for each direction over the solid angle 4π. The integrals in the RTE are replaced with numerical quadrature and the solid angles are discretised using polar and azimuthal angles and the Cartesian coordinates can calculated from the cosine of the angles. Each set of Cartesian co-ordinates is also weighted such that the total of the weights sum to 4π, which represents the integral over the unit sphere. Accuracy of the solution can be improved using a higher discretisation of directions albeit with an increase in computational cost.

The P1 radiation model is a spherical harmonic method and a subset of the P-N models [150]. The method is suitable for optically thick problems and can handle anisotropic scattering such as occurs in pulverised coal boilers. However, the DOM method is often used as it is more accurate than the P1 model [151].

The flow field and radiation can often be treated as uncoupled in incompressible combustible flow due to the differences in velocity scale and is treated as a quasi-steady state. Discrete time steps in transient problems should be large enough to ensure the quasi-steady state assumption is still valid. This means that there is no direct coupling of radiation and the CFD solution, however the solution is effected indirectly since radiation is dependent on the gaseous and particle radiative properties.

2.4.3 Gaseous radiative properties

In quantum mechanics, an atom or molecule which contains bound electrons centred around the nucleus can contain a discrete number of energy levels. The transition of an electron from one energy level to another is caused by the absorption (increasing energy level) of a passing photon or spontaneous emission of a photon (decreasing energy level) [147]. The energy of the photon is equivalent to the difference in discrete energy levels inside the molecule and the change in energy can be assumed to be inversely proportional to the wavelength λ of an electromagnetic wave, known as *Planck's law*.

The change in energy can also be classified into rotational, vibrational and electronic energy transitions which describe the degrees of freedom a molecule can move. Within each energy transition, there can be a number of energy modes which occur at a particular wavelength λ. Vibrational and rotational transitions occur at wavelengths in the infrared region of the spectrum which is typical in combustion environments [147]. An energy spectrum can be constructed which shows a series of absorption or emission bands representing the difference in energy at a particular wavelength. For example, CO_2 has emission bands at 2.7, 4.3 and 15 μm [152] in the infrared spectrum which correspond to different modes.

Tri-atomic molecules CO_2 and H_2O have strong absorption / emission bands in the infrared spectrum [152]. In the infrared spectrum, at temperatures typical in combustion, nitrogen and oxygen do not emit or absorb radiation [147]. Modelling the radiation from combustion in air has relatively low levels of CO_2 and H_2O and the overall gas composition is usually treated as gray. However, treating the combustion gas as gray can lead to significant errors when modelling oxy-fuel combustion since high concentrations of CO_2 and H_2O are present.

Modelling gaseous properties in a homogeneous fluid mixture, scattering exists only at a very small scale due to the influence of atoms and molecules and can be treated as negligible [147]. Therefore the spectral absorptivity needs to be modelled. There are a number of models that can be used to model radiative properties of gases. In general, three groups are available which are line-by-line models, band models and global models.

Line-by-line calculations solve the spectral radiative transfer equation for several hundred thousand wave numbers [147]. A large database for each of the wave numbers is needed, which can be obtained from spectroscopic databases such as HITRAN, or HITEMP which include combustion gases at high temperatures [153]. The computations are very computationally demanding and not feasible to use with CFD. The entire spectrum can be divided into a number of bands and the absorption coefficient is either uniform or changes smoothly over the bands [154]. Narrow-band models typically divide the spectrum into intervals (e.g. $\Delta\lambda \approx 25\ \mathrm{cm}^{-1}$) and examples include the Statistical Narrow Band (SNB) model [155] and narrow-band k-distribution model [156]. Wide-band models, such as the Exponential Wide Band Model (EWBM) [157,158], divide the spectrum into intervals which are concentrated near strong absorption and emission wavelengths whereby a profile function is then applied. Furthermore, the use of these models is limited to solvers where integral forms of the RTE are solved, such as the DTRM. Most CFD codes use a finite volume approach and as such have implemented the DO model. Further details on band models are given by Modest [147] and Viskanta and Mengüç [154].

Global models give mean absorption and emissivity values for a gas composition at a particular temperature and pressure. Polynomials can then be created from experimental tables, such as those by Hottel et al. [159] or tables created from more detailed models such as narrow band models [147]. The Weighted Sum of Gray Gas (WSGG) model [159] is a global model that uses a number of gray gases and one transparent gas to represent the entire spectrum. In general, the WSGG model relies on temperature dependent polynomials and a constant uniform pressure absorption coefficient for a particular pressure of species and path length. The most common constants are those of Smith et al. [160] for combustion in air which were derived from an exponential wide-band model. Polynomial tables are only available for partial pressure ratios of H_2O/CO_2 of 1 and 2 which are unsuitable for oxy-fuel conditions where partial pressures as low as 1/8 can exist [161]. Partial pressure lengths are also used and are calculated by the sum of CO_2 and H_2O multiplied by a specified length and in oxy-fuel combustion this can be almost four times as high compared to air-combustion [161].

A number of new WSGG constants have been proposed in the literature that are suitable for oxy-fuel combustion. The correlations for the model have been fitted based on SNB model results [161, 162], or more accurate line-by-line integration of spectroscopic databases [163]. Standard models are limited to particular ratios of CO_2 and H_2O, however this was accounted for by Johansson et al. [162] where the model has been modified to account for ratios between 0.125 and 2.

Kangwanpongpan et al. [163] compared a set of new WSGG constants and two sets of constants from Johansson et al. [161, 162] with solutions from line-by-line predictions using the HITEMP2010 database [153]. The paper highlighted the lowest error occurred from constants proposed by Kangwanpongpan et al. [163] with increased errors for Johansson et al. [162] followed by Johansson et al. [161].

The full-spectrum correlated-k (FSCK) model is another global model to represent the entire spectrum. Porter et al. [164] compared the gray WSGG model with constants proposed by Smith et al. [160] with the correlated FSCK model against SNB data for air and oxy-fuel type conditions in a simple box configuration with black walls. The FSCK model compared well against the SNB data for the radiative source term and the heat transfer at the wall in both air and oxy-fuel conditions. The gray WSGG approach over-predicted the heat transfer at the wall for all of the cases despite giving adequate predictions for the radiative source term in the air cases.

Edge et al. [35] performed CFD simulations of a 0.5 MW_{th} CTF in air and oxy-fuel tests for two different burners. The FSCK and gray WSGG approaches with constants proposed by Smith et al. [160] were used for gaseous radiative properties. The simulations were compared against radiative heat flux measurements and showed a closer agreement with the predictions using the FSCK than the WSGG approach. LES and RANS were also compared using the gray approach. Radiation was enhanced in the near burner zone with LES, and the authors attributed this to intermittency effects captured with the LES.

2.4.4 Particle radiation

In pulverised fuel systems, the contribution of particle radiation comes from the char, soot and fly-ash. Radiation from fly ash particles exceeds the contribution of radiation from char, soot as well as triatomic atoms such as CO_2 and H_2O [154]. Particles also absorb and scatter radiation. Scattering describes either the change in direction of radiation from being reflected off the particle, refracted after penetration of the particle or diffracted by the particle [147].

A gray assumption can be used for the particles where they do not depend on wavelength. The contribution of particle radiation can therefore be represented as a function of particle surface area, temperature and concentration with a constant value of absorptivity which is generally assumed to be about 0.9 [165].

Johansson et al. [166] numerically studied the influence of gas and particle radiation in air and oxy-fuel environments. The authors concluded that the effects of particle radiation outweighs gaseous radiative effects, and if the temperature and distribution of particle concentration is the same in air and oxy-fuel environments, little differences would be observed.

Chapter 3

Experimental facilities and data

CFD simulations of five experimental facilities are performed in this thesis. This chapter describes the facilities and available experimental data which will be used in subsequent chapters. In summary, the facilities are as follows:

(i) Laboratory swirl burner
(ii) Laboratory coal and methane burner
(iii) 100 kW_{th} combustion test facility
(iv) 250 kW_{th} combustion test facility
(v) 500 MW_e full-scale utility boiler

In Chapter 4, a NO_x model has been implemented into an in-house LES code, *PsiPhi*, and experimental data from the laboratory swirled gas burner and methane-coal burner is used to validate the model. The model is also implemented in the 100 kW_{th} Combustion Test Facility (CTF). The cases were chosen due to the detailed experimental data available and relative small scale geometry such that a number of LES could be performed within a reasonable computational cost. Results, excluding the predictions of NO have been published for the methane-coal burner by other authors [45]. Simulations of the laboratory swirl burner are the sole work of the author. In Chapters 5 and 6, a commercial CFD software package, Ansys fluent, is used due to the complexity and scale of geometry involved in each of the cases. In Chapter 5, coal combustion is simulated in a 250 kW_{th} CTF and validated against available experimental data. In Chapter 6, a theoretical study of coal and biomass combustion is performed under air and oxy-fuel conditions in a full scale utility boiler.

3.1 Laboratory swirl burner

The swirl burner is a laboratory-scaled gas burner based at the University of Sydney, Australia [167]. Experiments were performed as part of the International Workshop on Measurement and Computation of Turbulent Nonpremixed Flames [168]. The burner is an extension of a bluff-body burner also examined in the workshops. The purpose of the burner was to provide well-defined boundary conditions for a complex swirling flow that exhibits similar characteristics of that which occurs in practical combustors [167]. A number of experimental and numerical papers have been published on a variety of conditions for this burner [169–174] and the data is available online [175]. This allows a well-defined case for CFD model validation and development.

3.1.1 Burner geometry

A schematic of the burner is presented in Figure 3.1. The burner consists of a 3.6 mm diameter inlet providing the fuel which is surrounded by bluff body with an outer diameter of 50 mm. An annulus of primary swirled air which is 5 mm thick surrounds the bluff body. Three tangental air streams inclined at an angle of 15° are positioned 300 mm from the exit of the burner to provide axial and tangential velocities. A square wind tunnel with an inlet cross section of 305 × 305 mm^2 and an outlet cross section of 130 × 130 mm^2 provides co-flow around the burner [173].

3.1.2 Case description

The case examined in this study, named SM1, is given in Table 3.1 and is of a compressed natural gas (CNG) swirling flame. The case is described by four variables: the fuel velocity U_f, primary axial velocity U_s, primary tangential velocity W_s and co-flow velocity U_c. The swirl number in this burner is described by a geometric swirl number defined by $S_g = U_s/W_s$.

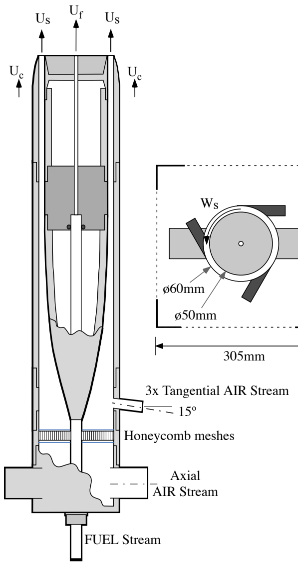

Figure 3.1: Schematic of bluff body swirled burner [175].

CASE	Fuel	U_f (m/s)	U_s (m/s)	W_s (m/s)	U_c (m/s)	S_g
SM1	CNG	32.70	38.20	19.10	20.00	0.5

Table 3.1: Experimental operating conditions for the Sydney burner.

3.1.3 Experimental data

Velocity measurements were performed using LDV (Laser Doppler Velocimetry) where the velocity of the gas was determined from the velocity of seeded particles. The sub-micron seeded particles were injected from the central fuel jet along with the fuel and an approximate error of the velocity measured was assumed to be 4% [167]. Simultaneous temperature and species measurements (CH_4, N_2, O_2, H_2O, CO and CO_2) were also taken and performed using a single point Raman-Rayleigh LIF (laser-induced fluorescence) technique [170]. The temperature was obtained from the Rayleigh signal using species densities and the ideal gas law. The LIF technique was also used to give concentrations of OH and NO as well as a more accurate prediction of CO [170].

3.2 Laboratory coal and methane burner

The laboratory scale burner is located at the CRIEPI (Central Research Institute of Electric Power Industry) in Japan, and experimental results have been published in the literature [176–178].

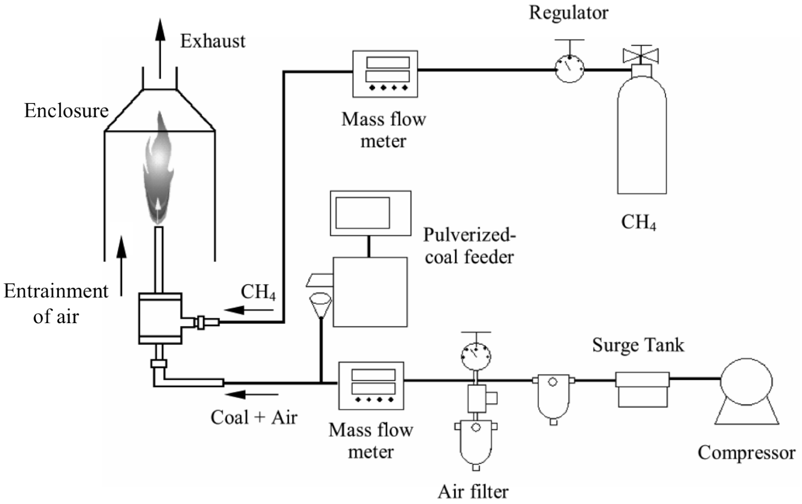

Figure 3.2: Schematic of the laboratory coal and methane burner [177].

3.2.1 Geometry and case description

Pulverised coal and air are carried into a burner with a pipe diameter of 6 mm (primary inlet) surrounded by an annulus with a thickness of 0.5 mm containing methane (secondary inlet) which is used to ignite the coal particles. The wall between the burner and the annulus of methane has a thickness 0.5 mm whereas the wall between the annulus and ambient air is 1 mm thick. An overall schematic set-up of the experiment is shown in Figure 3.2. The methane and carrier air are regulated by mass flow meters and the coal is controlled using a screw feeder. Entrainment would also be present from the surrounding air into the enclosure, however it was assumed not to affect the flame and a constant velocity of 0.6 m/s was used based on a previous study [45]. Further, the gases were not preheated and were assumed to be at ambient temperature.

Boundary	Species	Area (m^2)	Flow rate	Temperature (C)
Primary	Air	2.82×10^{-5}	2.07×10^{-4} Nm^3/s	20.0
	Coal		1.49×10^{-4} kg/s	
Secondary	Methane	1.18×10^{-5}	2.33×10^{-5} m^3/s	20.0
Entrainment	Air	3.13×10^{-2}	0.6 m/s	20.0

Table 3.2: Operating conditions for the CRIEPI burner.

The experimental conditions for the case examined are shown in Table 3.2. It should be noted that the coal is entrained into the flow and therefore some additional air may be present in the primary air stream. The authors performed a CFD simulation of the burner and reported that the entrainment contributed an extra 0.27×10^{-4} Nm^3/s [179]. This additional entrainment was included in the simulations.

Newlands coal was used in the experiments and the coal analysis is given in Table 3.3. The particle size diameter of the coal particles varied between 5 and 61 μm, with a mean diameter 33 μm.

Measurements of particle velocities were obtained by a non-intrusive shadow Doppler particle analyser (SPDA) and LDV equipment. The SPDA also allows for the measurement of non-spherical particles as well as their velocities. Measurements were taken for the axial as well as radial distributions at 60, 120 and 180 mm from the exit of the burner. The temperature of the coal particles were measured using a two-colour radiation pyrometer technique. Species measurements were also given by the authors [176], however the experimental technique is not mentioned. It was assumed that the gas analysis was operated using a probe directly in the flame and connected to a gas analyser. The values were assumed to be reported on a dry basis.

Ultimate analysis (a.r., w.t.%)		Proximate Analysis (d.a.f., w.t.%)	
Carbon	70.09	Fixed Carbon	68.27
Hydrogen	4.29	Volatile Matter	31.73
Oxygen	6.54		
Nitrogen	1.5		
Sulphur	0.39	Calorific value (MJ/kg)	
Ash	14.81	GCV (dry)	29.10
Moisture	2.60	NCV (dry)	28.34

Table 3.3: Coal analysis of Newlands coal.

3.3 100 kW$_{th}$ combustion test facility

The 100 kW$_{th}$ combustion test facility is located at RWTH Aachen University, Germany and experimental data has been published under oxy-fuel conditions [34].

3.3.1 Geometry and case description

The facility is a down-fired cylindrical furnace which is 2.1 m in length and has an inner diameter 0.4 m. A traversable burner that can move axially is used to allow measurements at different distances from the burner. A schematic of the furnace and the traversable burner is schematically shown in Figure 3.3(a).

The burner consists of a primary annulus which carries the carrier gas and coal. A secondary annulus with a swirled combustion oxidiser is present surrounding the primary stream. The primary and secondary annuli inject coal and combustion oxidiser, respectively, into a quarl. A tertiary stream surrounding the quarl supplies further combustion gases. A staging stream is also present which surrounds the burner and its purpose is to provide the remainder of the combustion gas. The use of the staging stream further reduces the gas velocities in the primary, secondary and tertiary streams which also increases the fuel-to-air ratio near the burner. Di-

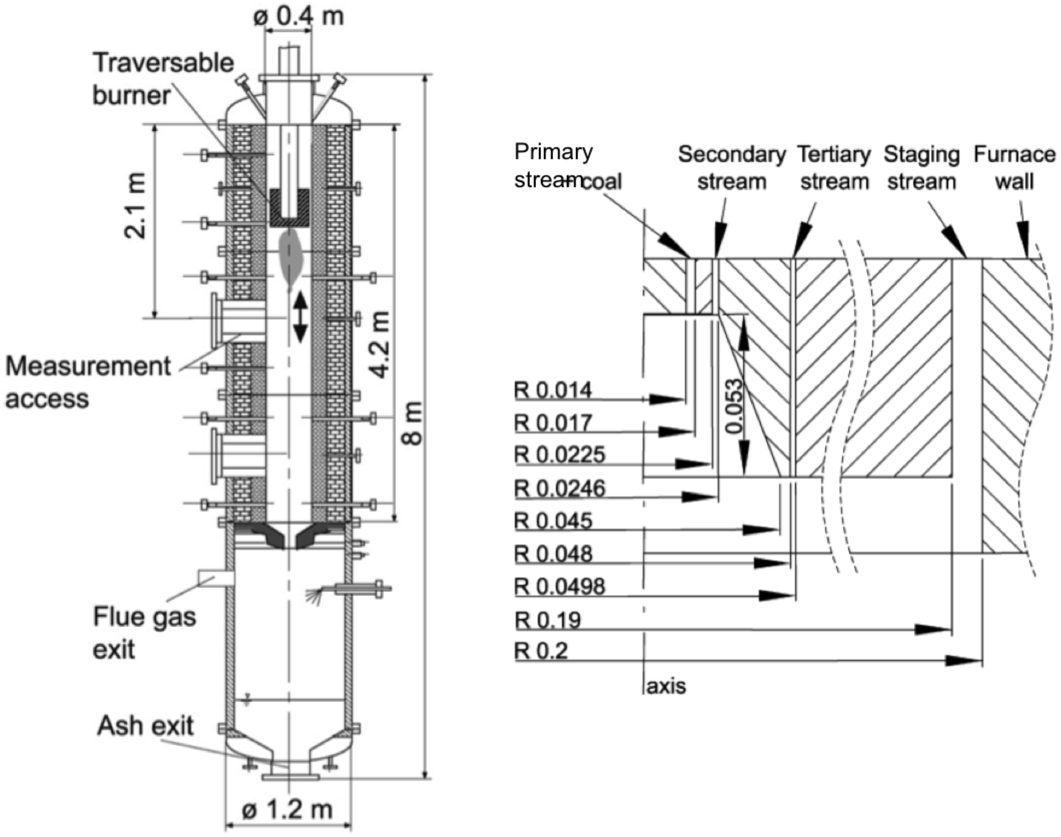

(a) (b)

Figure 3.3: Schematic of (a) the 100 kW CTF, and (b) its burner at RWTH Aachen University [34].

mensions of the burner are shown in Figure 3.3(b).

Experimental measurements of particle velocities, gas and particle temperatures and concentrations of oxygen and NO have been reported by the authors [34]. Laser Doppler Velocimetry (LDV) techniques were used to measure the velocities of the particles and intrusive measurement techniques were used for gas compositions and temperatures. A suction probe and a flue gas analyser were used to measure the concentrations of O_2, CO_2, CO and NO and an International Flame Research Foundation (IFRF) suction pyrometer was used to measure the gas temperatures.

The experiments were fired at a thermal rating of 40 kW_{th} and the mass flow rates, species concentrations and temperatures at the inlets of the burner are provided in Table 3.4. The oxidiser was a synthetic mixture of O_2 and CO_2, and the

	Flow rate (kg/hr)	O_2 conc. (vol. %)	CO_2 conc. (vol. %)	Temp. (°C)
Primary	17.6	19.0	81.0	40.0
Coal	6.5			
Secondary	26.6	21.0	79.0	60.0
Tertiary	1.5	21.0	79.0	60.0
Staging	54.9	21.0	79.0	900.0

Table 3.4: Operating conditions for the 100 kW_{th} CTF.

Ultimate analysis (a.r., w.t.%)		Proximate Analysis (d.a.f., w.t.%)	
Carbon	67.40	Fixed Carbon	53.26
Hydrogen	4.24	Volatile Matter	46.74
Oxygen	14.70		
Nitrogen	0.86		
Sulphur	0.30	Calorific value (MJ/kg)	
Ash	4.10	GCV (dry)	23.28
Moisture	8.40	NCV (dry)	22.15

Table 3.5: Coal analysis of the Rhenish lignite coal used in the 100 kW_{th} CTF.

volumetric O_2 concentration was kept at 19% in the primary stream which carries the coal while the other streams were kept at 21%. The remaining oxidiser was CO_2. The primary, secondary, tertiary and staging stream were preheated to 40, 60, 60 and 900°C, respectively. The secondary stream was swirled with a swirl number of 1.2.

Rhenish lignite coal was used in the experiments and the coal properties are given in Table 3.5.

3.4 250 kW_{th} combustion test facility

The combustion test facility (CTF) is located in Beighton, near Sheffield, England. The facility is part of the UK carbon capture and storage research centre (UKCC-SRC) Pilot-scale Advanced Capture Technology (PACT) sites across the U.K. which contains national facilities for research in carbon reducing technologies.

3.4.1 Experimental facility

The facility is a down-fired cylindrical furnace which is 4 m long and has an internal diameter of 0.9 m. The furnace is refractory lined with a thickness of 0.1 m and water-cooled for the first 3 m. A water seal is present at the bottom of the facility to provide a seal and allows for fluctuations in pressure. The facility is equipped with a gas mixing skid and a recycle stream for both synthetic as well as wet or dry flue gas recycle. Preheaters are also available to preheat the oxidising gas to the burner. The flue gas can be passed from the oxy-fuel rig to the stack or via an amine plant.

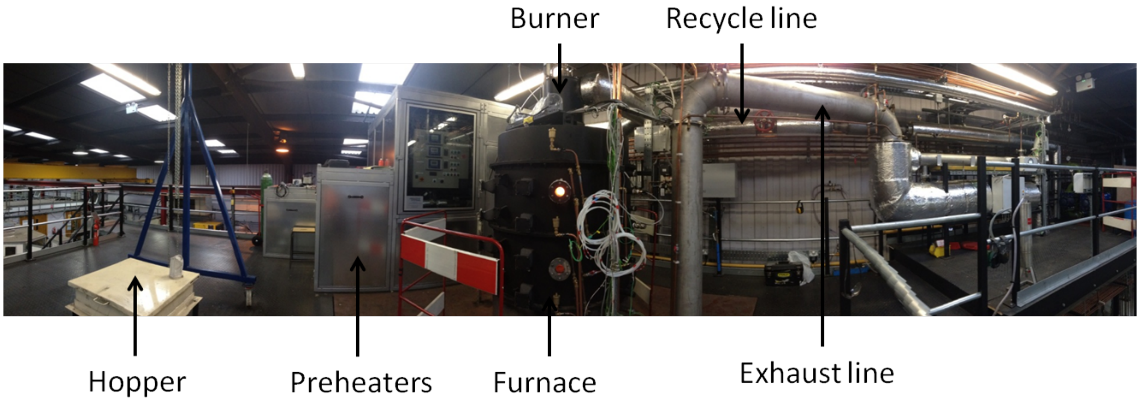

Figure 3.4: Layout of the upper mezzanine of the 250 kW_{th} CTF.

The test facility has the capability for non-intrusive measurements, such as particle image velocimetry (PIV) laser measurements, LDV measurements, 2D and 3D flame imaging. Intrusive measurements, such as in-flame gas sampling, gas temperature and heat flux measurements, are also possible. A mezzanine is installed in order to allow access to the ports for measurements near the flame zone and a photograph of the mezzanine level is shown in Figure 3.4. The Figure shows the hopper where coal is loaded, the preheaters to supply heat to the oxidiser, the burner, the first three sections of the furnace with a higher number of ports for intrusive and non-intrusive measurements in the first two sections, the exhaust and recycle lines.

3.4.2 Burner description

The burner is a commercial Doosan Babcock low-NO_x burner which has been scaled down to 250 kW_{th}. An image showing the burner with the quarl before installation is shown in Figure 3.5(a). The burner consists of a central inlet which provides natural gas and annuli delivering core air for initial heating of the furnace, a primary annulus for the coal and carrier gas with coal gutters, a flame holder to provide flame stability, and two annuli (secondary and tertiary registers) where swirled oxidiser is provided. In Figure 3.5(b) a disassembled view of the major components is shown. The assembled burner, as shown in Figure 3.5(c), fits into the top of the refractory

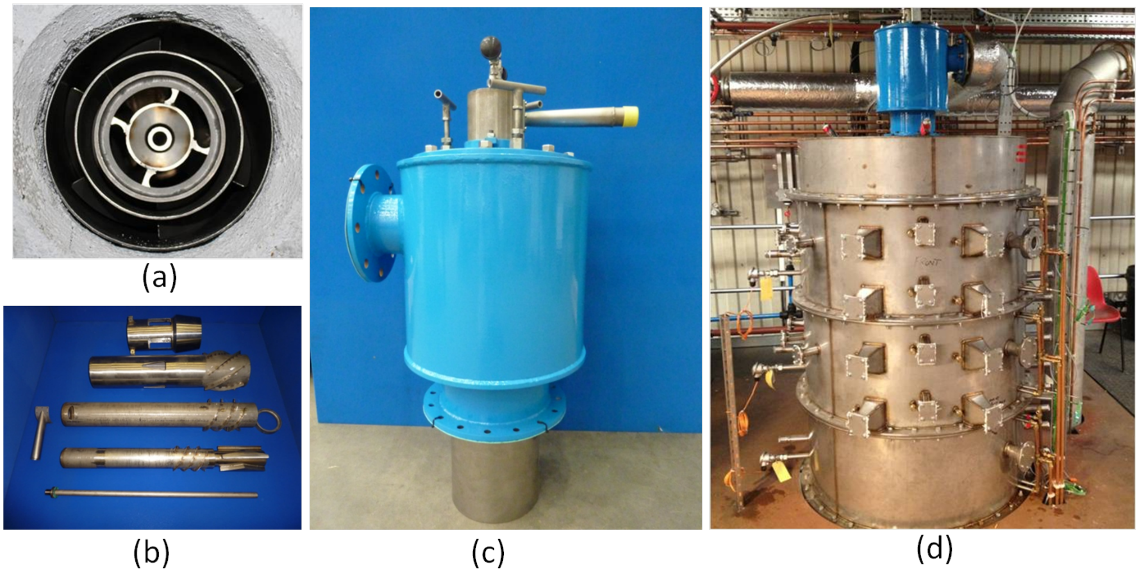

Figure 3.5: Images of the Doosan Babcock 250 kW_{th} coal burner (a) front view, (b) disassembled view showing from top to bottom: damper for tertiary and secondary split, tertiary inner pipe, secondary inner pipe, primary inner pipe, gas pipe, (c) assembled burner before installation and (d) burner installed in the CTF.

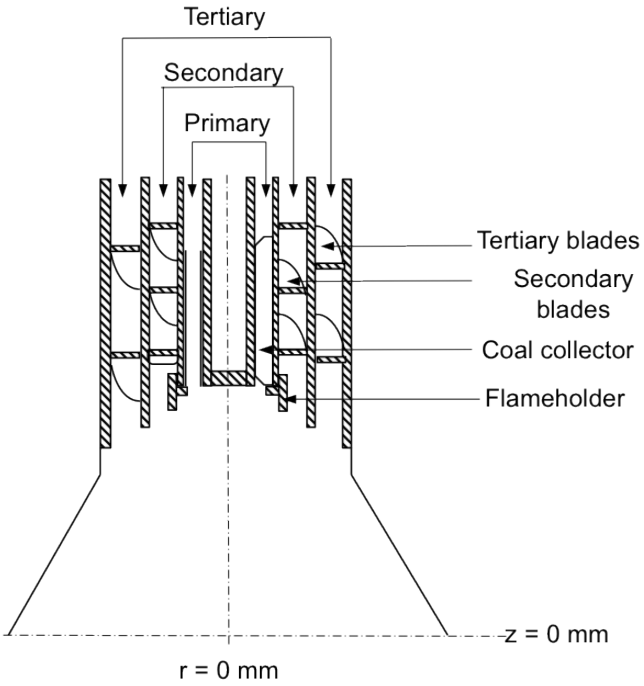

Figure 3.6: Schematic of the burner showing the location of registers, coal collector and flameholder.

which is 200 mm deep. A quarl of approximately 50 mm depth and at an angle of 25 degrees is created in the top section of the refractory. The installed burner is shown in Figure 3.5(d).

The location of the primary, secondary and tertiary registers, along with dimensions, are shown in Figure 3.6. The coal and carrier gas enter the burner and are swirled by blades (not shown) angled at 63° before being concentrated by four coal collectors and released into the furnace. Combustion air enters the burner and is split between a damper (not shown), which splits the air between the secondary and tertiary register. The flow is then further swirled by blades angled at approximately 64° and 33°, respectively. The blades are thin with a constant chord and angle, and therefore the swirl number S can be described by [180],

$$S = \frac{G_\psi}{G_x R_{outer}} = \frac{2}{3}\left[\frac{1-(R_{inner}/R_{outer})^3}{1-(R_{inner}/R_{outer})^2}\right]\tan\alpha \tag{3.1}$$

where G_{ψ}, G_x, R_{inner}, R_{outer} and α corresponded to the angular momentum, linear momentum, inner radius, outer radius of the pipe and the angle of the blade, respectively. Based on Equation (3.1), the swirl number for the primary, secondary and tertiary registers are 0.89, 0.93 and 0.29, respectively.

The split between the secondary and tertiary annuli defined by the damper is a critical parameter. Since the burner could not be easily disassembled, measurements using photographs and correspondence with the manufacturer was necessary. The recommendations for the burner split was to use CFD to predict the distribution in the flow for each of the cases and this was assessed in Chapter 5 since it depends on the flow rate and the position of the damper.

3.4.3 Furnace description

The side walls of the furnace are lined with a high density refractory material which is 0.1 m thick while the top of the furnace is 0.2 m thick. The layout of the different refractory materials which are labelled from parts A to E is given in Figure 3.7 with the corresponding thermal conductivities, at different temperatures described by the manufacturer which are shown in Table 3.6. The refractory materials are enclosed in carbon steel walls. The refractory material along the sides of the furnace (E)

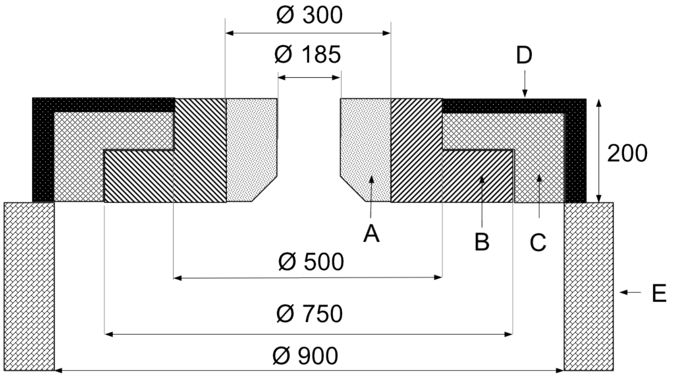

Figure 3.7: Cross section of the furnace outlining the different refractory materials.

		Thermal conductivity (W/m-K) at various temperatures (°C)						
Material	Location	200	400	600	800	1000	1100	1650
Durax C1850	A, B	-	-	-	-	2.1	-	-
Jonlite IC16	C	-	-	-	-	0.75	-	-
Skamolex	D	0.09	0.11	0.14	-	-	-	-
RCF1700	E	-	0.11	-	0.16	-	0.23	0.27

Table 3.6: Thermal conductivity for the refractory material used in the PACT facility, the locations correspond to those in Figure 3.7.

is a VecoForm RCF1700 refractory which is made of approximately 80% alumina and 20% silica. The refractory materials on the top section consists of a 1850 grade Durax refractory in the quarl (A) and part (B), Jonlite IC16 in part (C) and Skamolex Super-Isol in part (D).

Measurements are taken in the furnace at various ports located down the side of the furnace. Measurement locations at position z correspond to the distance from the exit of the quarl ($z = 0$), or equivalently the top of the inside of the refractory. The furnace is cylindrical and the radial distance r corresponds to the distance from the centreline ($r = 0$) to the inner wall of the refractory ($r = 450$ mm). For clarity, r and z are shown in Figure 3.6.

3.4.4 Experimental techniques

Gas temperature, chemical species concentration, radiative heat flux and carbon in ash were measured in the experiments.

A water-cooled IFRF Suction Pyrometer was used to measure the in-flame gas temperatures and is shown in Figure 3.8. Gas temperatures are measured using a thermocouple, however if it is introduced directly into the flame it can be affected

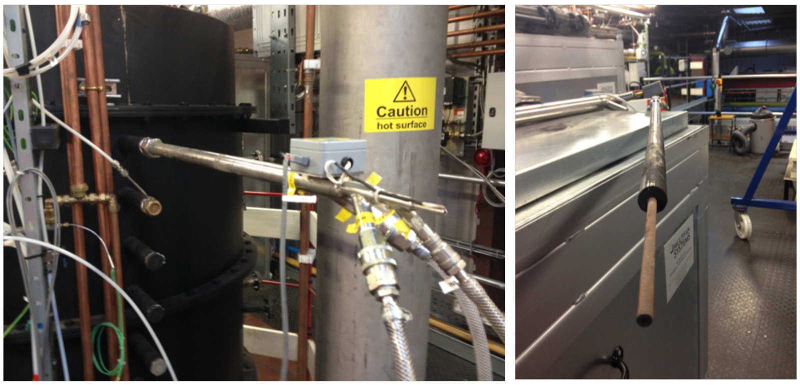

(a) (b)

Figure 3.8: Images of the IFRF suction pyrometer showing the (a) rear view, and (b) front view, showing radiation shield.

by radiation between the thermocouple and the surrounding environment leading to errors [181]. Therefore, a PtRh 30% ANSI type B thermocouple was used which was shielded by an alumina sheath to protect it from chemical attack and then by a radiation shield to minimise errors due to radiation. A hole 27 mm in diameter in the radiation shield, which is orientated away from the flame, draws in a sample of gas at a high velocity. The velocity of the gas has to be a minimum of 150 m/s to ensure that the thermocouple temperature is close to the temperature of the sampled gas [181]. The measurements are expected to reach equilibrium within 1 minute when the temperature is changed by 100°C [181]. Therefore, the temperature readings were monitored to ensure a change in temperature was observed when the probe was moved to a different location which was generally between 1 and 3 minutes depending on location. Over a period of time, the suction pyrometer can block from fly ash entering the probe, however this was regularly disassembled and a purge of compressed air was supplied to clear the fly ash after the probe was removed from the furnace.

In-furnace thermocouples are also placed in each 0.5 m section inside the furnace to measure the temperature. Type R thermocouples are used, however the

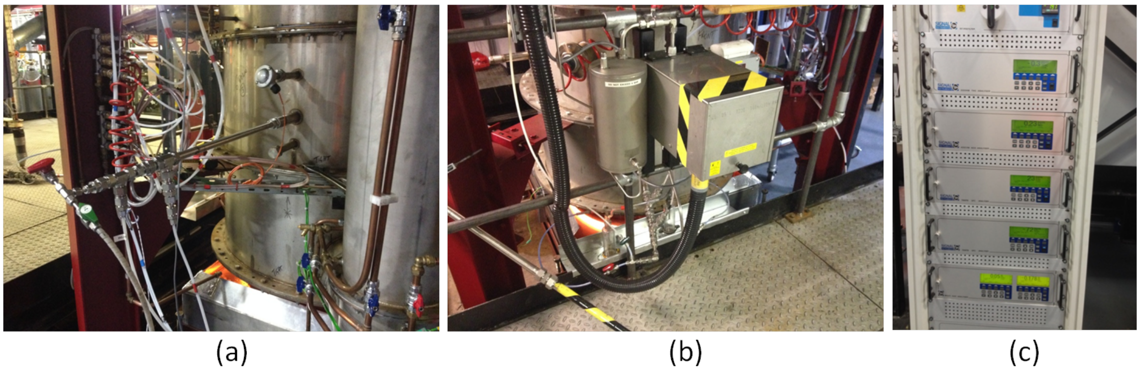
(a) (b) (c)

Figure 3.9: Images of the gas analysis probe configuration showing the (a) probe installed in furnace, (b) heated filter and Dreschel bottles, and (c) gas analyser.

thermocouples are not shielded by radiation from the wall. These measurements are used as an indicator of the temperature during the experiments and they are not a true representation of the gas temperature. Further, in-furnace thermocouples were not used for CFD validation. Thermocouples placed away from the flame in the exhaust could be used to measure the temperature of the flue gas as they are not influenced directly by radiation since they cannot "see" the flame or hot furnace walls. Exit temperature was not reported as it was inside the flue gas duct which was not modelled in the CFD simulations.

Gas species concentrations of O_2, CO_2, CO, SO_2 and NO were measured in the experiments and the set-up is shown in Figure 3.9. The values given by the analyser were reported on a dry volumetric basis. Either the exit composition was measured using a probe permanently secured in section 8 or an in-flame gas analysis was performed using a probe. The species concentrations are determined from several Signal gas analysers. The concentration of NO was detected using a 4000VM Heated Vacuum Chemiluminescence gas analyser, 7000FM Series GFC/IR analysers were used to monitor the concentration of SO_2 and CO and the concentration of O_2 and CO_2 was monitored by a 9000MGA Multi-gas analyser.

Gas was drawn in from the furnace by the use of a probe and for in-flame species measurements, the probe was water-cooled and orientated perpendicular to the centreline of the flame. The suction needed to draw in the sample was determined directly from the gas analyser and there was approximately a one minute delay in the response from the probe and sampling occurred over three minute intervals to ensure at least two minutes of data was collected. Since the probe would draw in particulates, Dreschel bottles containing glass wool were placed directly after the probe to collect the larger coal particles and fly ash before being passed through a number of filters. The sampled gas would then pass through a further filter before travelling through a heated line to remove moisture and filters with a pore size of 2 μm were also in place at the back of the analyser to prevent any remaining smaller particles entering the equipment. After every measurement, a purge of air is required to be blown back into the furnace to clear the inside of the probe as it was liable to blockage within 5 minutes of sampling especially in the flame zone. Further, only the exit composition was reported as stable readings could not be obtained with in-flame measurements near the burner zone.

A water-cooled solid collection probe was tested to collect ash samples which could later be analysed for carbon in ash (CIA) measurements and is shown in Figure 3.10. The probe is placed in a port at section 7 and uses a suction of approximately 5-10 l/min to acquire ash samples. Sampling lasts for approximately 15 minutes. The sample is first quenched (rapidly cooled) as it is sucked through the cooled probe and a removable heated filter house collects the sample. However, due to the low ash content of the El-Cerrejon coal (see Table 3.8), a very small sample was collected in the probe and the ash was instead collected from the filter further downstream of the exhaust. The CIA measurements were then performed in a laboratory in a heated furnace, however it is important to note that the ash reflects a day of testing rather than a well-defined experiment. In a full day of

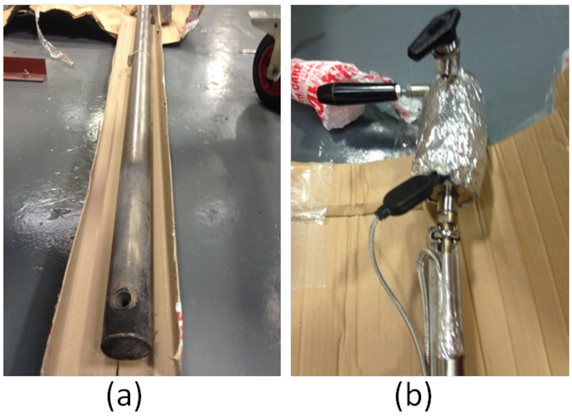

Figure 3.10: Images of the solid collection probe showing the (a) front view, and (b) rear view with the removable heated filter house.

testing, carbon may be retained in the ash as incomplete combustion may occur due to the initial heating of the furnace as well as the opening of ports for intrusive equipment such as the suction pyrometer or gas sampling probe.

A Medtherm GTW-50-24-21 584 Furnace Heat Probe with detachable parts was used to measure the radiative and total heat flux and is shown in Figure 3.11. The probe contains two methods to measure radiative heat transfer which is depicted in Figures 3.11(a) and (b). The probe contains a calcium fluoride window mount with a deflector (Figure 3.11(a)) that can deliver a nitrogen purge which cools the tip of the probe and deflects the combustion gases on the window, therefore measuring only the radiative heat transfer. The window could also be removed and the deflector reattached to deliver a nitrogen purge and measure radiative heat transfer (Figure 3.11(b)) . Both methods had separate calibration curves as the window would absorb some of the radiation. With the window removed, the nitrogen could be turned off thus allowing the sensor to be exposed to conductive, convective as well as radiative heat transfer, resulting in total heat flux.

For the radiative heat flux measurements, a nitrogen purge of approximately 3-4 bar was used and this was determined from observing the change in the heat flux results when varying pressures of nitrogen were used.

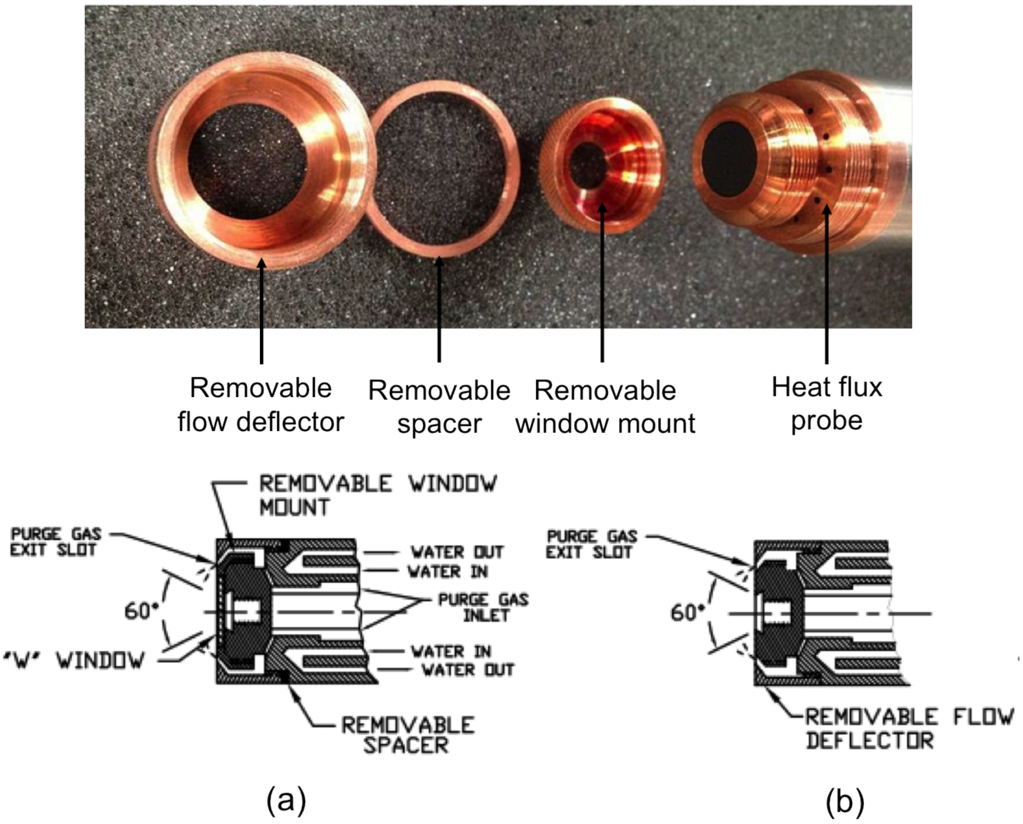

Figure 3.11: Images and illustration of the heat flux probe with a removable window. Radiative heat transfer can be measured by (a) using the window with nitrogen purge, or (b) removing the window and using a nitrogen purge.

3.4.5 Investigated cases

Two experiments were investigated at a 200 $\mathrm{kW_{th}}$ input with air as the oxidiser. The cases investigated are both with and without preheated combustion air, named air and air-preheat, respectively. The boundary conditions of the two experiments are shown in Table 3.7. The primary register delivers the coal with the carrier air and the combustion air is delivered into the burner before being split by the damper into the secondary and tertiary registers and the effect of altering the split can influence NO and CO concentrations in the flue gas. The split is defined as follows:

$$S_{sec,ter} = \frac{S_{mfr}}{T_{mfr}}$$

where S_{mfr} and T_{mfr} represent the mass flow rate in the secondary and tertiary registers, respectively, after the damper. The values were calculated using CFD in Section 5.1.1 and are shown in Table 3.7. The two different values are obtained since the damper position was changed between the two cases.

The fuel used was El-Cerrejon coal and the properties are given in Table 3.8. A Rosin-Rammler distribution [182] was fitted to the particle size distribution and the parameters are shown in Figure 3.12.

The outlet composition of both the air and air-preheat case are shown in Table 3.9. Since oxygen is generally calculated by the remainder from C, H, N, S, ash and moisture in the ultimate analysis, it may not be available for combustion. Therefore, a mass balance was performed with the flow rates in Table 3.7 and the coal analysis in Table 3.8 for both oxygen included and excluded. The total combustion air delivered into the system was approximately 3970 N l/min for both the air and air-preheated cases. For the air case, if a dry volumetric exit gas composition of 4.0% was

		air	air-preheat
Primary register			
	coal feed rate (kg/hr)	24.4	24.4
	carrier air (N l/min)	775.0	775.0
	temperature (°C)	18.3	20.0
Combustion air register			
	combustion air (N l/min)	3152.0	3150
	temperature (°C)	23.2	255.3
	split $S_{sec,ter}$	0.923	0.823
Purge			
	air (l/min)	46.7	46.7
	temperature (°C)	20.0	20.0

Table 3.7: Operating conditions for the air and air-preheat cases.

Ultimate analysis (a.r., w.t.%)		Proximate Analysis (d.a.f., w.t.%)	
Carbon	73.67	Fixed Carbon	59.26
Hydrogen	5.04	Volatile Matter	40.74
Oxygen	11.32		
Nitrogen	2.48		
Sulphur	0.38	Calorific value (MJ/kg)	
Ash	1.31	GCV (a.r.)	30.79
Moisture	5.81	NCV (a.r.)	29.49

Table 3.8: Coal analysis of the El-Cerrejon coal.

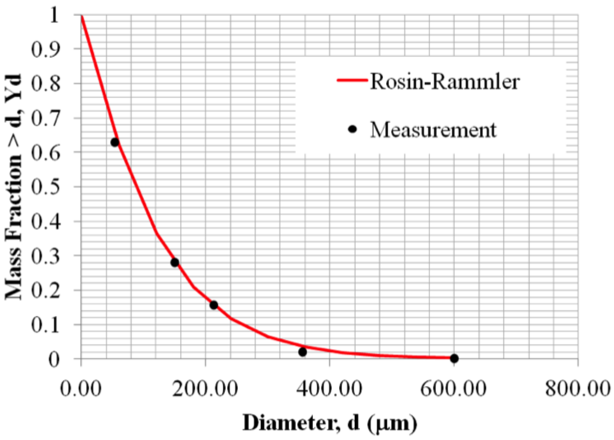

$$Y_d = e^{-(d/\bar{d})^n}$$

Parameter	Value
Mean diameter $\bar{d}$	110
Spread n	1.1
Minimum diameter	1.0
Maximum diameter	600.0

Figure 3.12: A Rosin-Rammler distribution for the El-Cellejon coal.

assumed, 3950 N l/min was required when oxygen was assumed to be not available for combustion whereas 3768 N l/min was required when oxygen was assumed to be available. A similar conclusion was found for the air-preheat case. Oxygen is not measured directly in Table 3.8 and based on the mass balance calculation, it was assumed the oxygen was not present or available for combustion. The inert substance was assumed to be retained in the ash.

The CIA measurements were taken from the fly ash that was collected on the filter after a test run. The values are high due to the relative low ash content of the fuel, but may be slightly higher than expected since the sample was collected over a

species	air	air-preheat
O_2 (dry, vol %)	3.8 ± 0.2	3.2 ± 0.1
CO_2 (dry, vol %)	15.5 ± 0.2	15.5 ± 0.3
CO (dry, ppm)	40 ± 5	7 ± 6
SO_2 (dry, ppm)	297 ± 9	284 ± 8
NO (dry, ppm)	276 ± 8	367 ± 14
Carbon in Ash (CIA) (%)	25.54	7.17

Table 3.9: Exit composition for the air and air-preheat cases.

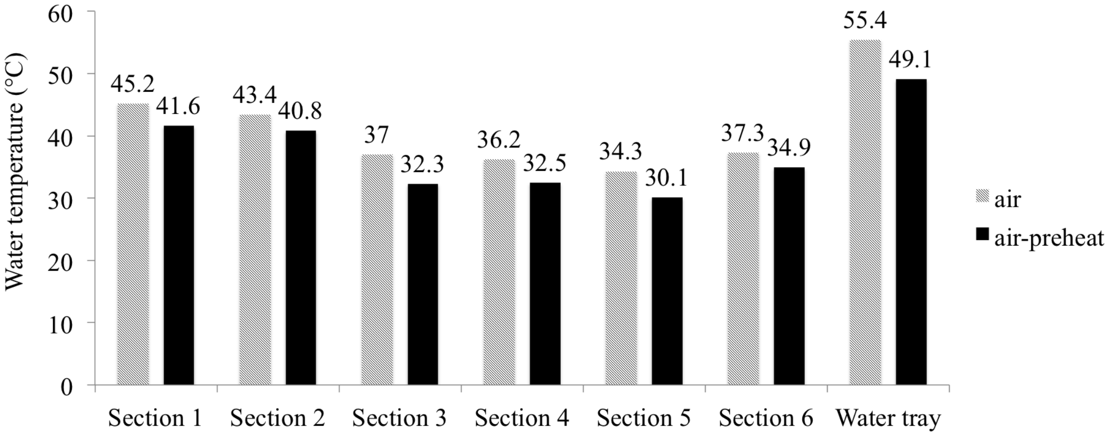

Figure 3.13: Average cooling water temperatures and water tray temperature for the air and air-preheat cases.

6 hour run which included the initial heating of the furnace and in-flame sampling that may have altered the flame.

The outlet water temperature of the first six sections and the temperature of the water in the water tray were also measured and averaged values are given in Figure 3.13. The temperature of the outer walls on the top of the furnace at different locations was also measured and on average was about 100-130°C. Further, radiative heat flux and in-flame temperature measurements were also performed and are reported in Chapter 5 with the CFD predictions.

3.5 Full-scale utility boiler

CFD simulations are performed in Chapter 6 on one of the 500 MW_e coal-fired utility boilers located at Unit A, Didcot Power Station in the UK. Although the Didcot A power station has closed under the LCPD directive in March 2013, validation data is available from a previous project [183]. Data from RWE's in-house power station model is also available for a further benchmark of the CFD simulation.

3.5.1 Boiler description

The coal-fired boiler is approximately 44 m × 30 m × 9 m (height × width × length). A computer-aided design (CAD) of the boiler and description of a single burner is shown in Figure 3.14 and dimensions are shown in Figure 3.15. The wall-fired boiler has 48 burners on the front wall organised in 4 rows of 12 where coal and combustion air enters the boiler. The bottom of the boiler contains a hopper region where bottom ash is deposited. The combustion of coal produces heat and tube banks exist throughout the boiler to heat up water to steam which is then fed to a series of steam turbines which are connected to generators to produce electrical power. The section considered for CFD modelling consists of the water walls surrounding the boiler, final reheater, secondary superheater and platen 1 and 2 superheaters. Further heat exchangers are also present further downstream where convective heat transfer dominates from the hot combustion gases, but are not considered in the CFD simulations as detailed geometry was unavailable. There are 36 tube banks for platen 1, 2 and the secondary superheaters which are arranged in parallel and 74 tube banks for the final reheater. The tube thickness for each of these banks is approximately 5 mm.

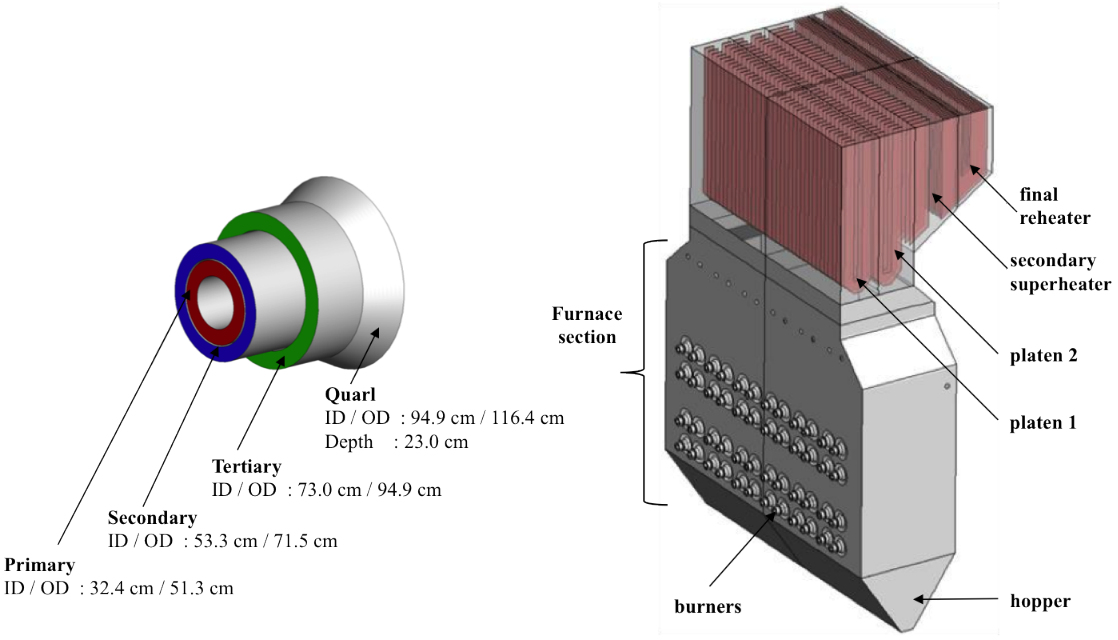

Figure 3.14: Schematic of a single burner and CAD drawing of the full-scale utility boiler.

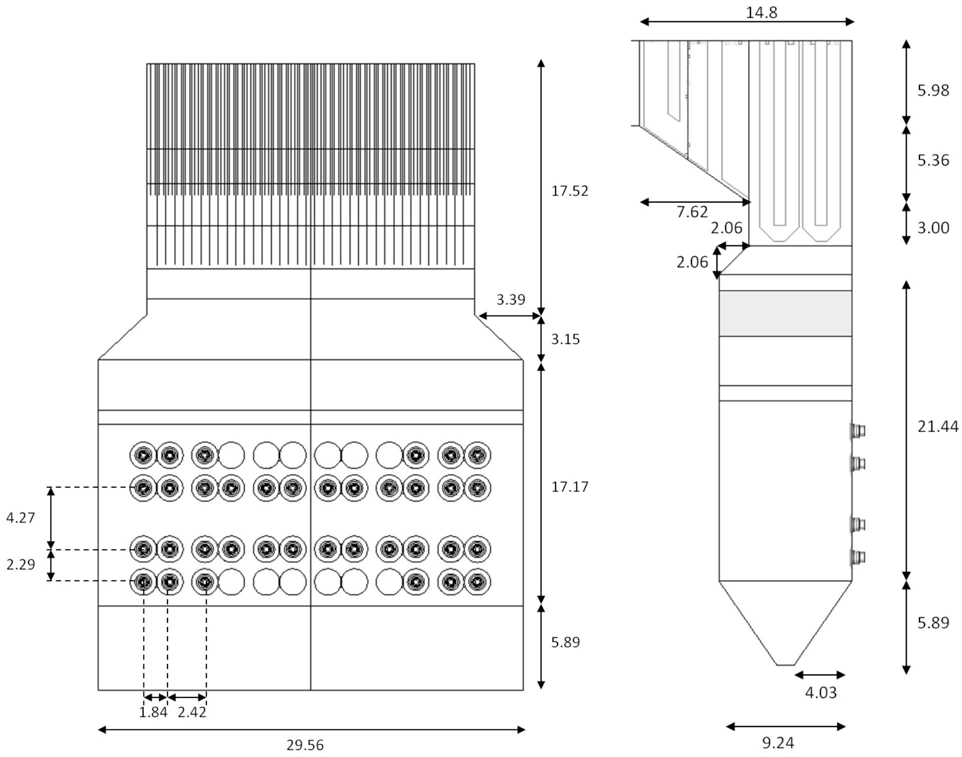

Figure 3.15: Dimensions (m) of the front and side view of the full-scale utility boiler.

3.5.2 Burner description

Doosan Babcock MK-III low-NO_x burners are used in the utility boiler. A simplified geometry is used in the CFD simulations and the dimensions of one of the burners are shown in Figure 3.14. Coal and air is carried through a primary register and preheated air with different degrees of swirl are carried through the secondary and tertiary registers. The angle of the swirled combustion air is 0°, 25° and 50° for the primary, secondary and tertiary registers. The simplified geometry has been cut after the end of the blades. The swirl direction alternates between a clockwise and then anti-clockwise direction pattern from the bottom left burner to the top right burner and this is illustrated in Figure 3.16.

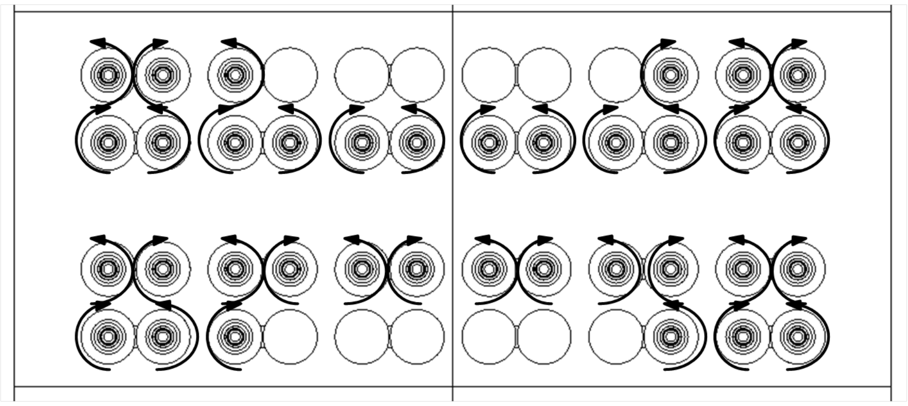

Figure 3.16: Dimensions of a burner and the swirl orientation along the front wall of the full-scale utility boiler.

	Flow rate (kg/s)	Temperature (K)
Coal	46.7	363
Primary × 36	2.94	293
Secondary × 36	2.20	549
Tertiary × 36	9.55	549
Leakage	16.0	293

Table 3.10: Air-coal boundary conditions for the full-scale utility boiler.

	In-house model (MW)
Water walls	456
Platen 1	106
Platen 2	110
SSH	110
FRH	79
Total	861

Table 3.11: Heat transfer values at the different tube banks for the air-coal case from the in-house data for the full-scale utility boiler.

	Exp. (K)	In-house model (K)
Furnace exit	1591	1656
Platen 1 exit	-	1135
Platen 2 exit	-	1282
SSH exit	-	1173
FRH exit/outlet	-	1054
Total	-	861

Table 3.12: Temperature values at the exit planes of the different tube banks for the air-coal case from the in-house data and experiments for the full-scale utility boiler.

3.5.3 Available data and boundary conditions

Data from RWE's in-house model and limited experimental data was used to benchmark the CFD simulations in Chapter 6. The in-house model has been tuned to the data from the power plant and is assumed to give a reasonable representation of the performance of the boiler. Further information and data from the in-house model, firing Pittsburgh No. 8 coal using 36 burners, was given by Edge [183] and is reported in Table 3.10. The case is known as air-coal. Air leakage for this section of the boiler was assumed to come from the ash hopper and based on a previous study was 3% of the total inlet air, equating to 16 kg/s [183]. The thermal efficiency of the power plant is assumed to be approximately 40% and the thermal input, based on

Ultimate analysis (a.r., w.t.%)		Proximate Analysis (d.a.f., w.t.%)	
Carbon	67.80	Fixed Carbon	61.87
Hydrogen	4.47	Volatile Matter	38.13
Oxygen	5.61		
Nitrogen	1.30		
Sulphur	2.12	Calorific value (MJ/kg)	
Ash	10.30	GCV (dry)	29.90
Moisture	8.40	NCV (dry)	27.39

Table 3.13: Pittsburgh No. 8 coal properties.

Devolatilisation	[62]	Char combustion	[100]
A (1/s)	3.8×10^{14}	A_i (kg m^{-2} s^{-1} Pa^{-1})	15.3
E_a (J/kmol)	2.3×10^8	E_{ai} (J/kmol)	1.52×10^8

Table 3.14: Pittsburgh No. 8 coal combustion properties.

the Net C.V., gives 1275 MW$_{\text{th}}$ to the boiler. The data from the in-house model and experiments are shown in Tables 3.11 and 3.12. Further, the overall heat transfer coefficient of 330 W/m^{2}K was chosen to represent the slagged walls and material of the tube banks inside the boiler based on previous studies [110, 183].

3.5.4 Fuel analysis

The coal fired in the experiments was a bituminous US coal, Pittsburgh No. 8 and a fuel analysis for the coal is given in Table 3.13. The particle size distribution is taken from a similar coal that was milled at Didcot A [110, 183] and a Rosin Rammler distribution [182] was fitted to the data with diameters between 1 and 300 μm with an average diameter 70 μm. The spread parameter was 1.19. The combustion analysis of Pittsburgh No. 8 is well documented in the literature, therefore devolatilisation rates and a high temperature volatile yield of 1.5 based on a typical heating rate of 10^5 K/s and a final temperature of 1773K using the FG-DVC code was used [62]. The fast-kinetic tar rate was chosen based on previous studies [134]. Intrinsic reactivity kinetics based on a wide selection of coals including Pittsburgh No. 8 was chosen based on the work of Williams et. al. [100]. The parameters are presented in Table 3.14.

Chapter 4

Integration of a NO_x model into an in-house LES code

Nitric oxides (NO_x) is a collective term for nitric oxide (NO), nitrogen dioxide (NO_2) and nitrous oxide (N_2O). Nitric oxides are by-products of the combustion process and are a significant pollutant source that can have a detrimental effect to human health and the environment [184]. In the atmosphere, NO can readily oxidise to NO_2 and both species are precursors to the formation of acid rain and participate in the formation of photochemical smog, while N_2O is considered a greenhouse gas. At high temperatures, NO is mainly formed with small amounts of NO_2, whereas the formation of N_2O is mainly significant at lower temperatures [133].

The European Union has strict emission limits for new power stations, where for a power plant over 300 MW the NO_x emission is limited to 150 mg/Nm^3 (dry basis, corrected to 6% oxygen in the flue gas) [13]. The control of NO_x emissions is therefore a concern and has received significant attention in the past four decades [133, 184]. Emission reduction techniques for NO_x include burner design, such as low-NO_x burners, over-fire air, air and fuel staging, reburning, flue gas recycle, selective catalytic reduction (SCR) and selective non-catalytic reduction (SNCR) [184]. Furthermore, the use of fuels with a lower nitrogen content will also help reduce NO_x emissions.

The formation and destruction of NO in combustion systems occurs via three main mechanisms: thermal NO, prompt NO and fuel NO. Thermal NO occurs when nitrogen is oxidised in the atmosphere, prompt NO occurs when hydrocarbon radicals react with the nitrogen in the flame and fuel NO occurs from the oxidation of fuel-bound nitrogen. Reburn NO is another reduction mechanism where hydrocarbon radicals react with the NO to form atmospheric nitrogen.

The reduction in $\mathrm{NO_x}$ may also be obtained using oxy-fuel combustion [185]. Experiments have shown lower emissions of $\mathrm{NO_x}$ in oxy-fuel compared to conventional air-combustion [186–188]. A combination of a lower amount of atmospheric nitrogen suppressing thermal $\mathrm{NO_x}$ formation and the introduction of NO in the flame zone from the recycled flue gas are believed to contribute to the lower NO emissions [103, 185].

Detailed modelling of $\mathrm{NO_x}$ formation and destruction provides insight into the reaction process and may ultimately assist the optimisation and design of combustion systems [184]. Within CFD codes, $\mathrm{NO_x}$ chemistry mechanisms have been widely used to estimate the $\mathrm{NO_x}$ concentrations [62, 103, 104, 134, 189, 190]. However, along with a detailed chemical mechanism for $\mathrm{NO_x}$, an accurate prediction also requires the correct representation of a turbulent flow field, temperature field and species distribution [103].

LES offers a more detailed approach in predicting a turbulent flow field compared to RANS methods that typically rely on a number of empirical constants that may not be suited for a wide range of flows. Coupled with an appropriate chemistry mechanism, it may also offer further accuracy in temperature and species distributions. However, due to memory and CPU limitations, it is not feasible to couple a detailed $\mathrm{NO_x}$ chemistry mechanism with a turbulent flow field in LES [191] and reduced mechanisms or tabulated methods are common approaches to overcome this issue.

The formation and destruction of minor species, such as NO, can occur on different time-scales compared to major species [184, 191] and this is a key difficulty for some combustion models. Tabulated models, such as the flamelet model [116], contain a wide range of species and reactions and can obtain good predictions for major species, but can be inaccurate for minor species such as NO [117, 191]. Variants of tabulated models, such as the unsteady flamelet model [117], the progress variable approach [191] and PDF transport approaches [192] have been used to successfully predict NO concentrations. However, the applicability of these models for pulverised fuel combustion is complicated due to unknown species concentration released during devolatilisation and the combination of homogeneous and heterogeneous reactions.

The prediction of NO can be decoupled from the main solution since the species is small and is assumed to have negligible effect on temperature, density or fluid flow. In this manner, the prediction of NO can be treated as a passive scalar and solved as a post-processing technique. A reduced mechanism is also used and this has been a popular technique for predicting NO_x in pulverised fuel systems where the CFD solution of turbulence, temperature, chemical species, devolatilisation and char mass release rates are obtained before predicting the concentration of NO [34, 62, 103, 104, 134, 189, 190].

The solution obtained from CFD is usually a RANS solution such that the values used in the NO_x post-processing model are time-averaged and the mean reaction rate is required. The chemical rates in the NO_x mechanism are typically based on premixed laminar flames or shock tube experiments [193]. To account for fluctuations in temperature and species present in turbulent flow on the chemical rate, a probability density function (PDF) can be used. The PDF is a statistical distribution of a randomly fluctuating variable at a fixed point in space sampled over an infinite amount of time [194]. The shape of the PDF is usually unknown, and an approach is to use a presumed-PDF shape such as a β function.

In LES, the use of a PDF may be replaced by the definition of a filtered density function (FDF). The FDF in an LES represents the variation that occurs with a point (or filter width space) at a particular time [194]. Mathematically, the PDF and FDF are similar in that they require a presumed shape as well as values for the mean and variance.

In this chapter, a reduced NO_x mechanism based on work performed by the University of Leeds [195] consisting of a thermal, prompt, fuel, N_2O intermediate and reburn mechanism have been implemented into the in-house LES code, *PsiPhi*. A similar approach has also been adapted in commercial software packages such as Ansys fluent [59]. To compute the mean reaction rates, a top-hat function outlined by Floyd et al. [194] has been used for the PDF/FDF shape. The results obtained from the model are compared against experimental data for three cases: the Sydney swirl methane burner, the CRIEPI methane coal burner and a 100 kW_{th} oxy-coal burner.

4.1 Description of in-house code

The *PsiPhi* code is used in this chapter. The code is an in-house LES solver written in modern FORTRAN which is based on numerical algorithms applied to the *flowsi* code developed at TU-Darmstadt and Imperial College by the Kempf group. The *PsiPhi* code has been used in the simulation of combustion problems including a non-premixed bluff body flame [76], turbulent opposed jets [196], a turbulent stratified jet [197] and a pulverised coal-methane flame [45, 198].

It has been noted that there is a need for efficient LES codes [151] and *PsiPhi* utilises modern FORTRAN vectorisation and parallelisation to speed up development and run-time [76]. A low-Mach Navier-Stokes equation is solved where density is only dependent on species composition and temperature ($\partial\rho/\partial p = 0$; $\partial\rho/\partial T < 0$). Dependent variables $\widetilde{\Psi}$ are calculated from the filtered conserved scalars $\widetilde{\Phi}$ which are solved on an equidistant Cartesian grid. A Cartesian mesh is advantageous for LES since the amount of numerical diffusion is reduced and issues surrounding filtering of anisotropic cells is minimised.

The numerical approach and models used in the following cases and applied within *PsiPhi* are described here. For spatial discretisation, a second-order central differencing scheme was used in this work to discretise the momentum equation and a TVD (total variation diminishing) scheme was applied to the other scalars to limit oscillations or numerical diffusion that may occur during the combustion simulation [199]. For the temporal discretisation of the transport equations, an explicit three-step low storage Runge-Kutta method is used which is third order accurate in linear problems and to maintain stability the CFL (Courant-Friedrichs-Lewy) condition is applied to determine the time-step width. For the inlet boundary conditions, a velocity profile along with artificial turbulent boundary conditions was used [83]. Also, the subgrid scale contribution for turbulent viscosity was modelled by the Smagorinsky model [200].

4.2 $\mathrm{NO_x}$ model

Thermal, prompt, fuel, N_2O intermediate and reburn mechanisms for the formation and destruction of NO have been included into *PsiPhi*. Extra transport species equations, based on Equation (2.21), are used for the filtered mass fraction of NO, hydrogen cyanide (HCN) and ammonia (NH_3), namely

$$\frac{\partial(\overline{\rho}\widetilde{Y_{NO}})}{\partial t} + \frac{\partial(\overline{\rho}\widetilde{Y_{NO}}\widetilde{u_j})}{\partial x_j} = \frac{\partial}{\partial x_j}\left(\overline{\rho}\left(\frac{\widetilde{\nu}}{Sc_l} + \frac{\nu_t}{Sc_t}\right)\frac{\partial\widetilde{Y_{NO}}}{\partial x_j}\right) + \widetilde{S_{NO}} \tag{4.1}$$

$$\frac{\partial(\overline{\rho}\widetilde{Y_{HCN}})}{\partial t}+\frac{\partial(\overline{\rho}\widetilde{Y_{HCN}}\widetilde{u_j})}{\partial x_j}=\frac{\partial}{\partial x_j}\left(\overline{\rho}\left(\frac{\widetilde{\nu}}{Sc_l}+\frac{\nu_t}{Sc_t}\right)\frac{\partial\widetilde{Y_{HCN}}}{\partial x_j}\right)+\widetilde{S_{HCN}} \tag{4.2}$$

$$\frac{\partial(\overline{\rho}\widetilde{Y_{NH_3}})}{\partial t}+\frac{\partial(\overline{\rho}\widetilde{Y_{NH_3}}\widetilde{u_j})}{\partial x_j}=\frac{\partial}{\partial x_j}\left(\overline{\rho}\left(\frac{\widetilde{\nu}}{Sc_l}+\frac{\nu_t}{Sc_t}\right)\frac{\partial\widetilde{Y_{NH_3}}}{\partial x_j}\right)+\widetilde{S_{NH_3}} \tag{4.3}$$

where $\widetilde{Y_k}$ is the filtered mass fraction of species k. The filtered mean chemical source term $\widetilde{S_k}$ in the cell is therefore the contribution from thermal, prompt, fuel, N_2O intermediate and reburn NO subroutines discussed Sections 4.2.1-4.2.5. The equations are valid if a common diffusivity is assumed amongst the equations (i.e. $D_{NO} = D_{HCN} = D_{NH3} = D$) and in this thesis, the laminar Sc_l and turbulent Schmidt number Sc_t was chosen to be 0.7 based on previous work [196, 197].

In order to account for fluctuations in the turbulent flow on the chemical reaction rate, a probability density function (PDF) or a filtered density function (FDF) can be used. This approach is commonly used to account for turbulent chemistry interaction (TCI). The mean source term $\widetilde{S_k}$ can then be related to the instantaneous source term S_k if dependent on a single variable ψ by [50],

$$\widetilde{S_k}=\int_{-\infty}^{\infty}f(\psi)S_k(\psi)d\psi \tag{4.4}$$

where ψ, $f(\psi)$ and S_k is a variable such as temperature or a species, a probability density function (PDF) and the instantaneous reaction source term of species k, respectively. A joint variable PDF may also be used with two or more variables if they are statistically independent. A single variable PDF with temperature was used in this work following a similar approach by Ma et al. [201]. Also, a presumed shape of a top-hat function was adopted as an alternative method to the popular β

functions that is commonly used, due to its ease of implementation [194]. Floyd et al. compared the β-PDF and top-hat PDF in LES and found the top-hat simulations to be stable and to differ only marginally to the β-PDF function [194].

The instantaneous rate of NO formation or destruction, S_{NO}, can be represented by the total contribution from thermal, prompt, fuel, N_2O intermediate and reburn NO evaluated at a variable ψ given by $S_{thermal,NO}$, $S_{prompt,NO}$, $S_{fuel,NO}$, $S_{inter,NO}$ and $S_{reburn,NO}$, respectively. Similarly, the instantaneous rate of HCN considers the fuel and reburn mechanism given by $S_{fuel,HCN}$ and $S_{reburn,HCN}$ respectively and the instantaneous rate of NH_3 considers only the contribution from the fuel mechanism given by S_{fuel,NH_3}. The equations:

$$S_{NO}\bigg|_{\psi} = \left[S_{thermal,NO} + S_{prompt,NO} + S_{inter,NO} + S_{fuel,NO} + S_{reburn,NO}\right]\bigg|_{\psi}, \tag{4.5}$$

$$S_{HCN}\bigg|_{\psi} = \left[S_{fuel,HCN} + S_{reburn,HCN}\right]\bigg|_{\psi}, \tag{4.6}$$

$$S_{NH_3}\bigg|_{\psi} = \left[S_{fuel,NH_3}\right]\bigg|_{\psi}. \tag{4.7}$$

show the contribution of each of the mechanisms in the NO, HCN and NH_3 source terms.

The reaction rates in the following sections are of the form

$$k_{x,i} = A_r T^{\beta} \exp\left(-E_a/(RT)\right), \tag{4.8}$$

unless otherwise specified, where x represents forward f or backward b reactions, A_r is the pre-exponential factor, β is the temperature exponent, E_a is the activation energy (J/kmol), R is the universal gas constant (8314.47 J/kmol-K) and T is the gas temperature (K).

Reaction Rate	A_r (m^3/kmol-s)	β (-)	E_a (J/kmol)
$k_{f,1}$	1.80×10^{11}	0	3.19027×10^{8}
$k_{f,2}$	1.80×10^{7}	1	3.89120×10^{7}
$k_{f,3}$	7.10×10^{10}	0	3.74200×10^{6}
$k_{b,1}$	3.80×10^{10}	0	3.53400×10^{6}
$k_{b,2}$	3.81×10^{6}	1	1.73108×10^{8}
$k_{b,3}$	1.7×10^{11}	0	2.04204×10^{8}

Table 4.1: Reaction rate parameters for thermal NO model [193].

4.2.1 Thermal route

Thermal NO formation is due to the separation of oxygen and nitrogen molecules to form NO at high temperatures typically above 1700 K [132]. Due to the lack of N_2 in an oxy-fuel environment the thermal NO formation will be relatively low, however in fuel lean air environments it will be much more important. It is determined by a highly temperature dependent set of reactions known as the extended Zel'dovich mechanism given by

$$\mathrm{O} + \mathrm{N_2} \underset{k_{b,1}}{\overset{k_{f,1}}{\longleftrightarrow}} \mathrm{N} + \mathrm{NO} \tag{4.9}$$

$$\mathrm{N} + \mathrm{O_2} \underset{k_{b,2}}{\overset{k_{f,2}}{\longleftrightarrow}} \mathrm{O} + \mathrm{NO} \tag{4.10}$$

$$\mathrm{N} + \mathrm{OH} \underset{k_{b,3}}{\overset{k_{f,3}}{\longleftrightarrow}} \mathrm{H} + \mathrm{NO} \tag{4.11}$$

where $k_{f,i}$ and $k_{b,i}$ represent the forward and backward reaction rates respectively for reactions $i = 1, 2, 3$. The rate constants were determined from numerous experiments mainly consisting of shock tube experiments, premixed flames and flow reactors and data was collated and evaluated by Hanison and Salimian [193] which are widely accepted in the literature. The rate values are given in Table 4.1 and the high activation energy of $k_{f,1}$ shows this is the rate limiting reaction.

The extended Zeldovich mechanism, (4.9) – (4.11), contains the following radicals of oxygen (O), nitrogen (N), hydroxide (OH) and hydrogen (H). These radicals may

Reaction Rate	A_r (m^3/ kmol-s)	β	E_a (J/kmol)
$k_{f,4}$	1.99×10^{11}	0	7.034×10^7
$k_{f,5}$	6.32×10^4	1.5	2.080×10^6
$k_{b,4}$	1.83×10^{10}	0	0
$k_{b,5}$	1.51×10^{11}	0	1.100×10^8

Table 4.2: Reaction rate parameters for O radicals [202].

not be available in simple combustion models used in CFD and assumptions can be made to give an expression for rate of formation of NO.

A steady state assumption for the rate of formation and consumption of N and H atoms can be assumed since these reactions reach equilibrium quickly and the source of thermal NO, $S_{thermal,NO}$ (kg/m^3-s), can be written as [132, 184]:

$$S_{thermal,NO} = W_{NO}\frac{d[\mathrm{NO}]}{dt} = 2W_{NO}k_{f,1}[\mathrm{O}][\mathrm{N_2}]\frac{\left(1 - \frac{k_{b,1}k_{b,2}[\mathrm{NO}]^2}{k_{f,1}[\mathrm{N_2}]k_{f,2}[\mathrm{O_2}]}\right)}{\left(1 + \frac{k_{b,1}[\mathrm{NO}]}{k_{f,2}[\mathrm{O_2}]+k_{f,3}[\mathrm{OH}]}\right)} \tag{4.12}$$

where W_{NO} is the molecular weight of NO (kg/kmol) and the concentrations of species $[k]$ are in units kmol/m^3. The rate of thermal NO formation is now a function of O_2, N_2, O and OH. Further assumptions can be made for an estimation of O and OH radicals. In tabulated models, such as the flamelet model [116], values of O and OH may be available and can be implemented directly into Equation (4.12). In models that use global mechanisms and ignore intermediate species, such as the eddy dissipation model [108], a semi-empirical expression can be used.

Semi-empirical expression for O and OH radicals

The estimation of O radicals is critical to the correct prediction of thermal NO [131, 184] which is clearly seen in Equation (4.12). In the post-flame region, it is accepted that O radicals will be in *equilibrium* with O_2 [184]. However, it has also been suggested that in the near flame region, values of O and OH greatly exceed their equilibrium values, known as *super-equilibrium* or partial equilibrium values [184, 203, 204].

O *equilibrium assumption*

An equilibrium assumption can be made for O radicals given by [205],

$$[\mathrm{O}] = 3.97 \times 10^5 T^{-0.5} [\mathrm{O_2}]^{0.5} \exp(-31090/T). \tag{4.13}$$

O *super-equilibrium assumption*

Alternatively, the O radical concentrations may be described by a super-equilibrium assumption [184, 201, 204],

$$[\mathrm{O}] = \frac{k_{f,4} k_{f,5}}{k_{r,4} k_{r,5}} \frac{[\mathrm{O_2}][\mathrm{CO}]}{[\mathrm{CO_2}]} \tag{4.14}$$

where the rates derived from the NIST database [202] are given in Table 4.2. This approximation may be appropriate under fuel rich regions and following a similar approach by Coelho et al. [204], Equation (4.14) can be applied in fuel rich regions while Equation (4.13) is applied elsewhere.

OH *super-equilibrium assumption*

The radicals of OH can be excluded which would occur in fuel lean conditions, or a partial equilibrium assumption could be used [206]:

$$[\mathrm{OH}] = 2.129 \times 10^2 T^{-0.57} [\mathrm{O}]^{0.5} [\mathrm{H_2O}]^{0.5} \exp(-4595/T). \tag{4.15}$$

4.2.2 Prompt route

The formation of NO may also be caused during the combustion of hydrocarbon which is known as prompt NO formation, and was first identified by Fenimore [131].

The formation of NO is a complex series of reactions, however it is generally believed that the reaction controlling prompt NO formation is given by,

$$\mathrm{CH} + \mathrm{N_2} \rightleftharpoons \mathrm{HCN} + \mathrm{N}.$$

Prompt NO formation is dependent on the number of hydrocarbons present in the fuel as well as the stoichiometry and fuel-rich conditions tend to form more prompt NO [132]. The rate of formation for a general hydrocarbon has been collated from experiments on a range of hydrocarbons at different stoichiometries, and the source term for Prompt NO, $S_{prompt,NO}$ (kg/m^3-s), can be given by [59, 195] :

$$S_{prompt,NO} = W_{NO}\frac{d[\mathrm{NO}]}{dt} = W_{NO} f_{corr} k_{pr} [\mathrm{O_2}]^a [\mathrm{N_2}][\mathrm{FUEL}] \exp(-E_a/RT) \qquad (4.16)$$

where f is a correlation factor and is given by [195],

$$f_{corr} = 4.75 + 0.0819n - 23.2\phi_{eq} + 32\phi_{eq}^2 - 12.2\phi_{eq}^3 \qquad (4.17)$$

where n is the number of carbon atoms in the hydrocarbon and ϕ_{eq} is the equivalence ratio. The correlation factor f_{corr} is only valid for hydrocarbons of the type $\mathrm{C}_n\mathrm{H}_{2n+2}$. The values of k_{pr} and the activation energy E_a are given by [207],

$$k_{pr} = 6.4 \times 10^9 (RT/p)^{a+1} \ , \ E_a = 3.03474125 \times 10^8 \ \mathrm{J/kmol}$$

where a is the oxygen reaction order and p is the pressure (Pa). The reaction order, suggested by De Soete [208] is used:

$$a = \begin{cases} 1.0 & \text{if } X_{O_2} \leq 4.1 \times 10^{-3} \,, \\ -3.95 - 0.9 \ln X_{O_2} & \text{if } 4.1 \times 10^{-3} < X_{O_2} \leq 1.11 \times 10^{-2}, \\ -0.35 - 0.1 \ln X_{O_2} & \text{if } 1.11 \times 10^{-2} < X_{O_2} < 0.03, \\ 0 & \text{if } X_{O_2} \geq 0.03, \end{cases} \tag{4.18}$$

where X_{O_2} is the mole fraction of oxygen.

In terms of coal combustion, prompt NO would result from volatile combustion. However it is difficult to determine the exact composition of volatiles produced during devolatilisation. The volatiles can be represented in the form, $C_xH_yO_z$ and therefore the correlation factor f_{corr} may not be suitable.

4.2.3 Reburn route

The NO_x reburn route is based on the model proposed by Kandamby et al. [209]. This involves the reduction of NO by hydrocarbon radicals CH_i to form HCN, by the reaction

$$CH_i + NO \longrightarrow HCN + \text{products.}$$

The reburn model can be directly linked with the fuel-NO route where the HCN is oxidised to NO or reduced to N_2. This route will be important for oxy-fuel combustion with recycled flue gas since the NO in the flue gas will be directly injected into the burner zone where a large concentration of hydrocarbon radicals exist.

The source term for NO, $S_{reburn,NO}$, and HCN, $S_{reburn,HCN}$, with units of kg/m^3-s can therefore be given by

$$S_{reburn,NO} = W_{NO}\frac{dY_{NO}}{dt} = -4.0 \times 10^{-7} W_{NO}(R_4 + R_5), \tag{4.19}$$

$$S_{reburn,HCN} = W_{HCN}\frac{dY_{HCN}}{dt} = 4.0 \times 10^{-7} W_{HCN} R_4, \tag{4.20}$$

where

$$R_4 = (k_a + k_b)\,[\text{FUEL}][\text{NO}],$$
$$R_5 = k_c \frac{k_{r,6}}{k_{f,6}}[\text{FUEL}][\text{NO}].$$

The rates used in the Arrhenius expressions are given in Table 4.3 and these rates are based on those for methane from Leung and Lindstedt [210].

Reaction Rate	A_r (m^3/kmol-s)	β	E_a (J/kmol)
k_a	5.30×10^{12}	-1.54	2.7977×10^7
k_b	3.31×10^{16}	-3.33	1.5090×10^7
k_c	3.06×10^{14}	-2.64	7.7077×10^7
$k_{f,6}$	1.02×10^8	1.60	1.3802×10^7
$k_{r,6}$	4.52×10^8	1.60	8.0815×10^7

Table 4.3: Reaction rate parameters for reburn NO model [210].

4.2.4 N_2O intermediate route

The N_2O intermediate route is based on that of Malte and Pratt [211]. The formation of NO can also form via N_2O and usually occurs at lower temperatures, rich oxygen concentrations and higher pressures. The two reactions that can be considered for the N_2O mechanism are,

$$\text{N}_2 + \text{O} + \text{M} \xleftrightarrow[k_{b,7}]{k_{f,7}} \text{N}_2\text{O} + \text{M}$$

$$N_2O + O \underset{k_{b,8}}{\overset{k_{f,8}}{\longleftrightarrow}} 2N_2O$$

where M is the concentration of third body reactions which can be represented by a sum of the species concentrations. Therefore, the reactions require the prediction of N_2O and O radicals. As shown in Section 4.2.1, the O radicals can be represented by an equilibrium or partial equilibrium approach. If N_2O can be represented as steady state, then it may be given by,

$$[N_2O] = \frac{k_{f,7}[N_2][O][M] + k_{b,8}[NO]^2}{k_{b,7}[M] + k_{f,8}[O]}$$

and the source of NO formation, $S_{inter,NO}$ (kg/m^3-s), can be given by,

$$S_{inter,NO} = W_{NO}\frac{d[NO]}{dt} = 2W_{NO}\left(k_{f,8}[N_2O][O] - k_{b,7}[NO]^2\right) \tag{4.21}$$

where the rates are given in Table 4.4.

Reaction Rate	A_r	β	E_a (J/kmol)
$k_{f,7}$	4.44×10^{38} (m^6/kmol^2-s)	-8.358	2.34751×10^8
$k_{b,7}$	4.00×10^{11} (m^3/kmol-s)	0	2.34751×10^8
$k_{f,8}$	2.90×10^{10} (m^3/kmol-s)	0	9.68720×10^7
$k_{b,8}$	1.45×10^{-26} (m^3/kmol-s)	9.259	9.68720×10^7

Table 4.4: Reaction rate parameters for N_2O intermediate model [211].

4.2.5 Fuel route

Most organic compounds contain some organically bounded nitrogen, called fuel-N and the formation of NO from fuel-N is called fuel-NO formation. During the combustion of a coal particle, some of the nitrogen is released as intermediate nitrogen compounds, such as HCN, NH_3 or NO, with the volatiles, known as vol-N, and the rest may be released or retained in the char, known as char-N. This split is highly dependent on the combustion conditions and coal type. The distribution between char-N and volatile-N is generally unknown and may have to be determined experimentally. Network pyrolysis models have been modified and can predict yields of char-N and volatile-N for a given coal composition such as FG-DVC (Functional Group-Depolymerisation Vaporisation Cross- linking) [94], FLASHCHAIN [95] and CPD (Chemical Percolation Devolatilization) [96]. The use of network models can give useful insight into a coal where experimental data is not available.

The route of fuel NO production and reduction in pulverised fuel combustion is complex. Generally, the following steps can be used to describe the process:

(i) The fuel bound nitrogen is split between the volatiles and char which is released during volatile combustion and char combustion.

(ii) The nitrogen compounds which are released are intermediates such as hydrogen cyanide (HCN) and/or ammonia (NH_3) or directly as NO. The intermediates are oxidised to form NO or reduced to form N_2.

(iii) The NO can be further reduced by heterogeneous char-surface reactions.

Nitrogen split

The nitrogen split between the volatiles and char can be described by a factor N_{split}, and the mass fraction of nitrogen in the volatiles $Y_{N,vol}$ and char $Y_{N,char}$ can be described by

$$Y_{N,char} = \frac{(\text{U.A.})_{\text{N}}^{\text{d.a.f.}}}{(\text{P.A.})_{\text{vol}}^{\text{d.a.f.}}\, N_{split} + (\text{P.A.})_{\text{char}}^{\text{d.a.f.}}} \tag{4.22}$$

$$Y_{N,vol} = N_{split} Y_{N,char} \tag{4.23}$$

where the following holds:

$$(\text{U.A.})_{\text{N}}^{\text{d.a.f.}} = (\text{P.A.})_{\text{vol}}^{\text{d.a.f.}}\, Y_{N,vol} + (\text{P.A.})_{\text{char}}^{\text{d.a.f.}}\, Y_{N,char}. \tag{4.24}$$

The terms $(\mathrm{U.A})_x^{\mathrm{d.a.f.}}$ and $(\mathrm{P.A})_x^{\mathrm{d.a.f.}}$ refer to the ultimate and proximate analysis on a dry ash free basis for a coal property x.

Rate of formation and destruction of HCN and NH$_3$

The rate of formation of intermediate species is based on the release of volatiles and the release of char. Therefore, the source of HCN, NH$_3$ and NO from volatiles and char can be described by,

$$\begin{aligned} S_{vol,HCN} &= \alpha_{HCN}\frac{S_{vol}Y_{N,vol}W_{HCN}}{W_N V}, \quad & S_{char,HCN} &= \beta_{HCN}\frac{S_{char}Y_{N,vol}W_{HCN}}{W_N V}, \\ S_{vol,NH_3} &= \alpha_{NH_3}\frac{S_{vol}Y_{N,vol}W_{NH_3}}{W_N V}, \quad & S_{char,NH_3} &= \beta_{NH_3}\frac{S_{char}Y_{N,vol}W_{NH_3}}{W_N V}, \\ S_{vol,NO} &= \alpha_{NO}\frac{S_{vol}Y_{N,vol}W_{NO}}{W_N V}, \quad & S_{char,NO} &= \beta_{NO}\frac{S_{char}Y_{N,vol}W_{NO}}{W_N V}, \end{aligned} \tag{4.25}$$

where S_{vol}, S_{char} and V correspond to the rate of release of volatiles (kg/s), release of char (kg/s) and cell volume (m^3) respectively. The constants α_{HCN}, α_{NH_3} and α_{NO} correspond to the fraction of nitrogen in the volatiles that have been converted to HCN, NH$_3$ and NO respectively. Similarly, the constants β_{HCN}, β_{NH_3} and β_{NO} correspond to the fraction of nitrogen in the char that have been converted to HCN, NH$_3$ and NO, respectively. Therefore, the following conditions must hold:

$$\begin{aligned} 0 \leq \quad & \alpha_{HCN} + \alpha_{NH_3} + \alpha_{NO} & \leq 1 \\ 0 \leq \quad & \beta_{HCN} + \beta_{NH_3} + \beta_{NO} & \leq 1 \end{aligned}$$

A route for fuel NO formation was suggested by Lockwood and Romo-Millanes [212] where the volatiles are converted to HCN and the char is converted to NO. Alternatively, the volatiles and the char may first be converted to HCN before being oxidised to NO or reduced to N$_2$, as proposed by Smoot [213]. The values of $\alpha_{HCN} = 1$ and $\beta_{NO} = 1$ with all of the other constants equal to zero would be an example of the Lockwood approach. The values of $\alpha_{HCN} = 1$ and $\beta_{HCN} = 1$ with

Reaction	$A_{r,i}$ (1/s)	E_i (J/kmol)
R_1	1.00×10^{10}	280451950
R_2	3.00×10^{12}	251151000
R_3	4.00×10^{6}	133947200
R_4	1.80×10^{8}	113017950

Table 4.5: Reaction rate parameters for HCN and NH_3 oxidation and reduction [208].

all the other values equal to zero would be an example of the Smoot approach.

Following the method by De Soete [208], the HCN and NH_3 intermediates can then be oxidised with O_2 to form NO via,

$$R_1 = A_{r,1} X_{HCN} X_{O_2}^a \exp(-E_1/RT), \tag{4.26}$$

$$R_3 = A_{r,3} X_{NH_3} X_{O_2}^a \exp(-E_3/RT), \tag{4.27}$$

or reduced with NO to form N_2 via,

$$R_2 = A_{r,2} X_{HCN} X_{NO} \exp(-E_2/RT), \tag{4.28}$$

$$R_4 = A_{r,4} X_{NH_3} X_{NO} \exp(-E_4/RT), \tag{4.29}$$

where a is the reaction order and the rates are given in Table 4.5.

The consumption of HCN can therefore be written as

$$S_{HCN,NO} = -R_1 \frac{W_{HCN} p}{RT} \qquad (\mathrm{kg/m^3\text{-}s}), \tag{4.30}$$

$$S_{HCN,N_2} = -R_2 \frac{W_{HCN} p}{RT} \qquad (\mathrm{kg/m^3\text{-}s}), \tag{4.31}$$

and the consumption of NH_3 can be written as

$$S_{NH_3,NO} = -R_3 \frac{W_{NH_3} p}{RT} \qquad (\text{kg/m}^3\text{-s}), \tag{4.32}$$

$$S_{NH_3,N_2} = -R_4 \frac{W_{NH_3} p}{RT} \qquad (\text{kg/m}^3\text{-s}). \tag{4.33}$$

NO from char

The reduction of NO can also be caused by a reaction with the char surface and can be modelled following the approach by Levy et al. [214]. The source can be given by,

$$S_{NO,char} = c_{particles} A_{BET} W_{NO} R_{char} \tag{4.34}$$

where $c_{particles}$, A_{BET} and R_{char} is the concentration of particles (kg/m^3), BET surface area of the pulverised fuel (m^2/kg) and the rate of reduction is given by

$$R_{char} = A_{r,char} p_{NO} \exp(-E_a/RT)$$

where $A_{r,char} = 230.0$ mol/m$^2_{\text{BET}}$-s-atm, $E_a = 142737485$ J/kmol and p_{NO} is the partial pressure of NO (atm).

Overall rates

Therefore, the overall fuel source terms for NO, HCN and NH_3 are therefore

$$S_{fuel,NO} = S_{vol,NO} + S_{char,NO} + S_{HCN,N_2} + S_{NH_3,N_2} - S_{HCN,NO} \tag{4.35}$$

$$- S_{NH_3,NO} - S_{NO,char}, \tag{4.36}$$

$$S_{fuel,HCN} = S_{vol,HCN} + S_{char,HCN} + S_{HCN,N_2} + S_{HCN,NO}, \tag{4.37}$$

$$S_{fuel,NH_3} = S_{vol,NH_3} + S_{char,NH_3} + S_{NH_3,NO} + S_{NH_3,N_2}. \tag{4.38}$$

4.2.6 Turbulence chemistry interaction

To compute the mean reaction rate, a PDF (with respect to time-averaged reaction rate) or a FDF (with respect to a spatially filtered reaction rate) can be applied as shown in equation (4.4). An assumed shape of PDF is needed and in this chapter, a top-hat function has been considered based on the work by Floyd et al. [194]. The function was chosen due its simple implementation and to eliminate some inconsistencies with the β function that were identified by Floyd et al. [194] when it was used in LES. For example, the β-function covers every sample in the sampled space (e.g. from 0 to 1), whereas the top-hat function can consider a narrow range within the sampled space (e.g. from a to b where $0 \leq a \leq b \leq 1$). The top hat function may not be valid in a RANS approach as non-zero probabilities could occur at an instance in time, but may be more applicable to a LES where small variances occur in sub-grid scale space [194, 215].

The function is used both as a PDF or a FDF depending on the numerical approach adopted. For example, when the rate is computed at each time step of the LES, the function is called a FDF but when the rate is computed as a post-processing technique separately from the LES, analogous to a RANS approach, the function is referred to as a PDF.

The properties of a PDF that must hold are:

(i) $f(\psi) \geq 0$, where the probability must be greater or equal to 0

(ii) $\int_{-\infty}^{\infty} f(\psi) d\psi = 1$, where the integration of all possible probabilities must sum to 1

The top hat function is used throughout this chapter and is given by

$$f(\psi) = \begin{cases} \frac{1}{t_0} & \text{if } a < x < b \\ \\ 0 & \text{otherwise} \end{cases} \tag{4.39}$$

where the distance between the minimum a and maximum points b is given by $t_0 = b - a$. The following relations hold with respect to the mean m and variance σ^2:

$$a = m - \frac{l}{2} \quad ; \quad b = m + \frac{l}{2} \quad ; \quad l = \sqrt{12\sigma^2}$$

A Dirac delta function is used at the limits a and b when the variance is sufficiently large.

To solve the integral, a left hand Riemann sum approach with n points was used, such that

$$\int_{\psi_{min}}^{\psi_{max}} g(\psi) d\psi \approx \sum_{i=1}^{n} g(\psi_{i-1})(\psi_i - \psi_{i-1}) \tag{4.40}$$

for the interval,

$$a = \psi_0 < \psi_1 < ... < \psi_n = b.$$

Therefore, the accuracy of the function $g(\psi)$ increases with the number of points n. For the top-hat function, a minimum of 2 points are needed since the function is simple, however when combined with the rate of NO, HCN and NH_3 due to the highly non-linear relationship between the reaction rate and temperature / species, more points may be needed.

Two approaches can be considered to compute the filtered chemical source term in Equation (4.4), namely,

(i) **At the end of the simulation**: This approach requires a mean, $\bar{m}$, and variance σ^2 value which is taken from the LES *at the end of a simulation*, after enough statistics have been collected to provide time-averaged values for the mean and variance. The only requirement, is the PDF needs to have an assumed shape, which is considered to be a top-hat function.

(ii) **At the end of each time step**: This approach solves the rate of NO formation *at the end of each time-step.* The instantaneous values of temperature and species are therefore the time and space-averaged values over the cell for that particular time-step. Due to the filtering procedure of LES, fluctuations may exist on the sub-grid scale. A FDF with an assumed shape can be used to represent the sub-grid fluctuations. The mean value is assumed to be the instantaneous cell value and the variance is computed from a sub-grid model. A common approach is to use resolved gradients [216],

$$\sigma_{sgs}^2 = C\Delta_w^2 \left(\frac{\partial \widetilde{\phi}}{\partial x_i} \cdot \frac{\partial \widetilde{\phi}}{\partial x_i} \right), \tag{4.41}$$

where $\widetilde{\phi}$ is the scalar in question and C is a constant value which was assumed to have the value of $C = 0.2$ based on the work by Bradley and Jones [216]. The approach can also neglect the sub grid scale FDF and solve the transport equations for the NO_x model after each time-step which assumes that the fluctuations present in the LES account for any turbulent chemistry interaction.

4.3 Validation cases

The NO_x model was tested against experimental data for three cases. The first is a laboratory scale burner with a swirled methane air flame. This case tests the NO_x

model against in-flame NO measurements for a gaseous flame. A grid study and various other parameters are performed to assess the accuracy of the solution. The second experiment is a laboratory-scale methane coal burner which mainly examines the fuel NO mechanism. The use of FG-DVC is used to determine devolatilisation rates and nitrogen partitioning as input parameters for the fuel NO mechanism. The simulation was carried out by Imperial College and has been published but without predictions of NO [45]. The third study is a 100 $\mathrm{kW_{th}}$ facility firing under oxy-fuel conditions and the simulation set-up was performed by Imperial College with the exception of NO predictions. This case allows the NO mechanisms to be tested under oxy-fuel combustion.

4.3.1 Laboratory swirl burner

In this section, LES is performed on the laboratory swirl burner described in Section 3.1. The fuel used is natural gas and the oxidiser is air which is swirled by tangential and axial air upstream of the burner. The fuel velocity is 32.7 m/s with a geometric swirl number S_g of 0.5 and the boundary conditions are shown in Table 3.1. The use of a gaseous laboratory burner with swirled combustion air was chosen for the following reasons:

- The burner is of laboratory scale and therefore can be considered computationally feasible for LES compared to an industrial furnace.
- The flow is complex containing a swirl and a bluff body, which is representative of industrial burners for stabilisation and turbulent mixing techniques.
- The burner and flame are well-characterised and detailed in-flame non-intrusive experimental data is available which does not disturb the flow field and allows for both flow field and chemistry validation. Experimental measurements of in-flame NO are also available which allows for the validation of the implemented $\mathrm{NO_x}$ model for thermal, prompt and reburn subroutines.

The flame has been studied extensively, both numerically [171–174] and experimentally [167, 169, 170] by a number of authors.

Numerical description and boundary conditions

Following a similar approach by other researchers who have performed LES on this case [171], the chemistry was described by a steady flamelet model with a single scalar dissipation rate of 10/s. The use of a top-hat filter was used for turbulence chemistry interaction in the flamelet model. The pre-processed flamelet table was computed using the FLAMEMASTER program [217] and used the GRI 3.0 mechanism [107] which contains 53 species and is suitable for natural gas combustion. The fuel used in the experiments was compressed natural gas, but it was assumed to be 100% methane. Radiation was neglected in the simulations as it has been suggested to be unrealistic in the steady flamelet model [117]. Furthermore, from the experimental photographs [170, 175], the flame appeared to produce little soot, thus suggesting that the visible radiation was small. The flame was also not enclosed and therefore radiative effects from the surrounding walls would also be negligible.

The inlet conditions consisted of a velocity profile based on theoretical studies of turbulent pipe flow [218]. The power law velocity profile for fully developed turbulent pipe flow is given by

$$u(r) = U_{max}\left(1 - \left|\frac{r}{R}\right|\right)^{\frac{1}{n}} \tag{4.42}$$

where R is the radius of the pipe, $u(r)$ is the axial velocity along the radius r, U_{max} is the maximum velocity and n is a constant. Integration of Equation (4.42), yields the bulk velocity U_{bulk} which can be related to the maximum velocity U_{max} by

$$\frac{U_{bulk}}{U_{max}} = \frac{2n^2}{(2n+1)(n+1)}. \tag{4.43}$$

For high Reynolds number flow, the value of $n = 7$ is generally accepted [218].

The Reynolds numbers for the fuel jet U_j and primary swirl U_s are 7200 and 75900 respectively [170, 172] and therefore, the value of $n = 7$ was used. To represent the tangential velocity of the primary air, a constant value of $W_s = 38.2$ m/s was used. In the co-flow stream, LDV and hot wire measurements were available and these were included directly as velocity profiles [175]. Artifical turbulence was generated at the inlets by the method of Kempf et al. [83, 84] with a lengthscale of 2.4 mm and a turbulent intensity of 2% based on the intensity of the coflow [175]. The inlet conditions were upstream of the exit of the burner and immersed boundaries were used based on recommendations by Kempf et al. [219] on a similar bluff body burner without the swirl. Initial tests without immersed boundaries revealed large differences between the simulations and experimental data near the burner. At the outlet a Neumann condition was set for all of the scalars, expect pressure, which was set to a zero gauge pressure. At the lateral boundary, a slip wall condition was used.

Sampling interval

In the simulation, an initial condition is prescribed and sufficient time must be allowed for the development of a transient solution. Also, it is also important to allow for the main turbulent structures to convect through the domain before sampling can occur. In swirling flow, this can be difficult to estimate. An initial coarse rectangular mesh of 75 × 75 × 200 mm was used with a uniform cell size of 0.9 mm and a number of points were taken in the domain to assess when the initial conditions had transitioned to the transient solution. The instantaneous plot of density at 40, 95 and 150 mm away from the burner on the axis are shown in Figure 4.1. Samples were also evaluated after 0.1 s, 0.25 s and 0.5 s and this showed little difference between the time-averaged results and therefore samples were obtained after 0.1 s.

(a) Density (kg/m^3) at z = 40 mm

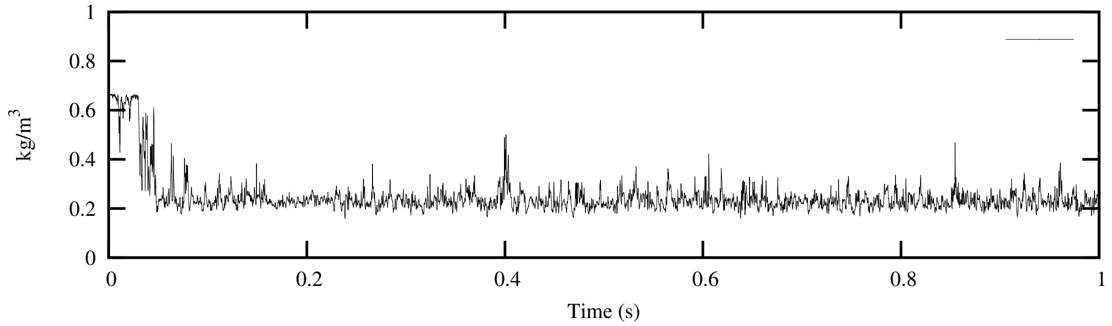

(b) Density (kg/m^3) at z 95 mm

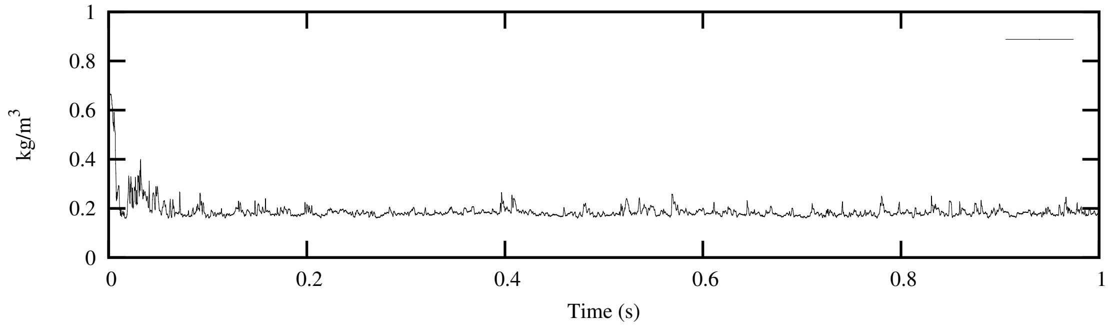

(c) Density (kg/m^3) at z = 150 mm

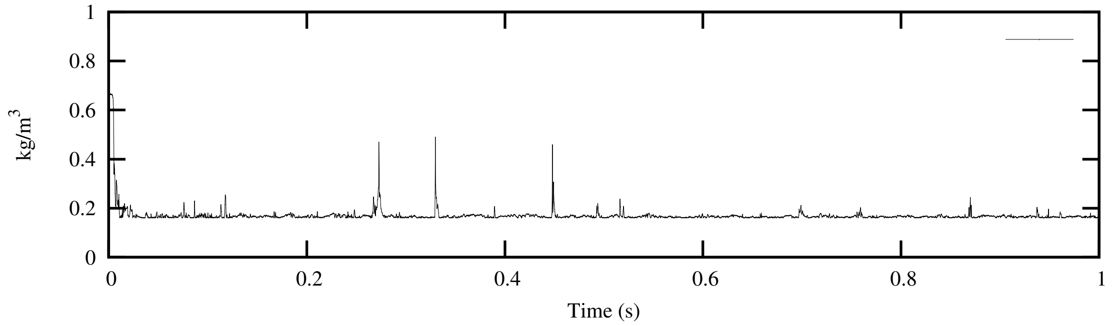

Figure 4.1: Instantaneous plots of density at (a) 40, (b) 95 and (c) 150 mm away from the burner on the centreline.

case	Cell size (mm)	Number of cells
coarse	0.90	≈ 1.5 million
medium	0.60	≈ 5.2 million
fine	0.45	≈ 12.3 million

Table 4.6: Investigated grid resolutions.

Influence of grid resolution

In this section, the influence of grid resolution is considered. Grid refinement is important to assess whether the grid is fine enough to sufficiently capture the flow characteristics. A finer grid may therefore lead to a more accurate solution. In LES, the solution cannot be grid independent since the filter width corresponds to the cell size. In order to assess the refinement with appropriate computational cost, the domain was assumed to be narrow, and have the dimensions 75 x 75 x 200 mm in width, height and length and the investigated cases are given in Table 4.6.

A snapshot of the axial velocity, temperature and mixture fraction from the medium mesh are shown in Figure 4.2. The images can be used to check if the simulation appears to be physically reasonable. The jet of methane can be seen at $r = 0$ mm and the primary air can be seen between $r = 25$ mm and $r = 30$ mm. The central jet decays quickly and a recirculation zone occurs on the bluff body of the burner distributing the mixture fraction and as a consequence, creating a relatively high temperature zone. The peak temperature occurs between $z = 50$ and $z = 100$ mm where the mixture fraction is approximately at stoichiometric levels (≈ 0.055). While a temperature contour plot may not be representative of a visible flame it may provide an indication since the higher temperatures will excite certain species and emit visible radiation. In comparison with the photographs [170,175], the flame shape appears to have been captured.

Vortex breakdown and jet precession has also been reported both experimentally [220] and numerically [172] with this flame. The asymmetry of the jet can be seen

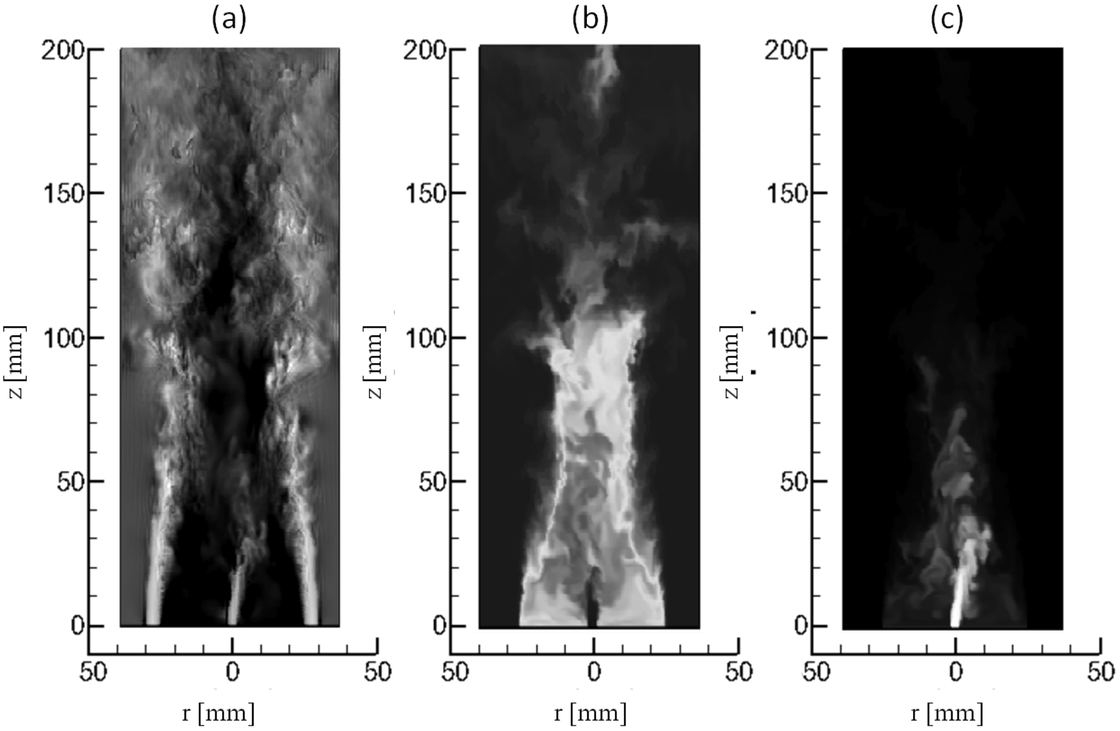

Figure 4.2: Snapshot of (a) axial velocity from 0 m/s (black) to 60 m/s (white), (b) temperature from 300 K (black) to 2200 K (white), and (c) mixture fraction from 0 (black) to 1 (white).

in Figures 4.2(a) and (c) and animations of the axial velocity and mixture fraction suggest jet precession may be evident. In Figure 4.2(a), the decay of the central jet is rapid and turbulent flow structures are evident further from the burner, suggesting the breakdown of the jet by vortex breakdown.

To quantitatively compare the grid quality, the results of axial velocity and mixture fraction for the three cases are compared with the experimental data in Figure 4.3. Overall, the medium and fine grid resolution compares well with the experimental data, whereas differences occur with the course mesh. The plot of the axial velocity along the centreline axis is given in Figure 4.3(a). In the experiments, the velocity appears to decays along the axis until approximately 65 mm where it becomes negative and a recirculation zone occurs until approximately 100 mm. The coarse, medium and fine meshes correctly capture the first velocity point at $z = 6.8$ mm in Figure 4.3(a), which is further confirmed with the radial profile at $z = 6.8$ mm

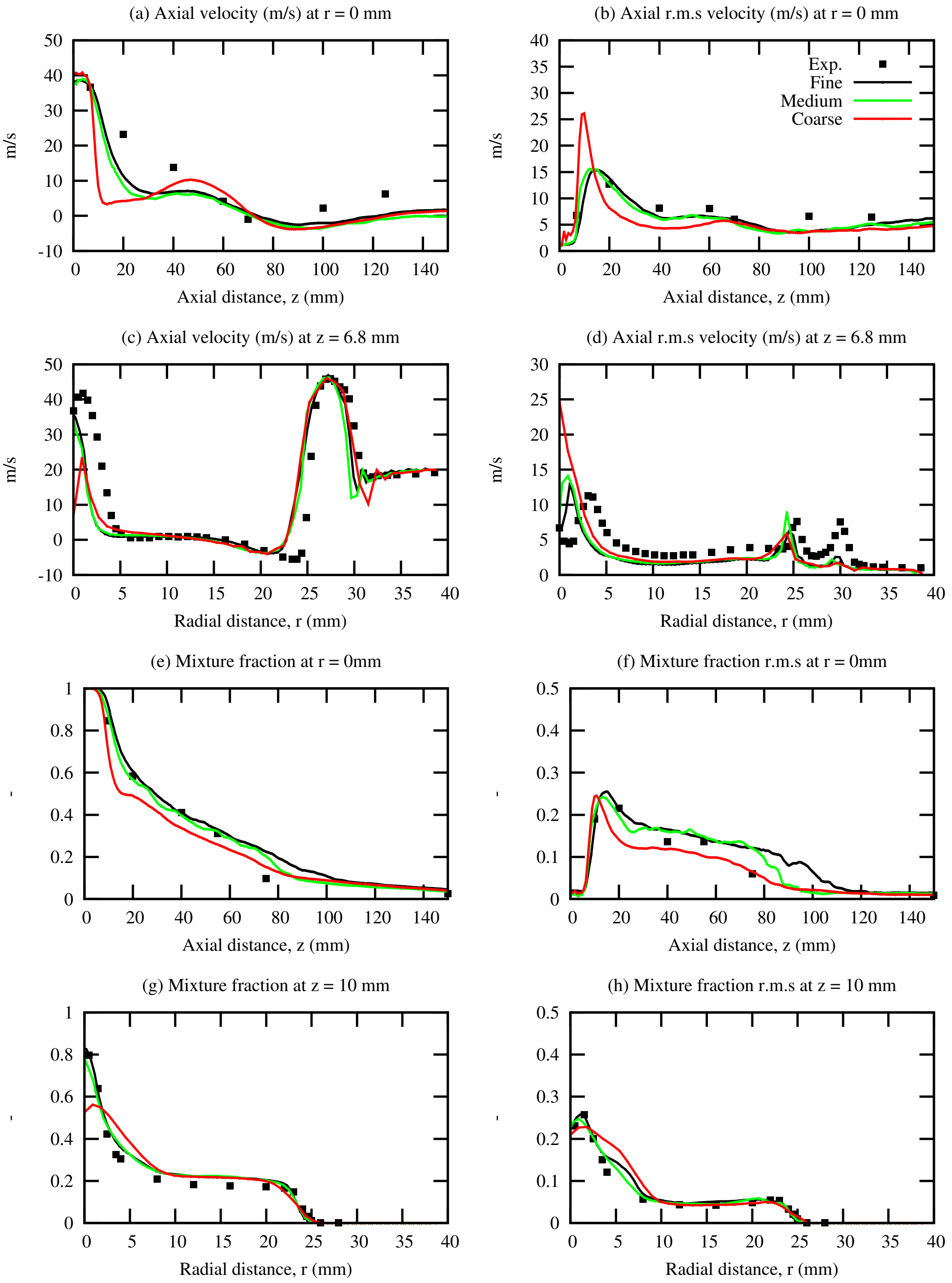

Figure 4.3: Comparison of results for different grid refinement levels.

case	Domain size in mm (H x W x L)	Number of cells
small	$75 \times 75 \times 200$	≈ 5.2 million
long	$75 \times 75 \times 400$	≈ 10.4 million
wide	$150 \times 150 \times 200$	≈ 20.8 million

Table 4.7: Investigated domain sizes.

in Figure 4.3(c). However there appears to be a stronger decay of the axial velocity along the centreline between $z = 20$ and $z = 40$ mm predicted in the simulations compared to the experimental data. The decay is marginally weaker as the grid is refined, thus suggesting this phenomena is independent of mesh refinement. The decay in mixture fraction at the same location in Figure 4.3(e) appears to compare well with the experimental data for the medium and fine meshes suggesting the need for more detailed experimental data between these points to adequately evaluate the flow dynamics.

The radial profiles and the fluctuations for the near burner zone are shown in Figures 4.3(c) and (d) for the axial velocity at 6.8 mm and Figures 4.3(g) and (h) for the mixture fraction at 10 mm away from the burner. Experimental data close to the burner exit helps assess the accuracy of the boundary conditions. The results compare well with the experimental data suggesting that the boundary conditions are adequate.

The wall clock time for the coarse, medium and fine mesh to achieve 0.28 s of simulated data were approximately 11, 43 and 161 hours, respectively, on 12 nodes shared by three quad core Intel X5560 2.8GHz processors on the University of Leeds HPC, ARC1.

Influence of domain size

The burner is an open flame where the walls are far from the flame and it is important to check how the boundaries influence the results. Three cases were investigated consisting of a *small* domain of 75 x 75 x 200 mm, a *long* domain where the outlet was extended away from the burner with a size of 75 x 75 x 400 mm and a *wide* domain where the lateral boundaries were increased so that the size was 150 x 150 x 200 mm on a grid size of 0.6 mm. The cases are summarised in Table 4.7.

The influence of the domain size on the solution is shown in Figure 4.4. In Figure 4.4(a), there is little difference in the axial velocity along the axis between the cases near to the burner with a steep axial decay present in all cases below $z < 40$ mm. Widening the domain also appears to have little impact on the solution. The main difference occurs when the length of the domain is extended, as shown in Figure 4.4(a) after $z = 75$ mm. The recirculation zone between $z = 75$ mm and $z = 100$ mm is captured in the *long* case, thus suggesting the boundary at the outlet is influencing the solution. In the short domain, both positive and negative axial velocity exists at the outlet, which suggests the flow has not fully developed by this point therefore invalidating the use of the Neumann condition.

Experimental observations and measurements suggest that another recirculation zone exists between the bluff body at $z = 0$ mm and $z \approx 43$ mm which is a toriodial shape [169]. The observations along with the predictions from the long domain are shown in Figure 4.5 and the LES simulation appears to capture the two recirculation zones adequately.

Summary

To assess the prediction of NO, it is important to have an accurate description of the flow field, temperature and species concentrations. Following the sensitivity studies,

(a) Axial velocity (m/s) at r = 0 mm

(b) Axial r.m.s velocity (m/s) at r = 0 mm

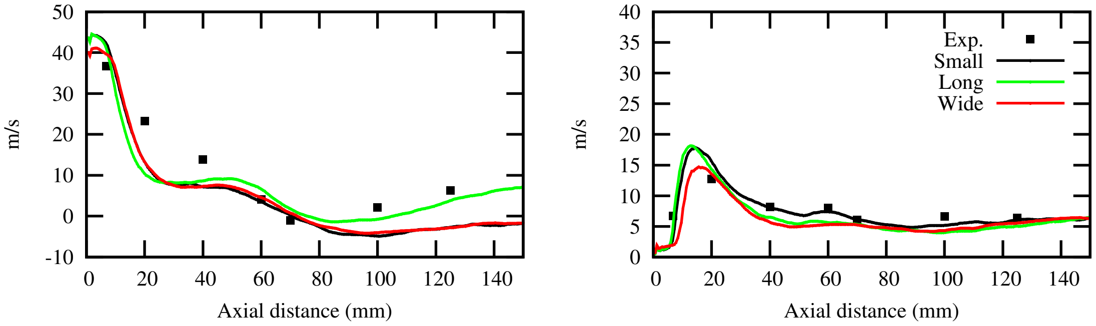

(c) Axial velocity (m/s) at z = 6.8 mm

(d) Axial r.m.s velocity (m/s) at z = 6.8 mm

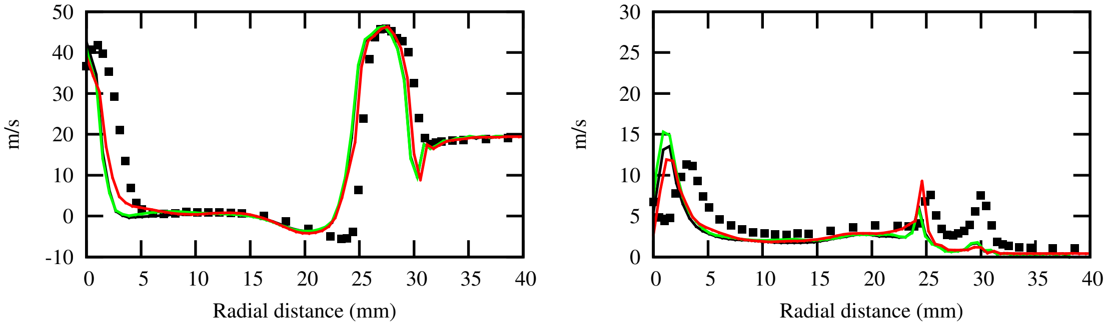

(e) Mixture fraction at r = 0mm

(f) Mixture fraction r.m.s at r = 0mm

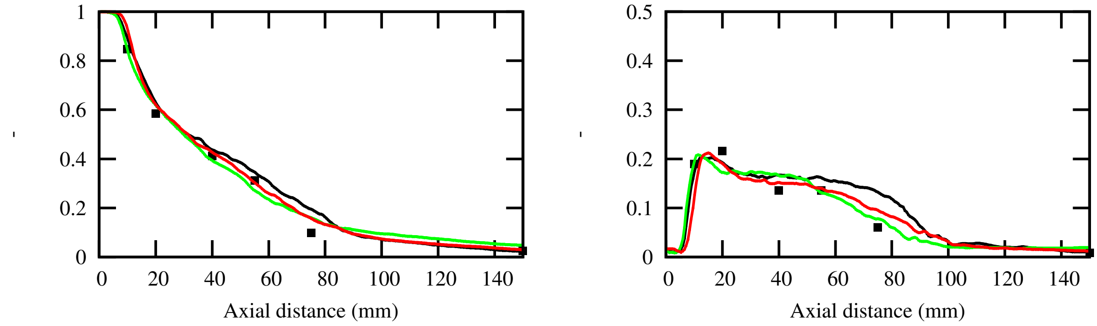

(g) Mixture fraction at z = 10 mm

(h) Mixture fraction r.m.s at z = 10 mm

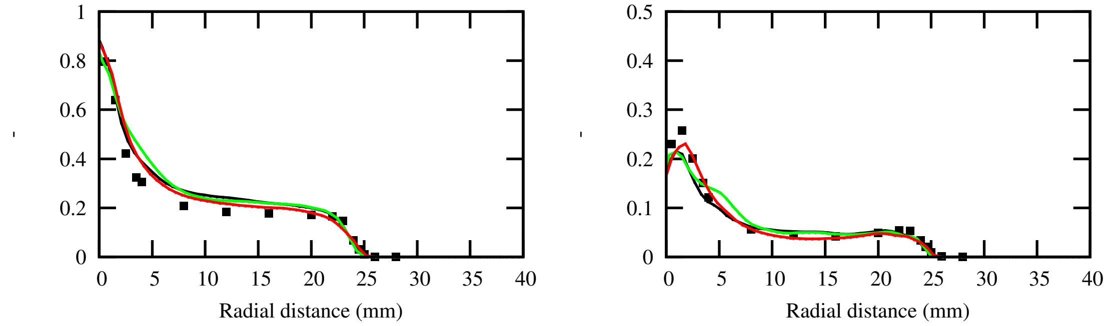

Figure 4.4: Comparison of results for different domain sizes: small (75 x 75 x 200 mm), long (75 x 75 x 400 mm), large (150 x 150 x 200 mm).

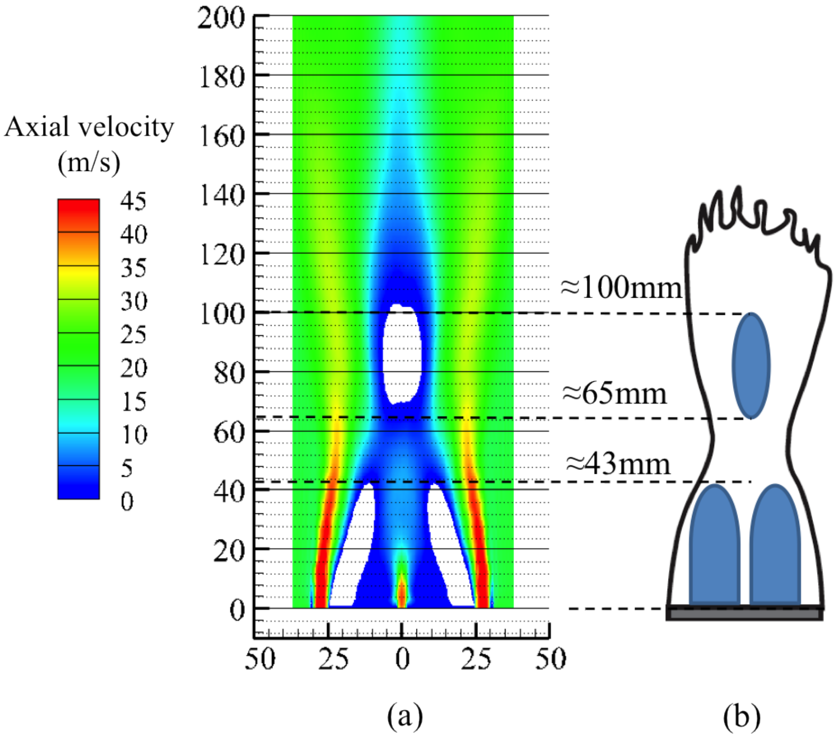

Figure 4.5: Comparison of (a) predicted recirculation zones against (b) those obtained from experiments [169].

the calculations were performed on grid size of 0.6 mm size with a domain size of 75 × 75 × 400 mm with a single scalar dissipation rate of 10/s and the simulation set-up is described in Table 4.8.

The predictions of axial and tangential mean and root mean square velocity at various axial locations ($z = 6.8$, 20, 40, 60, 70 and 125 mm away from the exit of the burner) in the radial direction are shown in Figures 4.6 and 4.9, respectively. A good agreement is found between the experimental predictions and the LES predictions. A slight deviation is shown near the burner zone (at z = 6.8 mm) where the swirled air is introduced ($z = 25$ mm until $z = 30$ mm). This deviation may be caused by the cubic cells which fail to represent the cylindrical shape of the burner producing a staircase effect instead of a smooth surface. Furthermore, a constant tangential velocity is used along with an axial velocity profile for the swirled air and a more representative velocity profile at this inlet may also reduce this discrepancy.

Model	Model parameter
Turbulence	LES, standard Smagorinsky-Lilly model with $C_{sgs} = 0.173$
Chemistry	Steady flamelet model based on GRI 3.0 mechanism with single scalar dissipation rate of 10/s and top-hat PDF
Grid size	75 x 75 x 400 mm
Cell size	0.6 mm equidistant cartesian grid
Momentum	Bounded central differencing scheme
Species	Total Variation Diminishing (TVD) scheme
Time-advance	Explicit third-order low storage Runge Kutta method
CFL number	0.7
Boundary conditions	Inlet: velocity profile
	Perturbation: artificial turbulence generator
	Outlet: Neumann condition
	External walls: slip
	Walls: immersed boundaries

Table 4.8: Model set-up for the Sandia SM1 case study.

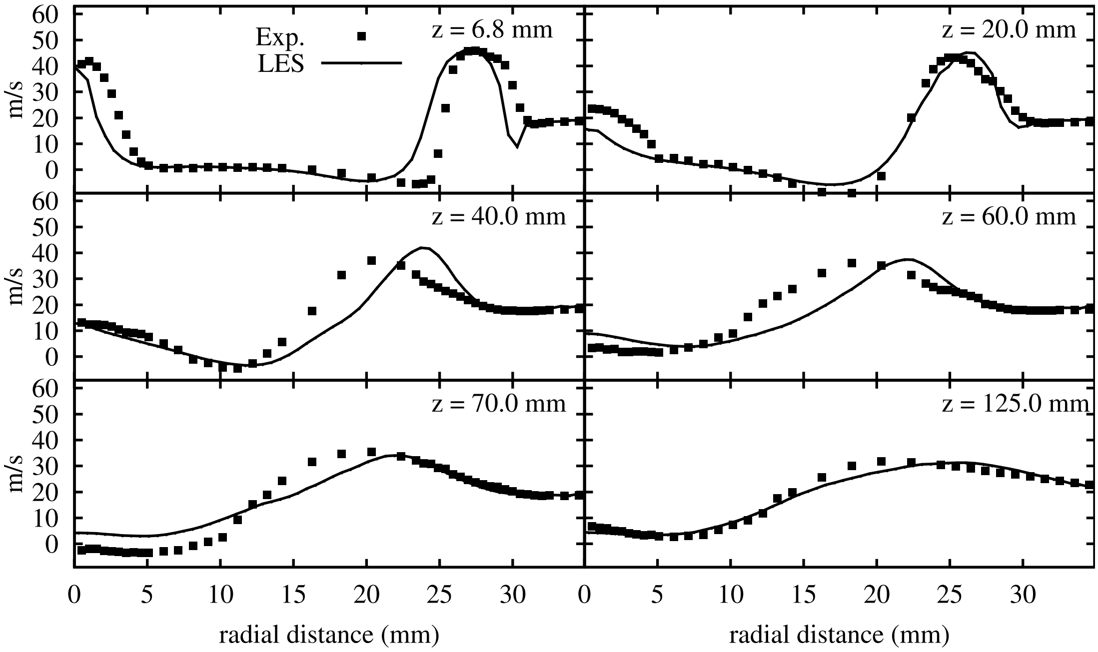

Figure 4.6: Experiment (symbols) and LES (line) of axial velocity (m/s).

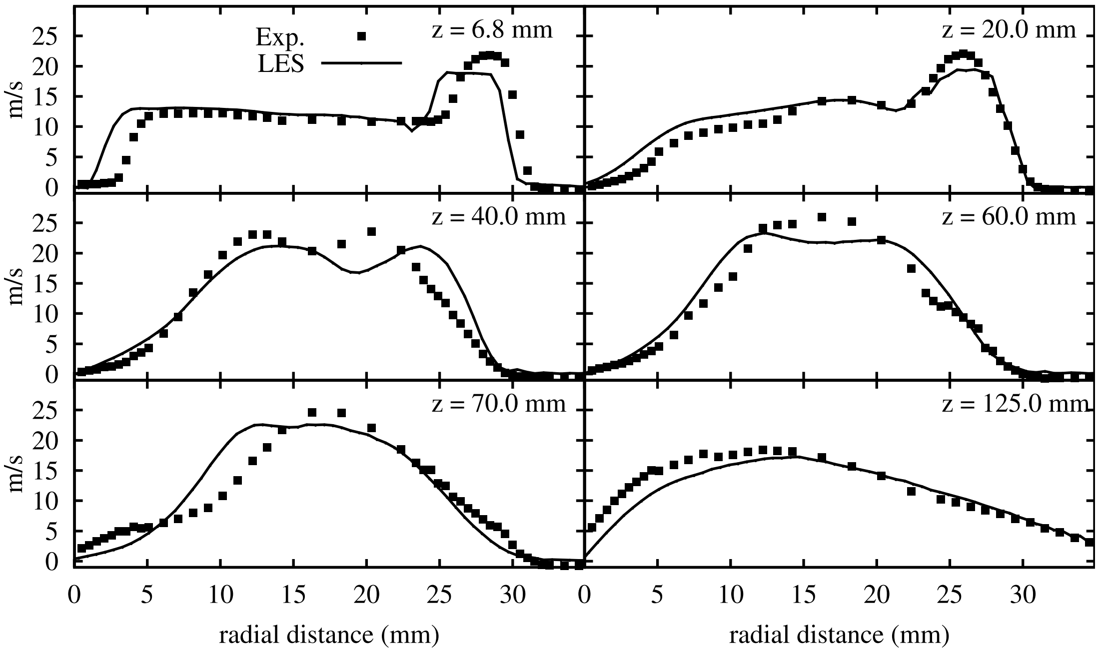

Figure 4.7: Experiment (symbols) and LES (line) of tangential velocity (m/s).

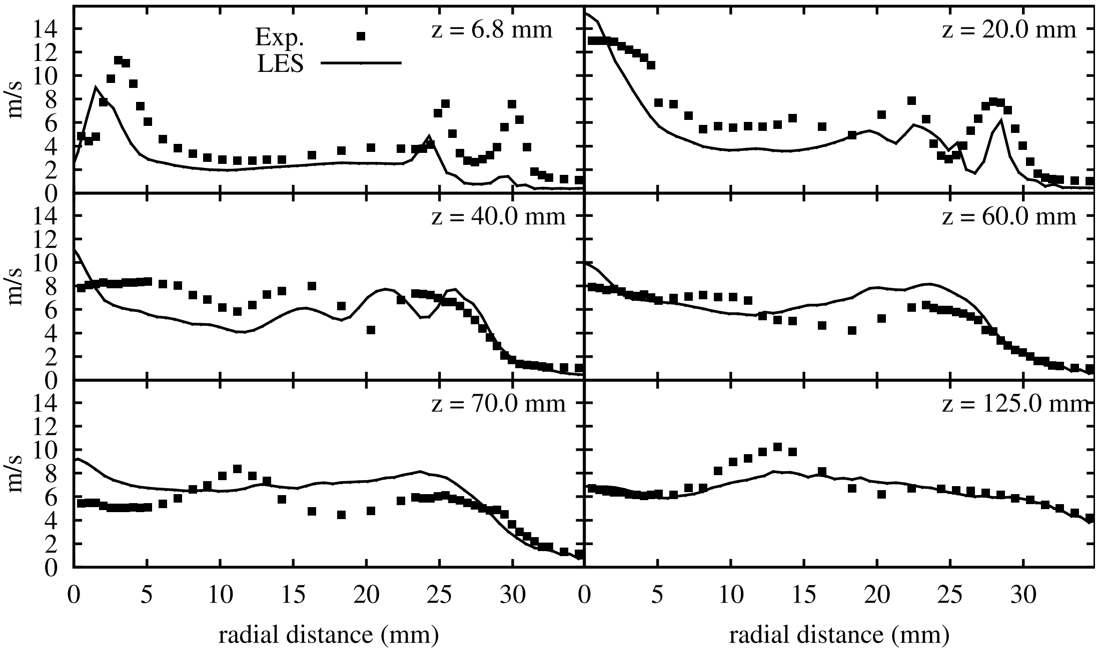

Figure 4.8: Experiment (symbols) and LES (line) of axial r.m.s. velocity (m/s).

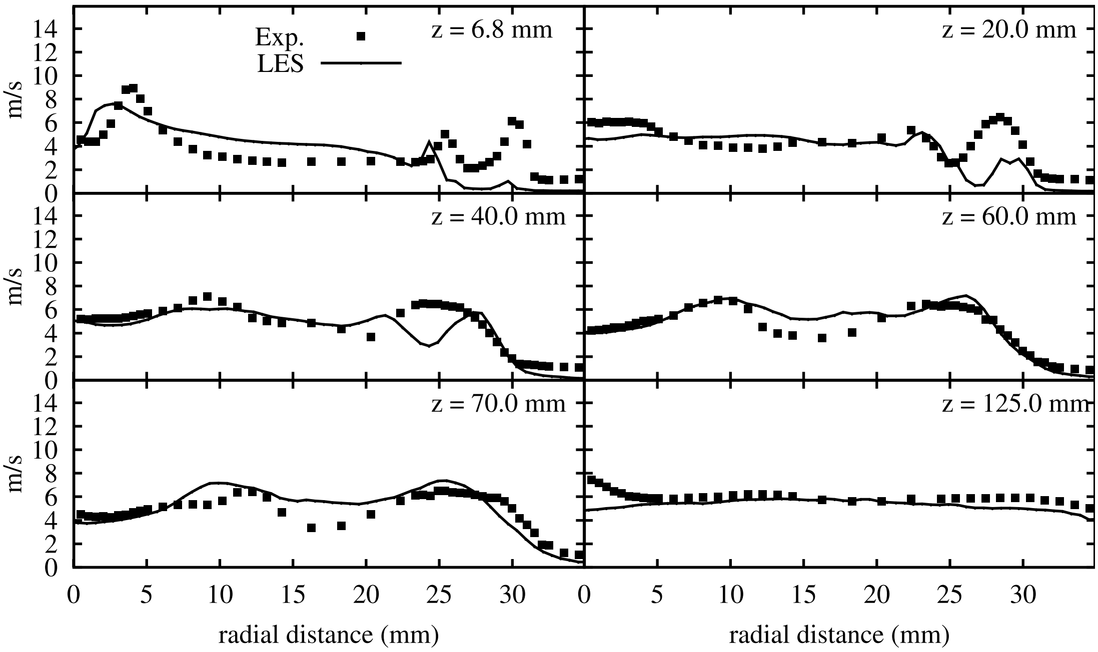

Figure 4.9: Experiment (symbols) and LES (line) of tangential r.m.s. velocity (m/s).

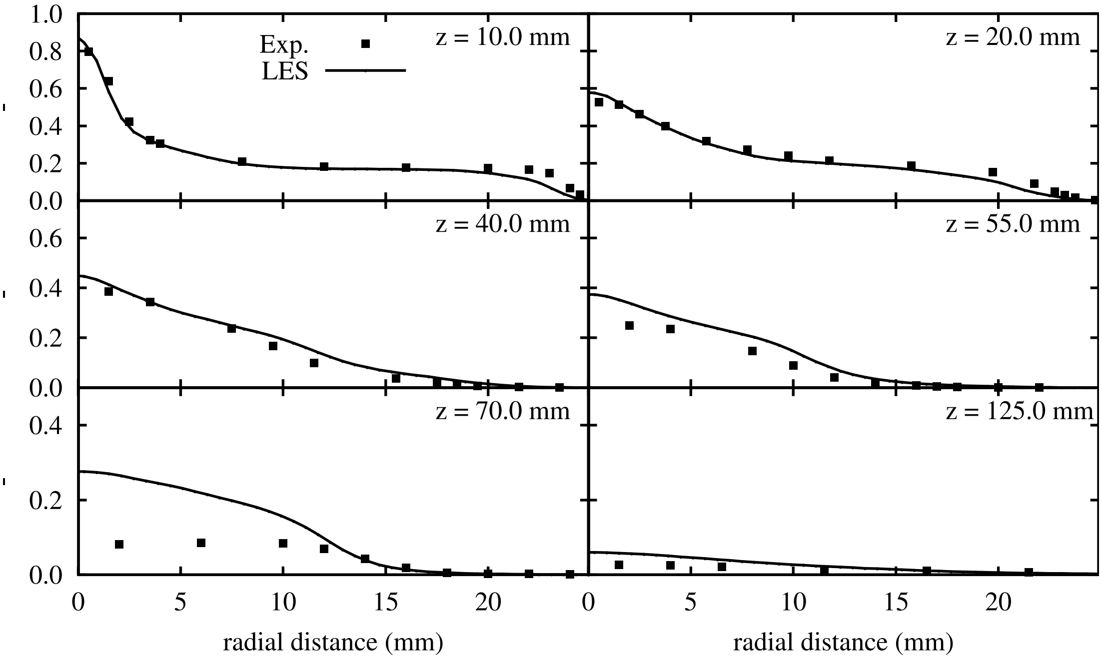

Figure 4.10: Experiment (symbols) and LES (line) of mixture fraction.

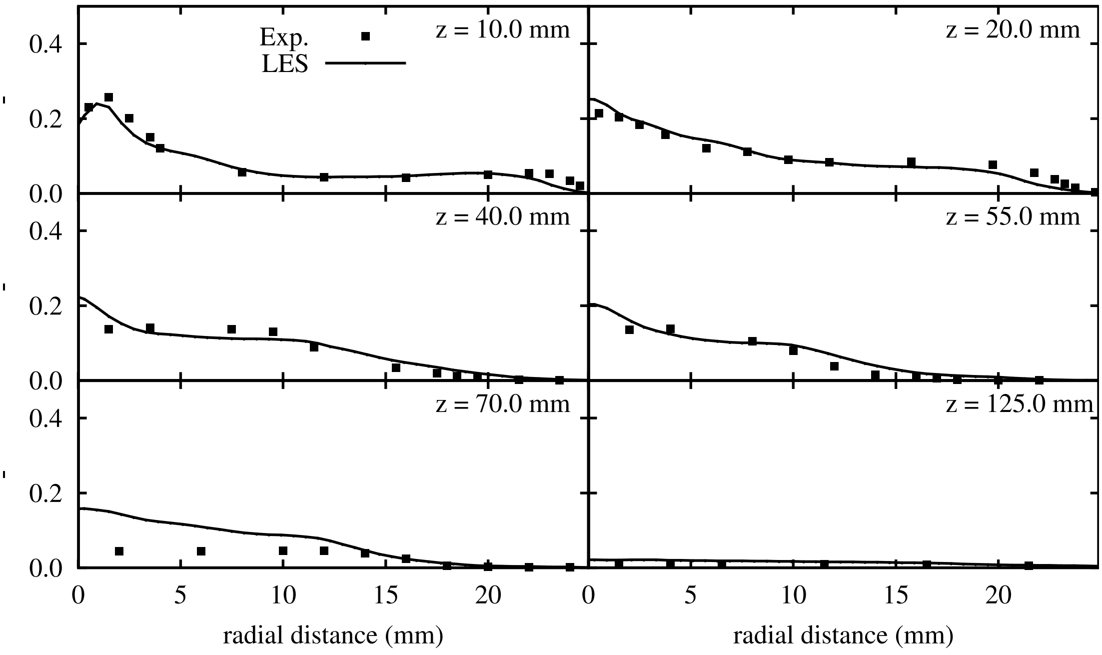

Figure 4.11: Experiment (symbols) and LES (line) of r.m.s. mixture fraction.

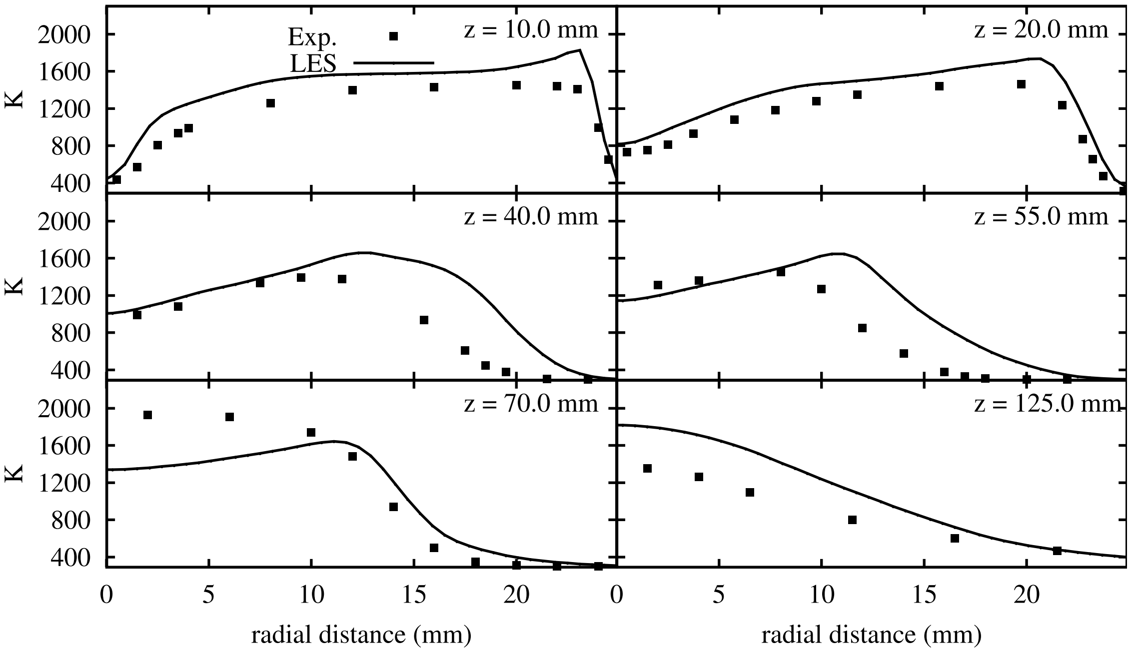

Figure 4.12: Experiment (symbols) and LES (line) of temperature (K).

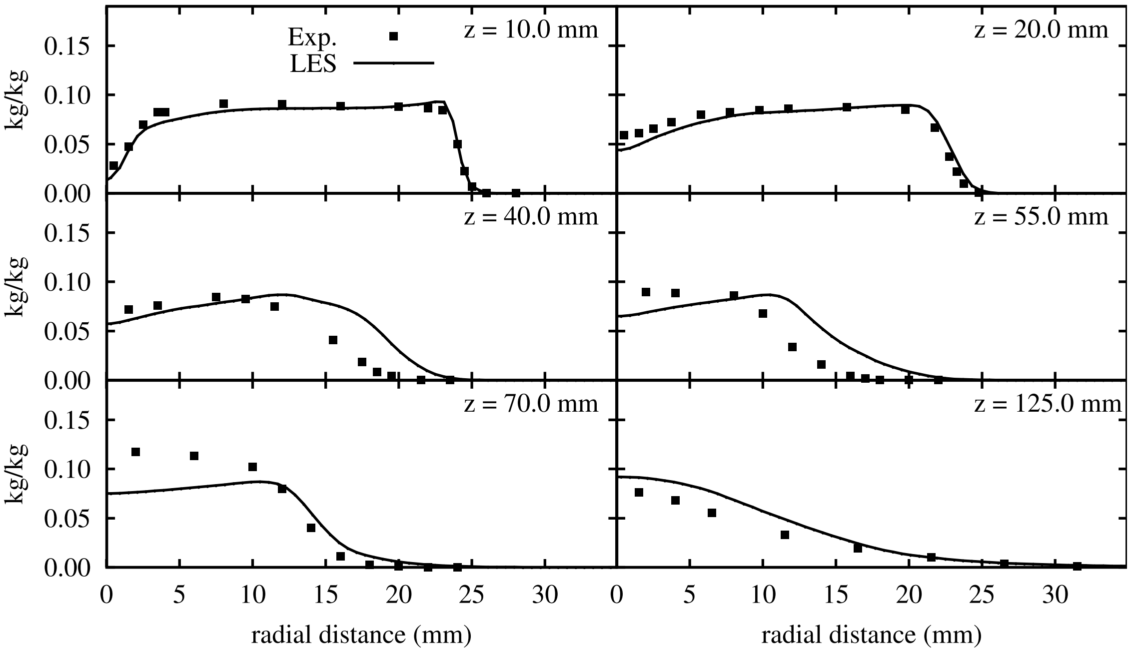

Figure 4.13: Experiment (symbols) and LES (line) of CO_2 mass fraction.

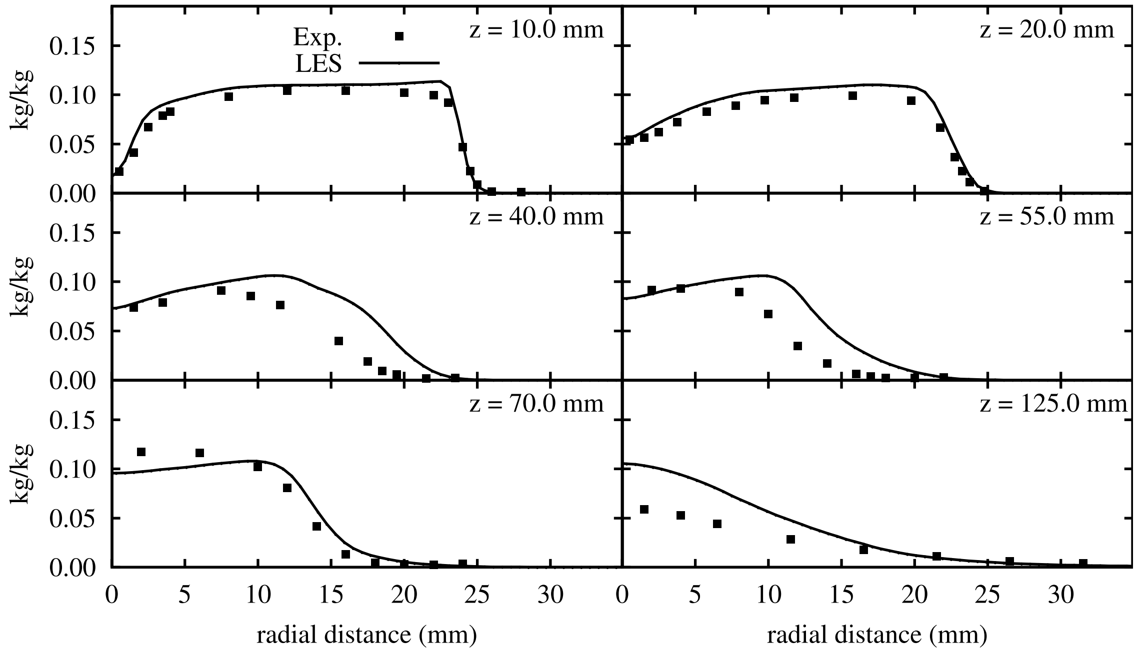

Figure 4.14: Experiment (symbols) and LES (line) of H_2O mass fraction.

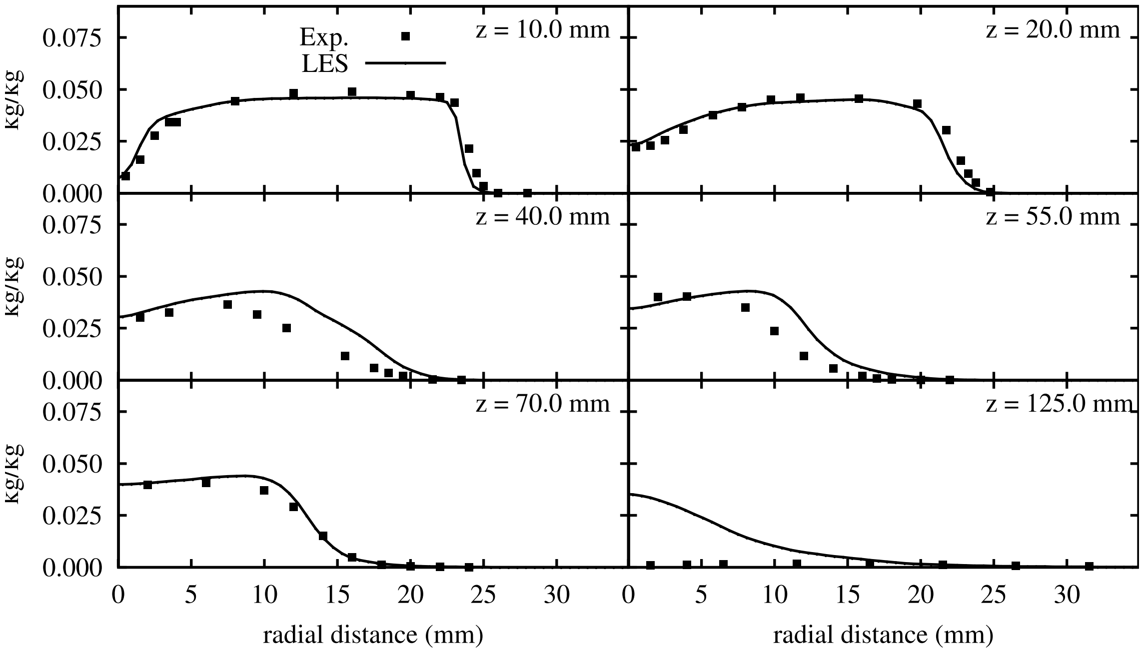

Figure 4.15: Experiment (symbols) and LES (line) of CO mass fraction.

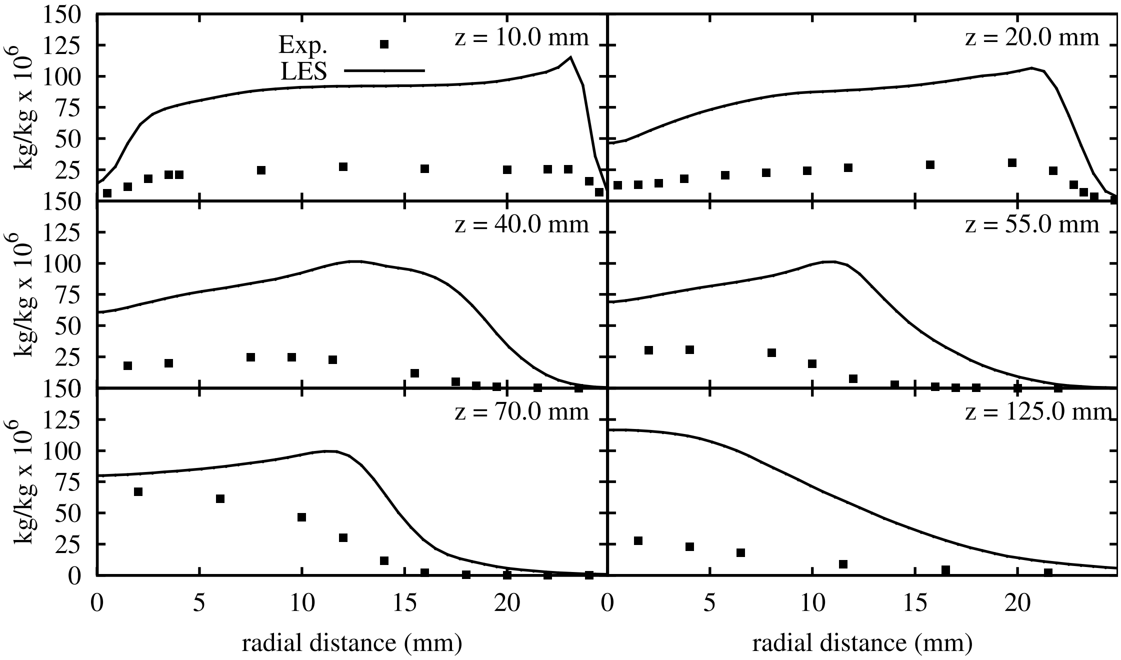

Figure 4.16: Experiment (symbols) and LES (line) of NO mass fraction predicted by the steady flamelet model.

The predictions of the mean and r.m.s mixture fraction are shown in Figures 4.10 and 4.11. The stoichiometric mixture fraction for methane is $Z_{st} = 0.055$ and it is clear from the results near to the burner at $z = 10$ mm, a fuel rich region exists in the recirculation zone at the bluff body. The LES predictions compare well against the experimental data, except at $z = 70$ mm where the LES over-predicts the mixture fraction. In the experiments, the mixture fraction is near stoichiometry and therefore captures a higher temperature at this position, as shown in Figure 4.12. Since the mixture fraction is over-predicted the temperature and species also do not compare well with the experimental data. For example, the temperature in Figure 4.12 is underpredicted by about 600 K.

Experimental data is also available for CO_2, H_2O, CO and NO. The prediction of these species distribution are important for the success of the NO_x model. The prediction of CO_2, H_2O, CO are given in Figures 4.13, 4.14 and 4.15, respectively, and compare well against the experimental data. In Figure 4.16, the prediction of NO is given from the flamelet model and shows that while the simulation of major species, such as CO_2 and H_2O are predicted well, there is a difficulty in the correct prediction of NO. It has been noted that slow forming species, such as NO, may be overestimated by an order of magnitude by the steady flamelet model [117].

Overall, the LES predictions compare well with the experimental data and it can be argued that the flow field, temperature and species concentration are adequately captured by the simulation. In the following sections, the results from the NO_x model are evaluated. The following investigations are performed:

(i) post-processing at the end of the simulation, where only the equations for NO, HCN and NH_3 are solved.

(a) *mean-valued source term*

The NO_x model is used as a post-processing technique where the mean values collected by the LES are used to compute the source terms and $\overline{S_k} = S_k$ in Equations (4.1)-(4.3), therefore ignoring any turbulent chemistry interaction.

(b) *time-averaged source term*

The NO_x model is used as a post-processing technique where the mean and variance values collected by the LES are used to give the shape of the top-hat function and Equation (4.4) is used to compute the source terms, thereby accounting for turbulent chemistry interaction. Only a single variable of temperature is considered.

(ii) computed at the end of every time step, where the equations for NO, HCN and NH_3 are computed at the end of each time-step.

(a) *instantaneous source term*

The source terms are calculated at the end of every time step from the instantaneous values in the LES. Turbulent chemistry interaction is accounted for by the large scale fluctuations resolved by the LES.

(b) *filtered source term*

The source term is calculated at the end of every time step where the effects of turbulent chemistry interaction are accounted for by both the large scale fluctuations resolved by the LES and the small scale fluctuations which are modelled by the use of a FDF and a sub-grid scale model with temperature as the fluctuating variable.

Case i. (a) Results

To evaluate the effect of the NO_x mechanisms on the Sydney burner, four different cases were performed. The computed mean values for O_2, N_2, H_2O, O and OH mass fractions along with density, ρ and temperature, T were used to compute the source terms for NO, HCN and NH_3 which were solved separately from the LES. Convergence was checked by monitoring a number of points in the solution. The solution took approximately 12 hours to solve on 16 processors with only a slight increase in computational time when more mechanisms were included. The four cases considered were:

(i) *t*: thermal mechanism only

(ii) *tp*: thermal and prompt mechanisms only

(iii) *tprf*: thermal, prompt, reburn and fuel mechanisms only[1]

(iv) *tprfn2o*: thermal, prompt, reburn, fuel and N_2O intermediate mechanisms.

---

[1] reburn and fuel mechanisms need to be solved simultaneously as the fuel mechanism contains the destruction of HCN, which is produced in the reburn mechanism

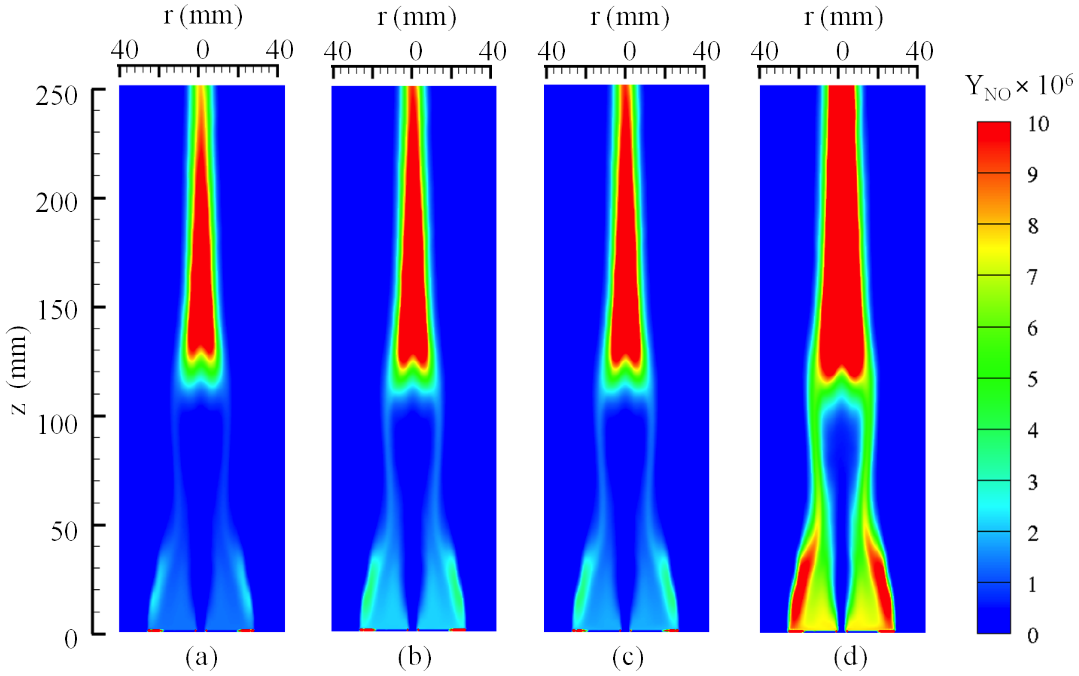

Figure 4.17: LES predictions of NO based on a post processing method when using (a) thermal mechanism, (b) thermal and prompt mechanisms, (c) thermal, prompt, reburn and fuel mechanisms, and (d) thermal, prompt, reburn, fuel and N_2O mechanisms.

The impact of the different mechanisms is shown in Figure 4.17. Thermal NO is predicted mainly in the post-flame zone, which is shown in Figure 4.17(a). The contribution of prompt NO can be seen near the base of the flame in Figure 4.17(b) where a marginal increase is observed due to the fuel rich zone below $z = 50$ mm, however further away from the flame in the fuel-lean region it has little effect. The addition of the reburn model shows a very marginal depletion of the concentration of NO in the fuel rich region as shown in Figure 4.17(c) where the hydrocarbons in the fuel rich region reduce the NO. These trends confirm the expected model performance described in Section 4.2.

Comparison with experimental data is shown in Figure 4.18. All of the mechanisms under predict the formation of NO, except at z = 150 mm where the *tprfn2o* case gives a reasonable prediction of NO. It is clear from the figures that the in-

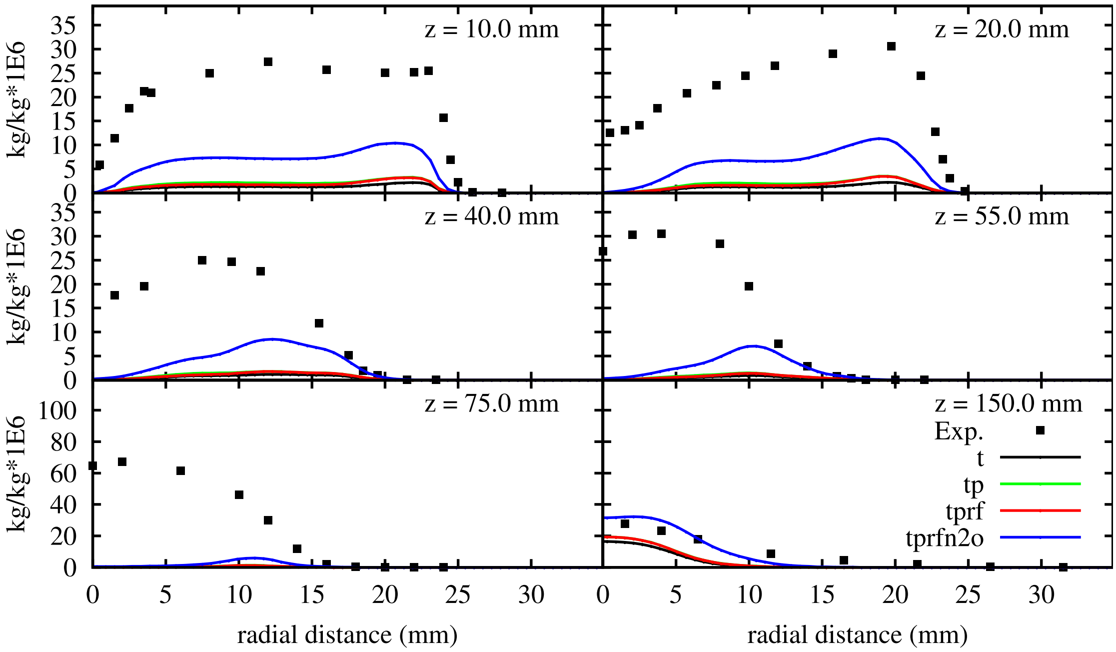

Figure 4.18: Experiment (symbols) and LES predictions (line) of NO based on a post processing method.

fluence of the N_2O mechanism is the most dominant and contributes about 60% of the overall NO formation in the near flame zone. Since the temperature in the near flame zone is lower than approximately 1700K, it is expected that the contribution of thermal NO to be relatively small. The largest deviation occurs at z = 75 mm where little NO is predicted. As mentioned previously in Figure 4.12, the prediction of temperature at z = 70 mm is under predicted by about 600K. In this region, the experimental temperatures of 2000K are shown which is good conditions for the formation of thermal NO. However, due to the under prediction of temperature, the NO_x model cannot capture these measurements. These results highlight the sensitivity of the NO_x model to temperature predictions.

The sensitivity of the O radical should be examined as it is a crucial species to predict due to its impact on both the thermal and N_2O intermediate mechanisms. The O radicals have thus far been taken from the mixture fraction table, but in some

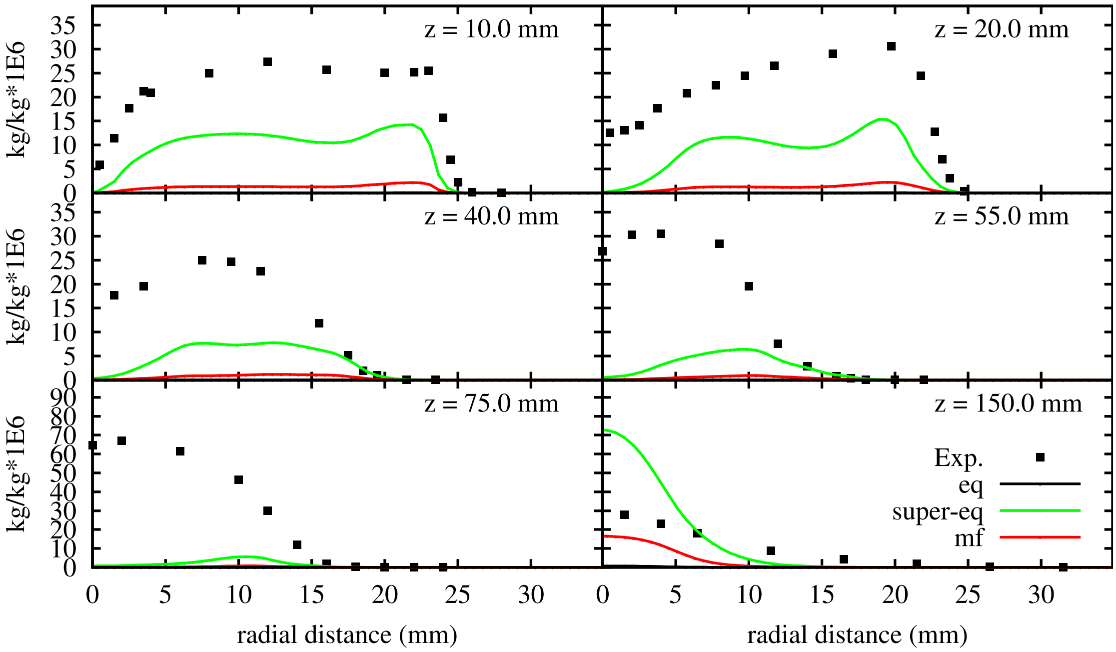

Figure 4.19: Experiment (symbols) and LES (line) of NO mass fraction when different assumption of O radical are used.

combustion sub-models these may not be available and semi-empirical expressions, such as Equations (4.13) and (4.14) may have to be used.

The equilibrium assumption (eq) given by Equation (4.13) and the super equilibrium (super-eq) assumption given by Equation (4.14) are shown against mixture fraction (mf) O radical predictions for thermal NO in Figure 4.19. It is evident that the equilibrium value is very small near the burner with respect to the other cases. In fact the concentration of NO is about an order of magnitude smaller and is barely visible on the graph. The equilibrium assumption is generally only valid in the post-flame region and therefore may not be applicable in these regions. In contrast, the super equilibrium approximation leads to a much higher prediction of NO. The super equilibrium assumption may be valid in the near flame zone where concentrations of O radicals greatly exceed the equilibrium values. Further downstream at 150 mm, the super equilibrium value may lead to an over prediction of thermal NO as this assumption may not be valid in this post flame zone. The approximation of O radicals from the mixture fraction table is lower than the super equilibrium assumption and higher than the equilibrium assumption for all of the locations examined in Figure 4.19. The calculation of O radicals are taken directly from a pre-computed table consisting of a number of reactions, species and scalar dissipation rate whereas the other assumptions are only based on a select number of species such as oxygen, carbon monoxide and carbon dioxide. Without experimental measurements of O radicals, it is difficult to conclude which approach provides satisfactory results, however the results demonstrate the importance of O radical approximation and the impact on thermal NO formation.

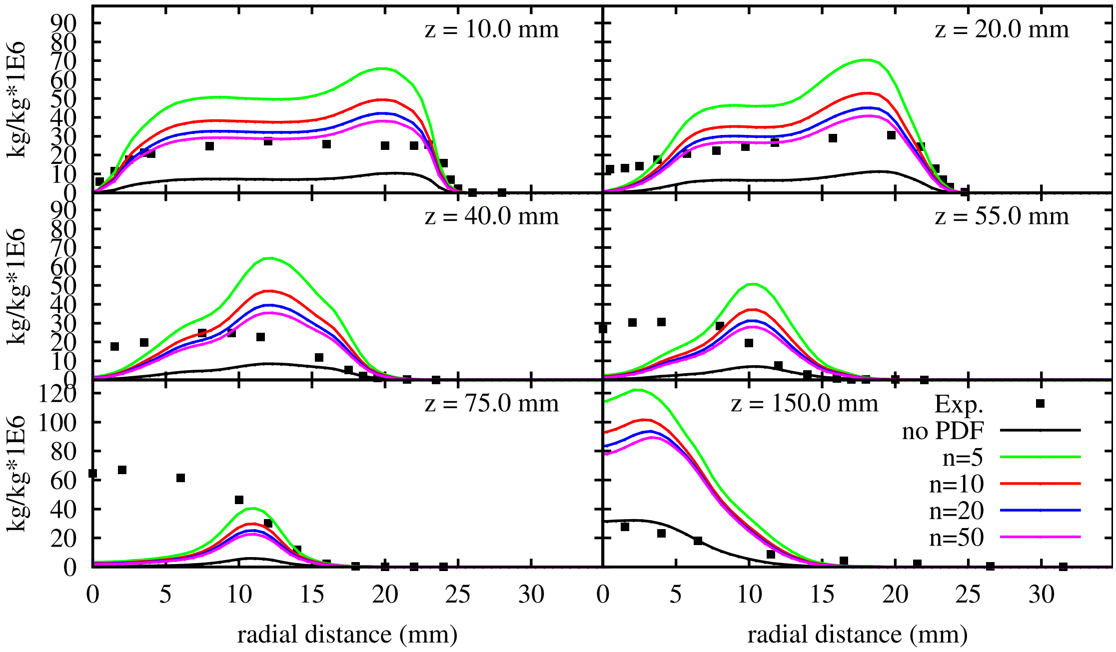

Figure 4.20: Experiment (symbols) and LES (line) of NO mass fraction when no PDF ($n = 0$) or a top-hat PDF is used with $n = 5$, 10, 20 and 50 points described by the method in Case i. (b).

Case *i*. (b) Results

The relationship between temperature, species concentrations and the formation of NO is highly non-linear and the use of time-averaged values alone may not be a suitable approximation for source terms and a PDF may be used to consider the fluctuations in time of temperature or species.

Figure 4.20 shows the prediction of the NO mass fraction for different discretisations of the integral in Equation (4.40). A single variable top-hat function was considered for fluctuations in temperature where n is the number of points in Equation (4.40) and the number of points examined were 5, 10, 20 and 50. To account for large variances in the PDF, the temperature was clipped to 293K and 2200K and Dirac functions were used at these limits.

Since the PDF shape is non-linear, more points are generally required to accurately resolve the shape and as the number of points increase, the overall value of NO decreases, thus highlighting a PDF discretisation dependency. The solution could be assumed to be independent of the PDF when $n = 20$ since there is little difference from the results obtained with $n = 50$. The trend of using a PDF shows a different shape compared to the solution when a PDF is not used. In Figure 4.20(a), peaks of NO occur at $r = 20$ mm where peak temperature and high fluctuations occur as shown in Figures 4.21(a) and (b). The fluctuations are relatively large throughout the domain, which is clearly shown to impact on the rates when fluctuations are ignored (Figure 4.22(a)) and included (Figure 4.22(b)-(d)). All of the rates exhibit similar trends and follow the pattern seen in Figure 4.21(c) for O radical mass fraction, thus highlighting the rates dependency on the prediction of species concentrations.

Case *ii*. (a) Results

Figure 4.23 shows the prediction of NO when the source term is computed using instantaneous values of O_2, N_2, H_2O, O and OH mass fractions along with density,

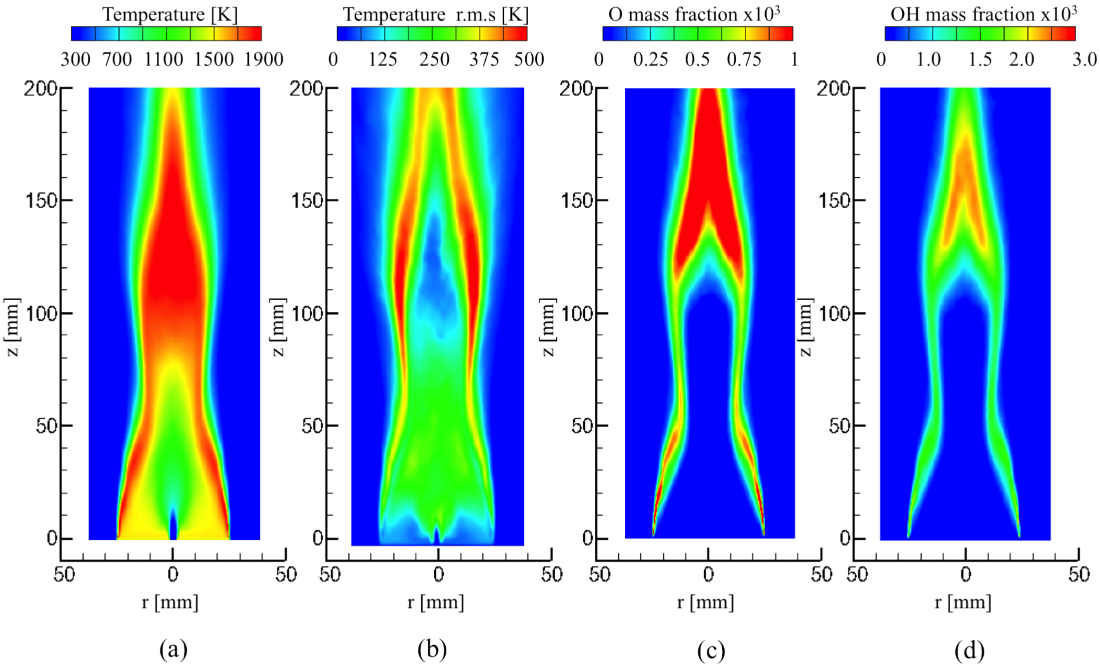

Figure 4.21: Statistically averaged contour plots of (a) mean temperature, (b) r.m.s temperature, (c) O mass fraction, and (d) OH mass fraction.

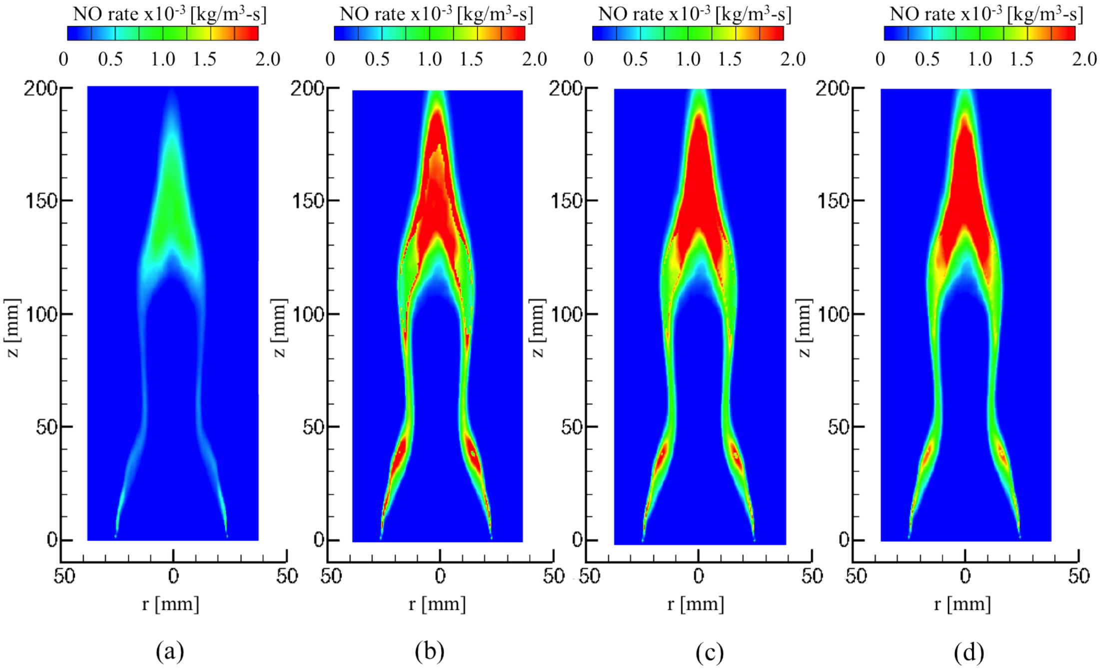

Figure 4.22: Contour plots of the mean rate of NO formation when (a) no PDF is used, (b) 5 PDF points are used, (c) 20 PDF points are used, and (d) 50 PDF points are used.

ρ and temperature, T at the end of each time step, but ignoring any sub-grid scale fluctuations (no FDF). The predictions follow a similar trend to the experimental data than those in Figure 4.20 which may be due to turbulent chemistry interaction effects being resolved directly by the LES. The fluctuations in NO mass fraction at every time-step are then smoothed by the averaging process, rather than applying a PDF function to account for the turbulent chemistry interaction, as performed in case *i* (b). Despite a similar trend, the results still under predict the concentration of NO at most locations.

Case *ii*. (b) Results

Figure 4.23 shows the prediction of NO when the source term is computed *at the end of every time step* using the top-hat FDF with 5 or 10 points to account for sub-grid scale fluctuations of temperature. Further independence of the FDF was not tested due to the increase in computational cost of this method as the FDF is recalculated at the end of every time step. The sub-grid scale variance defined in Equation (4.41) was used as the variance in the FDF. The trend of the predictions also exhibits a similar trend to the experimental data. Compared to case *ii* (a) when the FDF was ignored, the impact of using a FDF does not appear to have a significant effect to the in-flame NO prediction and it may be assumed that using more points to discretise the FDF may lead to a lower prediction of NO, similar to that of case *ii* (a). This may also imply that the mesh is sufficiently fine that the contribution of sub-grid scale fluctuations are minimal, therefore sub-grid scale effects of a coarser mesh would be expected to have more of an impact.

Summary

An LES was performed using the in-house code, *PsiPhi*. Good agreement was obtained for velocities, temperatures and species concentrations compared with experimental data ensuring the flow field and combustion has been adequately captured.

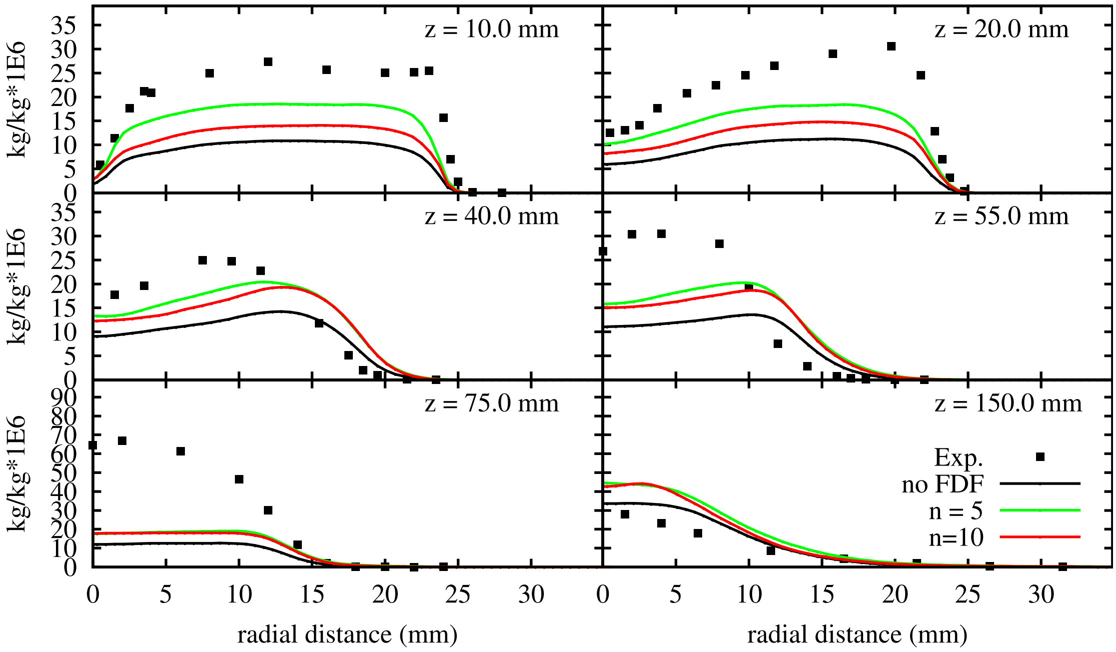

Figure 4.23: Experiment (symbols) and LES (line) of NO mass fraction for option 2(a) of no FDF (no FDF) and for option 2(b) when a top-hat FDF is used with $n =$ 5 or 10 points.

However, an over prediction of NO concentration was predicted by the flamelet model.

A global NO_x model was implemented into *PsiPhi* and the impact of various mechanisms and effects of a PDF / FDF were examined. The results highlighted the impact of O radicals in the thermal NO model and values from the mixture fraction table should be used where possible.

The NO_x model is decoupled from the main simulation and was to compute the formation of NO *at the end of the simulation*, after the LES had statistically converged which is analogous to a steady RANS approach, or *at the end of each time step*. The effects of turbulent chemistry interaction in both cases were also examined by assuming a top-hat function shape for the PDF or FDF. It was found that the application of the NO_x model *at the end of each time step* produced good trends with the experimental data. The results appeared to be independent of the sub-grid scale fluctuations, modelled by a top-hat FDF, which suggested the mesh was sufficiently fine that sub-grid scale variations had minimal impact on the prediction of NO. However, further investigation into sub-grid variance models should be performed and more detailed chemistry models may be needed to ensure the chemistry is sufficient to predict the formation of NO. The results highlighted that the majority of TCI is accounted for by the LES and therefore, a better trend is shown against the experimental data when NO is computed *at the end of each time-step* rather than *at the end of the simulation*.

4.3.2 Laboratory coal and methane burner

The CRIEPI burner is studied in this section and the boundary conditions have been discussed in Section 3.2 . The burner has been initially studied by Imperial College and has been previously published [45]. The following work considers a parameter study of different devolatilisation rates and the formation of NO from the implemented NO_x model. Grid study analysis for non-reactive and reactive flow has already been performed by Franchetti et al [45] and therefore it is not be repeated here.

In this section, the use of a network model, FG-DVC [94] is used to estimate devolatilisation rates and nitrogen partitioning of the coal. An investigation of devolatilisation rate is performed to ensure the simulation adequately represents the physical flow field and temperature / species distribution before assessing the predictions of NO from the implemented model and comparing with available experimental data.

Numerical set-up

The numerical set-up of the case is described in Table 4.9. An equidistant cell size of 0.5 mm was used in all of the cases with a domain size of 40 × 40 × 180 mm (W x D x H). Devolatilisation of the coal particle was assumed to be governed by a

Model	Model parameter
Turbulence	LES, standard Smagorinsky-Lilly model with $C_{sgs} = 0.173$
Gas-phase chemistry	Eddy dissipation model with two step chemistry [221]
	$CH_4 + 0.5\ O_2 \rightarrow CO + 2\ H_2O$
	$C_{2.98}H_{5.37}O_{0.50} + 2.58\ O_2 \rightarrow 2.98\ CO + 2.68\ H_2O$
	$CO + 0.5\ O_2 \rightarrow CO_2$
Char combustion	Intrinsic model [121,122]
	$A_i = 0.03$ (kg/m^2/s/Pa) $E_i = 1.794 \times 10^8$
	$A_{BET} = 250,000$ m^2/g
Devolatilisation rate	Single-step Arrhenius expression
	calculated from FG-DVC
Radiation	Discrete ordinates
	Constant particle emissivity $\epsilon_p = 0.85$
	Absorption coefficient $\kappa = 0.075\,(X_{\mathrm{CO_2}} + X_{\mathrm{H_2O}})$
Grid size	40 × 40 × 180 mm
Cell size	0.5 mm equidistant cartesian grid
Momentum	Flux blended upwind and bounded central differencing scheme
Species	Total Variation Diminishing (TVD) scheme
Time-advance	Explicit third-order low storage Runge Kutta method
CFL number	0.4
Boundary conditions	Inlet: velocity profiles
	Perturbation: artificial turbulence generator
	Outlet: Neumann condition
	External walls: slip

Table 4.9: Model set-up for the CRIEPI case study.

single rate Arrhenius expression which was computed by FG-DVC. The combustion of volatiles was assumed to be mixing limited and modelled with the eddy dissipation model for LES [59, 221]. The mixing rate was assumed to be controlled by the sub-grid-scale mixing rate:

$$\tau_{SGS}^{-1} = \sqrt{2S_{ij}S_{ij}}$$

where the strain rate tensor is given by

$$S_{ij} = \frac{1}{2}\left(\frac{\partial u_i}{\partial x_j} + \frac{\partial u_j}{\partial x_i}\right).$$

The overall reaction rate was therefore given by the minimum of the two rates,

$$R_{i,r} = \nu'_{i,r} M_{w,i} A \rho \tau_{SGS}^{-1} \min_{R}\left(\frac{Y_R}{\nu'_{R,r} M_{w,R}}\right)$$

$$R_{i,r} = \nu''_{i,r} M_{w,i} A B \rho \tau_{SGS}^{-1} \frac{\sum_P Y_P}{\sum_j^N \nu''_{j,r} M_{w,j}}$$

where $A = 4.0$, $B = 0.5$ and $\nu'_{i,r}$, $\nu''_{i,r}$ is the stoichiometric coefficient of reactant and product i, respectively in reaction r. The mass fraction of the reaction and product is given by Y_R and Y_P, respectively.

For the combustion of volatiles, the volatile compound was assumed to be of the form $C_xH_yO_z$ where $x = 2.98$, $y = 5.37$ and $z = 0.50$ which was derived from the proximate and ultimate analysis assuming a high temperature volatile yield of 1.5.

The other models in Table 4.9 are described in Chapter 2. All of the simulations were completed in 48 hours on 16 processors in the University of Leeds HPC, ARC1.

Influence of devolatilisation rate

The use of a network model, FG-DVC is used to estimate the devolatilisation rate in the simulations as well as the nitrogen partitioning between volatiles and char. The FG-DVC model was shown to provide good agreement compared to drop tube furnace and hot wire mesh measurements by Williams et al. [100] for a variety

Heating rate (K/s)	A_r (1/s)	E_a (J/mol)	N_{split}	$Y_{N,vol}$	$Y_{N,char}$
$\mathbf{10^5}$	8.89×10^6	5.82×10^4	0.79	1.49×10^{-2}	1.88×10^{-2}
$\mathbf{10^4}$	4.85×10^8	1.25×10^5	0.68	1.33×10^{-2}	1.96×10^{-2}
$\mathbf{10^3}$	1.43×10^3	5.93×10^7	0.58	1.19×10^{-2}	2.02×10^{-2}

Table 4.10: FG-DVC predictions for different heating rates up to 1623K at a residence time of 150 ms with the exception of 10^3 K/s where 1.5 s was used.

of coals. A similar approach is used here for Newlands coal. The heating rate was assumed to be either 10^3, 10^4 or 10^5 K/s up to 1623K at a residence time of either 1.5 s or 150 ms. An Arrhenius expression can then be curve fitted from the predictions of the FG-DVC code to provide a devolatilsation rate. The rates and nitrogen mass fractions in the coal and volatiles are shown in Table 4.10. The predictions from FG-DVC show that as the heating rate is increased then more nitrogen is released with the volatiles and less is retained in the char.

The settings for the $\mathrm{NO_x}$ model are shown in Table 4.11. For the fuel NO route, the nitrogen partitioning was used from FG-DVC as shown in Table 4.10 and the assumption by Lockwood [212] was also used where it is assumed that the volatiles are converted directly to HCN before being oxidised to NO while the char is directly converted to NO. Following the conclusions from Section 4.3.1, the source terms in the $\mathrm{NO_x}$ model are computed *at the end of each time step* and ignored any sub-grid scale fluctuations (case *ii* (a)).

The axial velocity, gas temperature and oxygen concentration is shown for the devolatilisation rate of 10^3 K/s in Figure 4.24. A jet of air containing coal particles is injected in the central jet at $r = 0$ mm and is surrounded by an annulus of methane. The ignition of methane produces a high temperature region near the annuli of the burner and depletes the oxygen in this region. Further, coal particles are heated from the high temperature region and then devolatilsation and char combustion

NO Model	Model parameters
Thermal	O radical: equilibrium (Equation (4.13)) OH radical: partial equilibrium (Equation (4.15))
Prompt	Contribution from methane $n = 1$, $\phi_{eq} = 1$ in Equation (4.17) Contribution from volatiles $n = 2.98$, $\phi_{eq} = 1$ in Equation (4.17)
Fuel	$Y_{N,vol}$ and $Y_{N,char}$ in Equation (4.25) taken from Table 4.10 Lockwood route [212] : vol → HCN, char → NO $\alpha_{HCN} = 1, \beta_{NO} = 1$ $\alpha_{NO} = \beta_{HCN} = \alpha_{NH_3} = \beta_{NH_3} = 0$ in Equation (4.25)
N_2O	O radical: equilibrium (Equation (4.13))
Reburn	Kinetics for methane combustion (Table 4.3)

Table 4.11: Model set-up of the NO_x model for the CRIEPI case study.

occurs later in the flame, as shown by the devolatilisation and char source terms in Figure 4.25.

The predictions of the different devolatilisation rates on the mean and r.m.s particle velocities along the axis are shown against experimental data in Figure 4.26 and at the radial distances z = 60, 120 and 180 mm away from the burner in Figure 4.27. The experimental data was obtained using LDV and shadow Doppler particle analyser (SDPA), however minor differences were observed by the authors between the techniques and only the LDV results are presented [176]. It is found that there is a good agreement between the LES predictions and the experimental data close to the burner exit, but deviates from the experimental data further away from the burner for all of the devolatilisation rates tested.

When a higher devolatilisation rate is used, the volatiles are released faster which

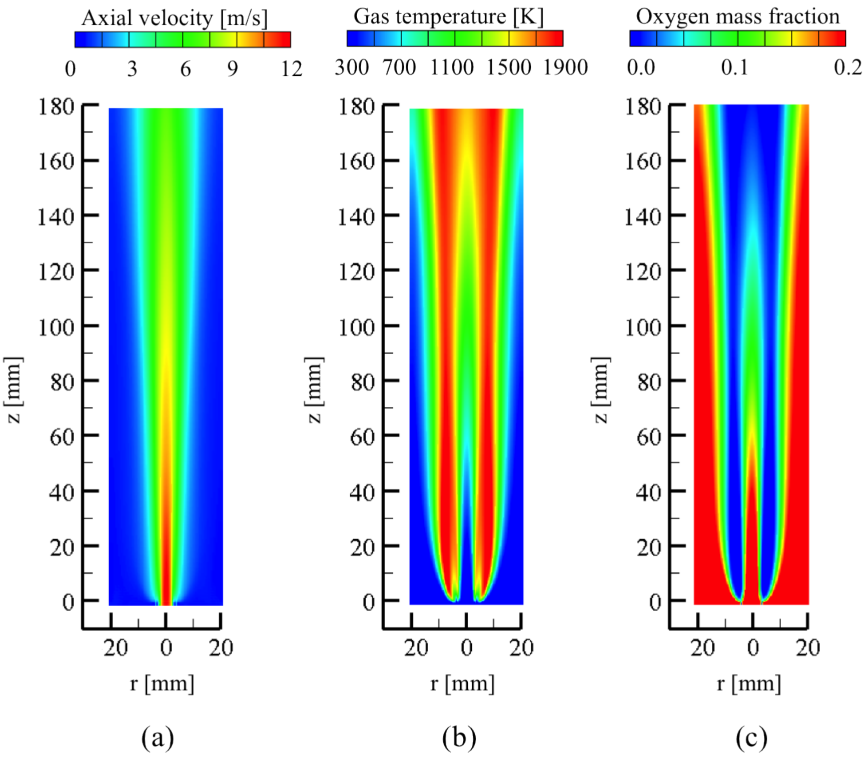

Figure 4.24: Contour plots of the (a) axial velocity, (b) gas temperature, and (c) oxygen mass fraction.

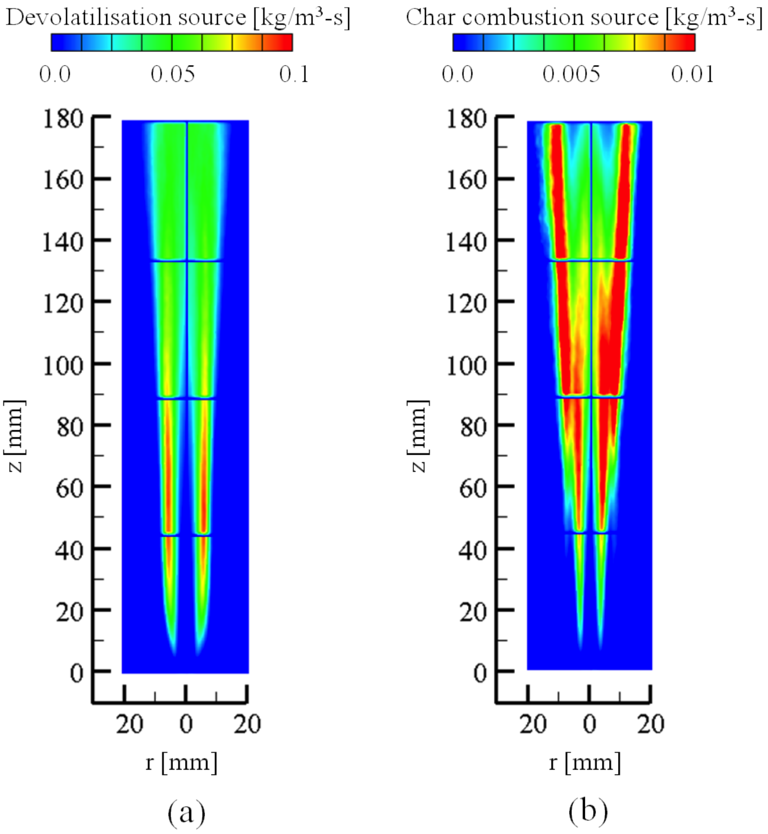

Figure 4.25: Contour plots of the (a) devolatilisation source term, and (b) char combustion source term.

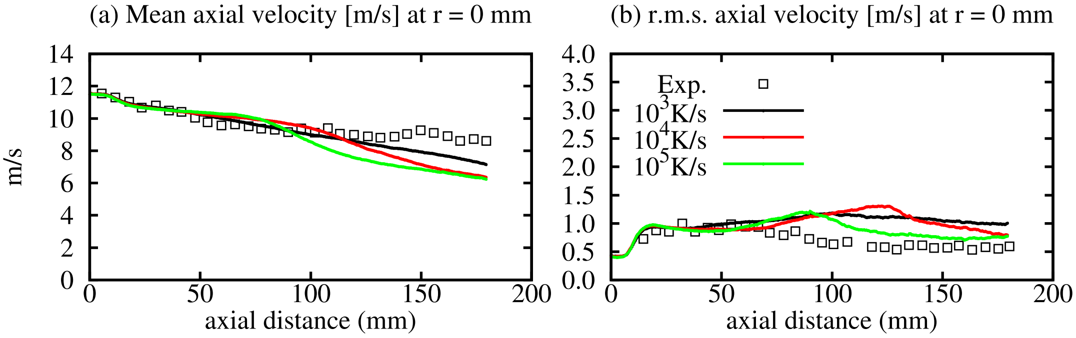

Figure 4.26: Comparison between experiments (symbols) and LES predictions for axial mean and r.m.s particle velocity along the axis.

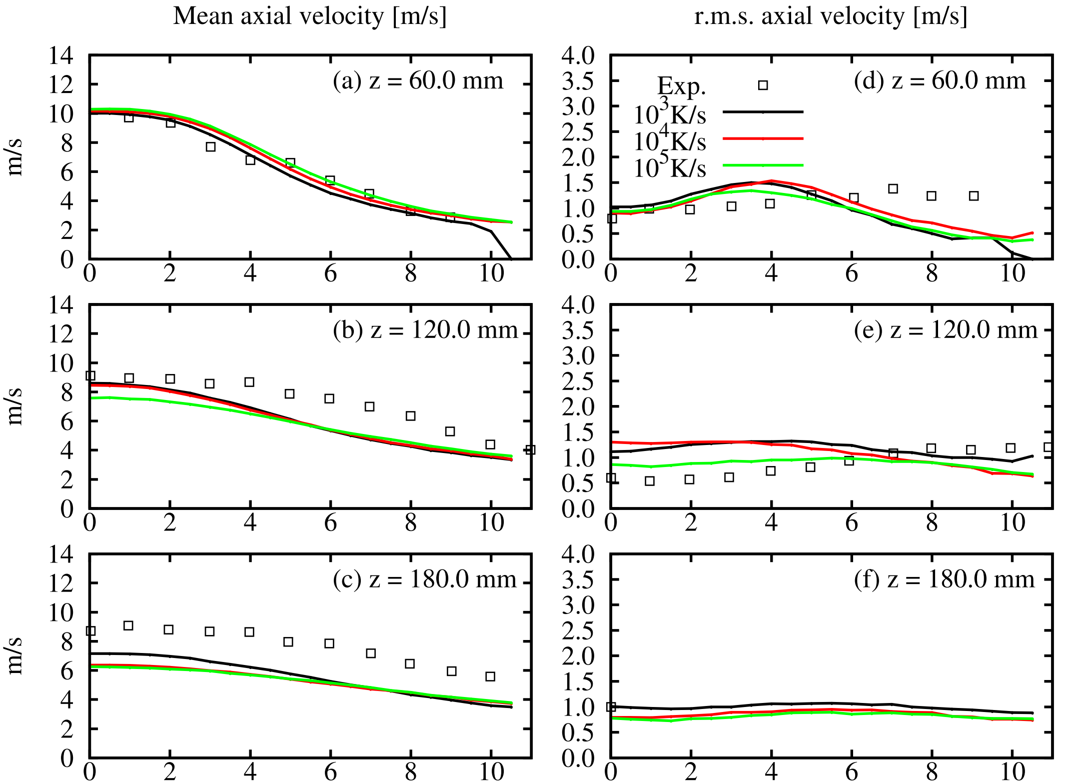

Figure 4.27: Comparison between experiments (symbols) and LES predictions for axial mean and r.m.s particle velocity at z = 60, 120 and 180 mm away from the burner.

then subsequently consumes the available oxygen releasing heat and producing CO_2 based on the eddy dissipation rate. From the predictions of mean O_2 and CO_2 concentrations, see Figure 4.28, it would appear that the rate of consumption for all of the devolatilisation rates are faster than those given in the experimental data. This suggests that either the volatiles are released too quickly or the rate of reaction governed by the eddy dissipation model is too fast or a combination of both. As suggested by Chen et al. [86], the empirical constants in the model may need to be altered between combustion problems, however a significant impact on the solution is seen by varying the rate of release of volatiles. In Figure 4.28(b) the oxygen is completely consumed along the axis of the flame for the higher devolatilisation rates of 10^4 and 10^5 K/s and as a consequence, more heat is released nearer to the burner which causes the particle temperature to increase as shown in Figure 4.28(a). However, when the oxygen is depleted, no further heat is added from the reaction and the particles cannot heat up any further. This occurs at $\approx$ 80 mm and $\approx$ 120 mm for the devolatilisation rates calculated for 10^5 K/s and 10^4 K/s, respectively, and observing those locations in Figure 4.26(a), the particle velocity is shown to decrease. Hwang et al. [177] suggested that the heat released from the gaseous phase may act to accelerate the particles in the experiments, a trend which appears to be observed in the simulations.

In Figure 4.28(a), a large discrepancy exists between the experimental data and the prediction from LES for particle temperature. The experimental technique employed measures the particle temperature by the authors was two-colour pyrometry. The measurement technique is based on line of sight and the authors suggested that the temperature can be strongly affected by soot and gaseous species [177]. The measurement is reported to occur along the axis of flame (at $r = 0$ mm), but interference may occur from hotter particles which would emit more radiation when the measurement is taken along a line of sight. Therefore, it can be assumed the particle temperatures in the measurements may not be along the axis of the

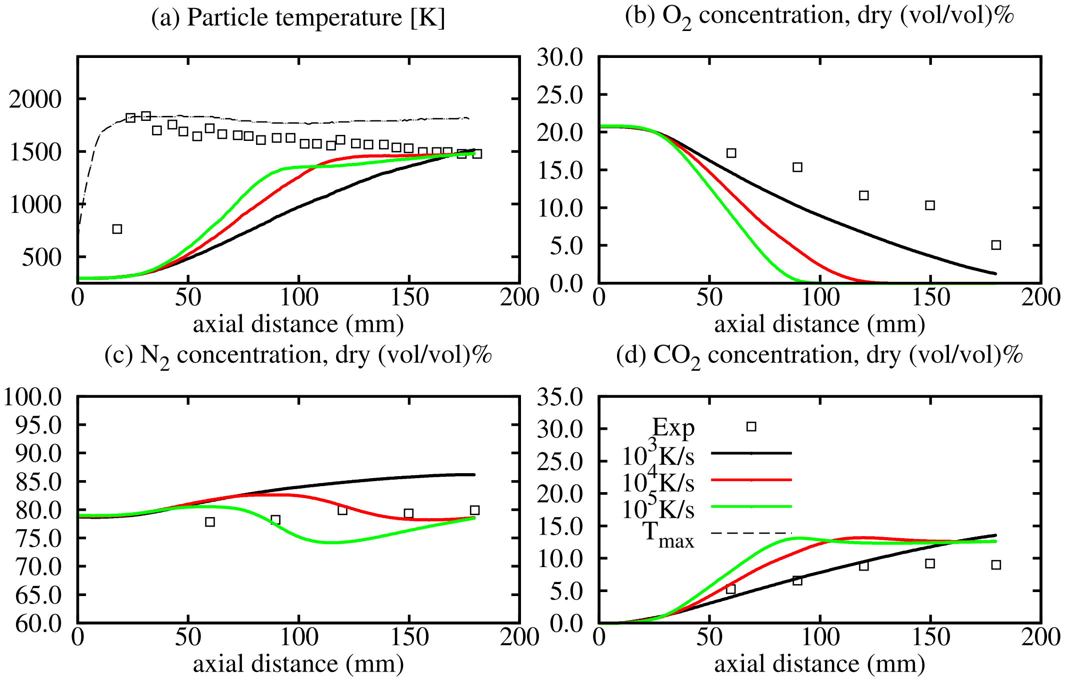

Figure 4.28: Comparison between experiments (symbols) and LES predictions for (a) particle temperature (b) dry O_2 volume fraction (c) dry N_2 volume fraction and (d) dry CO_2 volume fraction along the axis of the flame.

flame. Franchetti et al. [45] discussed the use of a weighted function with respect to temperature since the technique relies on radiation intensity which is a function of temperature to the fourth power. To illustrate the error that may occur when assuming the two-colour pyrometry technique measures the particle temperature along the axis of the flame, the particle temperature along the axis and the maximum particle temperature along a line of sight for the 10^3 K/s case (labelled T_{max}) are plotted in Figure 4.28(a). The T_{max} approach finds the maximum mean particle temperature at each axial distance from $r = 0$ to $r = 20$ mm. The T_{max} approach compares well with the experimental data, thus suggesting the values reported may not be exactly along the centreline of the flame, however the authors do note that this may be the case [177].

The prediction of the minor species (CO and NO) are compared against experimental data in Figure 4.29. It is observed that CO is significantly overpredicted,

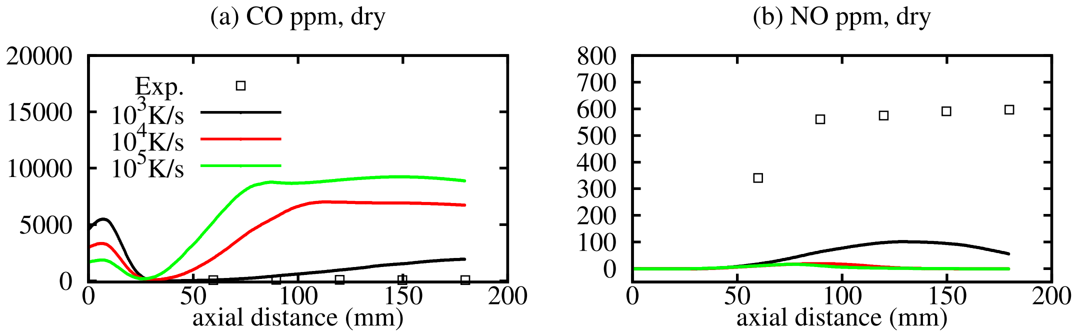

Figure 4.29: Comparison between experiments (symbols) and LES predictions for temperature and major species concentrations along the axis.

however the eddy dissipation model has been shown not to compare well with experimental data in other studies [111]. Further, the prediction of NO concentration is under predicted compared to the experimental data.

During devolatilisation, the model assumes the nitrogen containing species in the volatiles are evolved directly as HCN before being oxidised to NO and the rate of NO formation from char is directly related to the oxidation of the char. Therefore, the prediction of oxygen concentration, volatile release rate and char oxidation rate is important in modelling the rate of formation of NO. The rate of formation and destruction of NO for the different devolatilisation rates are shown in Figure 4.30. The rate of formation along the axis ($r = 0$ mm) decreases at approximately 100 mm and 80 mm for the devolatilisation rates of 10^4 K/s and 10^5 K/s. This is the same location as the complete consumption of oxygen shown in Figure 4.28(b), thus highlighting the dependency of NO formation on oxygen concentration. The source term for NO production and destruction when the devolatilisation rate of 10^3 K/s is used is shown in Figure 4.30(a), and when comparing with the oxygen distribution shown in Figure 4.24(c), shows a similar relationship.

To assess the impact of the contribution of each mechanism to the formation of NO, they can be considered separately. The following simulations consider the devolatilisation rates and nitrogen partitioning predicted from FG-DVC for the heat-

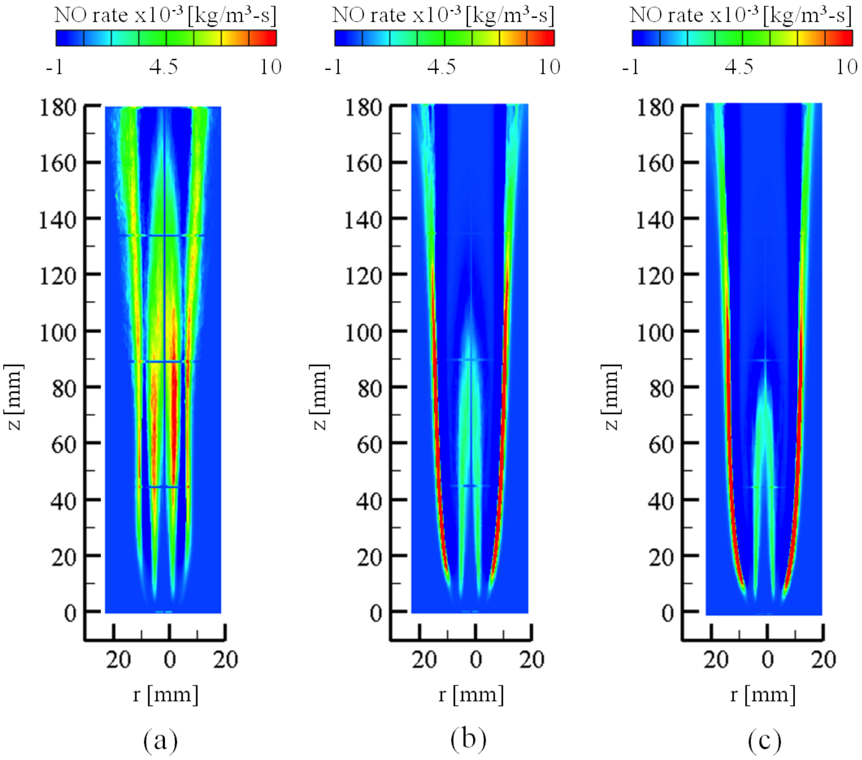

(a) (b) (c)

Figure 4.30: Source terms of NO for (a) 10^3 K/s, (b) 10^4 K/s, and (c) 10^5 K/s.

ing rate of 10^3 K/s as an adequate agreement was obtained with the experimental data for velocities, temperatures and major species concentrations. The rate is in contrast to 10^6 K/s suggested by the authors of the experiment [177]. The high value was assumed to occur from the heating of the coal particles from the methane flame, but since the flame is in an open environment, it is assumed that a lower heating rate may be present further away from the flame, thus justifying the lower heating rate parameters assumed in the simulation.

Influence of the mechanisms

The predictions of NO mass fraction and the source term when only the thermal, prompt and fuel mechanism are used are shown in Figures 4.31 and 4.32, respectively. It is clear that the dominant route of NO formation in coal combustion is through the fuel NO route which confirm similar conclusions to that proposed in the literature [184], whereas thermal and prompt NO mechanisms are shown to have little effect.

Thermal NO is formed in the high temperature zone surrounding the base of the flame where sufficient oxygen and nitrogen is available, but is further suppressed due to the limited oxygen concentration in the high temperature region. Prompt NO formation occurs in the fuel rich region of the flame where methane, nitrogen and oxygen exists in sufficient quantities. Due to the fast reaction rate of the eddy dissipation model, little prompt NO formation appears to occur from the volatiles and methane. The formation from the fuel NO mechanism occurs throughout the flame and produces a similar pattern to the char combustion rate shown in Figure 4.25(b). The volatiles are directly converted to HCN before being oxidised to NO and therefore sufficient oxygen is needed for this to occur. In oxygen depleted atmospheres, the HCN reduces to N_2, whereas in oxygen rich atmospheres HCN is oxidised to NO [59].

The pathway of conversion from coal-N to NO is still relatively unclear in the literature [184]. Therefore, different pathways can be assessed in the fuel NO mechanism to examine the impact on fuel NO formation.

Influence of routes

Two pathways have been considered for the conversion of volatile-N and char-N to NO. The first is that of Lockwood where volatile-N is converted directly to HCN before being oxidised to NO and char-N is directly converted to NO [212]. The second approach, known as the Smoot approach, where both volatile-N and char-N are converted directly to HCN before being oxidised to NO [213]. A third pathway was also tested where volatiles were converted to NH_3 and char was converted directly to NO. The results obtained using the three pathways are shown in Figure 4.33.

The main difference between the Lockwood and Smoot pathways is the fate of NO production from char. A lower mass fraction of NO is predicted when the Smoot pathway is compared to the Lockwood pathway along the axis and the results highlight the contribution of NO formation from the char.

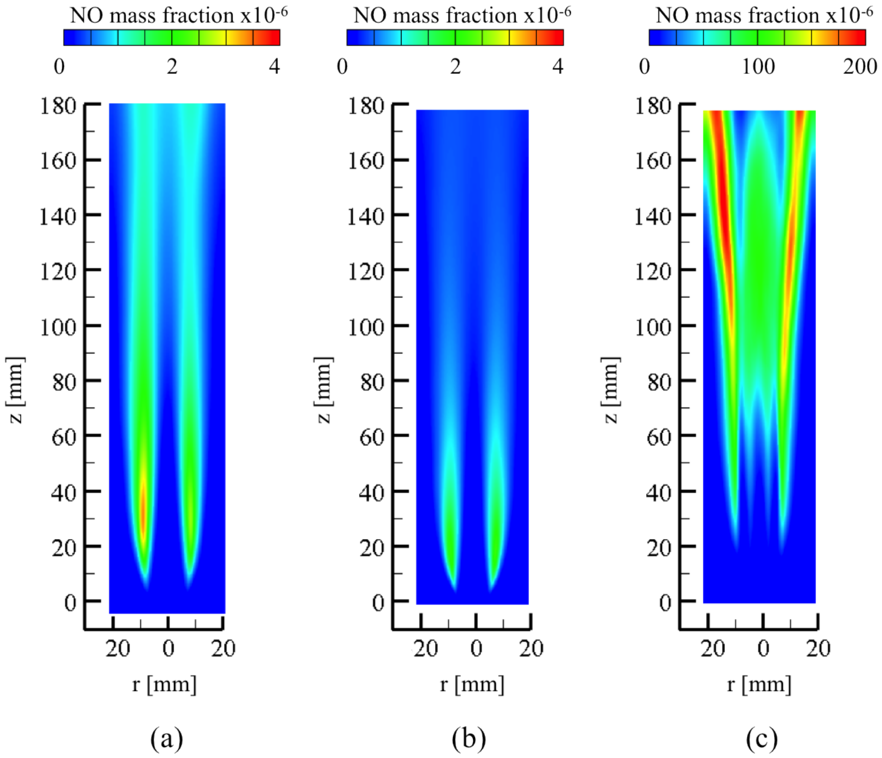

Figure 4.31: The mass fraction of NO when only the (a) thermal mechanism, (b) prompt mechanism, or (c) fuel mechanism is used.

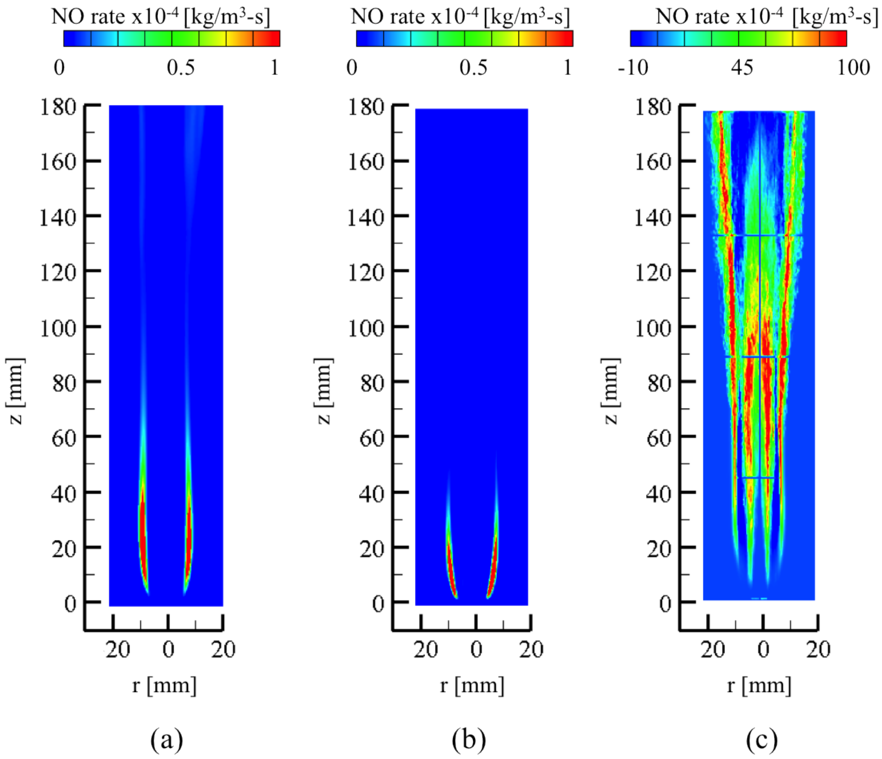

Figure 4.32: The source term of NO when only the (a) thermal mechanism, (b) prompt mechanism, or (c) fuel mechanism is used.

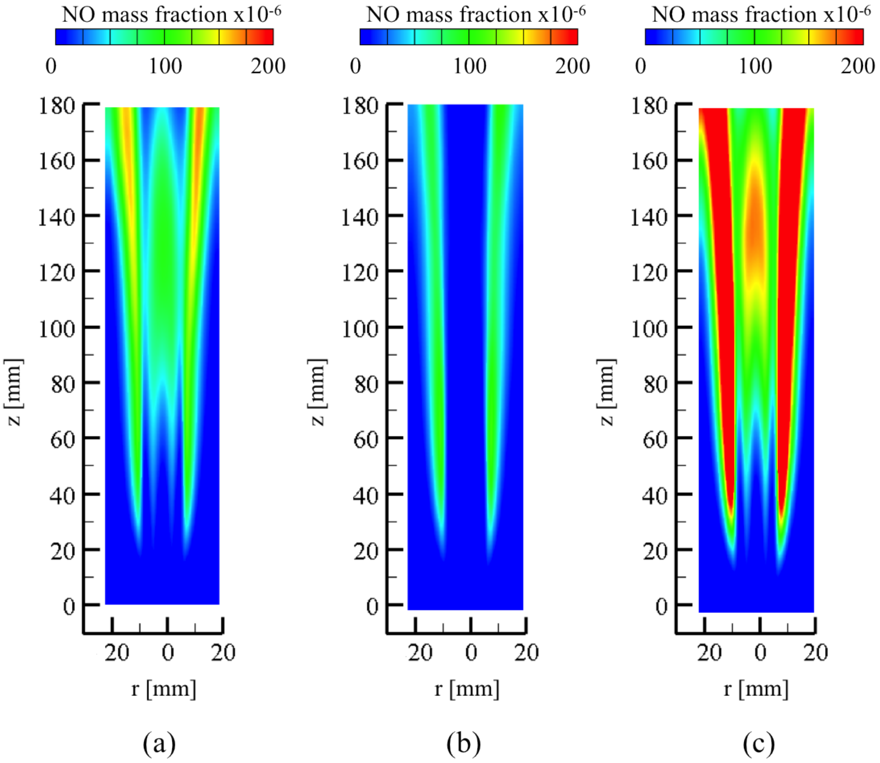

Figure 4.33: Mass fraction of NO for (a) vol → HCN, char → NO, (b) vol → HCN, char → HCN, and (c) vol → NH_3, char → NO.

The Lockwood mechanism with NH_3 as a precursor is shown in Figure 4.33(c), which shows an increase in NO formation compared to using HCN as a precursor from the volatiles. This suggests NH_3 is more readily oxidised to NO compared to HCN.

Summary

The NO_x model has been investigated for a coal-methane air flame and is an extension to the work performed by Imperial College [45]. It is found that the fuel NO mechanism has the most significant contribution to the formation of NO and the model has been shown to be sensitive to devolatilisation rate, char combustion rate and fuel NO pathway.

4.3.3 100 $\mathrm{kW_{th}}$ combustion test facility

In this section, the 100 $\mathrm{kW_{th}}$ combustion test facility is examined as described in Section 3.3. The results presented here only focus on the prediction of NO from the $\mathrm{NO_x}$ model, however the main flow features including temperature, oxygen and axial velocity are briefly described. The numerical set-up of the case was performed by Imperial College and is awaiting publication.

Numerical set-up

The numerical set-up of the case is described in Table 4.12. An equidistant cell size of 2 mm was used to represent the furnace with a size of $0.4 \times 0.4 \times 4$ m and immersed boundaries were used for the walls of the burner and furnace. The sub-grid viscosity was modelled using the standard Smagorinsky-Lilly model with a constant value of $C_{sgs} = 0.173$ [74, 75]. Devolatilisation was calculated using the single rate devolatilisation model [90] with the devolatilisation rate and high temperature volatile yield of 1.1 calculated from the CPD model [96]. The combustion of volatiles was modelled by the eddy-break up model for LES [221] and volatiles were assumed to be converted to CO before being oxidised to CO_2 by a second reaction. Other models included: the Baum & Street model [87] for char combustion and included char-O_2 and a char-CO_2 gasification reaction, the Discrete Ordinates model [149] for radiation with an expression for the absorption coefficient consisting of volatiles, O_2 and CO_2 and including the effects of particle radiation with a constant particle emissivity of $\epsilon_p = 0.85$.

The $\mathrm{NO_x}$ model included the thermal, prompt, fuel and reburn NO subroutines and the settings are described in Table 4.13. The nitrogen partitioning was taken from FG-DVC of the coal under a heating rate of 10^5 K/s up to a temperature of 1623K.

Model	Model parameter
Turbulence	LES, standard Smagorinsky-Lilly model with $C_{sgs} = 0.173$
Gas-phase chemistry	Eddy break up model with two step chemistry [221] $C_{2.60}H_{4.00}O_{0.87}N_{0.06}$ + 1.86 $O_2 \rightarrow$ 2.60 CO + 2.00 H_2O+ 0.03 N_2 CO + 0.5 $O_2 \rightarrow CO_2$
Char combustion	Baum & Street model [87] C(s) + $O_2\rightarrow$ CO $A = 0.005$, $E = -74000$ (J/mol-K) C(s) + $CO_2\rightarrow$ 2CO $A_r = 0.00135$, $E_a = -135500$ (J/mol-K) if $850 < T < 950$°C $A_r = 0.00635$, $E_a = -162000$ (J/mol-K) if $T \geq 950$°C
Devolatilisation rate	Single-step Arrhenius expression $(r = A_r T^{\beta} \exp(E_a/(RT)))$ $A_r = 4 \times 10^9$, $\beta = -0.9503$, $E_a = -10256.5278$, $R = 8.31$
Radiation	Discrete ordinates Constant particle emissivity $\epsilon_p = 0.85$ Absorption coefficient $\kappa = 0.2X_{vol} + 0.1\,(X_{\mathrm{CO_2}} + X_{\mathrm{H_2O}})$
Grid size	0.4 × 0.4 × 4.0 m
Cell size	2.0 mm equidistant cartesian grid
Momentum	Flux blended upwind and bounded central differencing scheme
Species	Total Variation Diminishing (TVD) scheme
Time-advance	Explicit third-order low storage Runge Kutta method
CFL number	0.4

Table 4.12: Model set-up for the Aachen case study.

NO Model	Model parameters
Thermal	O radical: equilibrium (equation (4.13))
	OH radical: partial equilibrium (equation (4.15))
Prompt	Contribution from volatiles
	$n = 2.6$, $\phi = 1$ in equation (4.17)
Fuel	$Y_{N,vol} = 1.24 \times 10^{-2}$ and $Y_{N,char} = 2.07 \times 10^{-2}$ in equation (4.25)
	Lockwood route [212] : vol → HCN, char → NO
	$\alpha_{HCN} = 1, \beta_{NO} = 1$
	$\alpha_{NO} = \beta_{HCN} = \alpha_{NH_3} = \beta_{NH_3} = 0$
	in equation (4.25)
Reburn	Kinetics for methane combustion (Table 4.3)

Table 4.13: NO_x model set-up for the Aachen case study.

Results

Instantaneous snapshots of axial velocity, gas temperature and oxygen mass fraction are shown in Figure 4.34. The primary air and swirled combustion air delivers the coal into the quarl before the furnace section. The region in the quarl is fuel-rich and ignition occurs and consumes all of the available oxygen. The staging stream is seen at $r = 200$ mm which delivers the rest of the combustion air to the flame and allows the rest of the available fuel to oxidise and this causes an increase in the temperature shown further from the burner. Further, devolatilisation and char combustion rates are shown in Figure 4.35 which shows that most of the devolatilisation is predicted to occur in the quarl region.

The comparison of mean axial velocity, temperature and oxygen concentration against experimental data is shown in Figures 4.36, 4.37 and 4.38, respectively. The axial velocity at all positions compare well with the experimental data ensuring the flow field is adequately captured. The gas temperature profiles are also predicted within a reasonable accuracy with the experimental data. However, there is a dis-

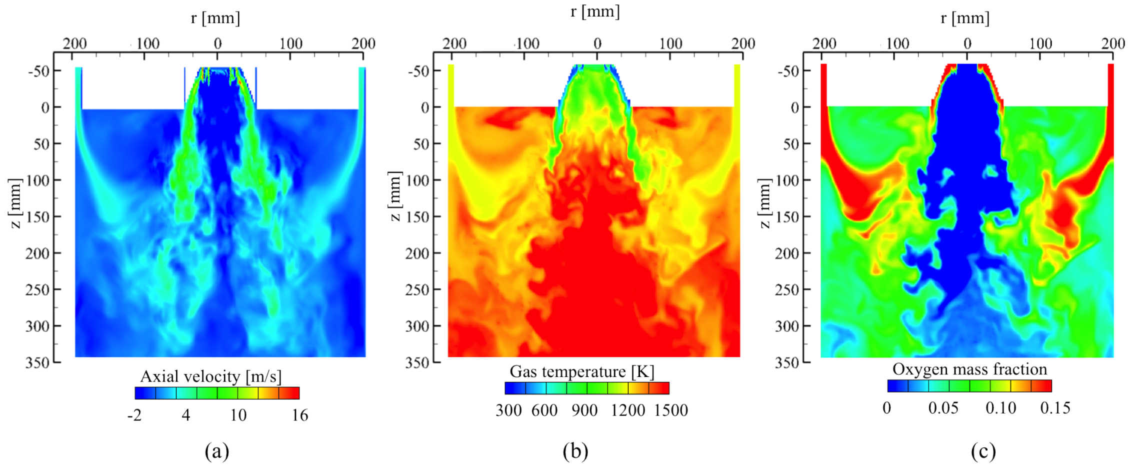

Figure 4.34: Instantaneous LES prediction of (a) axial velocity, (b) gas temperature, and (c) oxygen mass fraction.

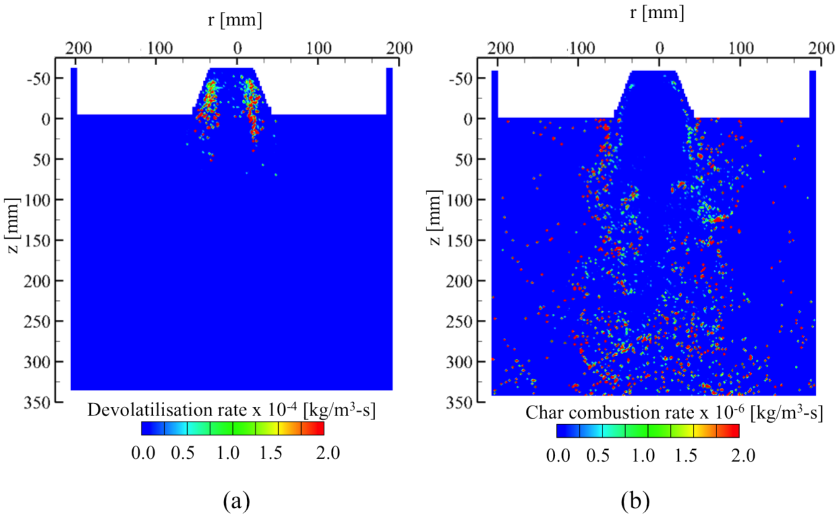

Figure 4.35: Instantaneous LES prediction of (a) devolatilisation rate, and (b) char combustion rate.

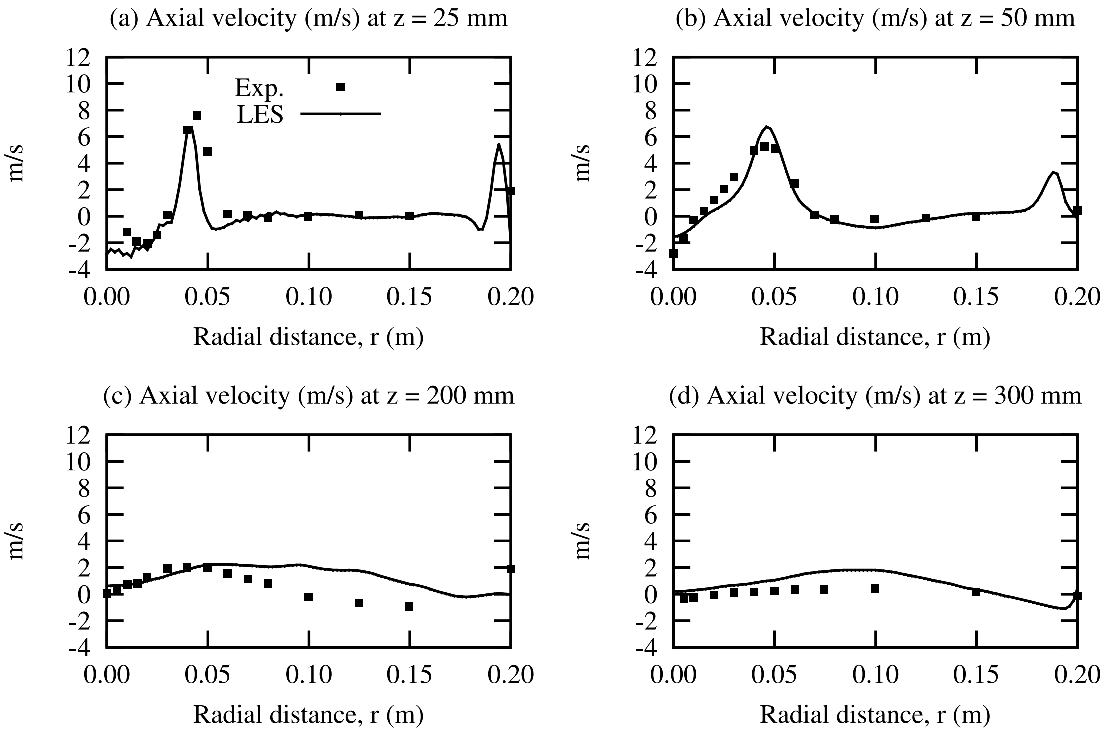

Figure 4.36: Experiment (symbols) and LES (line) of axial velocity.

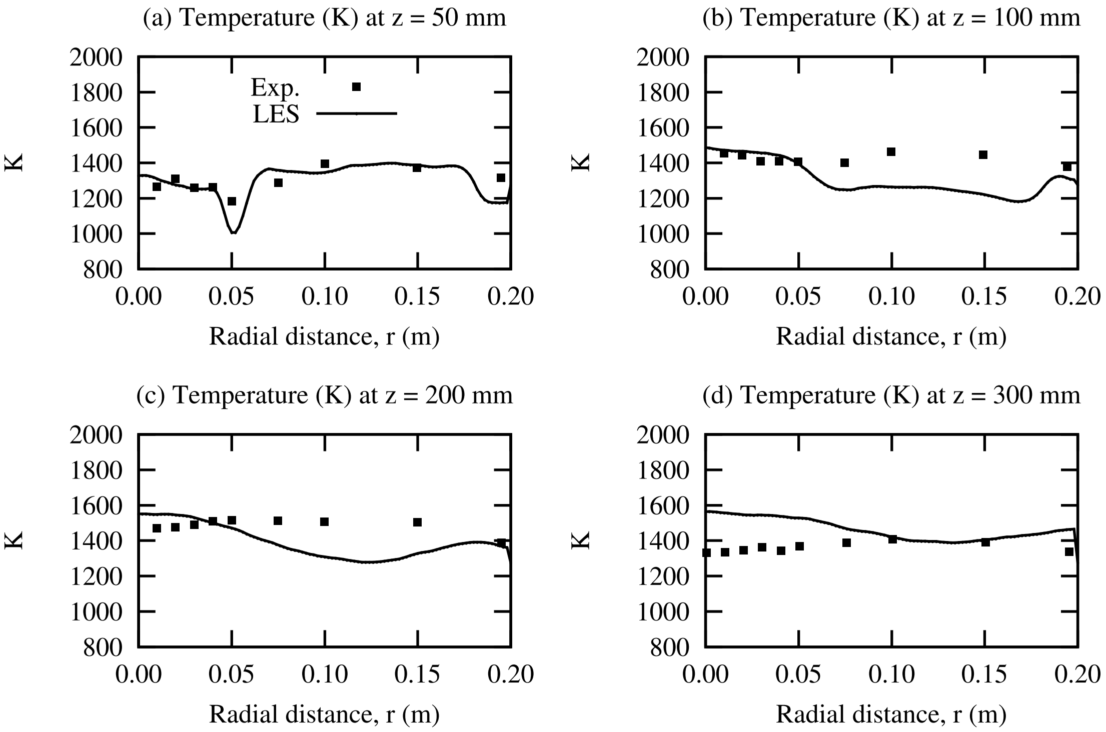

Figure 4.37: Experiment (symbols) and LES (line) of the temperature.

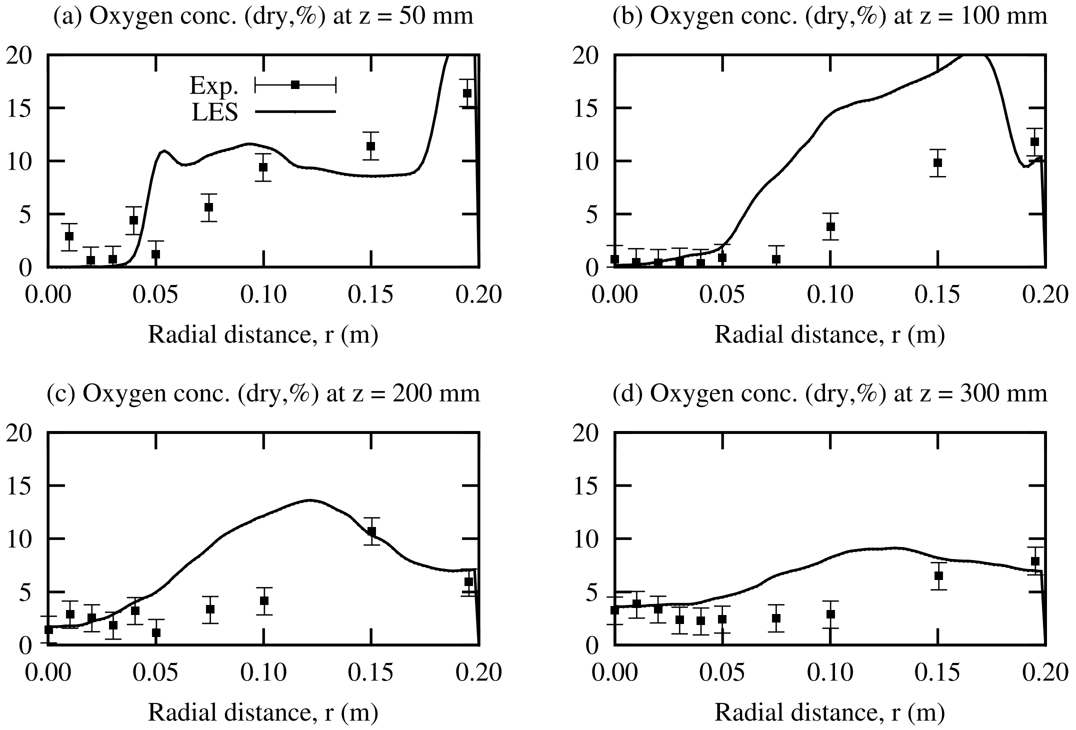

Figure 4.38: Experiment (symbols) and LES (line) of dry O_2 mole percent.

crepancy of 100 K further away from the burner at $z = 200$ and $z = 300$ mm. The experimental technique used to measure the gas temperature is an intrusive suction pyrometry and this could distort the flame. The probe draws in gas at a high velocity over a thermocouple to measure the temperature, but this measurement will be a volume average rather than a single point measurement. The volume is difficult to accurately measure and include in an experimental error, however an IFRF report suggests that the measured gas temperature could be considered as a spherical volume with a radius of 2.5 cm [222]. Therefore the temperature measurements are volume-average predictions rather than point measurements.

The oxygen concentration near the centreline of the furnace ($r < 0.05$ m) for the different locations appear to give a reasonable comparison with the experimental data. However, away from the centreline, the LES predictions deviate from the experimental data more significantly. The simplicity of the chemistry in the eddy break-up model may be the cause of the difference, however the probe used in the gas species measurements is also intrusive and will represent a volume measurement rather than a single point. The consumption of oxygen being an indication of the reaction rate, and therefore the heat release, may further explain the differences seen in the gas temperature predictions.

Despite the simple chemistry assumption, the LES simulation compares adequately with the experimental data and allows for an examination of the $\mathrm{NO_x}$ model to be performed.

$\mathrm{NO_x}$ model predictions

The $\mathrm{NO_x}$ model was solved at the end of every time step. The instantaneous plots of NO mass fraction, HCN mass fraction and the source term of NO are shown in Figure 4.39. The rate of formation is seen to occur in regions of high temperature and sufficient oxygen, where the flame front may exist. In the quarl zone, a high concentration of HCN is present which is from the devolatilisation of the coal. The HCN subsequently oxidises to NO in regions where O_2 is present. Further, the staging stream provides the oxygen and creates a recirculation zone between $r =$ 0.045 m and 0.2 m which distributes the concentration of NO in this region. The combustion of char will then contribute to the rest of the NO production further away from the flame.

To further understand the contribution of each of the models on NO formation, the instantaneous rates of thermal, prompt, fuel and reburn NO are shown in Figure 4.40. The inlet oxidiser consists only of O_2 and CO_2 and therefore nitrogen is only assumed to occur from the fuel mechanism when NO or HCN is reduced to N_2. Nitrogen is therefore solved as an extra transport equation in the $\mathrm{NO_x}$ model and this helps to examine the influence of the thermal and prompt mechanisms. When nitrogen is excluded, the source terms of the thermal and prompt mechanisms are zero. The rate of formation and destruction of thermal and prompt mechanisms are shown in Figures 4.40(a) and (b) and when compared to the fuel and reburn

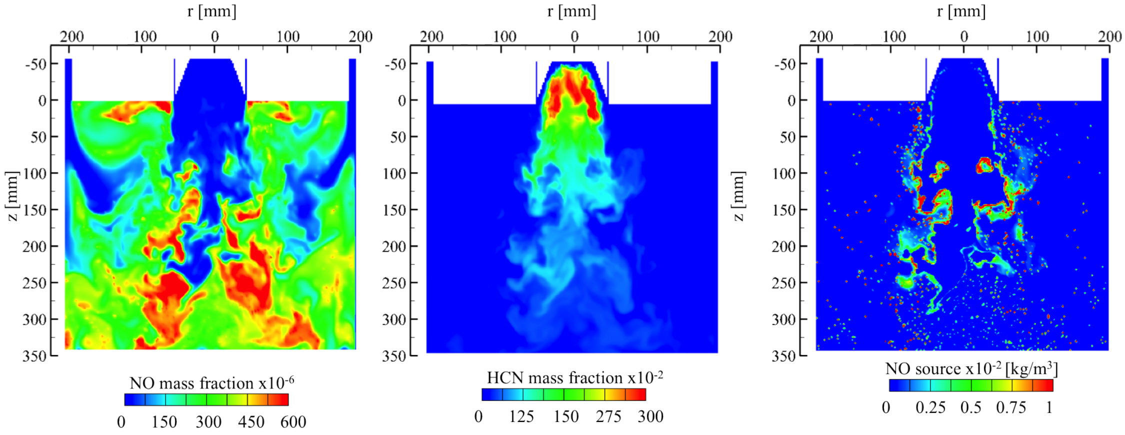

(a) (b) (c)

Figure 4.39: Instantaneous LES predictions of (a) mass fraction of NO, (b) mass fraction of HCN (c) source term of NO.

mechanisms, shown in Figures 4.40(c) and (d), the thermal and prompt source terms are several orders of magnitudes lower than the fuel and reburn source terms. The main mechanisms in oxy-fuel combustion are therefore the fuel mechanism followed by the reburn mechanism.

The fuel mechanism source term is shown in Figure 4.40(c) which shows the total rate of formation and destruction of NO and HCN. A strong rate of formation occurs in the quarl region where HCN from the volatiles are released. The destruction of HCN by the fuel mechanism causes a negative rate near the centre of the furnace.

The reburn rate in Figure 4.40(d) shows the destruction of NO produced in the quarl region as the high concentration of volatiles reduce with any NO formed in this region. It should be noted that the rates used for the reburn reactions are for methane and may not be entirely accurate, but the figure demonstrates that the model behaves as expected. It is expected that this may have more of a dominant effect when recycled flue gas is used since NO will be directly introduced into this region of the flame [129].

The predictions of NO are compared with the experimental data in Figure 4.41. There are some clear differences between the model predictions and the experimental data, however the overall concentrations at each location is similar. The differences

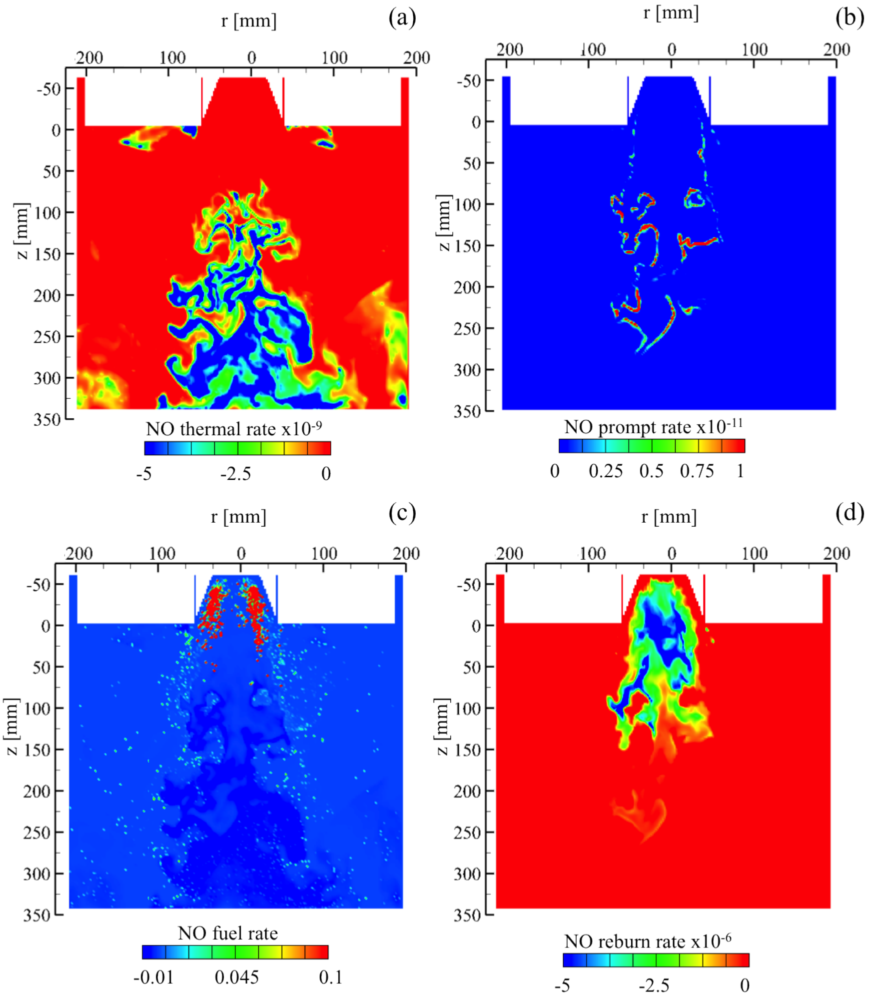

Figure 4.40: Instantaneous LES predictions of rates of (a) thermal, (b) prompt, (c) fuel, and (d) reburn mechanisms in kg/m^3-s.

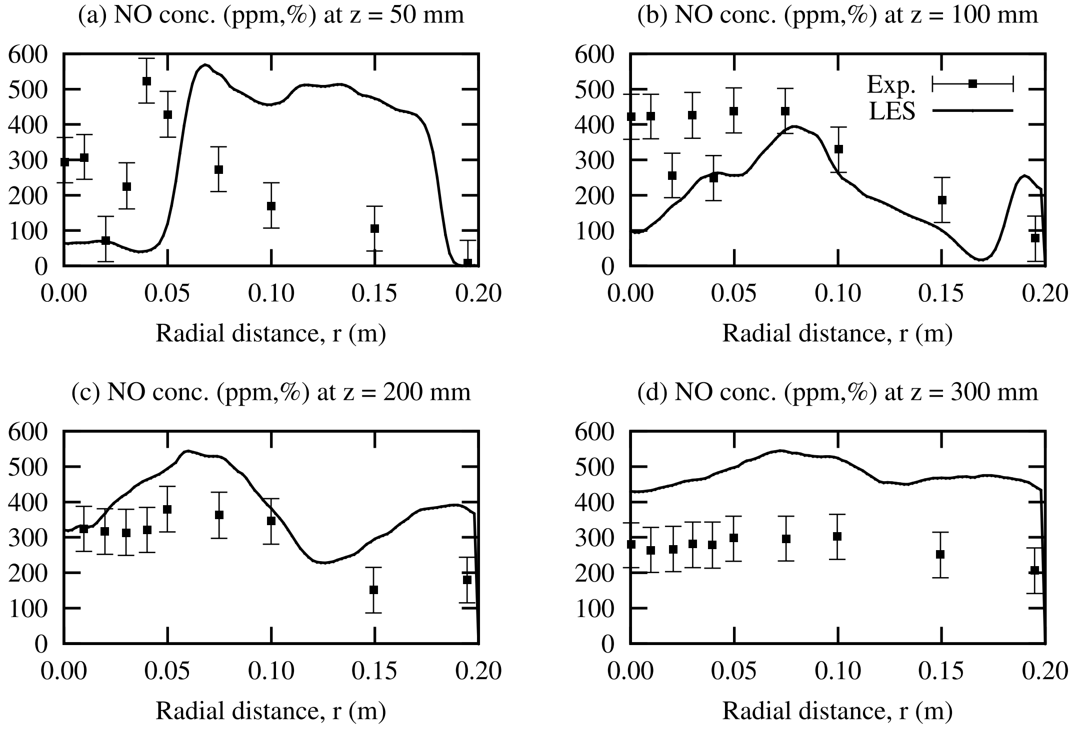

Figure 4.41: Experiment (symbols) and LES (line) of NO mole percent.

in oxygen concentration and temperature clearly have an impact on the predictions. For example, at $z = 50$ mm, the temperature predictions are reasonable, but the oxygen concentration deviates from the experimental data in a similar trend to the prediction of NO.

Summary

The NO_x model has been successfully implemented into a LES for an oxy-fuel 100 kW_{th} test facility. As shown in Section 4.3.2 with the CRIEPI burner, the NO_x model is very sensitive to the parameters in the fuel mechanism compared to other mechanisms. However, the NO_x model can give an indication of the levels of NO present in an oxy-fuel flame and that the main contribution is from the fuel and reburn mechanisms.

4.4 Conclusions

In this chapter, a NO_x model that is suitable for air-gas, air-coal and oxy-coal combustion has been implemented into an in-house LES code. The NO_x model has been validated against an air-methane flame where sensitivity studies of grid resolution and domain sizing have been performed. Two types of techniques were examined which investigated the influence of turbulent chemistry interactions. The first is analogous to the method used in steady RANS, where the formation of NO was calculated after the LES had statistically converged and was computed *at the end of the simulation* whereas the second approach was calculated *at the end of each time step.* The NO_x model was tested against a coal-methane flame and an investigation into devolatilisation rates and nitrogen partitioning was performed. The NO_x model was also incorporated into a LES of a combustion test facility firing coal under oxy-fuel conditions.

The NO_x model is similar to that implemented in the commerical software, Ansys fluent which is used in Chapters 5 and 6. Therefore, the findings from this chapter can be used in other CFD simulations in the following chapters.

The main findings are summarised as follows:

- The main contribution of NO formation in air and oxy-fuel flames was from the fuel NO mechanism, and careful selection of parameters in this mechanism are necessary for an accurate prediction of in-flame NO. The reburn NO mechanism was also shown to be important in the reduction of NO in the fuel-rich region in oxy-fuel combustion.

- In fuel-rich regions, the choice of O radical is important and should be selected from a detailed database, such as a flamelet table, where possible.

- When the formation of NO is calculated *at the end of each time step* rather than *at the end of the simulation*, the majority of turbulent chemistry interaction (TCI) is resolved by the LES. Furthermore, when a sufficiently fine mesh is used, turbulent scales are resolved at a small enough length scale that the impact of sub-grid scale fluctuations on the solution becomes less important. As a consequence, the filtered density function (FDF) representing the sub-grid fluctuations, becomes less significant on the prediction of NO. However, when calculating the formation of NO *at the end of the simulation*, in a manner analogous to a steady RANS approach, a probability density function (PDF) is required to account for the TCI.

In conclusion, the NO_x model was successfully implemented into the in-house LES code, *PsiPhi* and achieved adequate predictions of in-flame NO for three different simulations of experimental studies.

Chapter 5

Modelling of air and oxy-coal combustion in a pilot-scale 250 kW$_{\text{th}}$ combustion test facility

In this chapter, CFD simulations are performed on the 250 kW$_{\text{th}}$ PACT facility described in Section 3.4. CFD simulations are compared against experimental measurements for air-coal combustion with and without preheat combustion air, named *air* and *air-preheat*, respectively. The validated CFD simulations are then used to perform a numerical investigation of oxy-coal combustion.

The geometry of the burner and furnace of the 250 kW$_{\text{th}}$ PACT facility is complex, but may be simplified in order to reduce the computational cost of the CFD simulation and this is explained in Sections 5.1.1 and 5.1.2. The effects of mesh refinement on the solution is examined in Section 5.1.3 to ensure mesh independent results and the treatment of turbulence and gaseous radiative property models are investigated for the *air* cases in Sections 5.2 and 5.3, respectively. Experimental data is available for air-coal combustion to validate the CFD models used in Sections 5.1.1 - 5.3.

Following the CFD validation in air-coal combustion, a summary of the findings is presented in Section 5.4. The models are then applied to numerically examine the effects of oxy-coal combustion in Section 5.5 and a comparison between two gaseous radiative property models is also examined to demonstrate the differences in the prediction of radiative heat transfer at the furnace wall.

The novelty in this chapter includes the CFD modelling of the furnace and providing a CFD set-up for the validation of an advanced radiative property model.

5.1 Numerical set-up

CFD simulations are a valuable tool to provide insight into a particular problem, however are prone to errors from numerical schemes, mesh resolution, geometry simplifications, boundary conditions and choices in the treatment of turbulence, heat transfer and chemistry. To obtain some confidence in a CFD prediction, sensitivity studies and comparisons with experimental data can be performed.

Performing a CFD simulation requires the generation of a mesh describing the fluid region around or inside a particular geometry. Advances in meshing capabilities means that complex geometry can be easily described but usually with a large number of mesh cells, requiring more computational power and simulation time to calculate the CFD solution. A full-scale utility boiler will contain water walls, superheaters, reheaters, economisers and about 50 burners may exist. The length scales present in the boiler will range from a few millimetres in the burner to the order of 50 m. Therefore, a large number of cells will be needed to mesh a boiler requiring a high computational cost to produce a CFD solution, which is not practical when a number of sensitivity studies need to be performed in order to obtain some confidence in the CFD predictions and so simplifications of the geometry are usually necessary.

Due to the complexity of the burner and the number of ports on the furnace of the 250 $\mathrm{kW_{th}}$ CTF, the burner and facility was simplified. The full 3D CAD drawings, full 3D mesh and 3D periodic mesh, representing one quarter of the facility and burner are shown in Figure 5.1. The simplifications are discussed separately for the burner and furnace in Sections 5.1.1 and 5.1.2, respectively.

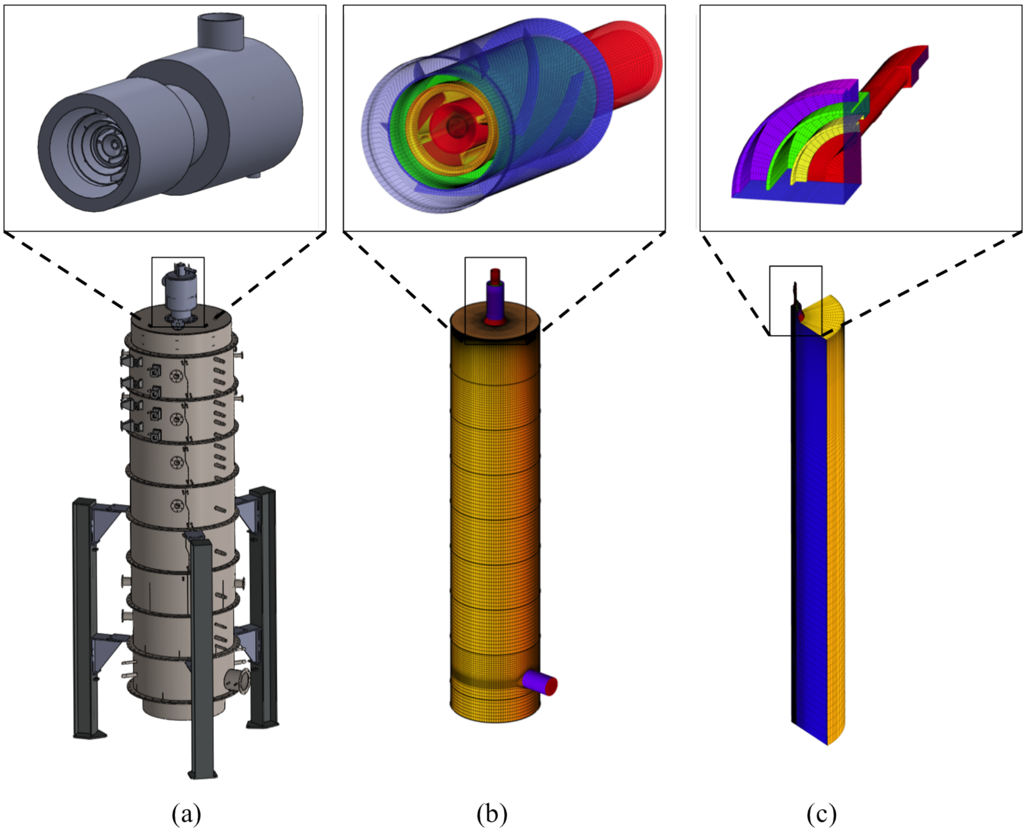
(a) (b) (c)

Figure 5.1: Burner and furnace (a) CAD drawings, (b) simplified full 3D mesh, and (c) simplified periodic mesh.

5.1.1 Burner simplification

The Doosan Babcock low-NO_x burner rated at 250 kW_{th} and installed in the PACT facility is shown in detail in Figure 5.2. The burner is designed to lower the formation of NO_x in the burner zone through controlled mixing of the fuel and oxidiser. The production of NO_x usually occurs in the hottest part of the flame when sufficient oxygen is available. In general, for a low-NO_x burner, a fuel rich/lean staging is used where a central fuel-rich region near the burner is created to minimise NO_x production and an outer fuel-lean region is created usually by means of a swirling flow to provide sufficient oxygen for burnout. In this burner, this can be achieved by limiting the amount of primary air to create a central fuel-rich region while the rest of the combustion air is delivered through the outer secondary and tertiary registers.

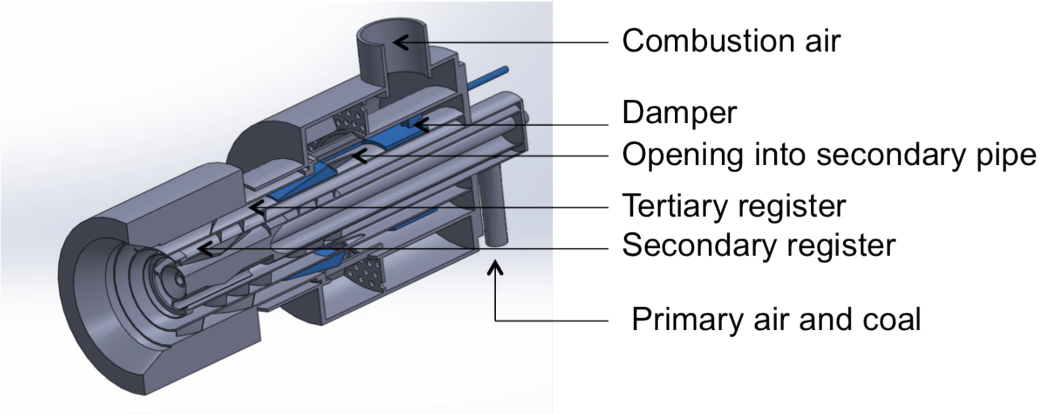

Figure 5.2: CAD cross section of the 250 $\mathrm{kW_{th}}$ Doosan Babcock burner.

The burner has three registers, named primary, secondary and tertiary. The primary register carries the coal and some combustion air into the furnace while the rest of the combustion air enters the burner into a wind box and a damper is used to control the flow to the secondary and tertiary registers. The use of the damper allows the length and shape of the flame to be controlled as well as $\mathrm{NO_x}$, CO and burnout.

The damper consists of a wedge shape which slides over the pipe of the secondary register. The wedge shape can block the tertiary register completely when fully pushed into the burner thus preventing any combustion air entering the tertiary register. Also, four equally spaced triangular openings are present on the secondary pipe to allow air to flow into the secondary register. Therefore when the damper is fully pushed in, the combustion air flows entirely into the secondary register. As the damper is pulled out of the burner, the damper slides over the triangular openings, thus limiting the combustion air into the secondary register and opens up an area for combustion air to flow into the tertiary register.

The ratio between the secondary and tertiary registers will be referred to as the

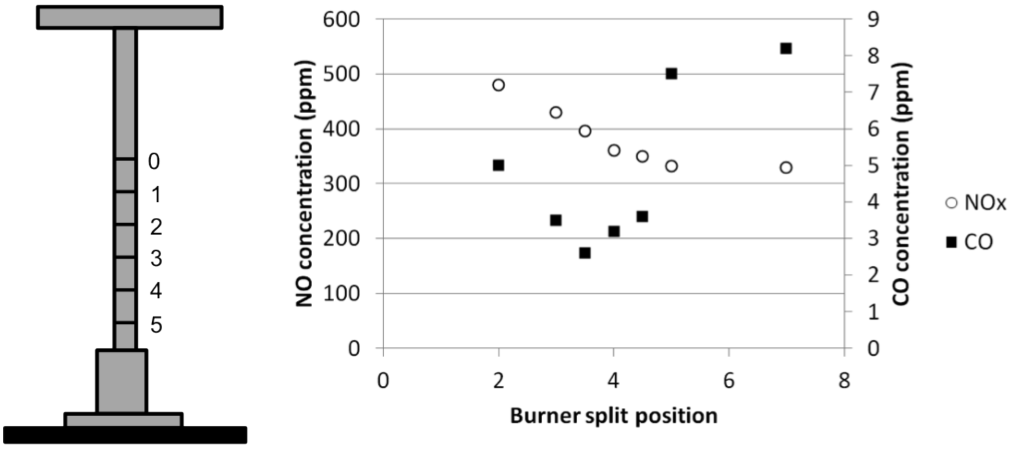

Figure 5.3: Schematic of damper level and positions, experimental exit compositions of NO_x and CO.

burner split and will be defined by

$$S_{sec,ter} = \frac{S_{mfr}}{T_{mfr}} \tag{5.1}$$

where S_{mfr} and T_{mfr} represents the mass flow rate in the secondary and tertiary registers, respectively, downstream of the damper. The burner split is an important parameter in the burner design, that needs to be optimised to control the NO, CO and burnout. To investigate the effect of damper position on NO and CO at the exit of the furnace, the damper lever was moved out of the burner in increments of 10 mm from position 0 (where the damper is fully inserted into the burner). The positions numbers $1, 2, 3, ...$ correspond to $10, 20, 30...$ mm from the fully inserted position. Experimental results from the air-preheat case are shown in Figure 5.3 along with the position and location of the damper lever.

Due to the complex geometry inside the burner, the geometry can be greatly simplified if only the primary, secondary and tertiary registers are considered ignoring the damper and wind box. Therefore, tetrahedral cells can be avoided and a hexahedral structured mesh can be obtained. Figure 5.1(b) shows a full 3D mesh including swirl veins, coal collectors and flame holder. There are four coal collectors that are located in the primary annulus at the exit of the burner and if the swirl veins are ignored (3 in the primary, 3 in the secondary and 6 in the tertiary) and instead represented by a swirl number, the burner is 90° periodic, as shown in Figure 5.1(c). In the experiments, the position of the damper was chosen to be position 3.5 for the air case and position 4 for the air-preheat case due to the relatively low NO and CO values obtained compared to other positions. Unfortunately, the position does not give an indication of the split between the secondary and tertiary registers defined in Equation (5.1) and therefore a preliminary detailed CFD simulation of the entire burner was performed to determine the burner split.

A coarse and fine mesh were used of the entire burner in each case to ensure grid independent solutions. In the air-case, two tetrahedral meshes of 4.8 m (coarse) and 12.9 m cells (fine) were used with inflation layers at the wall created in Ansys ICEM. In the air-preheat case, two multi-block meshes with conformal interfaces were used of sizes 1.5 m (coarse) and 11.0 m cells (fine) created in Ansys Mesher 14.5.7 with tetrahedral cells and an inflation layer on the walls surrounding the damper and wind box region and hexahedral cells were present in the rest of the domain. The refinement between the coarse and fine mesh was mainly in the tetrahedral regions surrounding the damper. At the time of the mesh generation of the full burner for the air case, a multi-block mesh was desired to reduce the cell count and Ansys Mesher 14.0 was initially tested but failed to produce a conformal mesh, whereas ICEM proved to be more robust. Details of the experiment from the air-preheat case were available after the examination of the air case. At this time, Ansys Mesher 14.5.7 was available which had a number of improvements to the multi-block algorithm and was able to produce a conformal mesh.

For the entire burner model in this section, a standard k-ε turbulence model was

	air	air-preheat
mass flow rate (kg/s)	6.761×10^{-2}	6.757×10^{-2}
combustion air temperature (°C)	23.2	255.0
species	air	air
damper position	3	4

Table 5.1: Boundary conditions for the burner split study of air and air-preheat cases.

used with standard wall functions. The k-ε realisable model was also tested but made little difference to the results. The boundary conditions are listed in Table 5.1 and a mass flow rate and pressure outlet were used for the inlet and outlet boundary condition, respectively.

The velocity magnitude for a cross section of the burner for the air-preheat case is shown in Figure 5.4. Air enters through the combustion air inlet before being distributed by diffusion holes. The air passes either through an annuli between the outer tertiary pipe and damper into the tertiary register or through the triangular holes into the secondary register. It is noted in Figure 5.4 that the primary register was not included in the simulation as it would not effect the secondary and tertiary registers. Furthermore, the swirl veins were not included as the focus was on the split of flow caused by the damper, this also helped to reduce the computational cost.

The CFD predictions of mass flow rates at the outlet of the secondary and tertiary registers are displayed in Table 5.2. In both cases, there is little difference in the results observed between the meshes and therefore the solution is grid independent. For the air case (position 3), the split is 0.923 and for the air-preheat case (position 4), the split is 0.823. As the damper is moved outwards, a larger opening is present in the tertiary and the opening for the secondary reduces. Therefore, more air is

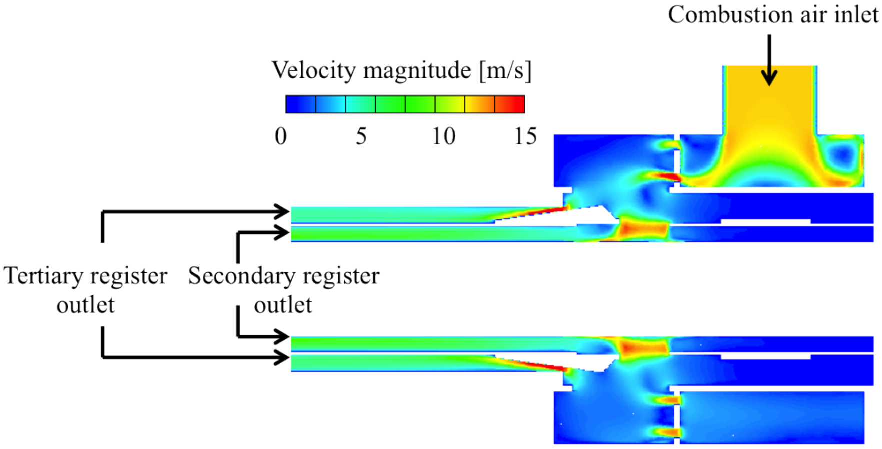

Figure 5.4: Velocity magnitude of a cross section of the burner when the damper is in position 4 for the air-preheat case.

	air	air-preheat
coarse mesh	4.8 m cells	1.5 m cells
secondary (kg/s)	3.267×10^{-2}	3.054×10^{-2}
tertiary (kg/s)	3.539×10^{-2}	3.708×10^{-2}
fine mesh	12.9 m cells	11.0 m cells
secondary (kg/s)	3.267×10^{-2}	3.054×10^{-2}
tertiary (kg/s)	3.539×10^{-2}	3.708×10^{-2}
split, $S_{sec,ter}$ in Equation (5.1)	0.923	0.823

Table 5.2: Results for burner split of air and air-preheat cases.

delivered through the tertiary as the damper position is increased. The split can now be used as a boundary condition in the simplified geometry for the mass flow rates of the secondary and tertiary registers.

5.1.2 Furnace characterisation

The inside of the refractory wall has a number of holes, as shown in Figure 5.1(a), which are used for optical and intrusive access into the furnace during experimentation. If the inside of the furnace is assumed to be a closed cylinder of 0.9 m in diameter, the internal surface area of one section, which each has a height of 0.5 m,

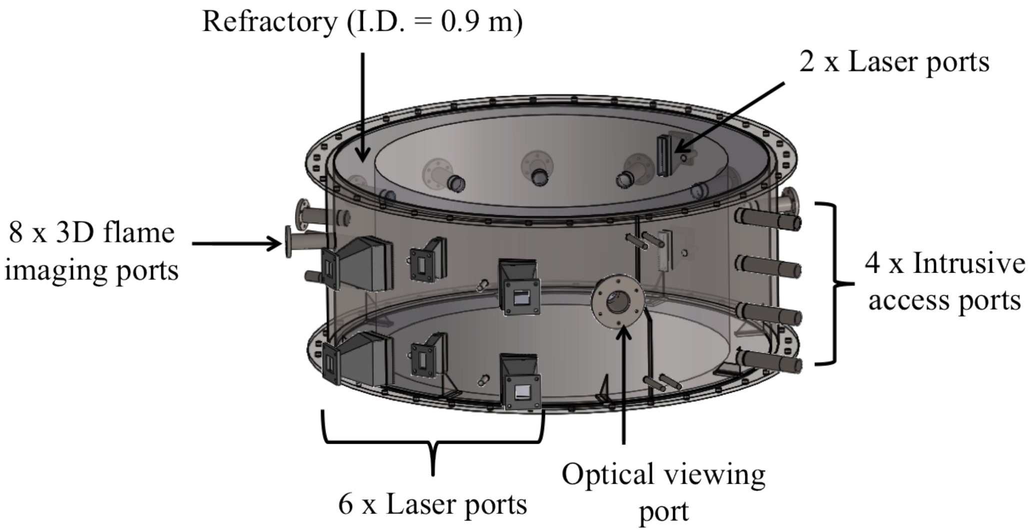

Figure 5.5: CAD drawing of the refractory lining and experimental ports for section 1 of the furnace.

would be 1.414 m^2. In the first two sections, the refractory has been cut to allow access for 8 laser ports, 8 3D imaging ports, 4 intrusive access ports and an optical viewing port. The total surface area cut away from inside of the refractory of the furnace is therefore approximately 0.057 m^2 for each of the two sections as computed by the CAD drawing in Figure 5.5. This is equivalent to a 4% reduction of refractory lining to give an internal surface area of 1.357 m^2. The other 6 sections in the furnace do not have laser or 3D flame imaging ports and only contain about 4 intrusive ports at each section, reducing the internal surface area of the refractory by approximately 0.2 %.

To simplify the geometry, it was assumed that the cuts in the refractory would have negligible influence on the flow dynamics and the furnace could be represented by a cylinder and the full 3D mesh with the burner and furnace is shown in Figure 5.1(b). Assuming the outlet in the last section of the furnace also has little impact on the solution, the mesh can be assumed to be periodic as shown in Figure 5.1(c). Therefore, the outlet is taken as the bottom of the furnace where the water seal is present. Furthermore, the thickness of the refractory and water jacket can be simplified to that of a thin wall boundary condition, where the wall can be represented with zero thickness with an imposed heat flux condition.

The difference in internal surface area between the cylindrical assumption and actual refractory lining could have an impact on the overall heat loss from the furnace. During the experiments, the steal ports reached a temperature of approximately 300°C while the water jacket surrounding the ports was between 40-60°C. Therefore, extra heat may be lost through these ports and escaped to the surrounding environment.

For a thin wall boundary condition, the heat flux at the wall Q_{wall} [W/m^2] can be calculated by the expression,

$$Q_{wall} = \frac{k_{wall}}{\Delta x} \left(T_{w,outer} - T_{w,inner} \right) + q_{rad,wall} \tag{5.2}$$

where k_{wall}, Δx, $T_{w,outer}$, $T_{w,inner}$ and $q_{rad,wall}$ is the thermal conductivity of the wall, wall thickness, outer wall temperature which is assumed to be the temperature of the cooling water, the inner wall temperature which is calculated from the turbulent law of the wall [57] and the heat flux at the wall due to radiation. It should be noted that this expression is technically only valid for a flat 1D wall, and in an annular wall, the surface area increases with increasing radius [223]. Nevertheless, expression (5.2) is used here to examine the impact of the heat loss that may occur through these two sections.

In order to evaluate the effect of heat loss, a preliminary CFD simulation needs to be performed. The mesh of a periodic burner and furnace was generated in Ansys ICEM consisting of structured, hexahedral cells and is shown in Figure 5.1(c). The use of a structured, hexahedral mesh when aligned with the flow can help reduce

Model	Model parameter
Turbulence	Reynolds stress model
Gas-phase chemistry	Eddy dissipation model with two step chemistry [108] $CH_4 + 0.5\ O_2 \rightarrow CO + 2\ H_2O$ $C_xH_yO_zN_kS_p + \alpha O_2 \rightarrow \beta CO + \gamma H_2O + \mu N_2 + \zeta SO_2$ $CO + 0.5\ O_2 \rightarrow CO_2$
Char combustion	Intrinsic model [121,122] $A_i = 0.03$ (kg/m^2/s/Pa) $E_i = 1.794 \times 10^8$ $A_{BET} = 10,670$ m^2/kg $C(s) + 0.5\ O_2 \rightarrow CO$
Devolatilisation rate	Single-step Arrhenius expression [90] $A_r = 9.19 \times 10^4$, $E_a = 6.97 \times 10^7$ (J/kmol) [100]
Radiation	Discrete ordinates (3 × 3) [149] Absorption coefficient given by WSGG constants [160] Particle emissivity $\epsilon_p = 0.9$, particle scattering factor $\sigma_p = 0.9$
Soot	Moss-Brokes coal derived soot model [137]
Particles	Eulerian-Lagrangian approach

Table 5.3: Model set-up for the CFD simulations of the PACT facility.

numerical diffusion compared to the use of tetrahedral cells. Further, the cells were concentrated near the burner and refinement was reduced further from the burner exit.

The CFD simulations for the air and air-preheat case were performed in Ansys fluent on a periodic mesh consisting of 285 k cells and the models used are shown in Table 5.3. Also, a steady state Reynolds Stress model with a linear pressure-strain model [224] excluding wall reflection terms [225] was used for modelling the turbulence since the flow is predominantly swirled. The devolatilisation was modelled using the single rate model [90] and the model constants were obtained from a similar coal examined using FG-DVC [100]. Further, a two step eddy dissipation model was used with a global two-step reaction. The char combustion was represented by the intrinsic model [121] and the rates were taken for a variety of coal chars [122]. Experimental data was available for the BET surface area, used in the intrinsic model, from the University of Nottingham as part of the OxyCAP-UK project, and was 10,670 m^2/kg. Also, the high temperature volatile yield of 1.57 was given by the University of Nottingham from drop tube furnace experiments. The radiative heat transfer equation was solved using the Discrete Ordinates (DO) model [149] with a discretisation of 3×3 and the gas absorption coefficient was represented by a WSGG approach with the model constants given by Smith and Friedman [160]. Constant particle emissivity of 0.9 and a scattering factor of 0.9 were assumed and particle radiation interaction was included. Also, soot was included in the simulations using a coal-derived soot model [137]. Discussion of these models has already been described in Chapter 2.

The boundary conditions at the inlet have already been discussed for the secondary and tertiary registers in Tables 5.1 and 5.2. The coal feed rate was 24.4 kg/hr giving a thermal input of 200 kW, and the primary air was maintained at 1.662×10^{-2} kg/s for both cases. The temperature in the primary was 291.45 K for the air case and 293.15 K for the air-preheat case. The outer temperature at the wall $T_{w,outer}$ in expression (5.2) is taken from experimental measurements of the cooling water at each section described in Figure 3.13. For the top section, which is not water cooled, the outer wall temperature was 400 K based on measurements during the experiments. Sections 7 and 8, which are also not water cooled, are well insulated and away from the high temperature region of the flame and therefore may have a lower outer wall temperature than the top section. Sections 7 and 8

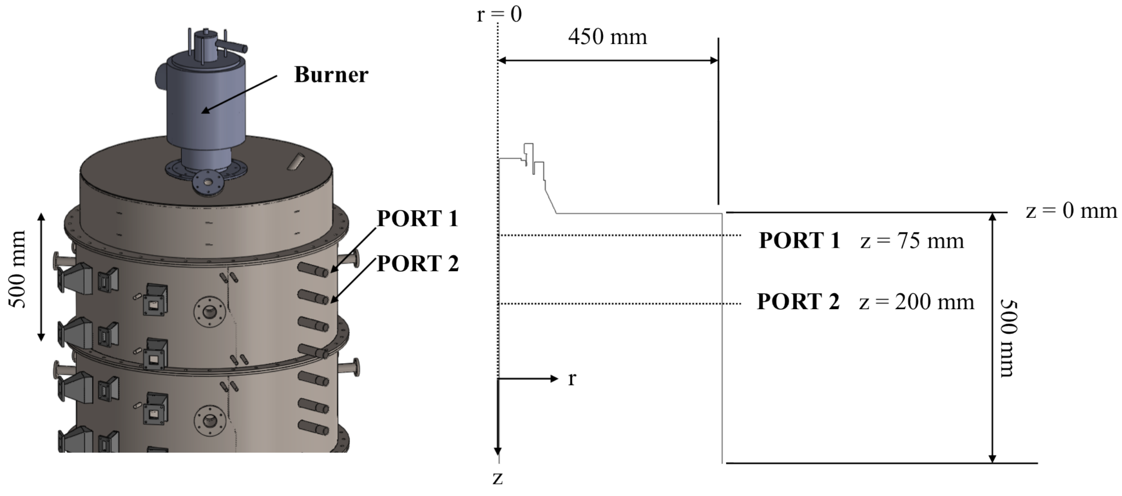

(a) (b)

Figure 5.6: Location of the examined position on the PACT facility within the first section (500 mm). Dimensions are in mm.

may also be further cooled since the facility is positioned in close proximity to an door which remained open during the experiments allowing for outside air to cool the outer metal shell of the facility. The outside air was recorded at 5-10 °C during the experiments and therefore, an outer wall temperature of 300 K was assumed for sections 7 and 8. The wall thickness Δx is 0.2 m for the top section and 0.1 m for the side sections. The side refractory is made from the RCF1700 material and the thermal conductivity k_{wall} of the material was previously given in Table 3.6. However, to examine the effects of heat loss from the openings in the first two sections, the thermal conductivity k_{wall} was examined for two cases:

1. **Max $\mathbf{k_{wall}}$:** thermal conductivity of 0.27 W/m-K based on the manufacturer values given in Table 3.6 for 1650°C for the whole refractory side wall.
2. **Blend $\mathbf{k_{wall}}$:** thermal conductivity of 0.92 W/m-K based on the surface area of the inner refractory in the first two sections where 96% of the refractory material is at 0.27 W/m-K and 4% is represented by steel at 16.27 W/m-K. The other six sections had a thermal conductivity of 0.27 W/m-K.

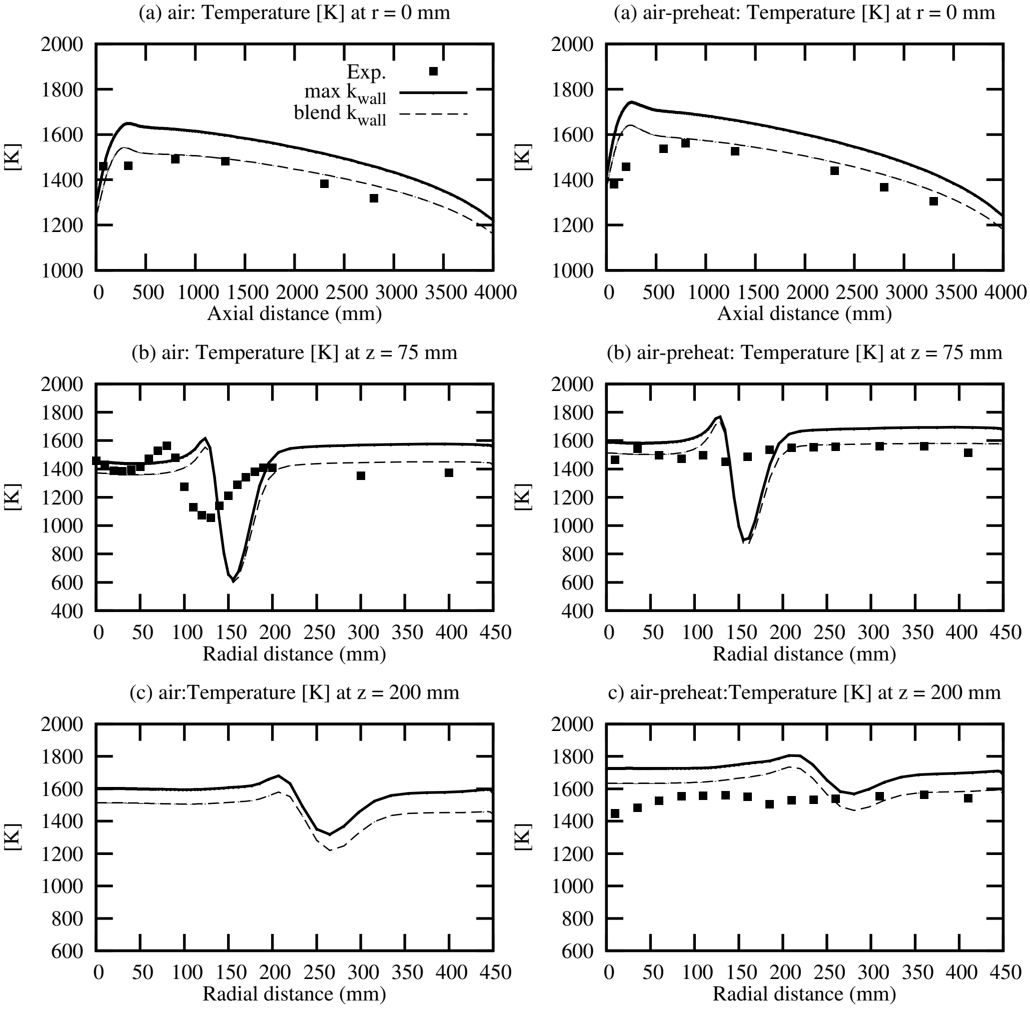

Figure 5.7: Plots of gas temperature against experimental data for the air case (left hand plots) and the air-preheat case (right hand plots) at (a) the centreline, (b) port 1, and (c) port 2.

The locations of the measurements considered in the following sections are shown in Figure 5.6. The gas temperature measurements were taken along the axis at $r = 0$ mm and at ports 1 and 2 which are 75 mm and 200 mm, respectively, away from the roof of the inner refractory. For the heat flux measurements, the location was taken at the inner wall of the refractory at $r = 450$ mm.

The effect of increasing the thermal conductivity from 0.27 W/m-K to 0.92 W/m-K in the first two sections is shown in Figure 5.7. The predicted temperature along the axis and at 75 mm and 200 mm have a better agreement with the experimental data for the air and air-preheat cases and it is clear that the temperature is reduced by approximately 100 K throughout the length of the furnace when the higher thermal conductivity is used. This higher heat loss is expected as the boundary condition in expression (5.2) increases the heat lost through the wall by conduction. In comparison with the experimental data, the results suggests that the heat loss through the ports is important and should be considered.

Only a simple modification of the thermal conductivity in the first two sections is examined in this thesis and a more accurate description could be obtained by modelling the ports and solving a separate solid region for the wall thickness. However, the results obtained compare well with the experimental data and the blend option of 0.92 W/m^2-K is therefore used in the first two sections of the furnace. To ensure that the results are independent of grid resolution, the results are further examined under a grid independence study in the next section.

5.1.3 Grid independence study

Refining the mesh may change the solution and the grid independent study assesses whether a solution is independent of the mesh by examining and comparing the solution between the finer and coarser meshes. A coarse, medium and fine mesh have been assessed to check for grid independence. The coarse mesh was 285k, medium was 730k and the fine was 1.5 million cells. The meshes were mainly refined in the radial and axial direction and are shown in Figure 5.8.

Only the air-preheat case is considered in this section and the CFD models used in the grid study were the same as Table 5.3. The thermal conductivity of the refractory wall in the first two sections is 0.92 W/m-K, while the remaining sections are 0.27 W/m-K. The boundary conditions at the inlet are the same as those used in Section 5.1.2.

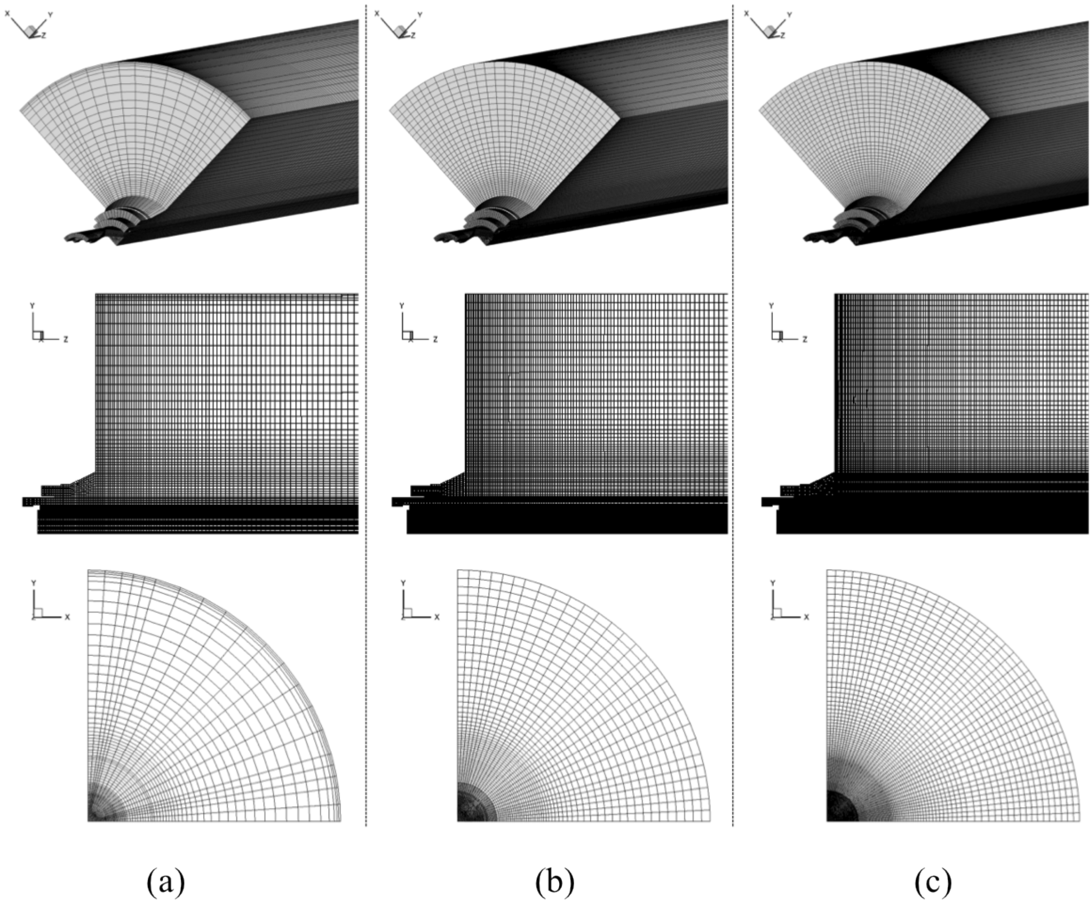

Figure 5.8: Views of (a) coarse, (b) medium, and (c) fine periodic meshes.

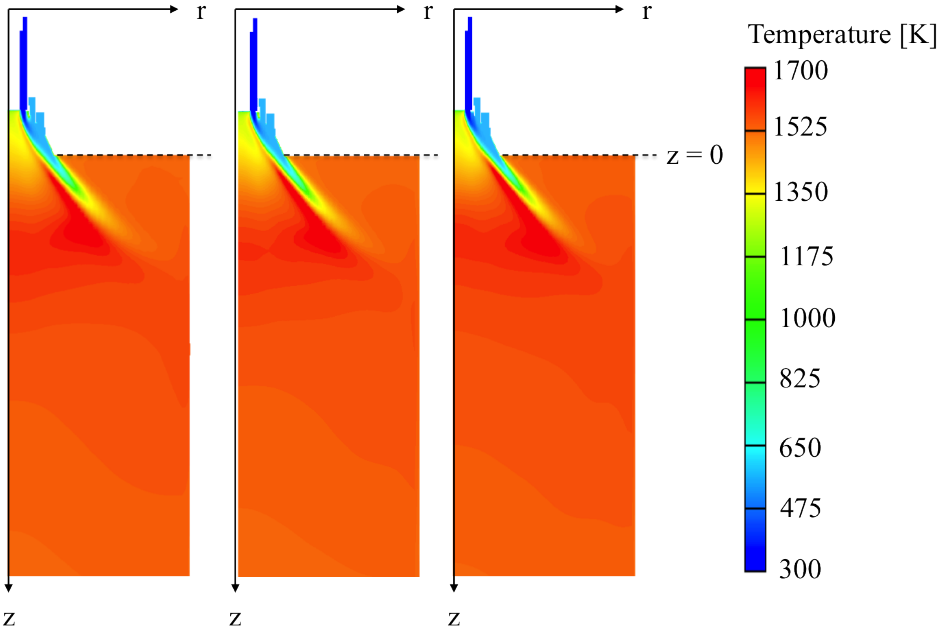

Figure 5.9: Contours of gas temperature for (a) coarse, (b) medium, and (c) fine meshes.

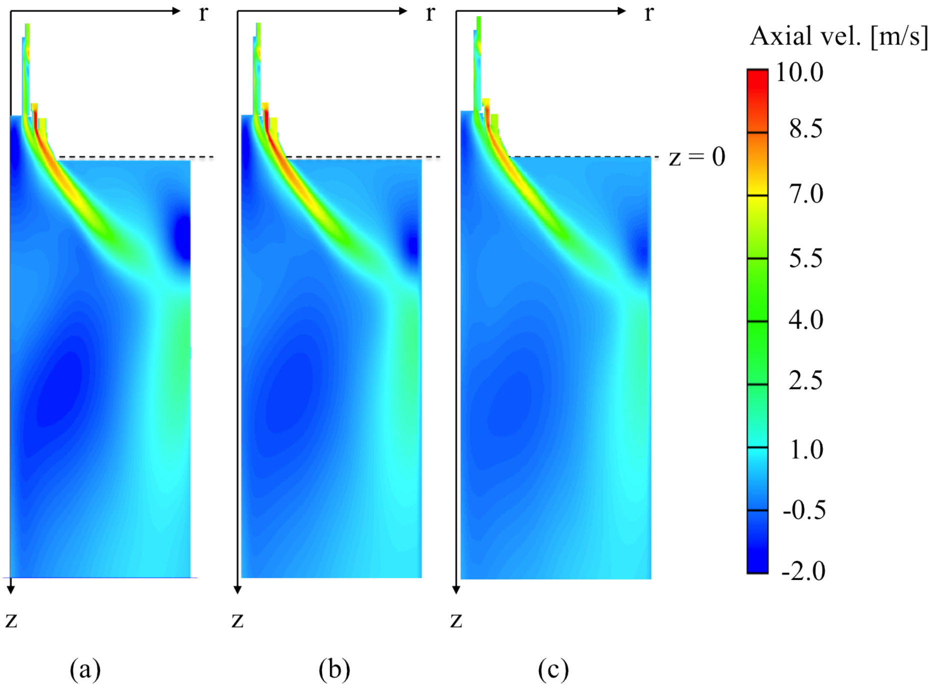

Figure 5.10: Contours of axial velocity for (a) coarse, (b) medium, and (c) fine meshes.

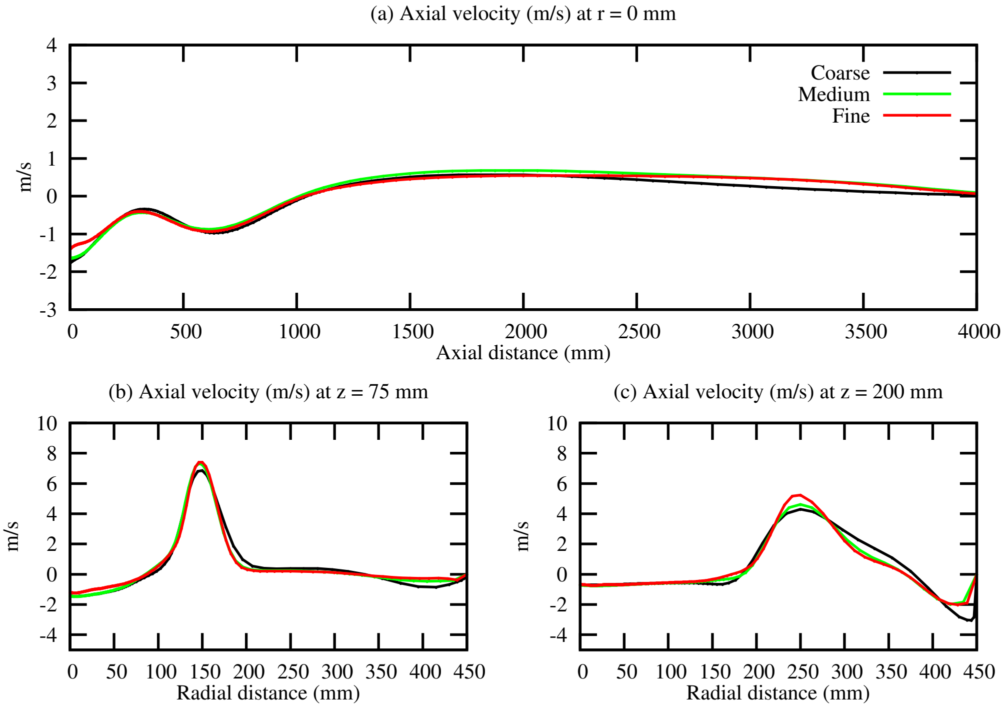
(a) Axial velocity (m/s) at r = 0 mm

(b) Axial velocity (m/s) at z = 75 mm

(c) Axial velocity (m/s) at z = 200 mm

Figure 5.11: Plots of axial velocity (a) along the axis, (b) at port 1, and (c) at port 2.

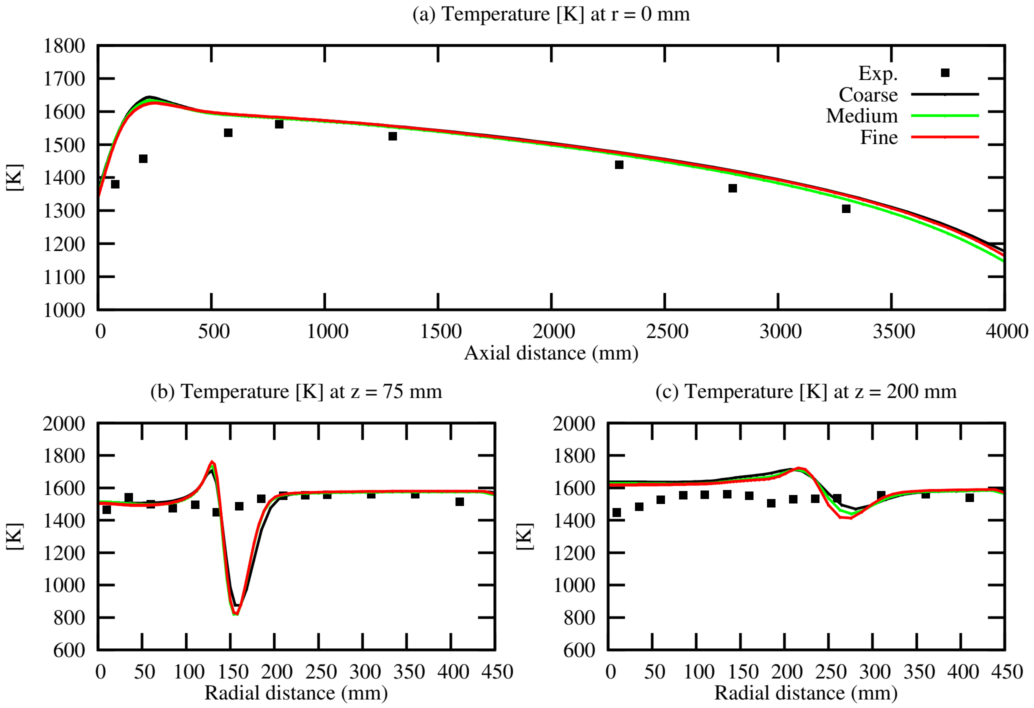
(a) Temperature [K] at r = 0 mm

(b) Temperature [K] at z = 75 mm

(c) Temperature [K] at z = 200 mm

Figure 5.12: Plots of gas temperature (a) along the axis, (b) at port 1, and (c) at port 2.

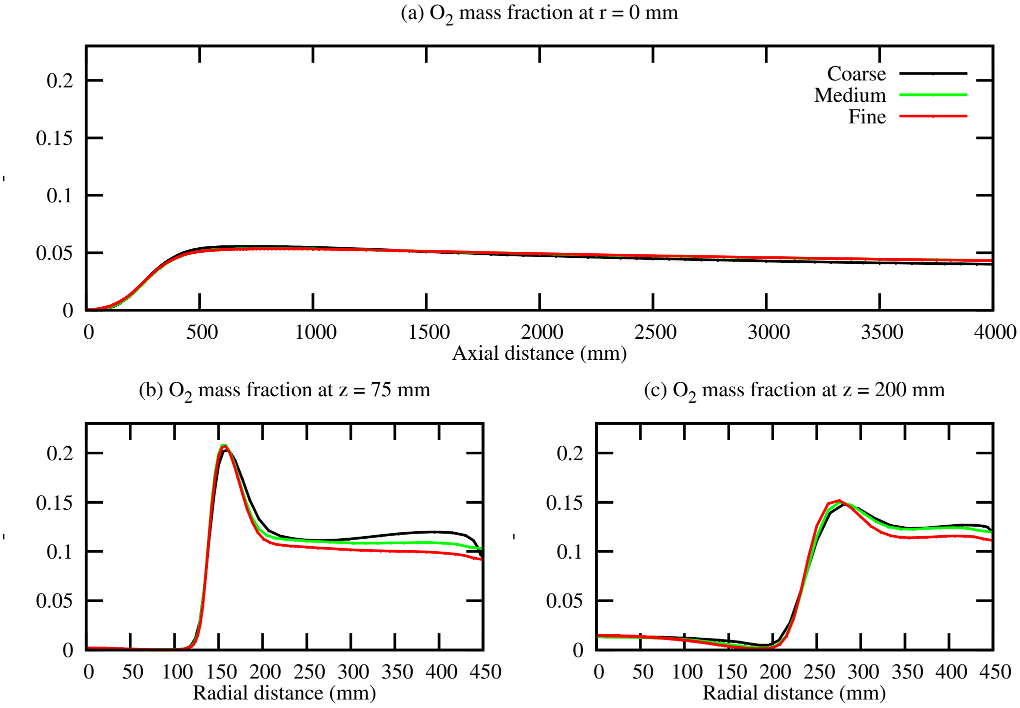

Figure 5.13: Plots of oxygen mass fraction (a) along the axis, (b) at port 1 (c) at port 2.

The contours of temperature and axial velocities for a cross section of the coarse, medium and fine meshes are shown in Figures 5.9 and 5.10, respectively. The primary, secondary and tertiary registers can be clearly seen and the streams appear to combine within the quarl region mixing the coal in the primary with the swirled combustion air. Ignition occurs within the quarl region, thus releasing heat and increasing the gas temperature which is then recirculated back to the burner by the recirculation zone along the centreline. The gas temperature appears to become much more uniform in the radial distance away from the burner. Further, the axial velocity decays away from the burner, but the strong swirled combustion air may reach the walls of the furnace before decaying.

From the contour plots, there is little difference between the results obtained from the coarse, medium and fine meshes. To examine the subtle differences, plots

	Exp.	Coarse	Medium	Fine
O_2(dry,%)	3.2 ± 0.1	3.9	4.2	4.2
CO_2(dry,%)	15.5 ± 0.3	14.6	14.3	14.3
CO (dry,ppm)	7 ± 6	3	4	4
SO_2 (dry,ppm)	284 ± 8	283	283	283
Carbon in Ash (CIA) (%)	7.17	0.35	1.66	1.62
NO (dry,ppm)	367 ± 14	1365 (a)	-	-
		308 (b)	-	-

Table 5.4: Composition of species concentrations at the exit of the PACT facility for the coarse, medium and fine mesh. NO concentration was calculated by (a) Lockwood route [212], and (b) Smoot route [213].

of velocity, temperature and heat flux are compared against the experimental data and are shown in Figures 5.11, 5.12 and 5.13 where the locations of the plots are described in Figure 5.6. The strong recirculation zone near to the burner ($z < 400$ mm) is shown more clearly in Figure 5.11. The cooler unburnt combustion air from the burner causes the decrease in the temperature and the peak in oxygen concentration at port 1 ($z = 75$ mm) at a radial distance of approximately 150 mm in Figures 5.12 and 5.13. The decrease in temperature is not captured in the experiments and intense mixing of the combustion gas may be present in this region which is not captured by the RANS simulation. Further, oxygen has been completely depleted near the centreline of the furnace ($r < 100$ mm) close to the burner in Figure 5.13(b), but appears to be recirculated between the unburnt combustion air and the furnace wall.

The exit composition of O_2, CO_2, CO, SO_2 and NO is shown in Table 5.4 for the grid study. It is observed that the CFD predictions are similar to the experimental data, thus suggesting the overall combustion chemistry is adequate. Surprisingly, the CO concentration is reasonable as this has been shown to differ from the experimental data when the eddy dissipation model is used [111]. However, since the CO concentration is very low, it suggests that complete combustion has taken place and all of the CO formed has converted to CO_2 by the end of the furnace. This can be further confirmed by the low CIA predicted in the CFD predictions. The predicted CIA is very low compared to the experimental data, however the value obtained for the CIA during the experiments is representative of a full day of testing which included start-up, shut-down and intervals of experimentation where a port would be open, and therefore the value may be relatively high. In contrast, the species concentrations were taken over a 30 minute period for the sole purpose of gathering species measurements.

The NO predictions are also shown in Table 5.4 for the coarse mesh. The thermal, prompt, fuel, N_2O and reburn mechanisms were all included but TCI was ignored. For the fuel NO mechanism, the nitrogen partitioning was given from DTF experiments conducted by Nottingham University and the values $Y_{N,vol} = 1.53 \times 10^{-2}$ and $Y_{N,char} = 4.08 \times 10^{-2}$ were used. The Lockwood route [212] and Smoot route [213] were tested and the Lockwood route clearly predicts a higher concentration of 1365 ppm compared to the Smoot route of 308 ppm which is in agreement with the findings in Section 4.3.2. The Smoot mechanism also agrees with the experimental data. It is clear that there is little difference in the results obtained with the different meshes and despite little difference between the species concentrations, the coarse mesh was used for further parameter studies.

5.2 Influence of the turbulence models

Turbulent mixing plays a key role in the combustion process as the reaction rate is generally limited by the amount of mixing that takes place between the fuel and the oxidiser. Therefore the choice of turbulence model is important in capturing the flow field, species distribution and combustion process. Approaches in CFD include RANS, LES and DNS techniques which have been discussed in Section 2.2. The approach of DNS is regarded as being too computationally expensive and therefore is not considered further.

The computational cost associated with steady RANS models is modest [39]. However, the majority of these models are linear-eddy viscosity models and rely on the Bousinessq assumption where the flow is assumed to be generally isotropic and anisotropic flows, such as highly swirling flows may not be adequately represented. Examples of these models include the k-ε and k-ω models. The Reynolds stress model (RSM) abandons the isotropic hypothesis and offers the potential to resolve anisotropic flows with more accuracy than the linear eddy viscosity models.

The use of LES eliminates some of the assumptions associated with RANS models, as well as reducing the number of empirical constants, since large eddies are numerically resolved and only sub-grid scales below a certain filter width are modelled. However, the disadvantage of this approach, compared to steady state RANS, is the increase in computational cost as the solution is inherently three-dimensional, transient and requires a sufficiently fine mesh.

5.2.1 RANS modelling

A discussion of the popular RANS models and their applicability in combusting flows was given in Section 2.2.2. The choice in turbulence model is examined here for the air-preheat case to determine the sensitivity of the solution. Solutions from the RSM model have already been presented in Section 5.1.3 and will also be presented here for comparison. Only the variants of the k-ε model are evaluated here due to their popularity in combustion problems [41–44, 58, 62, 63] and are listed as follows:

(i) k-ε std : The k-ε standard model [57], which is a two-equation model for k and ε used for a number of industrial flows including pulverised coal combustion [58], but it may not be suitable for swirling flow. The equation for k is derived mathematically, whilst the equation for ε is based on physical assumptions.

(ii) k-ε RNG : The k-ε RNG model [61] is a variation of the k-ε standard model. The model has been formulated to give improved predictions of low-Reynolds, near wall and highly swirling flow and has been used for simulations of pulverised fuel combustion [42, 62, 63].

(iii) k-ε real : The k-ε realisable model [64] is a variation of the k-ε standard model. The model includes a mathematically derived transport equation for ε which satisfy mathematical constraints which are in line with flow physics unlike the standard and RNG variants, as well as corrections to aid swirling flow [59]. Also, the model has been used in pulverised coal combustion simulations [41, 43, 44].

The results of the RANS turbulence models for temperature and axial velocity are shown in Figures 5.14, 5.15 and 5.16. The main differences occur in the velocities and the prediction of the recirculation zones. As shown in Figure 5.16(d) of the axial velocities along the centreline, the k-ε RNG approach gives a larger recirculation zone compared to the other models while the Reynolds Stress model predicts the smallest recirculation zone in this region. Theoretically, the Reynolds Stress model should be better for swirling flows, however without velocity measurements it is difficult to judge which model outperforms the others. The differences

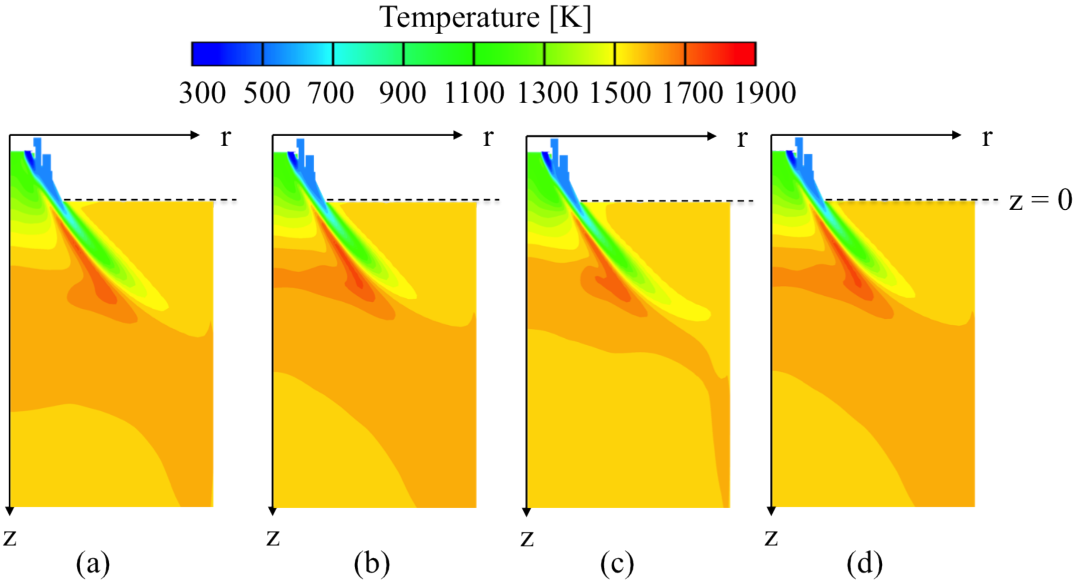

Figure 5.14: Plots of gas temperature for (a) RSM, (b) k-ε standard, (c) k-ε RNG, and (d) k-ε realisable models.

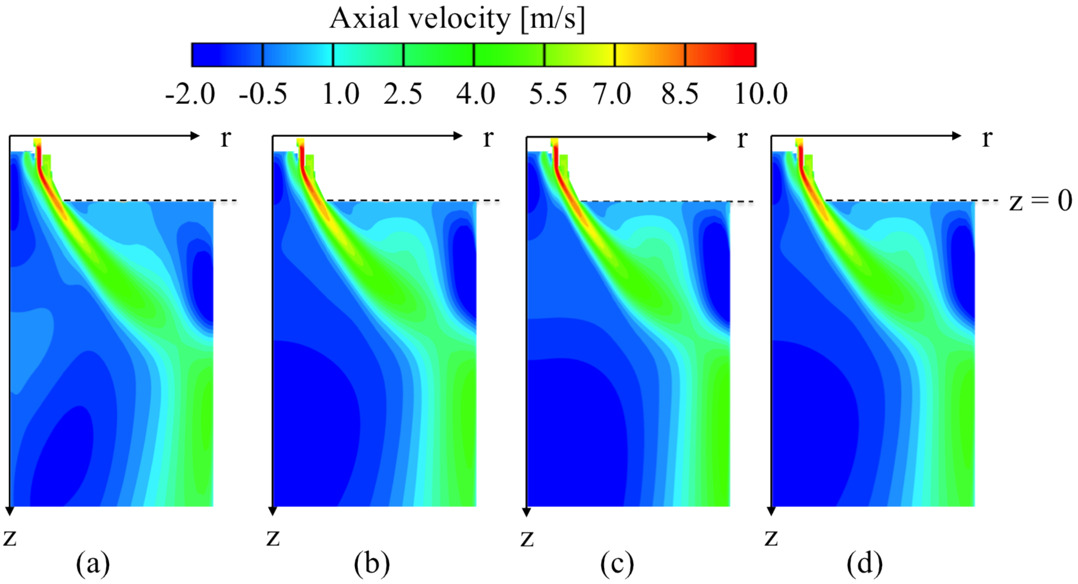

Figure 5.15: Plots of gas temperature for (a) RSM, (b) k-ε standard, (c) k-ε RNG, and (d) k-ε realisable models.

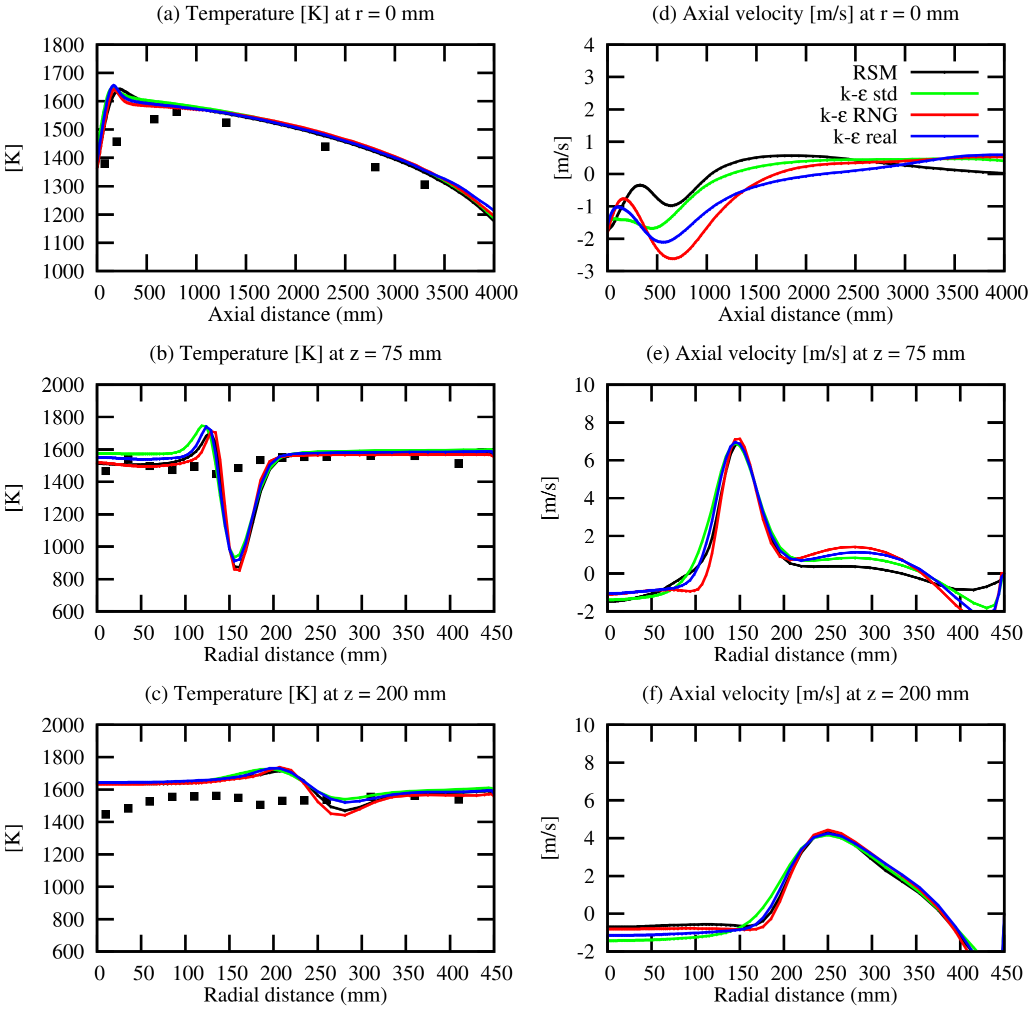

Figure 5.16: Temperature and axial velocity plots for the Reynolds Stress Model (RSM), k-ε standard (k-ε STD), k-ε RNG (k-ε RNG) and k-ε realisable (k-ε real) model.

in gas temperature distribution, shown in Figure 5.16, are difficult to distinguish and a slightly clearer picture is given by the contour plots in Figure 5.14. The peak temperature appears to be lowest in the RNG model and has a marginally different distribution of cold swirling combustion air from the burner. This is a result of the differences in the prediction of k and ε which alter the flow field and also represent the large eddy mixing timescale (k/ε) in the eddy dissipation model which governs the rate of reaction [108]. From the results, the maximum temperature occurs for the k-ε standard model followed by the realisable, RSM and RNG models. The slight temperature difference has a subsequent effect on the radiative heat flux (also referred to as surface incident radiation) and is shown in Figure 5.17 where the highest heat flux is predicted for the k-ε standard model followed by the realisable, RSM and RNG models. The main differences occur near the burner zone, however little differences occur further away from the burner highlighting the sensitivity of radiative heat flux measurements to temperature predictions caused by the changes in turbulence models.

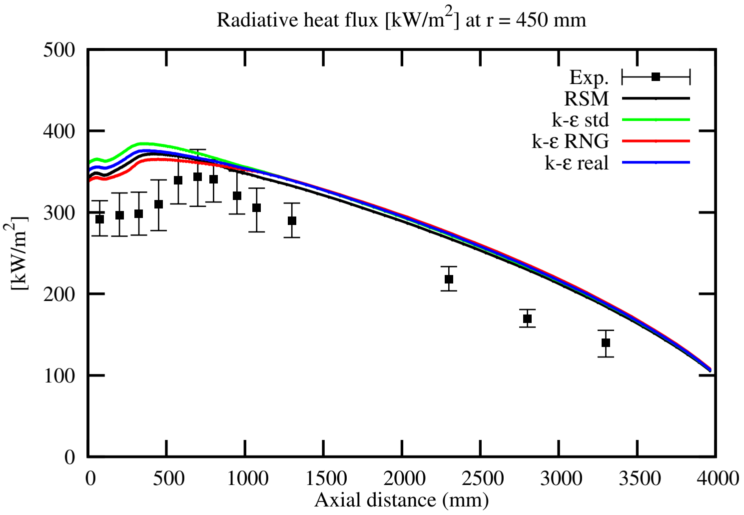

Figure 5.17: Surface incident radiation along the wall for the Reynolds Stress Model (RSM), k-ε standard (k-ε STD), k-ε RNG (k-ε RNG) and k-ε realisable (k-ε real) model.

5.2.2 LES modelling

In order to compute the LES, a full 3D simulation must be performed. As discussed in Section 2.2.3, the results for a LES where the filter width is the same as the cell size may not be grid independent as every time the mesh is refined, the filter width is also refined. However, a grid sensitivity study could be performed to assess the predictions as was performed for a relatively small domain with an efficient LES solver in Section 4.3.1. Due to the size of the geometry, an alternative method to assess the quality of a mesh for LES is used by considering a preliminary RANS solution as described in Section 2.2.3.

If we let the largest eddies in a turbulent flow have a characteristic length $\mathcal{L}$, then the length $\mathcal{L}$ can be assumed to be estimated by $\mathcal{L} \propto k^{1.5}/\varepsilon$, where k and ε are the turbulent kinetic energy and turbulent dissipation rate predicted by a RANS simulation. It has been suggested that for 80% of the kinetic energy to be resolved in a turbulent flow, the length scale of $\mathcal{L}_{LES} \approx \mathcal{L}/12$ would be needed [50,81]. Further, if a mesh cell has a characteristic length scale of $\mathcal{L}_{cell} = \sqrt[3]{C_{vol}}$, then to resolve 80% of the kinetic energy in a turbulent flow, it would require $\mathcal{L}_{cell} \leq \mathcal{L}_{LES}$. Therefore, a mesh refinement factor $\mathcal{L}_{cell}/\mathcal{L}_{LES}$ can be defined where a value greater than 1 requires a finer mesh. The mesh refinement factor for the coarse, medium and fine meshes that were used in Section 5.1.3 as well as a further refined mesh of 2.3 m cells is shown in Figure 5.18. When the mesh refinement factor is greater than 1, then this suggests the need for further refinement, which occurs at the walls as well as in the swirled combustion air region. The disadvantage of this method is in the prediction of k, ε as well as the assumption of characteristic cell length L_{cell} since the cells are not uniform. Furthermore, this criteria along with other quality criteria described in Section 2.2.3 may not be sufficient to yield an accurate simulation, and accuracy may only be determined by comparison with experimental data [196].

After assessment of the quality of the mesh, it can be rotated and copied to make a full 3D mesh but based on the results in Figure 5.18, the mesh still requires further refinement and a mesh greater than 9.2 m cells would be needed. However in order for the LES to be completed in a reasonable time, the medium mesh is selected giving a total of 2.9 m cells.

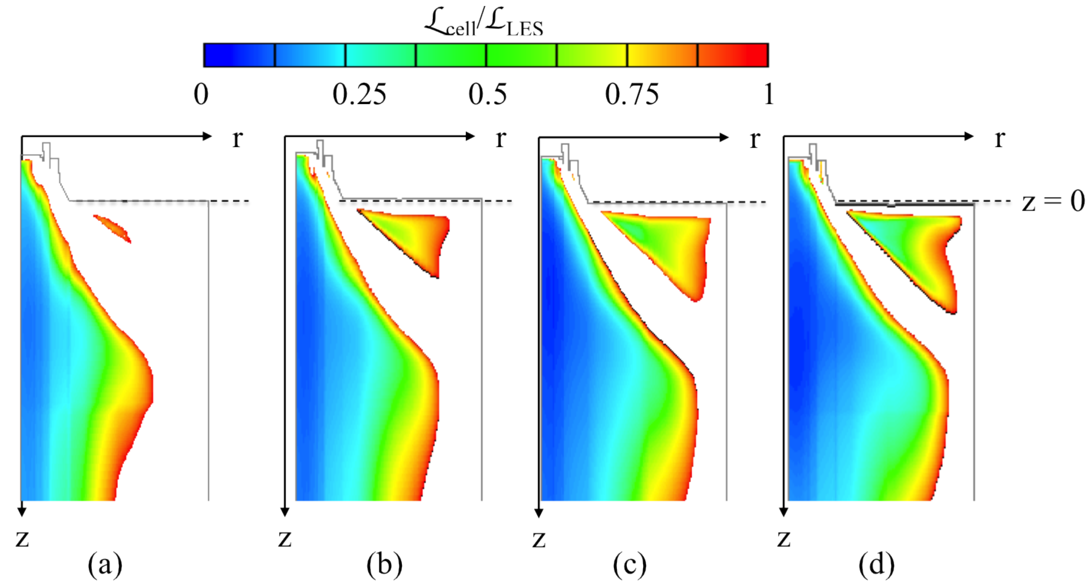

Figure 5.18: Mesh refinement factor on periodic meshes for (a) coarse mesh of 285k, (b) medium mesh of 730k, (c) fine mesh of 1.5m, and a (d) very fine mesh of 2.3 m cells.

A simulation was performed using RANS to give an initial solution before computing the LES. From an initial solution, turbulent structures need to be convected across the domain and an adequate duration must be allowed before a statistical steady state can be reached. The solution can then be sampled to gather statistics. The duration before statistical steady state was reached was estimated to be approximately 1 s based on the mean residence time of the flow in the furnace using the length of the domain and the bulk velocity of the primary register. The solution was sampled for a further 1 s to gather statistics.

Velocity boundary conditions were used with an artificial turbulence generator based on the vortex method [59]. The Smagorinsky-Lilly model with the constant $C_{sgs} = 0.173$ was also used, similar to the previous simulations performed in Chapter 4. A second-order bounded central differencing scheme was used for the momentum equation while a second-order upwind scheme was used for the species and energy equations. A second order implicit transient solver was used with a time-step of

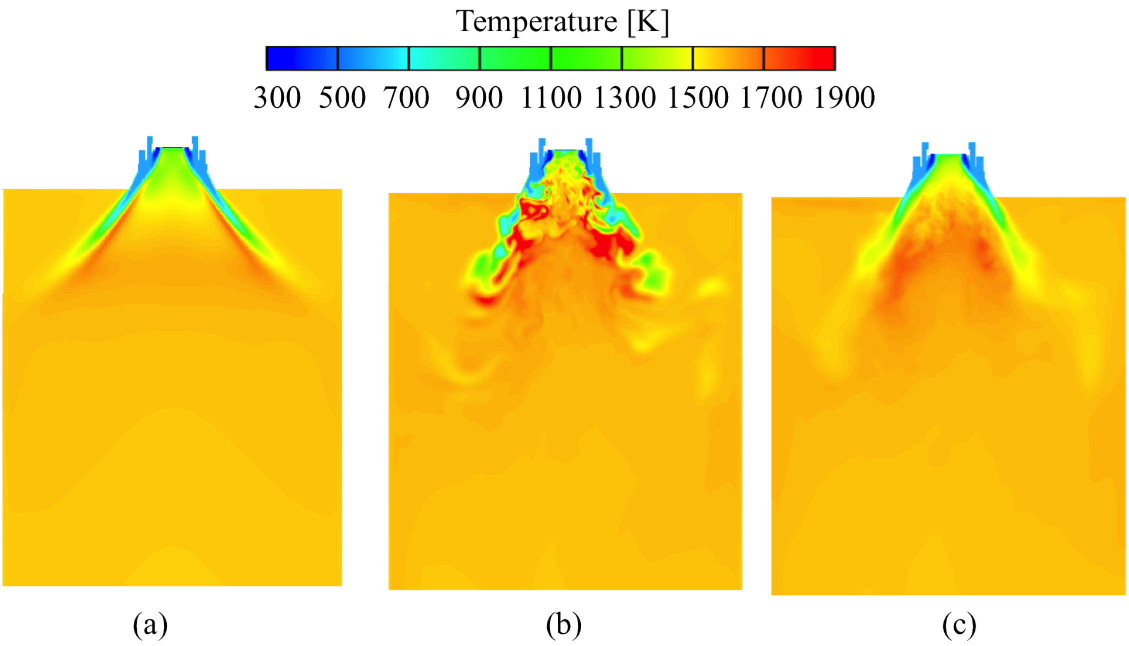

(a) (b) (c)

Figure 5.19: Contours of gas temperature from (a) steady RANS Reynolds stress model, (b) instantaneous LES snapshot, and (c) time-averaged LES.

1.0×10^{-4} s which was sufficient to ensure the CFL number was less than 1 in the majority of the domain.

Fluctuations in temperature and species are present in turbulent flames which emit and absorb radiation. The interaction between the turbulence and radiation is known as turbulent radiation interaction (TRI) and is seen as important to correctly account for radiative emissions [226, 227]. In LES, large scale fluctuations in a flame can be captured and this directly influences the instantaneous prediction of radiation. Sub-grid fluctuations have been shown to be negligible for optically thin flames [226], however for optically thick flames such as coal they may be important [226]. Since radiation is directly related to temperature, the instantaneous large scale fluctuations should have some impact on the solution. For comparison between the RANS and LES predictions, Figure 5.19 shows the gas temperature for the (a) steady state RANS simulation, (b) instantaneous LES and (c) time-averaged LES

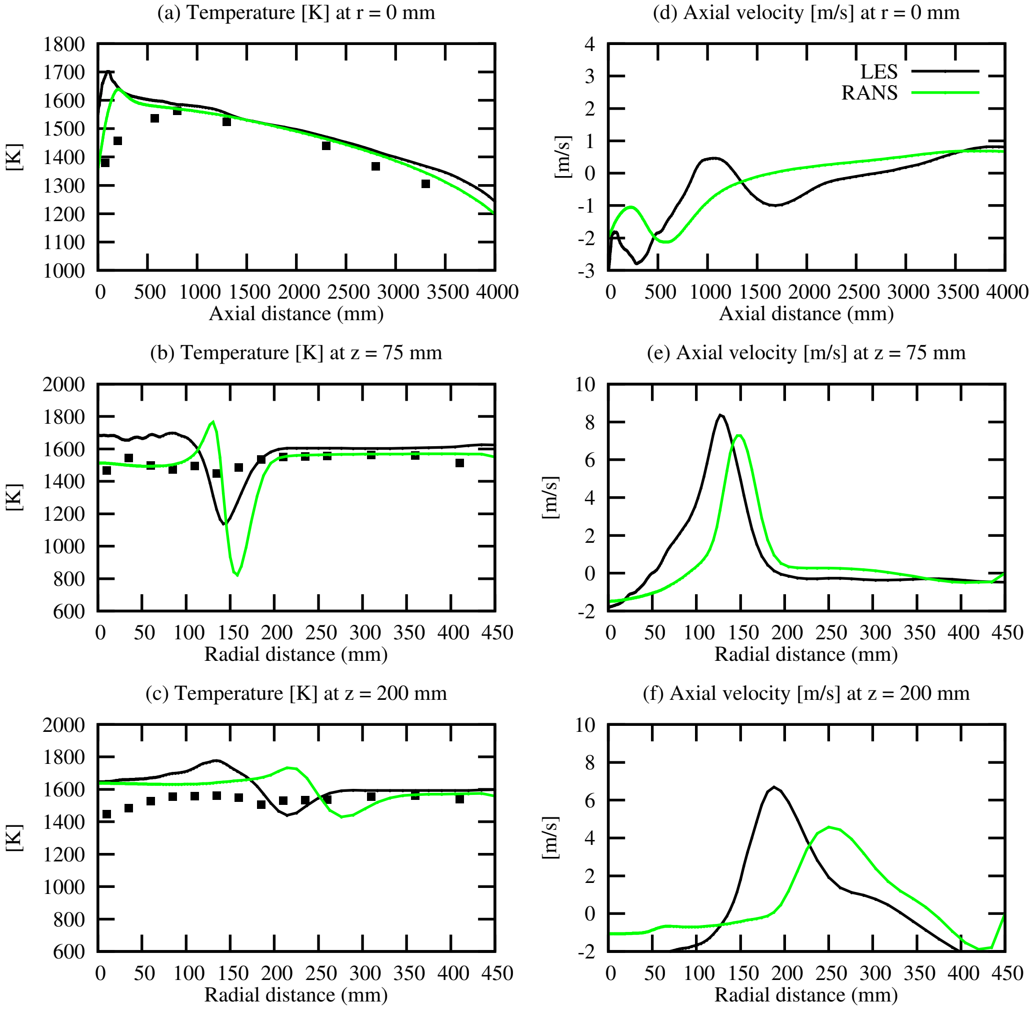

Figure 5.20: Temperature and axial velocity plots for the LES and RANS approaches.

results. The instantaneous LES predictions clearly show pockets of hot gases and higher temperatures than the RANS results. The fluctuations are averaged and yield similar temperatures to the RANS results, but appear to have a hotter region in the central region of the flame. This is confirmed in Figure 5.20(b) where the LES predicts a temperature around 200 K above the RANS simulation.

The higher temperatures in LES lead to higher radiative heat fluxes at the wall

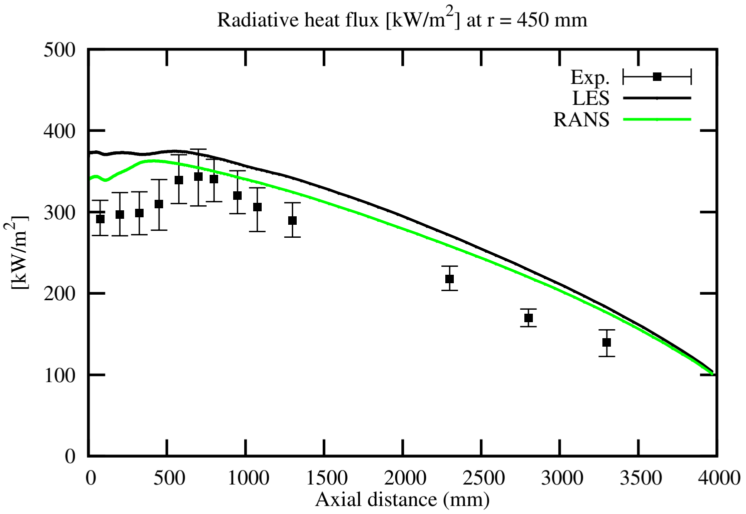

Figure 5.21: Surface incident radiation along the wall for the LES and RANS approaches.

and the prediction of surface incident radiation is shown in Figure 5.21. Whilst both RANS and LES over predict the experimental data, it is clear that the LES is higher than the RANS predictions near to the burner, where the axial distance of 0 m corresponds to the top of the refractory and exit of the quarl. Also, the trend is flatter in the LES compared to the RANS in the first 0.5 m and this distinction has also been noted by Edge et al. [35] who suggested that this may be due to the LES capturing intermittent effects of the flame. Also, the LES predicts a flatter temperature profile in Figure 5.20(b) at $z = 75$ mm, thus suggesting faster combustion and more heat release nearer to the burner.

The axial velocity in the flame for the LES and RANS is shown in Figure 5.20. A stronger recirculation zone in Figure 5.20(d) along the axis near to the burner is captured in the LES compared to the RANS, which may be a possible influence of the higher temperatures accelerating the fluid back to the burner. The peaks in axial velocity at $z = 75$ mm and $z = 200$ mm in Figures 5.20(e) and (f) also correspond to the cooler combustion air entering the burner and shows the peaks decay quicker in the RANS, but occur closer to the wall than in the LES.

In conclusion, the RANS and LES predictions appear to over-predict the radiative heat flux at the wall. Despite the temperature predictions being reasonable, the results demonstrate the sensitivity of the radiative heat flux to the temperature and suggest the need for an improved radiation model. The prediction from LES showed a flatter radiative heat flux profile which is mainly due to turbulent radiation interaction effects such as temperature fluctuations which produced regions of high gas temperatures during the instantaneous solution. The radial profiles obtained from the LES were also flatter than those from the RANS and they are more in-line with the predictions from the experimental data. However, the LES required a high computational resource, where the simulation took 2 months to obtain 2 s of simulation time. This time included queuing time on the Leeds University HPC ARC2 using 32 nodes with a time-step of 1×10^{-4} s on a mesh of 2.9 m cells. Furthermore, it was also suggested that further refinement to the mesh used was needed, such that it would take the mesh beyond 9.2 m cells.

5.3 Influence of gaseous radiative property models

In air and oxy-fuel combustion, concentrations of CO_2 and H_2O can exist which will emit and absorb radiation. To account for the gaseous properties, an absorption coefficient is specified in the radiative transfer equation (RTE) and a common simplification is to use global models as discussed in Section 2.4.3. Two global models that are assessed in this section are the WSGG model with constants proposed by Smith and Friedman [160] and the FSCK model proposed by Modest [147] and implemented via a user defined function (UDF) into FLUENT by Porter et al. [164].

Following a similar approach by Porter et al. [164], the implementation of the WSGGM in FLUENT uses a gray approach, while the implementation of the FSCK

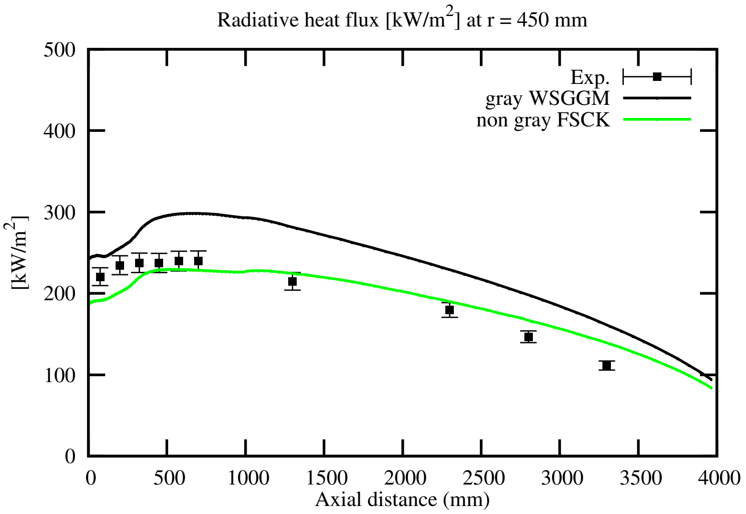

Figure 5.22: Radiative heat flux results and predictions from the gray WSGGM and the non gray FSCK approach for the air case.

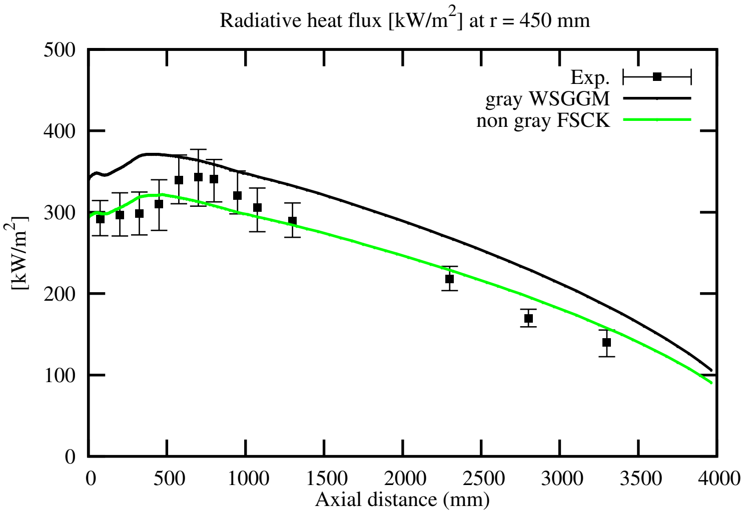

Figure 5.23: Radiative heat flux results and predictions from the gray WSGGM and the non gray FSCK approach for the air-preheat case.

is non-gray with 5 bands. Further, the RSM model is used for turbulence along with the CFD sub-models described in Table 5.3.

The CFD predictions are compared against experimental measurements of radiative heat transfer for the air and air-preheat cases and are shown in Figures 5.22 and 5.23. Figure 5.24 shows the temperature predictions against experimental data for the air and air-preheat case.

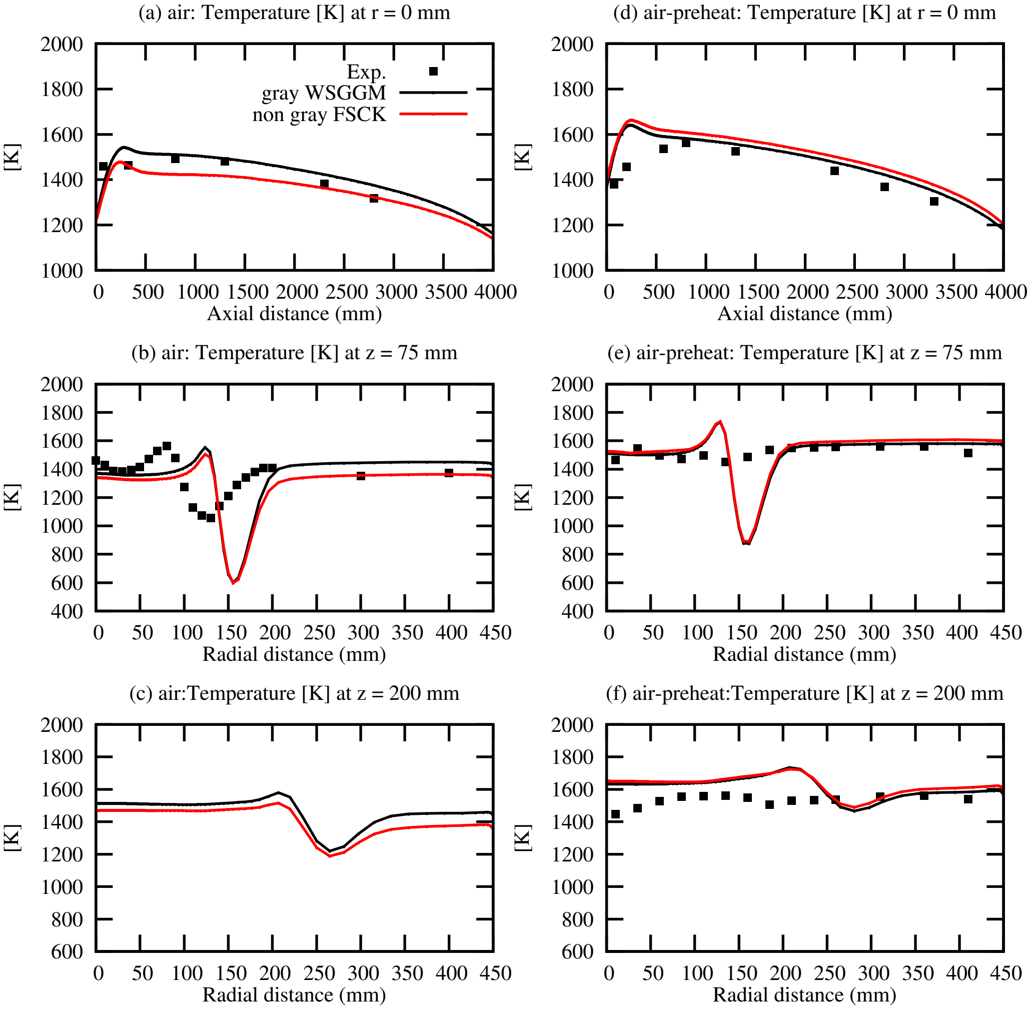

Figure 5.24: Temperature for the air case (a)-(c) and air-preheat case (d)-(f).

In both the air and air-preheat cases, the WSGG model over predicts the surface incident radiation to the wall. This may be a result of the simplified treatment of the partial pressures of CO_2/H_2O ratios where the constants are only accurate for the partial pressures of 1 and 2 [160]. Furthermore, the approach here solves the RTE for 1 band, whilst the FSCK solves the RTE for 5 bands. It has been noted by other authors, the use of a gray approach is inaccurate for the prediction of heat transfer and generally results in an over-prediction of radiative heat transfer [228, 229]. Also

	air			**air-preheat**		
	Exp.	WSGG	FSCK	Exp.	WSGG	FSCK
O_2(dry,%)	3.8 ± 0.2	4.1	5.8	3.2 ± 0.1	3.9	4.9
CO_2(dry,%)	15.5 ± 0.3	14.3	12.71	15.5 ± 0.3	14.6	13.6
CO (dry,ppm)	40 ± 5	11	31	7 ± 6	3	13
CIA (%)	25.5	1.5	9.5	7.2	0.4	5.3

Table 5.5: Composition of species concentrations at the exit of the PACT facility for the FSCK and WSGGM approaches.

Porter et al. [164] examined the two models against SNB data for a simple box with prescribed temperature and species fields representative of air and oxy-fuel combustion environments and concluded the gray WSGG approach over predicts the surface incident radiation whilst the non-gray FSCK model compared well with the benchmark data. A similar conclusion is found here, where the FSCK model predictions compare well with the experimental data for both the air and air-preheat cases and the FSCK model also improves the temperature near to the burner in the air case, but little difference is observed in the air-preheat case.

The comparison of the exit composition and CIA between the WSGG and the FSCK approaches is shown in Table 5.5. The FSCK approach appears to predict higher O_2 and CO concentration as well as a larger value of CIA compared to the WSGG model. A higher CIA value corresponds to more unburnt carbon remaining in the ash and is an indicator of incomplete combustion. Further, the temperatures in the FSCK are lower than the WSGG approach, as shown in Figure 5.24, which will influence the burnout of the char particle and may explain the higher CIA value in the FSCK approach. This is further confirmed by the prediction of the temperature at the outlet of the CFD domain for the air case, which is 780 K for the WSGG approach and 750 K for the FSCK approach. Similarly, the WSGG and FSCK approaches predicts 821 K and 796 K, respectively for the air-preheat case.

Char combustion has only been considered to occur from the reaction with O_2, however it may also be influenced by gasification reactions with CO_2 and H_2O which have been ignored here [86]. The inclusion of the C-CO_2 gasification reaction has been shown to improve oxygen profiles against experimental data in a 20 kW furnace [125]. Therefore, the gasification reactions may produce higher levels of CO and lower CIA which may also alter the concentration of CO_2 and O_2, thus possibly improving the predictions of both models against the experimental data.

Two CFD simulations on the air-preheat case were performed with the finite rate / eddy dissipation model and a multiple surface reaction model which included and excluded the C-CO_2 and C-H_2O gasification reactions. The reaction of C-O_2 was included in both cases and the model is similar to the kinetics/ diffusion limited model described in Section 2.3.3. The rates used were taken from the review by Chen et al. [86] and are for graphite and may not be applicable to this coal. Unfortunately, both models predicted almost complete burnout with similar exit compositions. The inclusion of the gasification reactions predicted a marginal reduction in CIA, but the values were $< 0.01\%$ that it is impossible to conclude whether or not the reactions had an impact on the solution. Therefore, the gasification reactions are not considered here and rates from experimental data applicable to this coal may be needed to improve the understanding of gasification reactions.

In conclusion, the use of the non-gray FSCK model appears to improve the predictions of radiative heat flux against experimental data for two air-coal combustion cases compared with the gray WSGGM. Discrepancies between the two approaches also occur with the outlet composition, where the FSCK approach causes higher levels of O_2, CO and CIA.

Additional memory requirement is needed for the FSCK model, and the simulations were performed from an initial WSGG solution. An additional 48 hours using 16 processors on the University of Leeds HPC, ARC2 was needed for a mesh of 285k cell to achieve convergence with the non-gray FSCK model. The total time was therefore 4 days, excluding queuing time.

5.4 Summary of air-coal results

The numerical set-up and choice of models was validated in Sections 5.1 - 5.3 for two air-coal cases by comparing sensitivity studies of the boundary conditions, turbulence models and radiative property model. This was needed such that sensible boundary conditions may be applied to the oxy-fuel simulation in Section 5.5. The main findings of the sensitivity studies are as follows:

- The burner and furnace were simplified so that the computational cost of the simulations could be reduced and this was achieved by using symmetry in the angular direction. This involved only modelling the burner upstream of the blades, ignoring the experimental ports in the furnace and the split between the secondary and tertiary register was computed from a preliminary CFD simulation. It was shown that the heat loss is important and a higher thermal conductivity of 0.92 W/m-K was used in the first two sections, whereas 0.27 W/m-K was assumed for the rest of the furnace.

- A grid independent study was performed on a periodic mesh and the results obtained were shown to be almost the same as when the coarse mesh was used.

- The predictions from a LES of the air-preheat case showed flatter profiles for temperature and higher heat fluxes near the burner zone compared to RANS. This may be attributed to the intermittent effects of the flame which are captured and then averaged during the LES.

- The radiative heat flux to the wall was influenced significantly by changing the gaseous radiative property model from WSGGM to FSCK. The FSCK results compared well with the experimental data for the radiative heat flux, while the predictions from the WSGG approach were overestimated. Also, the FSCK model was found to predict higher exit O_2, CO and CIA values than the WSGG model and this was attributed to the lower gas temperatures in the FSCK simulation.

The CFD simulations have been validated with respect to the air-coal combustion and the models and boundary conditions are taken forward to numerically examine the effects of oxy-fuel combustion in the next section.

5.5 Numerical investigation of oxy-coal combustion

In this section, several oxy-fuel cases have been numerically examined, named oxy25, oxy27.5, oxy30 and oxy32.5, and the boundary conditions are given in Table 5.6. The simulations consider a synthetic mixture of O_2/CO_2 as the oxidiser instead of air and the name of the case represents the overall oxygen concentration supplied to the burner. For example, the oxy30 case assumes a mixture of 30% O_2 and 70% CO_2. The simulations were based on the boundary conditions used in the air-preheat case for the same exit oxygen concentration of 3.9%, thermal input of 200 kW, burner split, preheated combustion air of 560 K and for these conditions the mass flow rates at the inlet were calculated based on a mass balance calculation. The addition of oxygen in the primary stream aids volatile oxidation and the stability of the flame, however a high oxygen concentration may cause auto-ignition and a low oxygen concentration may cause flame destabilisation [86]. Therefore the oxygen concentration in the primary register, where coal is delivered, was maintained at 21% which is similar to the oxygen concentration of air. The secondary and tertiary registers were therefore enriched to provide the desired overall oxygen concentration.

	oxy25	oxy27.5	oxy30	oxy32.5
Mass flow rate (kg/s)				
Coal feed rate	24.4	24.4	24.4	24.4
Primary	1.92×10^{-2}	1.70×10^{-2}	1.53×10^{-2}	1.38×10^{-2}
Secondary	3.46×10^{-2}	3.07×10^{-2}	2.75×10^{-2}	2.49×10^{-2}
Tertiary	4.31×10^{-2}	3.82×10^{-2}	3.43×10^{-2}	3.11×10^{-2}
Temperature (K)				
Primary	293.15	293.15	293.15	293.15
Secondary	528.48	528.48	528.48	528.48
Tertiary	528.48	528.48	528.48	528.48
O_2/CO_2 concentration (mass, %)				
Primary	0.16	0.16	0.16	0.16
Secondary	0.20	0.23	0.26	0.28
Tertiary	0.20	0.23	0.26	0.28
Calculated exit composition (dry O_2, %)				
Outlet	3.9	3.9	3.9	3.9

Table 5.6: Boundary conditions for the numerical oxy-fuel study in the 250 kW facility.

The combustion and turbulence models were the same as the air-preheat case and are outlined in Table 5.3, however the influence of the WSGG and FSCK approach is revisited in this section.

In air and oxy-fuel combustion, the dominant form of heat transfer is from radiation. Unlike N_2, the thermodynamic properties of CO_2 absorb and emit radiation and therefore it is expected to impact on the radiative heat transfer when CO_2 replaces the N_2 in the oxidiser stream.

It was shown in Section 5.3 that the FSCK model compared well with the exper-

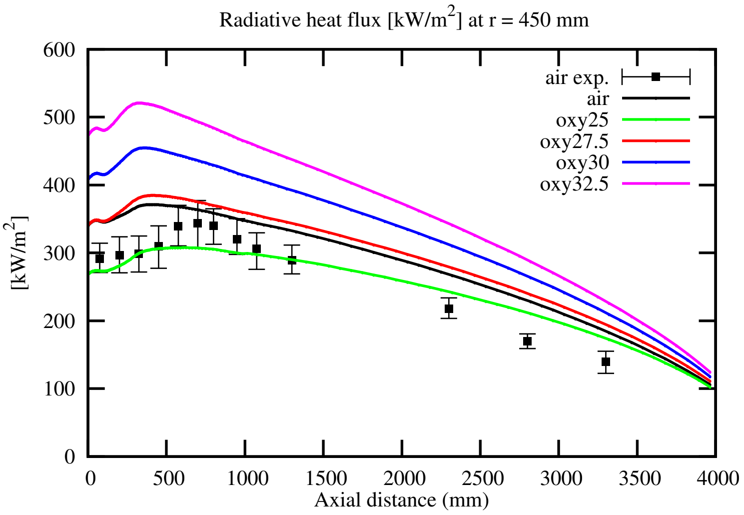

Figure 5.25: Air and oxy-fuel CFD predictions of surface incident radiation using the WSGG model in the PACT facility, experimental data from air-coal preheat experiments.

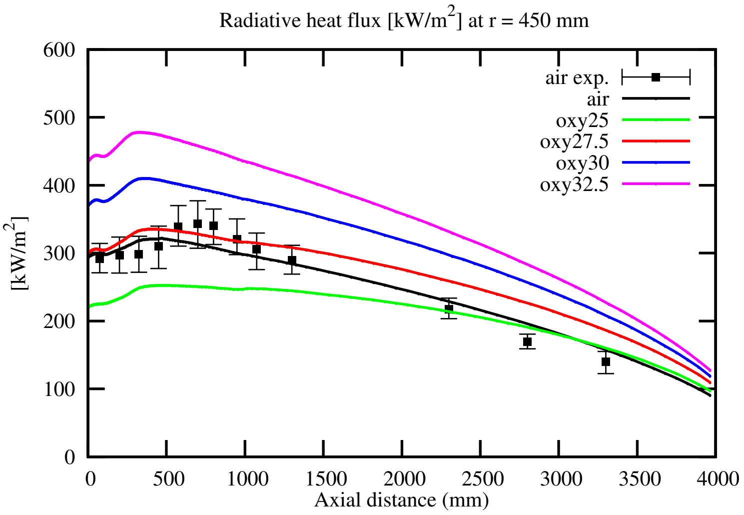

Figure 5.26: Air and oxy-fuel CFD predictions of surface incident radiation using the FSCK model in the PACT facility, experimental data from air-coal preheat experiments.

imental data for both the air and air-preheat cases, while the WSGG over predicted the radiative heat flux. For comparison, the WSGG model and the FSCK model are used to predict radiative heat flux and are shown in Figures 5.25 and 5.26, respectively. The CFD and experimental data from the air-preheat case are also shown for comparison. It is evident, that the WSGG predicts a higher radiative heat flux to the wall compared to the FSCK approach, which is in agreement with the find-

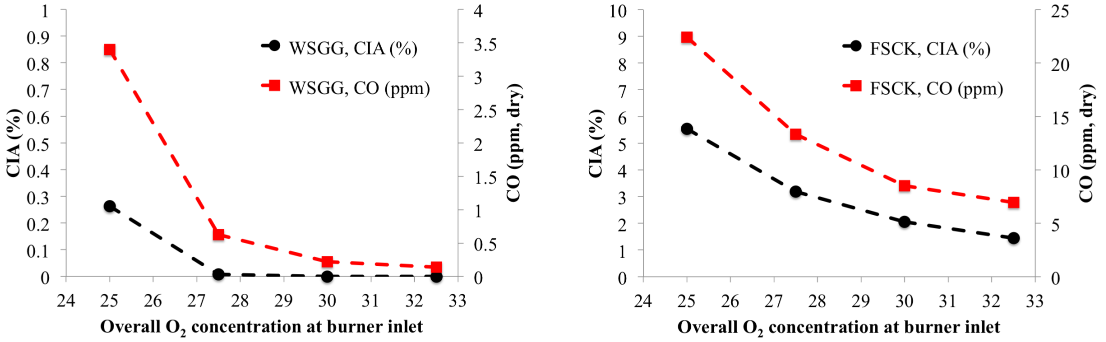

(a) (b)

Figure 5.27: Predictions of CIA and CO concentrations under oxy-fuel conditions for (a) WSGG, and (b) FSCK approaches.

ings in Section 5.3 and by Porter et al. [164]. Interestingly, to match the radiative heat flux for air-firing, the WSGG model predicts an overall oxygen concentration of 25% while the FSCK predicts a concentration of 27.5% and this highlights the importance in the treatment of radiative gaseous properties, especially in a retrofit application where it is important to match the heat transfer characteristics of air.

In contrast, radiative emissions from soot, char and fly ash have also been argued to be more important than a detailed description of gaseous radiative properties [154,166,230]. In this study, the ash content of the coal is relatively low and therefore it may not have such a prominent effect compared to coal with a higher ash content. Clearly, the impact of the more detailed FSCK approach over the one banded WSGG approach shows a difference of 50 kW/m^2, however the impact of particle radiation in the simulation still needs to be addressed. Regardless, the FSCK approach with a constant particle emissivity of 0.9 and a scattering[1] of 0.01 gives a very good agreement with the experimental data in air-coal combustion.

The prediction of CIA (also referred to as unburnt carbon) and CO concentra-

---

[1] Scattering is calculated in Ansys fluent by a scattering factor σ_p and particle emissivity ϵ_p by $(1-\epsilon_p)(1-\sigma_p)$, therefore with $\epsilon_p = 0.9$ and $\sigma_p = 0.9$ gives a scattering of 0.01.

tion at the exit of the facility is shown in Figure 5.27 for the WSGG and FSCK approaches. In both models, the prediction of the CIA and CO concentration reduces as the oxygen concentration at the burner increases. The opposite trend occurs for gas temperatures, which increases as the oxygen concentration at the burner inlet is increased, as shown in Table 5.7. Higher gas temperatures and higher partial oxygen pressures will encourage the oxidation of char in the intrinsic model and this would explain the reduction in unburnt carbon.

A similar trend also occurs for the temperature, CIA and CO concentration between the WSGG and FSCK approaches that occurred in the air case in Section 5.3. The FSCK model predicts lower temperatures, but higher CIA and CO compared to the WSGG approach. Further, higher concentrations of CO_2 and H_2O exist in the oxy-fuel cases compared to the air and therefore gasification reactions which have been ignored may reduce the CIA results presented here. Compared to the air-preheat predictions in Section 5.3 where CIA and CO is 0.4% and 3 ppm, respectively for the WSGG approach, the CFD simulations predict this to be lower when 27.5% oxygen concentration or higher is used at the burner inlet. Similarly, the CIA and CO for the air-preheat case using the FSCK model is 5.3% and 13 ppm respectively, and if an oxygen concentration of 27.5% or greater is used at the inlet of the burner, the values of CIA and CO will be lower than the air-firing simulation.

In conclusion, the FSCK model predicts lower radiative heat flux and temperatures but higher CIA and CO concentrations at the outlet compared to the WSGG model for both air and oxy-coal combustion. Both the gray WSGG and FSCK model conclude that an oxygen concentration of 27.5% will give a similar heat transfer, CO and CIA compared to their respective CFD simulation of air-coal combustion. Despite a similar trend between the models, the values predicted for the gray WSGG and FSCK are significantly different. Further, the results neglect the gasification

	Temperature (°C)			
	oxy25	oxy27.5	oxy30	oxy32.5
WSGG	811	820	826	831
FSCK	787	799	809	815

Table 5.7: Gas temperature at the exit of the PACT facility for the oxy-fuel cases comparing the FSCK and WSGGM approaches.

reactions of CO_2 and H_2O and these may reduce the CIA and CO predictions and impact the radiative heat flux at the wall.

5.6 Conclusions

In this chapter, CFD simulations have been validated against experimental data in two air-coal cases. The furnace and burner were simplified and the boundary conditions of heat transfer through the wall was examined. An investigation into turbulence models and approaches to modelling gaseous properties was also performed and compared against experimental data. After the CFD simulations were validated in air, a numerical study for a variety of synthetic oxy-fuel mixtures was performed using the WSGG and FSCK approaches for modelling gaseous radiative properties.

The main findings are outlined as follows:

- The non-gray FSCK approach to modelling the gaseous radiative properties achieved accurate predictions against experimental data obtained for two air-coal cases compared to the gray WSGGM approach which over predicted the radiative heat flux. This finding is in agreement with previous studies [164], further emphasising the use of non-gray FSCK over the gray WSGG approach when sufficient computational resources are available.
- The use of LES compared to RANS changed the temperature distribution and

heat flux profiles. Intermittencies caused by TRI predicted by the LES were averaged resulting in smoother temperature gradients and a flatter profile of radiative heat flux near the burner zone. A similar trend and observation has also been noted in a different test facility [35].

- Results highlight the differences between the gray WSGGM and non-gray FSCK model when modelling oxy-fuel combustion. The WSGGM approach produced higher radiative heat flux values compared to the FSCK approach.
- The FSCK model predicts lower radiative heat flux and temperatures but higher CIA and CO concentrations at the outlet compared to the WSGG model for both air and oxy-coal combustion. Both the WSGG and FSCK model concluded an oxygen concentration of 27.5% at the burner in oxy-fuel combustion would match the heat transfer, CO and CIA if compared to the CFD simulation of air-coal combustion with the same model. Despite a similar trend between the models, different values of radiative heat flux, CO and CIA were reported. The results neglected the gasification reactions of CO_2 and H_2O which may reduce the CIA and CO predictions, however the rates that were tested showed negligible difference for the air-preheat case and rates applicable to the El-Cerrejon coal should be tested.

Overall, the CFD predictions were successfully validated against experimental data for air-coal combustion, however the use of a non-gray FSCK approach was required. The combination of LES, FSCK and gasification reactions could provide further improvements and should be investigated in the future.

Chapter 6

Numerical investigation of a full-scale furnace

In this section, a full-scale utility boiler is numerically examined. The purpose of this chapter is to examine the effects of firing 100% coal and 100% biomass under air and oxy-fuel conditions in an existing 500 MW_e coal-fired utility boiler described in Section 3.5.

The motivation for the study is described in Section 6.1 followed by the numerical set-up in Section 6.2 and the boundary conditions used for the studies are described in Section 6.3. To obtain confidence in the CFD predictions, the simulations were benchmarked with an in-house model given by the power station which, based on empirical constants, gives an adequate representation of the performance of the boiler in Section 6.4. Demonstrating that CFD can adequately represent the boiler, the fuel was altered between coal and biomass and the oxidiser was investigated for air and oxy-fuel conditions under a wet flue gas recycle in Section 6.5.

The work in this chapter was a collaborative effort from a number of authors and was published by Black et. al [43] and Szuhanszki et al. [44]. The focus of the work investigates air-biomass combustion as well as the use of a wet-recycle for oxy-coal and oxy-biomass. Simulations involving a dry recycle of coal were performed previously by Edge et al. [110, 183] and some conclusions with respect to numerical set-up and boundary conditions are drawn from the previous work.

6.1 Introduction

There has been a significant interest in biomass combustion as it is perceived to lower the overall CO_2 emitted from a power station if the biomass fired is sustainably produced as the whole process could be seen as carbon neutral. A step further would be the integration of carbon capture and storage technologies which could lead to carbon negative emissions. With an increasing fleet of old power stations in the UK, there has been a recent interest in firing biomass in existing furnaces designed originally for coal.

It is therefore of interest to examine the performance of a boiler design for air-coal combustion when it is retrofitted to fire biomass or with oxy-fuel technology. In particular, the distribution of heat transfer in the furnace is important as it effects the steam cycle that drives the steam turbines which generates electrical power and produces revenue for the power plant operator. Therefore, CFD can be used as an engineering design tool to assess the combustion characteristics and heat transfer distribution inside a utility boiler that may be difficult or even impossible to achieve experimentally.

6.2 Numerical set-up

The mesh was created in Gambit and is a predominately structured mesh of approximately 4.1 m cells with a small region of polyhedral cells above the furnace section to provide a conformal interface to the superheaters. The mesh and a simplified burner are shown in Figure 6.1 where geometry simplifications have been performed to reduce the overall computational cost of the simulation. Since the problem is symmetrical then only half of the domain was considered, and the burner was simplified where the swirl veins were represented by axial and tangential velocities and since only 36 out of the 48 burners were firing, the other burners were not modelled.

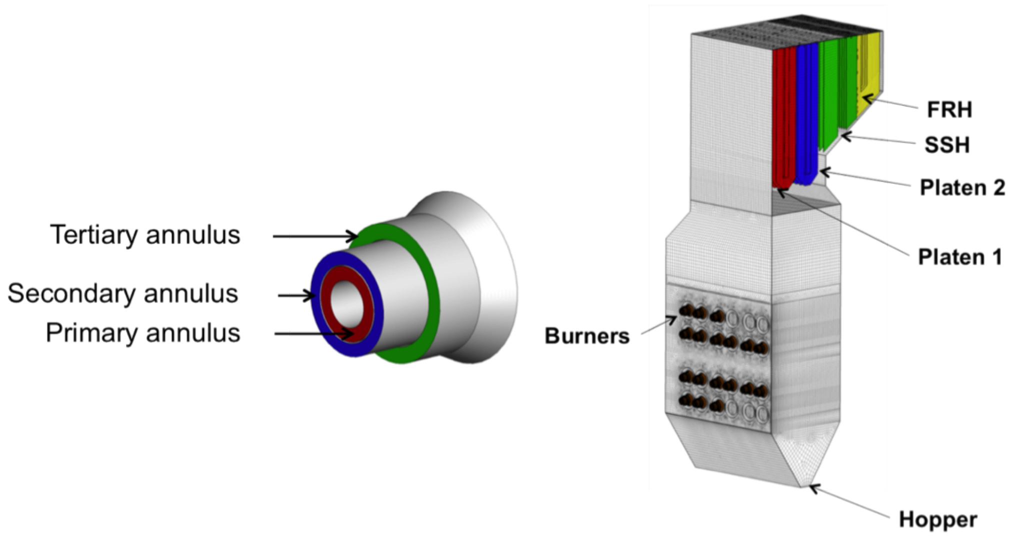

Figure 6.1: Schematic of the burner and the CFD mesh of full-scale utility boiler.

Further, the tube banks in the furnace only consider the superheaters up to the final reheater and it is assumed that the heat transfer in this section is dominated by radiation. Also, the thickness of the superheaters were ignored and modelled as thin walls.

The CFD simulations were performed using Ansys fluent v14.0 [59] and the models used are summarised in Table 6.1, which are similar to those examined in Chapter 5. The RANS k-ε realisable model [64] was chosen as a more stable solution was obtained, as evident from the monitored points of temperature and species in the flame zone, compared to the RSM and RNG k-ε models. Furthermore, the convergence criteria for the residuals of momentum was less than 1×10^{-3} and for the scalar equation was less than 1×10^{-5}, which could only be achieved for the k-ε realisable model. It is not possible to validate the turbulence model, since no detailed flow measurements were available and the k-ε realisable model has been used successfully by other authors to model coal and oxy-coal combustion [41, 230].

Radiation was solved using the discrete ordinates method [149] using gray WSGG approach with gaseous radiative properties of Smith and Friedman [160]. It was

Model	Model parameter
Turbulence	k-ε Realizable [64]
Gas-phase chemistry	Eddy dissipation model with two step chemistry [108]
	$C_xH_yO_zN_kS_p + \alpha O_2 \rightarrow \beta CO + \gamma H_2O + \zeta N_2 + \psi SO_2$,
	$CO + 0.5\ O_2 \rightarrow CO_2$
Char combustion	Intrinsic model [121]
	$C(s) + O_2 \rightarrow CO$
	Pittsburgh No. 8 : $A_i = 15.3$, $E_i = 1.52 \times 10^8$ (J/mol) [62]
	Wood : $A_i = 0.66$, $E_i = 7.48 \times 10^7$ (J/mol) [17]
Devolatilisation rate	Single-step model [90]
	Pittsburgh No. 8: $A_r = 3.8 \times 10^{14}$, $E_a = 2.3 \times 10^8$ (J/kmol) [62]
	Wood: $A_r = 6.0 \times 10^{13}$, $E_a = 2.5 \times 10^8$ (J/kmol) [42]
Radiation	Discrete ordinates method [149]
	Absorption coefficient: WSGG model, 1 band [160]
	Particle emissivity: 0.9
	Soot-radiation interaction [59, 231]
Soot	Coal-derived soot model [137]

Table 6.1: CFD models used in the numerical study of the full-scale utility boiler.

shown in Section 5.3, that this approach may lead to an over prediction of incident radiation and the FSCK model has a better agreement with the experimental data. When examined in oxy-fuel combustion in Section 5.5, it was concluded that both the WSGG and FSCK models each inferred the same oxygen concentration at the burner to match the models predictions of air-coal combustion, but the values of heat transfer from the WSGG was higher. The use of the FSCK model is recommended [164], however additional memory, run-time and storage was required which was not feasible at the time of the simulations. In Chapter 5, the FSCK model was applied to a mesh of 285 k cells which required around 4 days to reach a converged solution using a total of 2.3 GB of RAM with data files approximately 1.3 GB in size. In contrast, the WSGG approach on the same mesh used 1.2 GB of RAM and data files were approximately 362 MB in size[1]. In this chapter, a mesh of 4.1 million cells was used which was estimated to use 32.4 GB of RAM, 18.7 GB of storage per data file and double the overall simulation time to approximately 2 months if the FSCK model was used. It was therefore decided to proceed with the gray WSGG model which was estimated to require 17.0 GB of RAM, 5.2 GB of storage per data file and converge within one month.

The results presented in this chapter examine the trends in total heat transfer when different fuels and oxidiser conditions are used with CFD sub-models that have been validated for air-coal combustion in Chapter 5.

6.3 Fuel properties and boundary conditions

The coal used for the benchmark study (air-coal) and the oxy-coal studies was a bituminous coal, Pittsburgh No. 8 and the biomass chosen for the air-biomass and

---

[1] The additional memory and storage is due to the extra 4 bands needed for the FSCK model in the Discrete Ordinates method. In the gray WSGG method, a single band is needed and based on a discretisation of 3×3 per each octant of angular space 4π, this equates to $1 \times 8 \times 3 \times 3 = 72$ scalars per cell. With the FSCK approach, 5 extra bands are needed which equates to $5 \times 8 \times 3 \times 3 = 360$ scalars per cell.

	Pittsburgh No. 8	Dried wood
Ultimate analysis (d.a.f, wt%)		
Carbon	83.4	52.3
Hydrogen	5.5	6.4
Oxygen (by diff.)	6.9	41.1
Nitrogen	1.6	0.2
Sulphur	2.6	Trace
Proximate analysis (a.r., wt %)		
Fixed carbon	50.3	18.9
Volatile matter	31.0	72.6
Ash	10.3	5.7
Moisture	8.4	2.8
GCV (MJ/kg)	28.54	18.90

Table 6.2: Coal and biomass analysis used in the numerical study of the full-scale utility boiler.

oxy-biomass cases was dried wood. The proximate, ultimate analysis and calorific value of these fuels are given in Table 6.2.

The particle size distribution for the particles were described by a Rosin Rammler distribution [182]. The coal had a minimum size of 1 μm and a maximum size of 300 μm with a mean diameter of 70 μm and a spread factor of 1.19. The biomass particles, represented as spheres but with a shape factor, had a minimum size of 180 μm and a maximum size of 3000 μm with a mean diameter of 332 μm and a spread of 1.35 μm. The particle size distribution data for the biomass was assumed to be the same as that employed in a previous study [146].

Particles were modelled using an Eulerian-Lagrangian technique. In coal combustion, the particle size is assumed to be spherical, however this may not be a valid assumption for biomass particles. In this study, they were assumed to be cylindrical based on experimental observations [17]. The procedure in Ansys fluent assumes the particles are spherical and therefore with the use of a shape factor SF, the surface area of the cylindrical particle can be related to the surface area of an equivalent sphere. The particle surface area A_p then becomes:

$$A_p = \frac{s}{SF}$$

where s is the particle surface area of the equivalent sphere. Similarly, the drag coefficient is also modified for the particle using the correlations of Haider and Levenspiel [143]. A shape factor of 0.83 was chosen and aspect ratio of 2 based on simulations in a previous study [146].

The devolatilisation of the coal and biomass particles were both described by a single rate kinetic model [87]. The values for coal were taken from [62] where Pittsburgh No. 8 devolatilsation rates were calculated using the network model, FG-DVC [94]. The pre-exponential factor was $A_r = 3.8 \times 10^{14}$ and the activation energy was $E_a = 2.3 \times 10^8$ J/kmol. The values used for biomass were calculated in a similar manner using FG-BioMass [97] by Ma et al. [42] who derived $A_r = 6.0 \times 10^{13}$ and $E_a = 2.5 \times 10^8$. For both coal and biomass, the intrinsic char combustion model was used. Values were obtained from Backreedy et al. [62] for Pittsburgh coal and experimental data for wood [17].

The boundary conditions are given in Table 6.3. The boundary conditions for air-coal benchmark case, named *air-coal*, were taken from experimental and a power station modelling tool described in Edge [183]. The oxy-fuel cases are labelled with respect to the overall volumetric oxygen concentration introduced into the burners, named Oxy25 and Oxy30 for oxygen enrichment of 25% and 30%, respectively.

	Fuel	Air	Oxy25	Oxy30
Fuel feed rate (kg/s)	Coal	46.7	46.7	46.7
	Biomass	73.2	73.2	73.2
Oxidiser feed rate (kg/s)	Coal	529	500	402
	Biomass	534	461	375
Recycle rate (%, wet)	Coal	0	71	65
	Biomass	0	65	58
Exit O_2 (vol%, dry)	All fuels	5^c	5^c	5^c
Thermal input (MW_{th})	All fuels	1275^c	1275^c	1275^c
Air leakage (kg/s)	All fuels	16^c	16^c	16^c
Operating burners	All fuels	36^c	36^c	36^c

Table 6.3: Operating conditions for air and oxy-fuel cases in the numerical study of the full-scale utility boiler. The values given by ‘c’ denote the parameters which were used in the mass balance calculation for each of the cases.

Four parameters were used for the calculation of the fuel feed rate, oxidiser feed rate and recycle rate[2] in Table 6.3, which were the thermal input, the number of operating burners, the air leakage and the oxygen at the outlet of the furnace. The thermal input was 1275 MW_{th} for the air-coal case and was kept the same for the oxy-coal, air-biomass and oxy-biomass cases. Since biomass has a lower calorific value than the coal used, a higher mass flow rate is required. In a power station, the operating conditions are usually controlled by monitoring the oxygen in the flue gas at the exit of the furnace to ensure enough oxygen is supplied to the burner to allow for complete combustion. Volumetric oxygen concentrations, on a dry basis, are typically maintained at 3-6% [15, 128]. Therefore, the oxidiser feed rate and recycle rate in Table 6.3 were solved to give an O_2 concentration of 5%, based on the assumption of complete combustion with the inclusion of oxygen from the coal or biomass in the mass balance calculation. Air leakage was assumed to be 16 kg/s and is approximately 3% of the overall oxidiser feed rate assumed for air-coal. It

---

[2] The recycle rate is given by $100 \times m_{RFG}/(m_{RFG} + m_{PFG})$ where m_{RFG} is the mass flow rate of the recycled flue gas and m_{PFG} is the mass flow rate of the product flue gas.

	Platen 1	Platen 2	SSH	FRH	Water walls
Temperature [K]	700	720	800	800	623

Table 6.4: Steam temperatures of the tube banks in the full-scale utility boiler.

is difficult to accurately calculate the air leakage for this section of the boiler, and it is often reported much higher for older utility boilers [183]. It has been assumed that when converting to oxy-fuel combustion, some work will be done to reduce the ingress of air and therefore 16 kg/s of air is assumed to give a fair comparison between cases. In the oxy-fuel cases, a wet recycle was assumed since a theoretical study comparing wet and dry recycle in a power plant found a preheated wet-recycle the most promising configuration [28]. However, mixtures of moisture and CO_2 may cause corrosion issues and it is likely that some optimisation of the plant could be achieved through a mixture of wet and dry recycle option, but this has not been addressed in this chapter. The current technology capable of supplying the volume of oxygen required for a full-scale boiler would be from an air separation unit (ASU). A higher power consumption is required to have a higher purity of O_2 which will form a higher purity of CO_2 in the flue gas, therefore requiring a lower power consumption for CO_2 clean-up and compression. An oxygen purity of 95% - 97.5% is generally agreed to have the lowest overall plant consumption when considering the power requirement for the ASU and CO_2 compression [15, 28] and therefore the purity of oxygen in the oxidiser was assumed to be 95% O_2 and 5% impurities.

The water walls, platen 1, platen 2, SSH and FRH were modelled as thin walls and as outlined in Section 5.1.2, an effective wall resistivity was used to account for the wall thickness of the tube walls, deposition layer and heat transfer to the steam. The wall temperature was considered to be the steam temperature inside the tubes given in Table 6.4, and the wall emissivity was assumed to be 0.8. A previous study used the same boundary condition and found the value of 330 W/m^2-K for the

	air-coal	air-biomass	oxy25-coal	oxy30-coal	oxy25-biomass	oxy30-biomass
Mass flow rate [kg/s]						
Primary	2.9	2.9	2.8	2.6	2.2	2.1
Secondary	2.2	2.2	2.1	1.9	1.7	1.6
Tertiary	9.5	9.7	9.0	8.3	7.3	6.8
Temperature [K]						
Primary	363	363	363	363	363	363
Secondary	530	530	530	530	530	530
Tertiary	530	530	530	530	530	530
Oxygen concentration [mass, %]						
Primary	23.2	23.2	19.1	20.6	19.1	20.6
Secondary	23.2	23.2	23.8	25.5	29.7	31.7
Tertiary	23.2	23.2	23.8	25.5	29.7	31.7

Table 6.5: Burner boundary conditions for the numerical study of the full-scale utility boiler.

effective wall resistivity as an appropriate value, which lies in the range suggested by industry [110].

In the burner, the primary register carries the fuel with carrier air and the secondary and tertiary registers provide the main combustion air. The mass flow rates for a single burner for each of the cases is given in Table 6.5. The mass flow split is 20% primary, 15% secondary and 65% tertiary in the air-coal case and also in all the other cases. The primary air is preheated to a temperature of 363 K whereas the secondary and tertiary air is heated to 530 K. In the oxy-fuel conditions, it was assumed that the oxygen concentration would not be above 21% by volume since this is equivalent to the oxygen concentration in air and above this value could have safety implications as the coal could ignite. The oxygen concentration was therefore enriched in the secondary and tertiary registers such that the overall oxygen concentration from the burner was either 25% or 30%. Also, it was also assumed that the recycle ratio was taken after a particle removal device such as the ESP. An iterative procedure of a mass balance calculation assuming complete combustion and an exit concentration of dry oxygen of 5%, was used to calculate the composition of the inlet gases.

6.4 Air-coal benchmark simulation

Three different grid resolutions of 3.2, 4.1 and 4.8 million cells with refinement in the burner region, referred to as coarse, medium and fine, respectively were investigated for grid independence where the predictions of total heat transfer and exit temperature of the furnace were monitored. There was little difference between the results obtained using the medium and fine meshes, and therefore the medium mesh was selected.

The CFD predictions for the heat transfer from the air-coal case are shown against the in-house data in Table 6.6. It is clear from the table that the results are in good agreement for the overall total heat transfer which varies by only 2%. The predictions from the in-house model and the CFD predictions for each of the sections differ, which may be due to the fact that the in-house model is only a one

	In-house model [MW]	CFD [MW]
Water walls	456	457
Platen 1	106	99
Platen 2	110	136
SSH	110	101
FRH	79	52
Total	861	846

Table 6.6: Heat transfer (MW) from the in-house code and the prediction from CFD for the air-coal case in the full-scale utility boiler.

	Exp. [K]	In-house model [K]	CFD [K]
Furnace exit	1591	1656	1670
Platen 1 exit	-	1135	1208
Platen 2 exit	-	1282	1299
SSH exit	-	1173	1140
FRH exit/outlet	-	1054	1094
Total	-	861	846

Table 6.7: Gas temperature from the in-house code and the prediction from CFD for the air-coal case.

dimensional model of the furnace, whereas CFD is a three dimensional representation of the heat transfer in the boiler and therefore the distribution of heat transfer inside the furnace is expected to differ between the two models. Similarly, the predictions of temperature at planes after those sections are close to the in-house model predictions and experimental data, as shown in Table 6.7. The results suggest that CFD can adequately predict the overall heat transfer for this section of the boiler and the models adequately represent the combustion of coal in air. To investigate the possibility of retrofitting this boiler with oxy-fuel combustion, the use of CFD with the same boundary conditions at the walls and models can be used.

6.5 Air and oxy-fuel comparisons

In this section, a comparison between the air-coal, air-biomass, oxy25-coal, oxy25-biomass, oxy30-coal and oxy-30-biomass cases are discussed.

Comparing the cross sectional image of gas temperature in Figure 6.2, there is a visible difference in the temperature distribution and peak temperature inside the boiler for the air and oxy-fuel conditions. The increase in oxygen concentration increases the overall temperature in the boiler compared to the air-firing cases. This

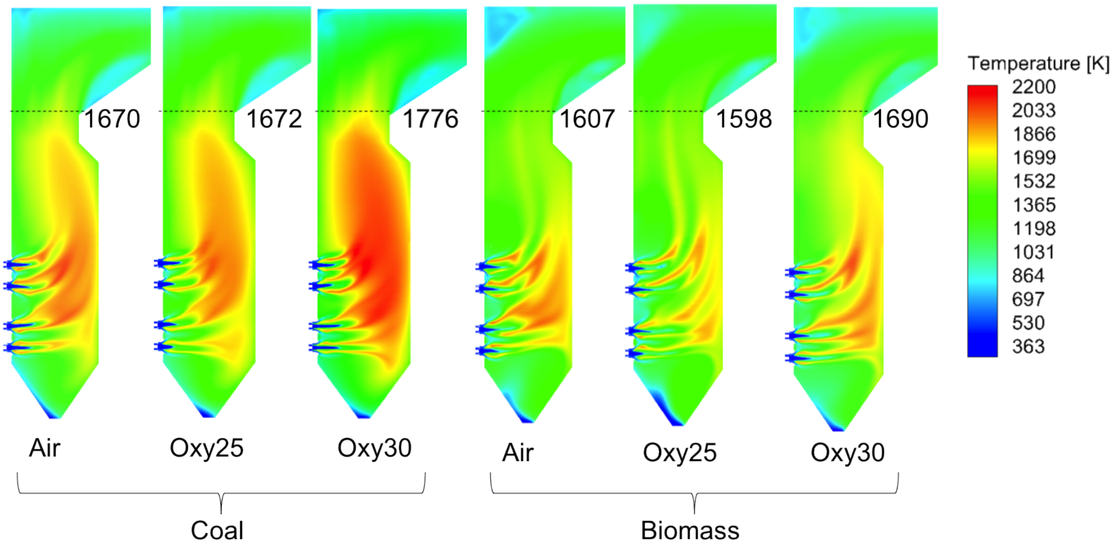

Figure 6.2: Gas temperature prediction along the third row of burners for coal and biomass fired under air and oxy-fuel conditions in the full-scale utility boiler.

is expected as a higher oxygen concentration generally increases the adiabatic flame temperature. Also, the mass weighted temperatures at the furnace exit are shown, which confirm the visible differences in the temperature.

The main difference occurs between the coal and biomass cases, see Figure 6.2, where lower temperatures are present in the biomass simulations. This may be attributed to the size of the particles since the large biomass particles will heat up slower compared to the finely ground coal. This may result in delayed ignition, devolatilisation and therefore heat release compared to coal combustion which is shown by the high temperature regions which occur further away from the burner in the biomass cases compared to the coal cases.

A cross section of the gas velocity in the boiler is shown in Figure 6.3. The trend shows lower velocities when the recycle ratio is reduced and is evident in both coal and biomass cases. The gas velocity is lower due to the higher density of CO_2 in oxy-fuel conditions compared to N_2 in air. For example, at the inlet temperature of 530 K, the density of nitrogen at atmospheric pressure is 0.64 kg/m^3 compared to

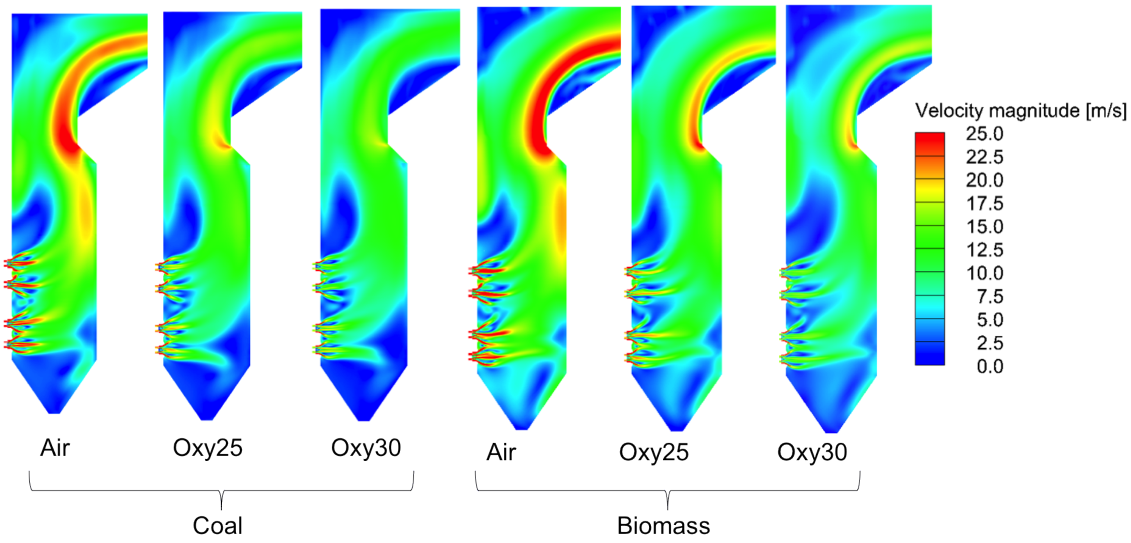

Figure 6.3: Prediction of velocity magnitude along the third row of burners for coal and biomass fired under air and oxy-fuel conditions in the full-scale utility boiler.

CO_2 which is 1.01 kg/m^3. As the mass fraction of oxygen increases, a lower mass flow rate, shown in Table 6.3, is needed to achieve a 5% exit oxygen concentration and this also reduces the velocity in the boiler. The lower velocities could impact the heat transfer further downstream, causing a reduction in the convective heat transfer since the mass flow through this section is lower. This will ultimately effect the heat performance of the boiler and if retrofitted with oxy-fuel the difference in mass flows would also need to be considered. Lower convective heat transfer has been observed in pilot scale studies as the recycle ratio is reduced [128]. In the following sections on heat transfer observations, this trend is not observed since the CFD only considers a section of the boiler which consists of boiler tubes where radiative heat transfer is dominant.

The difference in oxygen concentration is shown in Figure 6.4 and is a result of the different inlet concentrations defined in Table 6.5 with the lowest oxygen concentration occuring in the air-cases. Also, the ingress of air is shown at the bottom of the furnace in the hopper region.

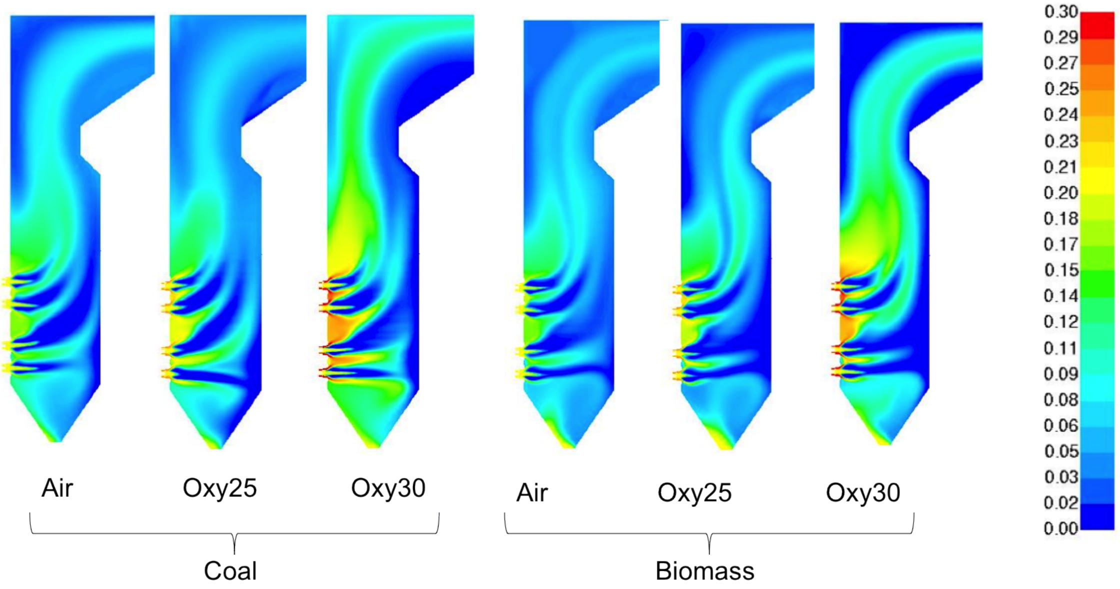

Figure 6.4: Mole fraction of oxygen along the third row of burners for coal and biomass fired under air and oxy-fuel conditions in the full-scale utility boiler.

The distribution of carbon dioxide is shown in Figure 6.5. In the oxy-fuel cases, higher CO_2 concentrations are shown for the coal cases compared to the biomass cases. However this is primarily due to a higher recycle ratio needed in coal than biomass, as shown in Table 6.3. A similar explanation can be given between the oxy-fuel cases Oxy25 and Oxy30, where at the higher oxygen concentration case, Oxy30, the CO_2 concentration at the inlet is lower than that of the Oxy25 case since the recycle ratio reduces from 71% to 65% in coal and 65% to 58% in biomass. It is important to note that this is based on a wet recycle and therefore there is a significant portion of moisture in the flue gas. Further, drying and flue gas clean-up downstream of the boiler would result in higher purity levels.

For the air-coal and air-biomass cases, the CO_2 concentrations at the exit are similar due to the same thermal input, air-leakage and exit oxygen concentration. Therefore, the use of biomass alone gives no significant reduction in CO_2 emitted to the stack without the use of a CCS technology, such as oxy-fuel or post-combustion capture. Biomass can only be seen to reduce CO_2 emissions released into the atmosphere without CCS if it is resequestered by crops grown to replace the biomass

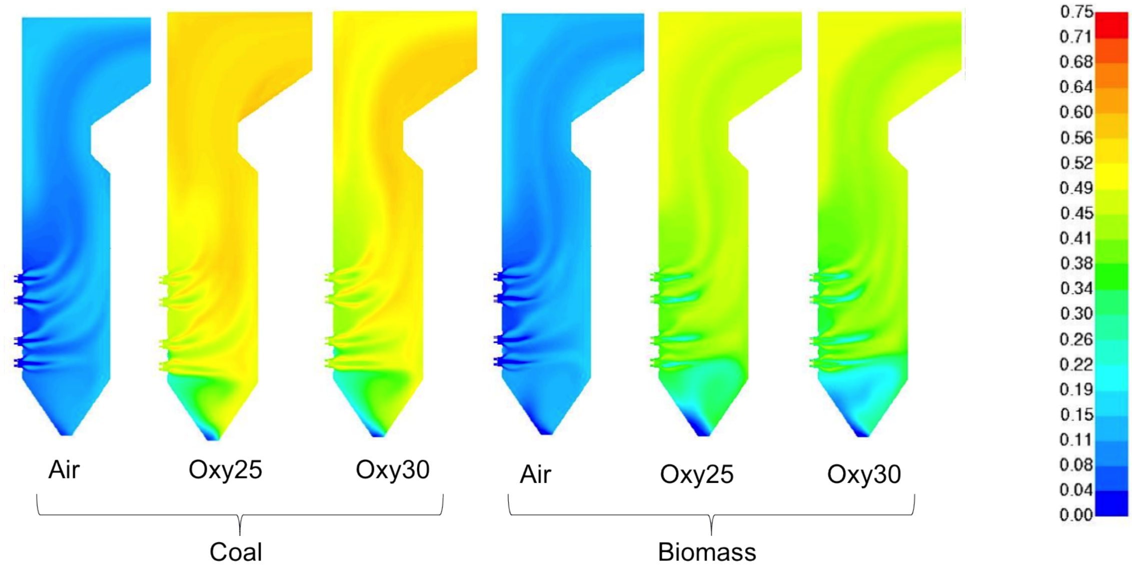

Figure 6.5: Mole fraction of carbon dioxide along the third row of burners for coal and biomass fired under air and oxy-fuel conditions in the full-scale utility boiler.

burned. However, a large quantity of biomass is burned (73.2 kg/s in this study), producing a large quantity of CO_2 (128 kg/s) which will need to be absorbed by plants in the carbon cycle. While it appears to be a good idea in principle, it will be very hard to scientifically justify whether or not the whole process could be carbon neutral on this scale.

As shown in Chapter 4, the dominant route of formation of NO in pulverised fuel combustion is from the fuel nitrogen. Therefore, it is expected that emissions of NO_x will be lower in biomass combustion due to the lower nitrogen content of the fuel in both air and oxy-fuel conditions compared to coal combustion, shown in the ultimate analysis in Table 6.2. Also, the emission of NO_x is also expected to be lower in oxy-fuel combustion compared to air combustion due to the lack of atmospheric nitrogen which will reduce the formation of thermal NO.

Comparing the overall heat transfer in Figure 6.6, the air-biomass results predict an overall lower total heat transfer by 15%, despite the same thermal input and similar excess air. The difference in temperature distribution inside the boiler, as

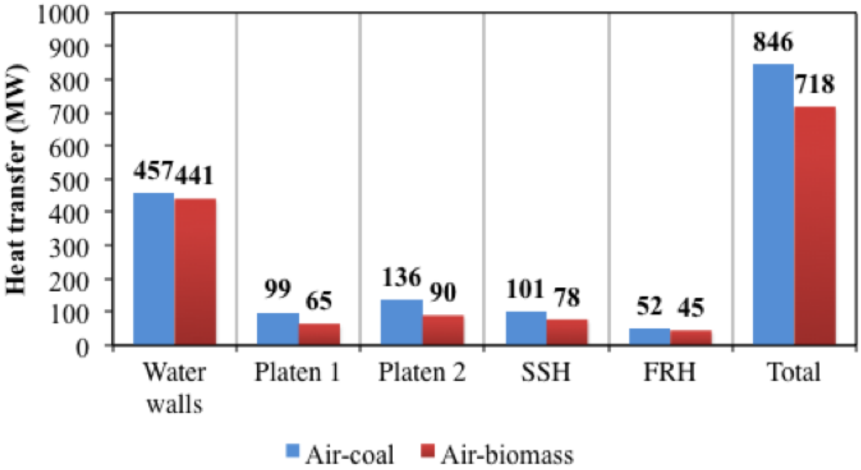

Figure 6.6: Heat transfer predictions between air-coal and air-biomass cases at various superheater sections and water walls in the full-scale utility boiler.

shown in Figure 6.2, may be the dominant cause of lower heat transfer in air-biomass and air-coal. However, it has been suggested that particle radiation from char, soot and fly-ash plays a dominant role in radiative heat transfer in pulverised fuel combustion [154, 166]. The biomass particles are much larger than the finely ground coal and will have a lower overall surface area, and therefore biomass will have a lower radiative emission from the particles compared to coal. Furthermore, since the ash content is lower in biomass, the radiative emission from ash will also be lower in biomass compared to coal. On this basis, it can be argued that a combined effect of radiative particle emission and temperatures result in the lower heat transfer observed in Figure 6.6.

The difference in heat transfer between air-coal, oxy25-coal and oxy30-coal is shown in Figure 6.7. It is observed that as the oxygen concentration is increased from 25% to 30%, the heat transfer and therefore the total heat transfer in this section is increased. As the oxygen concentration increases, the adiabatic temperature should increase. The theoretical change in temperature is replicated in Figure 6.2 and subsequently would be the main cause of the increased heat transfer. As the temperature increases, the radiative heat transfer to the walls also increases. It

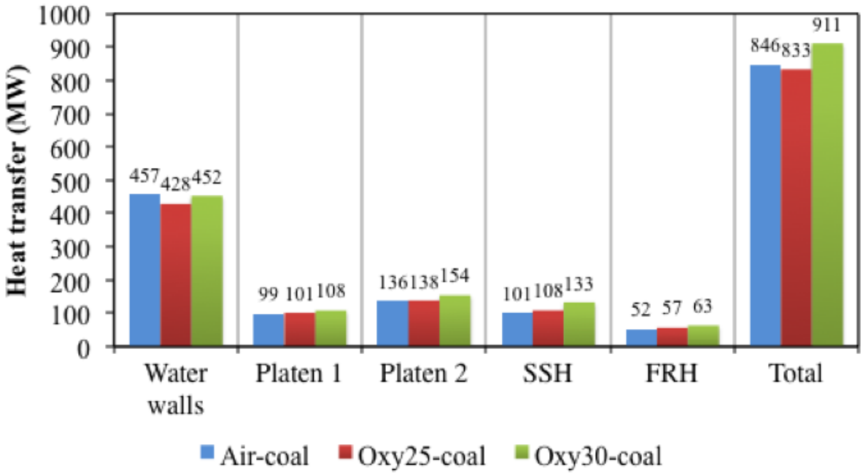

Figure 6.7: Heat transfer predictions between air and oxy-coal cases at various superheater sections and water walls in the full-scale utility boiler.

might be expected that further downstream, where convective heat transfer dominates, that the heat transfer may be lower in the higher oxy-fuel cases since more heat is absorbed in the radiative section and a lower mass flow passes through this section. In comparison to the air-coal case, the total heat transfer distribution is lower in the oxy25 case and higher in the oxy30 case and to match the total heat transfer an oxygen concentration between 25-30% may be needed based on the simulations.

A comparison of oxy-biomass with air-biomass is given in Figure 6.8. A higher oxygen concentration leads to a higher heat transfer, a similar trend to the oxy-coal results which is clearly a result of higher temperatures. However, the total heat transfer for this section is lower by approximately 17% and 8% for the oxy25-biomass and oxy30-biomass cases, respectively, compared to the air-coal simulation. Therefore, for oxy-biomass combustion, an oxygen concentration of above 30% may be needed, or alterations to the boiler may be needed to achieve similar heat transfer characteristics compared to air. Therefore a higher oxygen concentration will dilute the flue gas and lower the exit CO_2 concentration which might increase costs in the purification and compression units.

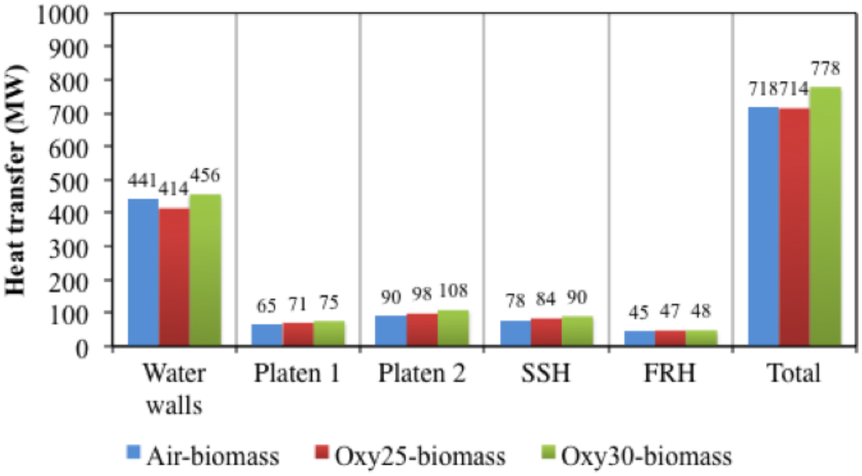

Figure 6.8: Heat transfer predictions between air and oxy-biomass cases at various superheater sections and water walls in the full-scale utility boiler.

6.6 Conclusions

In this chapter, a full-scale utility boiler design for air-coal combustion was simulated to assess the differences when firing coal or biomass under air or oxy-fuel conditions. The CFD combustion models were based on those chosen and validated in the modelling of a 250 kW_{th} in Chapter 5 for air-coal combustion.

The main findings are listed as follows:

- Within the limitation of the numerical model, the results suggest to match heat transfer characteristics in air-coal, that an oxygen mole fraction of 25% to 30% may be needed when firing coal. This is similar to a number of other suggestions on pilot scale plants [232–234].
- Switching to 100% biomass firing at full-load may be possible but the maximum thermal rating of the boiler may be lowered. A redesign of the boiler may be needed to achieve similar heat transfer characteristics to that of air-coal.
- In terms of oxy-biomass combustion, further oxygen enrichment may be needed to match the heat transfer characteristics of air-coal. However this can have

safety implications when using high levels of oxygen and this will hinder the purity of CO_2 in the flue gas, thus increasing costs in the purification and compression units.

Chapter 7

Conclusions and further work

The warming caused by climate change is unequivocal and since a major source of CO_2 is released from coal-fired power plants then it is imperative to apply carbon mitigating technologies, such as oxy-fuel combustion. Oxy-fuel combustion is near commercialisation, however technological barriers may still be evident if physical and chemical processes, such as the distribution of heat transfer, emissions and burnout from a boiler, which are important for power station operators, are not completely understood. The application of CFD with combustion sub-models is a tool that may give further insight and confidence in the deployment of oxy-fuel combustion. Since the combustion environment is different from that of air, conventional air-based sub-models may no longer be applicable. Therefore, the purpose of this thesis was to examine advanced combustion sub-models suitable for oxy-fuel combustion.

7.1 Conclusions

In this thesis, work has been presented on air and oxy-fuel environments which involved assessing the predictive capabilities of CFD combustion sub-models in labratory-scale burners, pilot-scale facilities and full-scale utility boilers. Particular attention was given to NO predictions coupled with the use of LES, a non-gray radiative gaseous property model and the impact of firing coal as well as biomass in a full-scale utility boiler.

The objectives of the thesis were described in Section 1.7 and are as follows:

(i) Collaborate with Imperial College and develop a CFD model for oxy-coal combustion.

(ii) Perform time-averaged RANS and LES in a CTF under air and oxy-fuel conditions and investigate suitable sub-models for oxy-coal combustion.

The contribution to these tasks are described in the following paragraphs.

The first objective was achieved in Chapter 4 where the in-house LES code *PsiPhi* was further developed by the implementation of a $\mathrm{NO_x}$ model. An analysis and validation of the model was performed under oxy-coal combustion, but also highlighted the flexibility of the model for gas and air-coal combustion. The model was sensitive to the chemical mechanism, however when coal was used as the fuel, the fuel-$\mathrm{NO_x}$ mechanism was the dominant source of NO in both air and oxy-coal environments. Also, when the $\mathrm{NO_x}$ model was solved *at the end of each time-step* of the LES rather than as a post-processing method performed *at the end of the simulation*, which is analogous to a steady RANS approach, most of the turbulent chemistry interaction was resolved by the LES. This was primarily due to the use of a fine grid, which subsequently led to sub-grid fluctuation effects on the prediction of NO being less significant. However, turbulent chemistry interaction effects could not be ignored when the $\mathrm{NO_x}$ model was solved *at the end of each time step.*

The second objective successfully applied both steady state RANS and LES modelling to a 250 $\mathrm{kW_{th}}$ CTF under air and oxy-coal combustion in Chapter 5. The CFD simulations were validated under air-coal combustion and the FSCK model, which is a more suitable radiative property model for oxy-coal combustion than the gray WSGGM approach was also tested. Results obtained from the non-gray FSCK model highlighted an improvement to the predictions of radiative heat flux. Oxy-fuel combustion studies were then performed highlighting the radiative heat flux is predicted to be higher while the CIA and CO is predicted to be lower in the gray

WSGG approach compared to the non-gray FSCK approach.

Due to the need for commercialisation of oxy-fuel technology, and the recent interest in biomass as a renewable source, CFD was used to numerically examine a full-scale utility boiler firing coal and biomass under air and oxy-fuel combustion, see Chapter 6. The validated sub-models used in Chapter 5 were used for all of the simulations, and benchmark data for an air-coal case compared well against the CFD model. The predictions of the biomass combustion highlighted a different heat transfer distribution which may result in the derating of an existing coal-fired boiler if switching to 100% biomass. Also, oxy-biomass was simulated as it has the potential for carbon-negative emissions, and the CFD simulations suggested that the boiler may have to operate with high oxygen inlet concentrations ($> 30\%$) to match that of its design specifications for air-coal combustion.

In this thesis, two CFD codes have been employed, namely the in-house LES code, *PsiPhi*, and a commercial CFD software package, Ansys fluent. For development purposes, an in-house code is advantageous as the source code is accessible unlike most commercial software packages which have a black-box configuration where subroutines within the code remain hidden from the user and this is one of the reasons why *PsiPhi* was used in Chapter 4. A further difference between the codes lies in the approach taken to generate the numerical mesh. The in-house code uses equidistant Cartesian cells which has difficulties in resolving the complex geometry or near wall modelling but allows for a structured, simpler code enabling a low computational cost as computer memory is accessed and stored in a structured manner. With respect to LES, the equidistant cells can further mitigate issues regarding anisotropic filters that may be present when local grid refinement is used. Due to the relatively simple geometry in the cases studied in Chapter 4, this was a further reason for using *PsiPhi*. Unstructured grids and local grid refinement in

Ansys fluent allows for a complex geometry to be used, however since Ansys fluent treats the mesh as unstructured, a high computational cost may be involved. Due to the complex geometry of the burner in the pilot scale facility, and the size of the utility boiler in Chapters 5 and 6, respectively, Ansys fluent was employed. Despite the differences in the codes, it has been demonstrated in this thesis that both codes produce physically reasonable predictions compared against experimental data for a number of air and oxy-fuel combustion cases.

7.2 Areas for further research

The investigation of the NO_x model in Chapter 4 suggested a number of improvements and parameter studies that may need to be performed. One key study would be to determine the impact of sub-grid scale turbulent chemistry interaction in LES by examining the influence of the shape and sub-grid scale variance model used in the FDF. Furthermore, the results suggested that the FDF may not have a significant impact on the solution, however only a single variable FDF with a top-hat function and the resolved gradient model [216] was tested. Results with other shapes, such as the β function, multiple variable FDFs and other SGS models, could be investigated. Furthermore, an overall improvement to the chemical kinetics may be beneficial as well as an attempt to pre-process the NO_x model into a look-up table to reduce the overall computational cost.

The investigation of the non-gray FSCK model to model gaseous radiative properties in the PACT facility in Chapter 5 highlighted an improved prediction of the radiative heat transfer to the wall when compared to experimental measurements in air-coal. A logical next step is to validate the non-gray FSCK model against the experimental data obtained in the oxy-fuel combustion studies. Further, optimisation of the model will play a key role in the application of the model in a full-scale furnace.

Improvements were shown to occur with the prediction of the in-flame gas temperatures in Chapter 5 when a RANS approach to turbulence was replaced by LES. A significant increase in computational time is required due to the transient nature of LES. A further investigation that needs to be performed is the sensitivity of the combustion simulations to the SGS model as this will have an impact on the flow field, temperature, species and heat flux, especially in coarse cells where the SGS contribution may be relatively high. Performing the LES on a finer grid to examine the impact of turbulent radiation interaction would be beneficial since the LES predictions were shown in Chapter 5 to have a higher radiative heat flux than RANS. A further improvement may be the combination of LES and the non-gray FSCK model. Reasonable computational resources are needed to achieve this and will probably be restricted to laboratory and pilot-scale facilities unless an efficient LES solver is employed. A future study may also investigate the use of *PsiPhi* and compare the results obtained against the available experimental data to further validate the combustion sub-models within the code.

The simulations in the full-scale boiler of biomass combustion ignored the effects of thermal gradients which may be important when large particles are used [41,146]. An area of improvement would be the investigation of the impact of a thermal gradients model within a CFD model of a pilot-scale CTF, ideally compared against experimental data. The model could then be applied to the simulations in Chapter 6 to examine the importance of thermal gradients in biomass particles within a full-scale utility boiler.

An ideal area of future research would be the simulation of coal and biomass under air and oxy-fuel conditions using a combination of LES with the non-gray

FSCK model and thermal gradient model. The 250 $\mathrm{kW_{th}}$ CTF has the capability and equipment to provide radiative heat flux, in-flame temperature and species measurements which provide a necessary platform to validate CFD combustion sub-models. Also, the CTF has the capability to provide particle velocity measurements through laser diagnostics, thus providing flow field measurements ideal for LES. Ports are also available for 2D/3D flame imaging which can give non-intrusive temperature measurements and determine flame flicker frequencies which may also be compared with frequency data from LES. Therefore, further work should include a number of experiments to provide the necessary validation data for CFD combustion sub-models.

In conclusion, a key focus on CFD modelling of oxy-fuel combustion should also be on the design and optimisation of second generation burners and boilers as oxy-fuel technology reaches commercialisation. Oxy-fuel combustion not only offers the opportunity to be a carbon reduction technology, but adds a further flexibility with respect to enriched oxygen and recycle ratio configuration which could lead to better combustion efficiency. This will ultimately increase the lifespan of the limited fossil fuels that remain in the world.

Bibliography

[1] British Petroleum. BP Statistical Review of World Energy, June 2013.

[2] British Petroleum. BP Energy Outlook 2030. London, January 2013.

[3] International Energy Agency (IEA). World Energy Outlook 2012, 2012.

[4] IEA Clean Coal Centre. Tracking Clean Energy Progress 2013, IEA input to the Clean Energy Ministerial, 2013.

[5] British Petroleum. BP Satistical Review of World Energy 2012. `http://www.bp.com/statisticalreview`, 2012. Accessed 05/04/2012.

[6] Çigdem K. A. and Tayfun B. Forecasting of CO_2 emissions from fuel combustion using trend analysis. *Renewable and Sustainable Energy Reviews*, 14(9):2906–2915, 2010.

[7] Intergovernmental Panel on Climate Change. *Climate Change 2007: The Physical Science Basis. Contribution of Working Group I to the Fourth Assessment Report of the Intergovernmental Panel on Climate Change.* Cambridge University Press, Cambridge, United Kingdom and New York, NY, USA, 2007.

[8] UNFCCC. Doha amendment to the Kyoto Protocol to the United Nations Framework Convention on Climate Change. `http://unfccc.int/kyoto_protocol/doha_amendment/items/7362.php`, December 2012. Accessed 20/06/13.

[9] Tans P. and Keeling R. Trends in Carbon Dioxide. NOAA/ESRL and Scripps Institution of Oceanography. http://www.esrl.noaa.gov/gmd/ccgg/trends/, October 2013.

[10] United States Energy Information Administration. International Energy Outlook 2010. `http://www.eia.gov/oiaf/ieo/index.html`, 2010. Accessed 23/12/2010.

[11] Carbon Dioxide Information Analysis Centre (CDIAC). `http://cdiac.ornl.gov/ftp/ndp030/CSV-FILES/global.1751_2007.csv`, 2007. Accessed 12/02/2011.

[12] UNFCCC. Kyoto Protocol. `http://unfccc.int/kyoto_protocol/items/2830.php`. Accessed 12/02/2011.

[13] EU-Lex. Directive 2010/75/EU of the European Parliament and of the Council on industrial emissions (integrated pollutant preventional and control). *Official Journal of the European Communities*, 334:17–119, 2010.

[14] The National Archives. Climate Change Act 2008. `http://www.legislation.gov.uk/ukpga/2008/27/contents`, 2008. Accessed 12/02/2011.

[15] Toftegaard M. B., Brix J., Jensen P. A., Glarborg P., and Jensen A. D. Oxy-fuel combustion of solid fuels. *Process in Energy and Combustion Science*, 36:581–625, 2010.

[16] DECC. UK Bioenergy Strategy. URN: 12D/077, London, 2012.

[17] Lu H., Warren R, Peirce G, Ripa B, and Baxter L. L. Comprehensive study of biomass particle combustion. *Energy Fuels*, 22:282639., 2008.

[18] International Energy Agency (IEA). Technology Roadmap Carbon Capture and Storage. Paris, France, 2013.

[19] VGB PowerTech e.V. CO_2 Capture and Storage: VGB Report on the State of the Art. `http://www.vgb.org/vgbmultimedia/Fachgremien/Umweltschutz/VGB+Capture+and+Storage.pdf`, 2004. Accessed 13/02/2011.

[20] Horn F. L. and Steinberg M. Control of carbon dioxide emissions from a power plant (and use in enhanced oil recovery) . *Fuel*, 61:415–422, 1982.

[21] Florin N. and Fennell P. Carbon capture technology: future fossil fuel use and mitigating climate change. `http://workspace.imperial.ac.uk/climatechange/Public/pdfs/Briefing%20Papers/Grantham%20Briefing%20paper_Carbon%20Capture%20Technology_November%202010.pdf`, 2010. Accessed 13/02/2011.

[22] British Broadcasting Corportation. Clean coal plants get go-ahead. `http://news.bbc.co.uk/1/hi/sci/tech/7586569.stm`, 2008. Accessed 03/06/2011.

[23] Davidson R. M. and Santos S. O. Oxyfuel combustion of pulverised coal. Technical Report CCC/168, IEA Clean Coal Centre, June 2010.

[24] Murciano L. T., White V., Petrocelli F., and Chadwick D. Sour compression process for the removal of SO_x and NO_x from oxyfuel-derived CO_2. *Energy Procedia*, 4:908 – 916, 2011. 10th International Conference on Greenhouse Gas Control Technologies.

[25] Halland E. K., Johansen W. T., and Riis F. CO_2 Storage Atlas Norweigen North Sea. http://www.npd.no/Global/Norsk/3-Publikasjoner/Rapporter/PDF/CO2-ATLAS-lav.pdf.

[26] Abraham B. M., Ashbury J. G., and Lynch E. P. Coal-oxygen process provides CO_2 for enhanced recovery. *Oil and Gas Journal*, 80(11):68–70, 1982.

[27] Wang C. S., Berry G. F., Chang K. C., and Wolsky A. M. Combustion of Pulverized Coal Using Waste Carbon Dioxide and Oxygen. *Combustion and Flame*, 72:301–310, 1988.

[28] Nakayama S. and Noguchi Y. Pulverized Coal Combustion in O_2/CO_2 Mixtures on a Power Plant for CO_2 Recovery. *Energy Convers. Mgmt*, 33(5-8):379–386, 1992.

[29] Kimura N., Omata K., Kiga T., Takano S., and Shikisima S. The characteristics of pulverized coal combustion in O_2/CO_2 mixtures for CO_2 recovery. *Energy Convers. Mgmt*, 36(6-9):805–808, 1995.

[30] Kiga T., Takano S., Kimura N., Omata K., Okawa M., Mori T., and Kato M. Characteristics of pulverized-coal combustion in the system of oxygen/recycled flue gas combustion. *Energy Consvers. Mgmt*, 38:S129–S134, 1997.

[31] Wall T., Liu Y., Spero C., Elliott L., Khare S., Rathnam R., Zeenathal F., Moghtaderi B., Buhre B., Sheng C., Gupta R., Yamada T., Makino K., and Yu J. An overview of oxyfuel coal combustion - State of the art research and technology development. *Chemical Engineering Research and Design*, 87(8):1003–1016, 2009.

[32] Douglas M. A., Chui E., Tan Y., Lee G. K., Croiset E., and Thambimuthu K. V. Oxy-fuel combustion at the CANMET Vertical Combustion Research Facility, 2001. In: Proc. of the First National Conference on Carbon Sequestration, Washington, DC, USA, 14-17 May.

[33] Gharebaghi M., Irons R. M. A., Ma L., Pourkashanian M., and Pranzitelli A. Large eddy simulation of oxy-coal combustion in an industrial combustion test facility. *International Journal of Greenhouse Gas Control*, 5(1):S100 – S110, 2011.

[34] Toporov D., Bocian P., Heil P., Kellermann A., Stadler H., Tschunko S., Förster M., and Kneer R. Detailed investigation of a pulverized fuel swirl flame in CO_2/O_2 atmosphere. *Combustion and Flame*, 155(4):605 – 618, 2008.

[35] Edge P., Gubba S. R., Ma L., Porter R., Pourkashanian M., and Williams A. LES modelling of air and oxy-fuel pulverised coal combustion - impact on flame properties. *Procedings of the Combustion Institute*, 33(2):2709–2716, 2011.

[36] Vattenfall. The Schwarze Pumpe pilot plant. `http://www.vattenfall.com/en/ccs/schwarze-pumpe_73203.htm`, 2010. Accessed 23/05/2011.

[37] Vattenfall. Oxycoal UK. `http://www.vattenfall.com/en/ccs/oxycoal-uk.htm`, 2010. Accessed 23/05/2011.

[38] Callide Oxyfuel Project. The Callide Oxyfuel Project. `http://www.callideoxyfuel.com/`. Accessed 23/05/2011.

[39] Versteeg H. K. and Malalasekera W. *An Introduction to Computational Fluid Dynamics: The Finite Volume Method*. Pearson Education Limited, second edition, 2007.

[40] Warzecha P. and Boguslawski A. LES and RANS modeling of pulverized coal combustion in swirl burner for air and oxy-combustion technologies. *Energy*, (66):732–743, 2014.

[41] Gubba S. R., Ingham D. B., Larsen K. J., Ma L., Pourkashanian M., Tan H. Z., Williams A., and Zhou H. Numerical modelling of the co-firing of pulverised coal and straw in a 300 MW_e tangentially fired boiler. *Fuel Processing Technology*, 104:181 – 188, 2012.

[42] Ma L., Jones J. M., Pourkashanian M., and Williams A. Modelling the combustion of pulverized biomass in an industrial combustion test furnace. *Fuel*, 86(12-13):1959 – 1965, 2007.

[43] Black S., Szuhánszki J., Pranzitelli A., Ma L., Stanger P. J., Ingham D. B., and Pourkashanian M. Effects of firing coal and biomass under oxy-fuel conditions in a power plant boiler using CFD modelling. *Fuel*, 113:780 – 786, 2013.

[44] Szuhánszki J., Black S., Pranzitelli A., Ma L., Stanger P. J., Ingham D. B., and Pourkashanian M. Evaluation of the Performance of a Power Plant Boiler Firing Coal, Biomass and a Blend Under Oxy-fuel Conditions as a CO_2 Capture Technique. *Energy Procedia*, 37:1413 – 1422, 2013.

[45] Franchetti B. M., Cavallo Marincola F., Navarro-Martinez S., and Kempf A. M. Large Eddy simulation of a pulverised coal jet flame. *Proceedings of the Combustion Institute*, 34(2):2419 – 2426, 2013.

[46] Yamamoto K., Murota T., Okazaki T., and Taniguchi M. Large eddy simulation of a pulverised coal jet flame ignited by a preheated gas flow. *Procedings of the Combustion Institute*, 33:1771–1778, 2011.

[47] Acheson D. J. *Elementary Fluid Dynamics.* Oxford University Press, first edition, 1990.

[48] Poinsot T. and Veynante D. *Theoretical and Numerical Combustion.* Edwards, first edition, 2001.

[49] Ferziger J. H. and Perić M. *Computational Methods for Fluid Dynamics.* Springer, 2002.

[50] Pope S. B. *Turbulent Flows.* Cambridge University Press, 2000.

[51] Richardson L. F. *Weather Prediction by Numerical Process.* Cambridge University Press, 1922.

[52] Kolmogorov A. N. The local structure of turbulence in incompressible viscous fluid for very large Reynold numbers. *Dokl. Akad. Nauk SSSR*, 30:9–13, 1941.

[53] Luo K., Wang H., Fan J., and Yi F. Direct Numerical Simulation of Pulverized Coal Combustion in a Hot Vitiated Co-flow. *Energy & Fuels*, 26(10):6128–6136, 2012.

[54] Kempf A. M. LES Validation from Experiments. *Flow Turbulence Combustion*, 80:351–373, 2008.

[55] Hawkes E. R., Sankaran R., Sutherland J. C., and Chen J. H. Direct numerical simulation of turbulent combustion: fundamental insights towards predictive models. *Journal of Physics: Conference Series*, 16(1):65, 2005.

[56] Spalart P. and Allmaras S. A. One-Equation Turbulence Model for Aerodynamic Flows. *AIAA Paper*, 92-0439, 1992.

[57] Launder B. E. and Spalding D. B. The numerical computation of turbulent flows. *Computer Methods in Applied Mechanics and Engineering*, 3(2):269 – 289, 1974.

[58] Peters A. A. F. and Weber R. Mathematical Modeling of a 2.4 MW Swirling Pulverized Coal Flame. *Combustion Science and Technology*, 122(1-6):131–182, 1997.

[59] ANSYS Inc. *FLUENT Theory Guide*, 2013.

[60] Dally B. B., Fletcher D. F., and Masri A. R. Flow and mixing fields of turbulent bluff-body jets and flames. *Combustion Theory and Modelling*, 2(2):193–219, 1998.

[61] Yakhot V., Orszag S. A., Thangam S., Gatski T. B., and Speziale C. G. Development of turbulence models for shear flows by a double expansion technique. *Physics of Fluids A: Fluid Dynamics (1989-1993)*, 4(7):1510–1520, 1992.

[62] Backreedy R. I., Fletcher L. M., Ma L., Pourkashanian M., and Williams A. Modelling pulverised coal combustion using a detailed coal combustion model. *Combust. Sci. and Tech*, 178:763–787, 2006.

[63] Shamami K. K. and Birouk M. Assessment of the Performances of RANS Models for Simulating Swirling Flows in a Can-Combustor. *The Open Aerospace Engineering Journal*, 1:8–27, 2008.

[64] Shih T., William W. L., Shabbir A., Yang Z., and Zhu J. A new k-epsilon eddy viscosity model for high reynolds number turbulent flows. *Computers & Fluids*, 24(3):227 – 238, 1995.

[65] Wilcox D. *Turbulence Modelling for CFD*. DCW Industries Inc, 3rd edition edition, 1993.

[66] Menter F. R. Improved Two-Equation k-ω Turbulence Models for Aerodynamic Flows. Technical report, NASA Technical Memorandum TM-103975, 1992.

[67] Denaro F. M. What does Finite Volume-based implicit filtering really resolve in Large-Eddy Simulations? . *Journal of Computational Physics*, 230(10):3849 – 3883, 2011.

[68] Lund T. S. The use of explicit filters in large eddy simulation. *Computers & Mathematics with Applications*, 46(4):603 – 616, 2003. Turbulence Modelling and Simulation.

[69] Bose S. T., Moin P., and You D. Grid independent large-eddy simulation using explicit filtering. In *Center for Turbulent Research: Annual Research Briefs 2008*, page 173, 2008.

[70] Speziale C. Turbulence Modeling for Time-Dependent RANS and VLES: A Review. *AIAA Journal*, 36(2):173–184, 1998.

[71] Deardorff J. W. A numerical study of three-dimensional turbulent channel flow at large Reynolds numbers. *J. Fluid Mech*, 41:453–480, 1970.

[72] Speziale C. G. Galilean invariance of subgrid-scale stress models in the large-eddy simulation of turbulence. *J. Fluid Mech*, 156:55–62, 1985.

[73] Yeoh G. H. and Yuen K. K., editors. *Computational Fluid Dynamics in Fire Engineering*. Butterworth-Heinemann, Burlington, 2009.

[74] Lilly D. K. On the Application of the Eddy Viscosity Concept in the Interial Sub-range of Turbulence. Technical report, NCAR Manuscript No. 123, 1966.

[75] Lilly D. K. The representation of small-scale turbulence in numerical simulation experiments. Technical report, NCAR Report No. 281, 1966.

[76] Kempf A. M., Geurts B. J., and Oefelein J. C. Error analysis of large-eddy simulation of the turbulent non-premixed sydney bluff-body flame. *Combustion and Flame*, 158(12):2408 – 2419, 2011.

[77] Scotti A., Meneveau C., and Lilly D. K. Generalized smagorinsky model for anisotropic grids. *Physics of Fluids A: Fluid Dynamics (1989-1993)*, 5:2306, 1993.

[78] van Driest E. R. On Turbulent Flow Near a Wall. *Journal of the Aeronautical Sciences*, 23(23):1007–1011,1036, 1956.

[79] Nicoud F. and Ducros F. Subgrid-Scale Stress Modelling Based on the Square of the Velocity Gradient Tensor. *Flow, Turbulence and Combustion*, 62:183–200, 1999.

[80] Germano M., Piomelli U., Moin P., and Cabot W. H. A dynamic subgrid-scale eddy viscosity model. *Physics of Fluids*, 3:1760–1765, July 1991.

[81] Celik I. B., Cehreli Z. N., and Yavuz I. Index of Resolution Quality for Large Eddy Simulations. *Journal of Fluids Engineering*, 127(6):949–958, 2005.

[82] Meneveau C. and Katz J. Scale-Invariance and Turbulence Models for Large-Eddy Simulation. *Annu. Rev. Fluid Mech.*, 32:1–32, 2000.

[83] Kempf A. M., Klein M., and Janicka J. Efficient Generation of Initial- and Inflow-Conditions for Transient Turbulent Flows in Arbitrary Geometries. *Flow, Turbulence Combustion*, 74:67–84, 2005.

[84] Klein M., Sadiki A., and Janicka J. A digital filter based generation of inflow data for spatially developing direct numerical or large eddy simulations. *Journal of Computational Physics*, 186:652–665, 2003.

[85] Coal Online. Fundamentals of coal combustion. `http://www.coalonline.org/site/coalonline/content/Viewer/81591/6247/5247_1.html/Fundamentals-of-coal-combustion`, 2007. Accessed 11/01/2011.

[86] Chen L., Yong S. Z., and Ghoniem A. F. Oxy-fuel combustion of pulverized coal: Characterization, fundamentals, stabilization and CFD modeling. *Progress in Energy and Combustion Science*, 38(2):156 – 214, 2012.

[87] Baum M. M. and Street P. J. Predicting the Combustion Behavior of Coal Particles. *Combust. Sci. Tech.*, 3(5):231–243, 1971.

[88] Yu J., Lucas J. A., and Wall T. Formation of the structure of chars during devolatilisation of pulverised coal and its thermoproperties: A review. *Progress in Energy and Combustion Science*, 33:137–170, 2007.

[89] Kimber G. M. and Gray M. D. Rapid devolatilisation of small coal particles. *Combustion and Flame*, 11(4):360–362, 1967.

[90] Badzioch S. and Hawksley P. G. W. Kinetics of Thermal Decomposition of Pulverized Coal Particles. *Ind. Eng. Chem. Process Des. Develop.*, 9(4):521–530, 1970.

[91] Kobayahsi H., Howard J. B., and Sarofim A. F. Coal Devolatilization at High Temperatures. *Symposium (International) on Combustion*, 16(1):411–425, 1976.

[92] Fletcher T. H. and Hardesty D. R. Compilation of Sandia Coal Devolatilization Data: Milestone Report. *SAND92-8209*, 1992.

[93] Ubhayakar S. K., Stickler D. N., von Rosenberg C. W., and Gannon R. E. Rapid devolatilization of pulverised coal in hot combustion gases. *Proceedings of the Combustion Instit*i*ute*, 16(1):427–436, 1976.

[94] Bassilakis R., Zhao Y., Solomon P. R., and Serio M. A. Sulfur and nitrogen evolution in the Argonne coals. Experiment and modeling. *Energy & Fuels*, 7(6):710–720, 1993.

[95] Niksa S. FLASHCHAIN Theory for Rapid Coal Devolatilization Kinetics. 6. Predicting the Evolution of Fuel Nitrogen from Various Coals. *Energy & Fuels*, 9(3):467–478, 1995.

[96] Genetti D. *An Advanced Model of Coal Devolatilization Based on Chemical Structure.* PhD thesis, Brigham Young University, 1999.

[97] Chen Y., Charpenay S., Jensen A., Wojtowicz M. A., and Serio M. A. Modeling of biomass pyrolysis kinetics. *Symposium (International) on Combustion*, 27:1327, 1998.

[98] Lewis A. D. and Fletcher T. H. Prediction of Sawdust Pyrolysis Yields from a Flat-Flame Burner Using the CPD Model. *Energy & Fuels*, 27(2):942–953, 2013.

[99] Backreedy R. I., Habib R., Jones J. M, Pourkashanian M., and Williams A. An extended coal combustion model. *Fuel*, 78:1745–1754, 1999.

[100] Williams A., Backreedy R., Habib R., Jones J. M., and Pourkashanian M. Modelling coal combustion: the current position. *Fuel*, 81(5):605 – 618, 2002.

[101] Jovanović R., Milewska A., Swiatkowski B., Goanta A., and Spliethoff H. Sensitivity analysis of different devolatilisation models on predicting ignition point position during pulverized coal combustion in O_2/N_2 and O_2/CO_2 atmospheres. *Fuel*, 101(0):23 – 37, 2012. 8th European Conference on Coal Research and Its Applications.

[102] Rathnam R. K., Elliott L. K., Wall T. F., Liu Y., and Moghtaderi B. Differences in reactivity of pulverised coal in air (O2/N2) and oxy-fuel (O_2/CO_2) conditions. *Fuel Processing Technology*, 90(6):797 – 802, 2009.

[103] Álvarez L., Gharebaghi M., Jones J. M., Pourkashanian M., Williams A., Riaza J., Pevida C., Pis J. J., and Rubiera F. Numerical investigation of NO emissions from an entrained flow reactor under oxy-coal conditions. *Fuel Processing Technology*, 93(1):53 – 64, 2012.

[104] Álvarez L., Gharebaghi M., Jones J. M., Pourkashanian M., Williams A., Riaza J., Pevida C., Pis J. J., and Rubiera F. CFD modeling of oxy-coal combustion: Prediction of burnout, volatile and NO precursors release. *Applied Energy*, 104(0):653 – 665, 2013.

[105] Solomon P. R., Serio M. A., and Suuberg E.M. Coal pyrolysis: Experiments, kinetic rates and mechanisms. *Progress in Energy and Combustion Science*, 18(2):133 – 220, 1992.

[106] Williams A., Pourkashanian M., and Jones J. M. Combustion of pulverised coal and biomass. *Progress in Energy and Combustion Science*, 27(6):587 – 610, 2001.

[107] Smith G. P., Golden D. M., Frenklach M., Moriarty N. W., Eiteneer B., Goldenberg M., Bowman C. T., Hanson R. K., Song S., Gardiner W. C., Lissianski V. V., and Zhiwei Q. `http://www.me.berkeley.edu/gri_mech/`. Accessed 17/06/2013.

[108] Magnussen B. F. and Hjertager B. H. On mathematical modelling of turbulent combustion with special emphasis on soot formation and combustion. *Symposium (International) on Combustion*, 16(1):719–729, 1977.

[109] Spalding D. B. Mixing and chemical reaction in confined turbulent flames. *Thirteenth Symposium (International) on Combustion*, pages 649–657, 1971.

[110] Edge P.J., Heggs P.J., Pourkashanian M., Stephenson P., and Williams A. A reduced order full plant model for oxyfuel combustion. *Fuel*, 101(0):234 – 243, 2012. 8th European Conference on Coal Research and Its Applications.

[111] Breussin F., Lallemant N., and Weber R. Computing of Oxy-Natural Gas Flames using Both a Global Combustion Scheme and a Chemical Equilibrium Procedure. *Combustion Science and Technology*, 160(1):369–397, 2000.

[112] Magnussen B. F. On the Structure of Turbulence and a generalized Eddy Dissipation Concept for Chemical Reaction in Turbulent Flow. Technical report, 19th American Institute of Aeronautics and Astronautics Aerospace Science Meeting, St. Louis, Missouri, USA, January 1981.

[113] Westbrook C. K. and Dryer F. L. Simplified Reaction Mechanisms for the Oxidation of Hydrocarbon Fuels in Flames. *Combustion Science and Technology*, 27(1-2):31–43, 1981.

[114] Jones W. P. and Lindstedt R. P. Global reaction schemes for hydrocarbon combustion. *Combustion and Flame*, 73(3):233 – 249, 1988.

[115] Andersen J., Rasmussen C. L., Giselsson T., and Glarborg P. Global Combustion Mechanism for Use in CFD Modeling under Oxy-Fuel Conditions. *Energy and Fuels*, 23(3):1379–1389, 2009.

[116] Peters P. Laminar diffusion flamelet models in non-premixed turbulent combustion. *Progress in Energy and Combustion Science*, 10(3):319 – 339, 1984.

[117] Pitsch H., Chen M., and Peters N. Unsteady flamelet modeling of turbulent hydrogen-air diffusion flames. *Symposium (International) on Combustion*, 27(1):1057 – 1064, 1998. Twenty-Seventh Sysposium (International) on Combustion Volume One.

[118] Carpenter A. M., Niksa S., SRI International, Scott D. H., and Wu Z. Fundamentals of coal combustion. `http://www.coalonline.info/site/coalonline/content/browser/81591/Fundamentals-of-coal-combustion`, 2007. Accessed 12/03/2014.

[119] Mitchell R. E., Kee R. J., Glarborg P., and Coltrin M. E. The effect of CO conversion in the boundary layers surrounding pulverized-coal char particles. *Symposium (International) on Combustion*, 23(1):1169 – 1176, 1991. Twenty-Third Symposium (International) on Combustion.

[120] Field M. A. Rate of combustion of size-graded fractions of char from a low rank coal between 1200K-2000K. *Comb. Flame*, 13:237–252, 1969.

[121] Smith I. W. The Combustion Rates of Coal Chars: A Review. *19th Symp. (Int'l) on Combustion*, pages 1045–1065, 1982.

[122] Smith I. W. The intrinsic reactivity of carbons to oxygen. *Fuel*, 57(7):409 – 414, 1978.

[123] Hurt R., Sun J., and Lunden M. A Kinetic Model of Carbon Burnout in Pulverized Coal Combustion. *Combustion and Flame*, 113(12):181 – 197, 1998.

[124] Gharebaghi M., Irons R. M., Pourkashanian M., and Williams A. An investigation into a carbon burnout kinetic model for oxycoal combustion. *Fuel Processing Technology*, 92(12):2455 – 2464, 2011.

[125] Kuhr C., Ehmann M., Rehfeldt S., Bergins C., Maier J., Scheffknecht G., and Wu S. Modeling of Char Combustion in CO_2/O_2 and N_2/O_2 atmospheres. In *The 35th international technical conference on clean coal and fuel systems.*, 2010.

[126] Guo X., Tay H. L., Zhang S., and C. Li. Changes in Char Structure during the Gasification of a Victorian Brown Coal in Steam and Oxygen at 800°C. *Energy & Fuels*, 22(6):4034–4038, 2008.

[127] Várhegyi G., Szabó P., Jakab E., Till F., and Richard J.R. Mathematical Modeling of Char Reactivity in Ar-O_2 and CO_2-O_2 Mixtures. *Energy & Fuels*, 10(6):1208–1214, 1996.

[128] Smart J. P., O'Nions P. O., and Riley G. S. Radiation and convective heat transfer, and burnout in oxy-coal combustion. *Fuel*, 89:2468–2476, 2010.

[129] Normann F., Andersson K., Leckner B., and Johnsson F. Emission control of nitrogen oxides in the oxy-fuel process. *Progress in Energy and Combustion Science*, 35:385–397, 2009.

[130] Williams A., Jones J. M., Ma L., and Pourkashanian M. Pollutants from the combustion of solid biomass fuels. *Progress in Energy and Combustion Science*, 38(2):113 – 137, 2012.

[131] Fenimore C. P. Formation of Nitric Oxide in Premixed Hydrocarbon Flames. *13th Symp. Int. Comb.*, page 373, 1971.

[132] Glassman I. and Yetter R. A. *Combustion.* Elsevier, fourth edition, 2008.

[133] Glarborg P., Jensen A. D., and Johnsson J. E. Fuel nitrogen conversion in solid fuel fired systems. *Progress in Energy and Combustion Science*, 29(2):89 – 113, 2003.

[134] Jones J. M., Patterson P. M., Pourkashanian M., Williams A., Arenillas A., Rubiera F., and Pis J. J. Modelling NO_x formation in coal particle combustion at high temperature: an investigation of the devolatilisation kinetic factors. *Fuel*, 78(10):1171 – 1179, 1999.

[135] Hansen S. and Glarborg P. A Simplified Model for Volatile-N Oxidation. *Energy & Fuels*, 24(5):2883–2890, 2010.

[136] Ahn J., Okerlund R., Fry A., and Eddings E. G. Sulfur trioxide formation during oxy-coal combustion. *International Journal of Greenhouse Gas Control*, 5, Supplement 1:S127 – S135, 2011. Oxyfuel Combustion Technology - Working Toward Demonstration and Commercialisation.

[137] Brown A. L. and Fletcher T. H. Modeling Soot Derived from Pulverized Coal. *Energy & Fuels*, 12(4):745–757, 1998.

[138] Hayashi J., Hashimoto N., Nakatsuka N., Tsuji H., Watanabe H., Makino H., and Akamatsu F. Soot formation characteristics in a lab-scale turbulent pulverized coal flame with simultaneous planar measurements of laser induced incandescence of soot and Mie scattering of pulverized coal. *Proceedings of the Combustion Institute*, 34(2):2435 – 2443, 2013.

[139] Stimpson C. K., Fry A., Blanc T., and Tree D. R. Line of sight soot volume fraction measurements in air- and oxy-coal flames. *Proceedings of the Combustion Institute*, 34(2):2885 – 2893, 2013.

[140] Morris W. J., Yu D., and Wendt J. O. L. A comparison of soot, fine particle and sodium emissions for air- and oxy-coal flames, with recycled flue gases of various compositions. *Proceedings of the Combustion Institute*, 34(2):3453 – 3461, 2013.

[141] Yang Y. B., Sharifi V. N., Swithenbank J., Ma L., Darvell L. I., Jones J. M., Pourkashanian M., and Williams A. Combustion of a single particle of biomass. *Energy & Fuels*, 22(1):306–316, 2008.

[142] Wadell H. The coefficient of resistance as a function of Reynolds number for solids of various shapes. *Journal of the Franklin Institute*, 217(4):459 – 490, 1934.

[143] Haider A. and Levenspiel O. Drag coefficient and terminal velocity of spherical and nonspherical particles. *Powder Technology*, 58(1):63 – 70, 1989.

[144] Ranz W. E. and Marshall W. R. Evaporation from drops. Parts I & II. *Chem. Eng. Progr.*, 48:141–146, 1952.

[145] Ma L., Gharebaghi M., Porter R., Pourkashanian M., Jones J. M., and Williams A. Modelling methods for co-fired pulverised fuel furnaces. *Fuel*, 88(12):2448 – 2454, 2009. 7th European Conference on Coal Research and Its Applications.

[146] Gubba S. R., Ma L., Pourkashanian M., and Williams A. Influence of particle shape and internal thermal gradients of biomass particles on pulverised coal/biomass co-fired flames. *Fuel Processing Technology*, 92(11):2185 – 2195, 2011.

[147] Modest M. F. *Radiative Heat Transfer Second Edition.* Academic Press, 2003.

[148] Lockwood F. C. and Shah N. G. A new radiation solution method for incorporation in general combustion prediction procedures. *Symposium (International) on Combustion*, 18(1):1405 – 1414, 1981. Eighteenth Symposium (International) on Combustion.

[149] Murthy J. Y. and Mathur S. R. Finite Volume Method for Radiative Heat Transfer Using Unstructured Meshes. *Journal of Thermophysics and Heat Transfer*, 12(3):313–321, 1998.

[150] Sazhin S.S., Sazhina E.M., Faltsi-Saravelou O., and Wild P. The P-1 model for thermal radiation transfer: advantages and limitations . *Fuel*, 75(3):289 – 294, 1996.

[151] Edge P., Gharebaghi M., Irons R., Porter R., Porter R. T. J., Pourkashanian M., Smith D., Stephenson P., and Williams A. Combustion modelling opportunities and challenges for oxy-coal carbon capture technology. *Combustion Engineering Research and Design*, 2011. doi:10.1016/j.cherd.2010.11.010.

[152] Grosshandler W. L. Radiative heat transfer in nonhomogeneous gases: A simplified approach. *International Journal of Heat and Mass Transfer*, 23(11):1447 – 1459, 1980.

[153] Rothman L. S., Gordon I. E., Barber R. J., Dothe H., Gamache R. R., Goldman A., Perevalov V. I., Tashkun S. A., and Tennyson J. HITEMP, the high-temperature molecular spectroscopic database. *Journal of Quantitative Spectroscopy and Radiative Transfer*, 111(15):2139 – 2150, 2010. XVIth Symposium on High Resolution Molecular Spectroscopy (HighRus-2009) XVIth Symposium on High Resolution Molecular Spectroscopy.

[154] Viskanta R. and Mengüç M. P. Radiation heat transfer in combustion systems. *Progress in Energy and Combustion Science*, 13(2):97 – 160, 1987.

[155] Goody R. M. A statistical model for water-vapour absorption. *Quarterly Journal of the Royal Meteorological Society*, 78(336):165–169, 1952.

[156] Goody R., West R., Chen L., and Crisp D. The correlated-k method for radiation calculations in nonhomogeneous atmospheres. *Journal of Quantitative Spectroscopy and Radiative Transfer*, 42(6):539 – 550, 1989.

[157] Edwards D. K. and Menard W. A. Comparison of Models for Correlation of Total Band Absorption. *Appl. Opt.*, 3(5):621–625, May 1964.

[158] Edwards D. K. and Balakrishnan A. Thermal radiation by combustion gases. *International Journal of Heat and Mass Transfer*, 16(1):25 – 40, 1973.

[159] Hottel H. C. and Sarofim A. F. *Radiative Transfer*. McGraw-Hill, 1967.

[160] Smith T. F., Shen Z. F., and Friedman J. N. Evaluation of Coefficients for the Weighted Sum of Gray Gases Model. *ASME*, 104:602–608, 1982.

[161] Johansson R., Andersson K., Leckner B., and Thunman H. Models for gaseous radiative heat transfer applied to oxy-fuel conditions in boilers. *International Journal of Heat and Mass Transfer*, 53(1):220 – 230, 2010.

[162] Johansson R., Leckner B., Andersson K., and Johnsson F. Account for variations in the H_2O to CO_2 molar ratio when modelling gaseous radiative heat transfer with the weighted-sum-of-grey-gases model. *Combustion and Flame*, 158(5):893 – 901, 2011.

[163] Kangwanpongpan T., França F. H. R., Corrêa da Silva R., Schneider P. S., and Krautz H. J. New correlations for the weighted-sum-of-gray-gases model in oxy-fuel conditions based on HITEMP 2010 database. *International Journal of Heat and Mass Transfer*, 55(25):7419 – 7433, 2012.

[164] Porter R., Liu F., Pourkashanian M., Williams A., and Smith D. Evaluation of solution methods for radiative heat transfer in gaseous oxy-fuel combustion environments. *Journal of Quantitative Spectroscopy and Radiative Transfer*, 111(14):2084 – 2094, 2010.

[165] Grosshandler W. L. and Monteiro S. L. P. Attenuation of Thermal Radiation by Pulverized Coal and Char. *Journal of Heat Transfer*, 104(4):587–593, 1982.

[166] Johansson R., Leckner B., Andersson K., and Johnsson F. Influence of particle and gas radiation in oxy-fuel combustion. *International Journal of Heat and Mass Transfer*, 65:143 – 152, 2013.

[167] Masri A. R., Pope S. B., and Dally B. B. Probability density function computations of a strongly swirling nonpremixed flame stabilized on a new burner. *Proceedings of the Combustion Insitute*, 28:123–131, 2000.

[168] Sandia National Laboratories. International Workshop on Measurement and Computation of Turbulent Nonpremixed flames. http://www.sandia.gov/TNF/abstract.html.

[169] Kalt P. A. M., Al-Abdeli Y. M., Masri A. R., and Barlow R. S. Swirling turbulent non-premixed flames of methane: flow field and compositional structure. *Procedings of the Combustion Institute*, 29:1913–1919, 2002.

[170] Masri A. R., Kalt P. A. M., and Barlow R. S. The compositional structure of swirl-stabilised turbulent nonpremixed flames. *Combustion and Flame*, 137:1–37, 2004.

[171] Kempf A. M., Malalasekera W., Ranga-Dinesh K. K. J., and Stein O. Large Eddy Simulations of Swirling Non-premixed Flames With Flamelet Models: A Comparison of Numerical Methods. *Flow Turbulence Combust*, 80:351–373, 2008.

[172] Stein O. and Kempf A. M. LES of the syndney swirl flame series: A study of vortex breakdown in isothermal and reacting flows. *Proceedings of the Combustion Institute*, 31:1755–1763, 2007.

[173] Stein O., Kempf A. M., and Janicka J. LES of the syndney swirl flame series: an inital investigation of the fluid dynamics. *Combust. Sci. and Tech.*, 179:173–189, 2007.

[174] Hu L. Y., Zhou L. X., and Luo Y. H. Large-Eddy Simulation of the Sydney Swirling NonPremixed Flame and Validation of Several Subgrid-Scale Models. *Numerical Heat Transfer, Part B: Fundamentals*, 53(1):39–58, 2008.

[175] Sydney University. Swirl Flows and Flames Database, Experimental Data Download Site, available at:. http://sydney.edu.au/engineering/aeromech/thermofluids. Accessed 13/02/2011.

[176] Hwang S. M., Kurose R., Akamatsu F., Tsuji H., Makino H., and Katsuki M. Application of Optical Diagnostics Techniques to a Laboratory-Scale Turbulent Pulverized Coal Flame. *Energy & Fuels*, 19:382–392, 2005.

[177] Hwang S. M., Kurose R., Akamatsu F., Tsuji H., Makino H., and Katsuki M. Observation of a Detailed Structure of Turbulent Pulverized-Coal Flame by Optical Measurement (Part 1, Time-Averaged Measurement of Behavior of Pulverized-Coal Particles and Flame Structure). *Tans. Jpn. Soc. Mech. Eng.*, 71(710):2560–2567, 2006.

[178] Hwang S. M., Kurose R., Akamatsu F., Tsuji H., Makino H., and Katsuki M. Observation of a Detailed Structure of Turbulent Pulverized-Coal Flame by Optical Measurement (Part 2, Instantaneous Two-Dimensional Measurement of Combustion Reaction Zone and Pulverized-Coal Particles). *Tans. Jpn. Soc. Mech. Eng.*, 71(711):2754–2760, 2006.

[179] Hashimoto N., Kurose R., and Shirai H. Numerical simulation of pulverized coal jet flame employing the TDP model. *Fuel*, 97(0):277 – 287, 2012.

[180] Beér J. M. and Chigier N. A. *Combustion Aerodynamics.* Applied Science Publishers Ltd, 1972.

[181] Coraggio G. Measurement Equipment Suction Pyrometer. Technical Report Doc. No. C76/y/1/17b, IFRF, 2009.

[182] Rosin P. and Rammler E. The Laws Governing the Fineness of Powdered Coal. *Journal of the Institute of Fuel*, 7:29–36, 1933.

[183] Edge P. *Modelling and simulation of oxy-coal fired power plants.* PhD thesis, University of Leeds, 2011.

[184] Hill S. C. and Smoot L. D. Modeling of nitrogen oxides formation and destruction in combustion systems. *Progress in Energy and Combustion Science*, 26(4):417 – 458, 2000.

[185] Buhre B. J. P., Elliott L. K., Sheng C. D., Gupta R. P., and Wall T. F. Oxy-fuel combustion technology for coal-fired power generation. *Progress in Energy and Combustion Science*, 31:203–307, 2005.

[186] Andersson K., Normann F., Johnsson F., and Leckner B. NO Emission during Oxy-Fuel Combustion of Lignite. *Industrial & Engineering Chemistry Research*, 47(6):1835–1845, 2008.

[187] Kühnemuth D., Normann F., Andersson K., Johnsson F., and Leckner B. Reburning of Nitric Oxide in Oxy-Fuel Firing - The Influence of Combustion Conditions. *Energy & Fuels*, 25(2):624–631, 2011.

[188] Stadler H., Christ D., Habermehl M., Heil P., Kellermann A., Ohliger A., Toporov D., and Kneer R. Experimental investigation of NO_x emissions in oxycoal combustion. *Fuel*, 90(4):1604 – 1611, 2011.

[189] Cao H., Sun S., Liu Y., and Wall T. F. Computational Fluid Dynamics Modeling of NOx Reduction Mechanism in Oxy-Fuel Combustion. *Energy & Fuels*, 24(1):131–135, 2010.

[190] Arenillas A., Backreedy R. I., Jones J. M., Pis J. J., Pourkashanian M., Rubiera F., and Williams A. Modelling of NO formation in the combustion of coal blends. *Fuel*, 81(5):627 – 636, 2002.

[191] Godel G., Domingo P., and Vervisch L. Tabulation of NO_x chemistry for Large-Eddy Simulation of non-premixed turbulent flames . *Proceedings of the Combustion Institute*, 32(1):1555 – 1561, 2009.

[192] Pope S. B. PDF methods for turbulent reactive flows. *Progress in Energy and Combustion Science*, 11(2):119 – 192, 1985.

[193] Hanson R. K. and Salimian S. Survey of Rate Constants in the N/H/O System. In Jr. W. C. Gardiner, editor, *Combustion Chemistry*, pages 361–421. Springer-Verlag, 1984.

[194] Floyd J., Kempf A. M., Kronenburg A., and Ram R. H. A simple model for the filtered density function for passive scalar combustion LES. *Combustion Theory and Modelling*, 13(4):559–588, 2009.

[195] Williams A., Pourkashanian M., and Rowlands L. A review of NO_x formation and reduction mechanisms in combustion systems, with particular reference to coal. *Journal of the Institute of Energy*, 70:102–113, 1997.

[196] Pettit M. W. A., Coriton B., Gomez A., and Kempf A. M. Large-Eddy simualtion and experiments on non-premixed highly turbulent opposed jet flows. *Proceedings of the Combustion Institute*, 33:1391–1399, 2011.

[197] Cavallo Marincola F., Ma T., and Kempf A. M. Large eddy simulations of the Darmstadt turbulent stratified flame series. *Proceedings of the Combustion Institute*, 34(1):1307 – 1315, 2013.

[198] Stein O. T., Olenik G., Kronenburg A., Cavallo Marincola F., Franchetti B. M., Kempf A. M., Ghiani M., Vascellari M., and Hasse C. Towards Comprehensive Coal Combustion Modelling for LES. *Flow Turbulence Combust*, 90:859–884, 2013.

[199] Kempf A. M. *Large-Eddy Simulation of Non-Premixed Turbulent Flames.* PhD thesis, Technische Universität Darmstadt, 2003.

[200] Smagorinksy J. General circulation experiments with the primitive equations I. The Basic Experiments. *Monthly Weather Review*, 91(3):99–164, 1963.

[201] Ma C. Y., Mahmud T., Hampartsoumian E., Richardson J., and Gaskell P. H. Mathematical Modelling of Nitric Oxide Formation in Turbulent Diffusion Flames Doped with a Nitrogen Compound. *Combustion Science and Technology*, 160(1):345–367, 2000.

[202] Manion J. A., Huie R. E., Levin R. D., Burgess Jr. D. R., Orkin V. L., Tsang W., McGivern W. S., Hudgens J. W., Knyazev V. D., Atkinson D. B., Chai E., Tereza A. M., Lin C-Y., Allison T. C., Mallard W. G., Westley F., Herron J. T., Hampson R. F., and Frizzell D. H. NIST Chemical Kinetics Database, NIST Standard Reference Database 17, Version 7.0 (Web Version), Release 1.6.8, Data version 2013.03, National Institute of Standards and Technology, Gaithersburg, Maryland, 20899-8320. http://kinetics.nist.gov/, March 2013.

[203] Homer J. B. and Sutton M. M. Nitric oxide formation and radical overshoot in premixed hydrogen flames. *Combustion and Flame*, 20(1):71 – 76, 1973.

[204] Coelho P. J. and Carvalho M. G. Mathematical Modelling of NO Formation in a Power Station Boiler. *Combustion Science and Technology*, 108(4-6):363–382, 1995.

[205] Westenberg A. A. Kinetics of NO and CO in Lean, Premixed Hydrocarbon-Air Flames. *Combustion Science and Technology*, 4(1):59–64, 1971.

[206] Westbrook C. K. and Dryer F. L. Chemical kinetic modeling of hydrocarbon combustion. *Progress in Energy and Combustion Science*, 10(1):1 – 57, 1984.

[207] Dupont V., Pourkashanian M., Williams A., and Woolley R. The reduction of NO_x formation in natural gas burner flames. *Fuel*, 72(4):497 – 503, 1993.

[208] De Soete G. G. Overall reaction rates of NO and N_2 formation from fuel nitrogen . *Symposium (International) on Combustion*, 15(1):1093 – 1102, 1975. Fifteenth Symposium (International) on Combustion.

[209] Kandamby N., Lazopoulos G., Lockwood F. C., Perera A., and Vigevano L. Mathematical Modeling of NO_x Emission Reduction by the Use of Reburn Technology in Utility Boilers. In *ASME Int. Joint Power Generation Conference and Exhibition*, 1996.

[210] Leung K. M. and Lindstedt R. P. Detailed kinetic modeling of C_1 -C_3 alkane diffusion flames . *Combustion and Flame*, 102(12):129 – 160, 1995.

[211] Malte P. C. and Pratt D. T. Measurement of atomic oxygen and nitrogen oxides in jet-stirred combustion. *Symposium (International) on Combustion*, 15(1):1061 – 1070, 1975. Fifteenth Symposium (International) on Combustion.

[212] Lockwood F. C. and Romo-Millanes C. A. Mathematical modelling of fuel-NO emissions from pf burners. *J. Inst. Energy*, pages 144–152, 65.

[213] Smoot L. D. and Smith P. J. $\mathrm{NO_x}$ Pollutant Formation in a Turbulent Coal System. In *Coal Combustion and Gasification*, page 373, 1985.

[214] Levy J. M., Chen L. K., Sarofim A. F., and Beer J. M. NO/Char Reactions at Pulverized Coal Flame Conditions. In *In 18th Symp. (Intl.) on Combustion, The Combustion Institute.*, 1981.

[215] Kempf A. M., Geurts B. J., Ma T., Pettit M. W. A., and Stein O. T. "Quality Issues in Combustion LES. *J Sci Comput*, 49:51–64, 2011.

[216] Branley N. and Jones W. P. Large Eddy simulation of a turbulent non-premixed flame. *Combustion and Flame*, 127(12):1914 – 1934, 2001.

[217] Pitsch H. A C++ computer program for 0-D and 1-D laminar flame calculations. RWTH, Aachen.

[218] Schlichting H. *Boundary Layer Theory.* Springer, eighth edition, 2000.

[219] Kempf A. M., Lindstedt R. P., and Janicka J. Large-eddy simulation of a bluff-body stabilized nonpremixed flame. *Combustion and Flame*, 144:170–189, 2006.

[220] Al-Abdeli Y. M. and Masri A. R. Precession and Recirculation in Turbulent Swirling Isothermal Jets. *Combustion Science and Technology*, 176(5-6):645–665, 2004.

[221] Zhou L. X., Hu L. Y., and Wang F. Large-eddy simulation of turbulent combustion using different combustion models. *Fuel*, 87:3123–3131, 2008.

[222] International Flame Research. IFRF Report (Doc No. G25/y/01). Technical report, IFRF.

[223] Bergman T. L., Lavine A. S., Incropera F. P., and Dewitt D. P. *Fundamentals of Heat and Mass Transfer.* John Wiley & Sons, Ltd, seventh edition, 2011.

[224] Launder B. E., Reece G. J., and Rodi W. Progress in the development of a Reynolds-stress turbulence closure. *Journal of Fluid Mechanics*, pages 537–566, 1975.

[225] Gibson M. M. and Launder B. E. Ground effects on pressure fluctuations in the atmospheric boundary layer. *Journal of Fluid Mechanics*, 86:491–511, 1978.

[226] Poitou D., Amaya J., Hafi M. E., and Cuénot B. Analysis of the interaction between turbulent combustion and thermal radiation using unsteady coupled LES/DOM simulations . *Combustion and Flame*, 159(4):1605 – 1618, 2012.

[227] Gupta A., Haworth D. C., and Modest M. F. Turbulence-radiation interactions in large-eddy simulations of luminous and nonluminous nonpremixed flames. *Proceedings of the Combustion Institute*, 34(1):1281 – 1288, 2013.

[228] Nakod P., Krishnamoorthy G., Sami M., and Orsino S. A comparative evaluation of gray and non-gray radiation modeling strategies in oxy-coal combustion simulations. *Applied Thermal Engineering*, 54(2):422 – 432, 2013.

[229] Yin C. Nongray-Gas Effects in Modeling of Large-Scale Oxy-Fuel Combustion Processes. *Energy & Fuels*, 26(6):3349–3356, 2012.

[230] Hjärtstam S., Johansson R., Andersson K., and Johnsson F. Computational Fluid Dynamics Modeling of Oxy-Fuel Flames: The Role of Soot and Gas Radiation. *Energy & Fuels*, 26(5):2786–2797, 2012.

[231] Sazhin S. S. *An Approximation for the Absorption Coefficient of Soot in a Radiating Gas.* FLUENT Europe Ltd, 1994.

[232] Weller A. E., Rising B. W., Boiarski A. A., Nordstrom R. J., and Barrerr R. J. Experimental evaluation of firing pulverized coal in a CO_2/O_2 atmosphere. *Argonne National Laboratory*, 1985. ANL/CNSV-TM-168.

[233] Woycenko D., Ikeda I., and van de Kamp W. Combustion of pulverized coal in a mixture of oxygen and recycled flue gas. Technical Report F98/Y/1, International Flame Research Foundation, 1994.

[234] Woycenko D., van de Kamp W., and Roberts P. Combustion of pulverized coal in a mixture of oxygen and recycled flue gas. Technical Report F98/y/2, International Flame Research Foundation, 1995.